

**SEISMIC AND LITHOLOGICAL CHARACTERIZATION AND SOURCE ROCK POTENTIAL OF THE
APTIAN NASKAPI SHALE MEMBER, LOGAN CANYON FORMATION, OFFSHORE NOVA SCOTIA.**

by

Anne Catherine Hargreaves

Submitted in partial fulfillment of the requirements
for the degree of Master of Science

at

Dalhousie University
Halifax, Nova Scotia
March 2021

©Copyright by Anne Catherine Hargreaves, 2021

Table of Contents

<i>List of Tables</i>	<i>x</i>
<i>List of Figures</i>	<i>xi</i>
<i>Abstract</i>	<i>xix</i>
<i>List of Abbreviations Used</i>	<i>xx</i>
<i>Glossary</i>	<i>xxi</i>
<i>Acknowledgments</i>	<i>xxvi</i>
<i>Chapter 1: Introduction</i>	<i>1</i>
1.1 <i>Overview</i>	<i>1</i>
1.2 <i>Importance of Study</i>	<i>3</i>
1.3 <i>Area of Study</i>	<i>4</i>
1.4 <i>Primary Research Objectives and Methods</i>	<i>8</i>
1.5 <i>Thesis Questions</i>	<i>9</i>
1.6 <i>Hypothesis</i>	<i>9</i>
1.7 <i>Thesis Format</i>	<i>9</i>
<i>Chapter 2: Geological Setting</i>	<i>11</i>
2.1 <i>Introduction</i>	<i>11</i>
2.2 <i>Regional Geology and Tectonics</i>	<i>12</i>
2.3 <i>Stratigraphy of the Scotian Shelf</i>	<i>14</i>
2.4 <i>Cretaceous Period</i>	<i>15</i>
2.4.1 <i>Cretaceous Sea Level</i>	<i>16</i>
2.4.1.1 <i>The Effect of Volcanism on Sea Level</i>	<i>17</i>
2.4.1.2 <i>Water Sequestration on Land</i>	<i>18</i>
2.4.1.3 <i>Deglaciation and Isostatic Rebound</i>	<i>18</i>
2.5 <i>Cretaceous Formations</i>	<i>19</i>
2.5.1 <i>Aptian Stage</i>	<i>20</i>
2.5.2 <i>Naskapi Member</i>	<i>20</i>
2.5.3 <i>Other Cretaceous and Cenozoic Formations</i>	<i>22</i>
2.5.3.1 <i>Banquereau Formation</i>	<i>22</i>

2.5.3.2 Wyandot Formation.....	23
2.5.3.3 Petrel Member.....	23
2.5.3.4 Dawson Canyon Formation.....	24
2.5.3.5 Logan Canyon Formation.....	24
2.5.3.6 Marmora Member.....	24
2.5.3.7 Sable Member.....	25
2.5.3.8 Shortland Shale.....	25
2.5.3.9 Cree Member.....	25
2.5.3.10 Missisauga Formation – Upper Member.....	26
2.5.3.11 O-Marker.....	26
2.5.3.12 Missisauga Formation – Middle Member.....	27
2.5.3.13 Missisauga Formation – Lower Member.....	27
2.5.3.14 Verrill Canyon Formation.....	27
2.5.3.15 Abenaki Formation.....	28
2.6 Summary.....	28
Chapter 3: Ocean Circulation.....	31
3.1 Ocean Water Movement.....	31
3.1.1 Coriolis Effect.....	31
3.1.2 Ekman Transport.....	33
3.1.3 Meridional Overturning Circulation.....	34
3.1.4 Ocean Circulation and Temperature Gradients.....	35
3.1.5 $\delta^{18}\text{O}$ and Salinity.....	36
3.2 Ocean Layers.....	37
3.2.1 Depth of Sediment Disturbance.....	38
3.3 Upwelling and Downwelling Currents.....	38
3.3.1 Upwelling.....	39
3.3.2 Downwelling.....	40
3.4 Tectonics.....	40
3.4.1 Central American Seaway.....	41

3.4.2 Cretaceous Ocean Circulation Models.....	41
3.4.3 Upwelling and Downwelling Zones in Circulation Models.....	44
3.5 Summary.....	47
Chapter 4: Organic-Rich Deposits in the Proto-North Atlantic Ocean.....	48
4.1 Introduction.....	48
4.2 Source Rock Characteristics.....	48
4.2.1 Source Rock and Oil and Gas Deposits.....	49
4.3 Petroleum System Events and Processes.....	50
4.4 Organic Matter.....	51
4.4.1 Organic Facies.....	52
4.4.2 The Carbon Cycle Overview.....	52
4.4.3 Kerogen.....	53
4.4.4 Total Organic Carbon.....	55
4.4.4.1 Rock Eval Pyrolysis and Kerogen.....	55
4.4.4.1.1 van Krevelen and pseudo van Krevelen Plots.....	55
4.4.5 Climate.....	58
4.4.5.1 Milankovitch Cycles.....	59
4.4.6 Organic-Rich Shale.....	60
4.4.6.1 Black Shale.....	60
4.4.7 Sedimentation Rate.....	61
4.4.7.1 Preservation of Organic Matter.....	63
4.4.7.2 Terrigenous Sediments.....	63
4.4.7.3 Productivity.....	64
4.5 Oceanic Anoxic Events.....	64
4.5.1 Introduction.....	65
4.5.2 Oceanic Anoxic Event Characteristics.....	66
4.5.2.1 Anoxic Conditions.....	66
4.5.2.2 Biolimiting Nutrients.....	67
4.5.2.3 Positive δ^{13} Excursions.....	67

4.5.2.4 Paleogeography.....	70
4.5.2.5 Pyrite and Other Minerals	70
4.5.2.6 Marine Transgressions.....	72
4.5.2.7 Thermohaline Circulation.....	74
4.5.2.7.1 Neodymium Isotopes.....	74
4.5.2.8 Igneous and Volcanic Rocks.....	74
4.5.2.8.1 Basalts.....	74
4.5.2.8.2 Submarine Volcanoes.....	75
4.5.2.8.3 Large Igneous Provinces.....	75
4.5.2.9 Strength of Lithosphere.....	76
4.6 Cretaceous Oceanic Anoxic Events.....	78
4.7 Proto-Atlantic Aptian Organic-Rich Deposits.....	80
4.7.1 Metals in Organic Matter.....	83
4.7.2 Oxygen Isotope Data.....	83
4.7.3 Note on Fossil Assemblages and Thermal Gradients in Black Shale.....	84
4.7.4 Tethyan Organic-Rich Deposits.....	85
4.7.5 Carbonate Cycles.....	87
4.8 Proto-Atlantic Regions of Interest.....	88
4.8.1 Trinidad.....	88
4.8.2 Morocco.....	89
4.8.2.1 Moroccan Cretaceous Stratigraphy.....	91
4.8.2.2 Moroccan Sequence Stratigraphy.....	92
4.8.3 Georges Bank.....	93
4.8.4 La Luna Formation – Venezuela.....	93
4.8.5 Eastern Equatorial Atlantic.....	95
4.8.6 Eastern Pacific – Costa Rica.....	95
4.8.7 Demerara Rise.....	96
4.8.8 Offshore Angola.....	97

4.8.9 Other South Atlantic Cretaceous Black Shale Deposits.....	97
4.9 Summary.....	98
Chapter 5: Data and Methods.....	101
5.1 Data Examined.....	101
5.2 Workflow for Compiling and Interpreting Data.....	101
5.3 Cuttings Examination.....	103
5.3.1 Canstrat™ Lithology Logs.....	104
5.3.1.1 Rock Type.....	106
5.3.1.2 Rock Colour.....	107
5.3.1.3 Visual Porosity.....	108
5.3.1.4 Oil Stain.....	108
5.3.1.5 Grain Size.....	109
5.3.1.6 Cementation.....	110
5.3.2 Canstrat™ Coding.....	111
5.3.3 Sources of Error with Canstrat™ Log Data.....	113
5.3.4 Lithology Logs from Natural Resources Canada BASIN Database..	114
5.4 Wireline Log Data.....	115
5.4.1 Gamma Ray Logs.....	115
5.4.2 Resistivity Logs.....	117
5.4.3 Sonic Logs.....	118
5.4.4 Density Logs.....	119
5.4.5 Neutron Logs.....	121
5.4.6 Neutron – Density Logs.....	121
5.4.7 “Delta Log R” Method of Analysis.....	122
5.5 Mapping in Petrel™.....	125
5.5.1 Deterministic and Stochastic Algorithms.....	125
5.5.2 Facies Modeling and Petrophysical Modeling.....	127
5.6 Temperature vs. Depth Plots.....	127
5.7 Shale Analysis.....	129

5.7.1 Shale Volume Analysis.....	129
5.7.2 Total Organic Carbon.....	129
5.7.2.1 Rock Eval Pyrolysis.....	129
5.8 Cross Sections from Formation Top Picks.....	134
5.8.1 Cross Sections from Wireline Log Formation Top Picks.....	134
5.9 Seismic Interpretation.....	135
Chapter 6: Results.....	137
6.1 Introduction.....	137
6.2 Cross Sections.....	138
6.3 2D and 3D Maps of the Naskapi Member and Missisauga Formation.....	140
6.3.1 2D Structure Contour Maps.....	140
6.3.2 3D Maps.....	140
6.3.3 Isochore Map for Naskapi Vertical Thickness.....	140
6.4 NRCAN BASIN Data Maps.....	146
6.4.1 Total Organic Carbon (TOC) Map from Rock Eval Pyrolysis Data...146	
6.4.2 Vitrinite Reflectance Map.....	148
6.4.3 Temperature Map.....	150
6.4.4 Comparison of Temperature Data to Vitrinite Reflectance Data...150	
6.5 Lithological Attribute Maps of the Naskapi Member.....	152
6.5.1 Dominant Lithology as Stochastic or Deterministic Models.....	152
6.5.2 Colour.....	156
6.5.3 Limestone Content.....	160
6.5.4 Shale Content.....	160
6.5.5 Sand Content.....	160
6.5.6 Siltstone Content.....	165
6.5.7 Siderite Content.....	165
6.5.8 Marlstone Content.....	165
6.5.9 Clay Content.....	169
6.5.10 Fossil Debris Content.....	169

6.5.11 Green Shale Content.....	169
6.5.12 Calcite Cement Content.....	169
6.5.13 Oil Stain.....	174
6.5.14 Visual Porosity.....	179
6.6 Continuous Wireline Log Data Maps in 2D and 3D.....	188
6.6.1 Shale Volume (V_{shale}) Calculated from Gamma Ray Logs Mapped in 2D.....	190
6.6.2 Gamma Ray Log Values Mapped in 2D.....	191
6.6.3 Density Log Values Mapped in 2D.....	192
6.6.4 Resistivity Log Values Mapped in 2D.....	194
6.6.5 Sonic Log Values Mapped in 2D and Modelled in 3D.....	195
6.6.5.1 Velocity Calculated from Sonic Logs Mapped in 2D and Modelled in 3D.....	198
6.7 Seismic Horizon Maps.....	200
6.7.1 2D & 3D Maps of the Naskapi Member & Missisauga Formation.....	200
Chapter 7: Discussion.....	206
7.1 Discussion of Controls on Naskapi Member Deposition and Organic Content.....	206
7.2 Thermal Maturity.....	209
7.3 Cross Sections.....	212
7.4 Lithology Data Maps.....	212
7.5 Wireline Data Maps.....	214
Chapter 8: Conclusion and Recommendations.....	216
8.1 Conclusions.....	216
8.2 Future Work Recommendations.....	217
References.....	218
List of Appendices.....	242
Appendix A: List of Canstrat Lithology Logs.....	242
Appendix B: Naskapi Isopach for Wells in Study Area.....	248

<i>Appendix C: Intervals of Naskapi Member Mapped – Lithology Counts.....</i>	<i>253</i>
<i>Appendix D: Canstrat LAS Mnemonics.....</i>	<i>260</i>
<i>Appendix E: Canstrat Log Lithology Symbols.....</i>	<i>266</i>
<i>Appendix F: Naskapi DST Temperature Values Plotted.....</i>	<i>273</i>
<i>Appendix G: Naskapi TOC Values Plotted.....</i>	<i>275</i>
<i>Appendix H: Cross Sections – Well Lists and Map View.....</i>	<i>287</i>
<i>Appendix I: Average Vitrinite Reflectance Values.....</i>	<i>297</i>
<i>Appendix J: Cross Sections 1-9.....</i>	<i>300</i>
<i>Appendix K: Anne Hargreaves Thesis Committee.....</i>	<i>303</i>
<i>Appendix L: List of Equations.....</i>	<i>304</i>
<i>Appendix M: Extended Abstract.....</i>	<i>305</i>

List of Tables

Table 2.1: <i>Comparison of age ranges from various studies focused on determination of the age of the Cretaceous Aptian Stage.....</i>	20
Table 4.1: <i>Oceanic anoxic events of the Cretaceous.....</i>	79
Table 5.1: <i>Density values of minerals, fluids, and hydrocarbons.....</i>	120
Table 5.2: <i>Lithology types and their typical response in the three main wireline logs...132</i>	
Table 5.3: <i>Source rock generative potential using TOC, S1, and HI to describe the quality of a source rock.....</i>	132
Table 5.4: <i>Table of Hydrogen Index (HI) values and S2/S3 ratios generated from a pyrogram and the resulting hydrocarbon type.....</i>	133
Table 5.5: <i>Thermal Maturation determination using results from the pyrogram that can be used to delineate the top and bottom of the oil window in a formation.....</i>	133

List of Figures

Figure 1.1: Area of study, Scotian Basin, offshore Nova Scotia.....	5
Figure 1.2: Location of study area key wells on the Scotian Shelf that are listed in Appendix A.....	6
Figure 1.3: The key wells on the ExxonMobil MegaMerge seismic area used in the study.....	7
Figure 2.1: A simple Wilson cycle opening phase as seen in the proto-Central-Atlantic...	11
Figure 2.2: Basins on the Scotian Margin.....	12
Figure 2.3: Generalized chronostratigraphic chart of the Scotian Basin.....	14
Figure 2.4: Late Cretaceous schematic of the geography, topography, and bathymetry of the world after the breakup of Pangea.....	15
Figure 2.5: General climatic paleotemperature during the Triassic, Jurassic, and Cretaceous periods.....	16
Figure 2.6: Chronostratigraphic chart of the Cretaceous Period from 145 – 66 Ma.....	16
Figure 2.7: Lithology variations of the Naskapi Member as observed in conventional cored from Sable C-67, and Grand Pre G-08 wells.....	22
Figure 3.1: Global winds and relationship to latitude.....	32
Figure 3.2: The Ekman spiral.....	33
Figure 3.3: Chart showing the present-day meridional overturning circulation.....	34
Figure 3.4: Ocean layers profile – Greenland to Antarctica longitudinal transect.....	37
Figure 3.5: Model of the mean velocity vectors of surface waters and at 4 km subsurface in $cm\ s^{-1}$	43

Figure 3.6: <i>This figure of the Cretaceous continental configurations is a model by Trabucho-Alexandre which clearly shows the areas where the average vertical velocity points to areas of upwelling (positive velocity)</i>	46
Figure 4.1: <i>Petroleum systems event chart for the Scotian Basin, offshore Nova Scotia</i>	51
Figure 4.2: <i>Schematic outlining present day carbon flux</i>	53
Figure 4.3: <i>Types of Kerogen and their potential for generating hydrocarbons</i>	54
Figure 4.4: <i>Van Krevelen Diagram</i>	56
Figure 4.5: <i>Pseudo Van Krevelen diagram showing data plotted from a pyrogram</i>	57
Figure 4.6: <i>Schematic showing the major processes at work during an oceanic anoxic event (OAE)</i>	65
Figure 4.7: <i>Ocean stratification during an oceanic anoxic event</i>	67
Figure 4.8: <i>Carbon isotope ($\delta^{13}C_{org}$) and sea level curves from the Barremian through the Aptian, Albian, Cenomanian, and Turonian of the Cretaceous Period</i>	69
Figure 4.9: <i>Fossil and mineral constituent alteration patterns during the Upper Aptian-Lower Albian OAE 1b event</i>	73
Figure 4.10: <i>This chart shows the Mesozoic with the main extinction events, emplacement of large igneous provinces (LIPs) and continental flood basalts</i>	76
Figure 4.11: <i>Stratigraphy of the Scotian Basin during the Cretaceous Period, 65.5-145.5 Ma</i>	78
Figure 4.12: <i>Configuration of the continental areas during the Cretaceous (Cenomanian-Albian) time at approximately 100 Ma +/- 10 Ma</i>	82
Figure 4.13: <i>Generalized Trinidadian Stratigraphy</i>	89
Figure 4.14: <i>Offshore Moroccan Cretaceous stratigraphy</i>	91

Figure 4.15: <i>Correlation of lithostratigraphic units in the Georges Bank Basin, offshore eastern USA (Massachusetts area)</i>	93
Figure 4.16: <i>Generalized stratigraphic column of the Alturitas oilfield in Venezuela</i>	94
Figure 5.1: <i>Flow chart outlining workflow with available data</i>	103
Figure 5.2: <i>An example of a litholog prepared by Canstrat™</i>	104
Figure 5.3: <i>Example of percentage values (50%, 75% and 90%) of major lithological constituent of cuttings sample</i>	106
Figure 5.4: <i>Canstrat™ colour coding of rock types</i>	107
Figure 5.5: <i>U.S. Wentworth scale of grain size estimation</i>	109
Figure 5.6: <i>Grain roundness and angularity comparison</i>	110
Figure 5.7: <i>Grain sorting comparator</i>	110
Figure 5.8: <i>Canstrat™ log number EC39 (Sable Island E-48)</i>	111
Figure 5.9: <i>Canstrat™ log coded in ASCII format</i>	112
Figure 5.10: <i>An example in detail of a line of lithology interval coding from Figure 5.9</i>	112
Figure 5.11: <i>LAS 2.0 header for Triumph P-50</i>	113
Figure 5.12: <i>Log sample from the Missisauga H-54 well through a section showing the Naskapi Member</i>	115
Figure 5.13: <i>Sample of a Gamma Ray log</i>	116
Figure 5.14: <i>An example the Delta Log R method for determining the organic richness of a sandstone and shale succession, South Venture O-59</i>	124

Figure 5.15: <i>Differences between a deterministic algorithm and a stochastic algorithm.....</i>	<i>126</i>
Figure 5.16: <i>Illustrations showing the difference between a spline and kriging.....</i>	<i>126</i>
Figure 5.17: <i>Pyrogram showing the change of organic compounds from the rock sample with increasing time and heat.....</i>	<i>131</i>
Figure 5.18: <i>Schematic map of the cross sections and locations used in the study.....</i>	<i>135</i>
Figure 5.19: <i>Plan view of MegaMerge Cube and the layout of the seismic lines used in creating 2D and 3D maps of the Naskapi Member and Missisauga Formation tops.....</i>	<i>135</i>
Figure 6.1: <i>Cross sections sample through wells Ojibwa E-07 and Naskapi N-30.....</i>	<i>139</i>
Figure 6.2: <i>Contour map of the elevation depth of the top of the Naskapi Member as determined from lithostratigraphic picks from the cross section utilizing gamma ray, density, sonic, and resistivity logs.....</i>	<i>141</i>
Figure 6.3: <i>Contour map of the elevation depth of the top of the Missisauga Formation as determined from lithostratigraphic picks from the cross section utilizing gamma ray, density, sonic, and resistivity logs.....</i>	<i>142</i>
Figure 6.4: <i>3D model of the top of the Naskapi Member (TVDss m).....</i>	<i>143</i>
Figure 6.5: <i>3D model of the depth of the Missisauga Formation (TVDss m).....</i>	<i>144</i>
Figure 6.6: <i>Isochore map showing the thickness of the Naskapi Member.....</i>	<i>145</i>
Figure 6.7: <i>Total organic carbon (TOC) values as determined by GSC data in the BASIN Database.....</i>	<i>147</i>
Figure 6.8: <i>Vitrinite reflectance (VR) values as determined by GSC data in the BASIN Database.....</i>	<i>149</i>
Figure 6.9: <i>Temperature values from DST data as reported to the GSC in the BASIN Database.....</i>	<i>151</i>

Figure 6.10: Example of a deterministic algorithm, where the grid cells between the known datapoints (wells) are evenly and smoothly contoured.....	154
Figure 6.11: Example with the same data points (wells) as Figure 6.10, but now exhibiting a stochastic algorithm, where random variability has been factored in.....	155
Figure 6.12: Example of colours as indicated by Canstrat™ descriptions from drill cuttings.....	157
Figure 6.13: Quality assurance map showing the proportion of the colour that is green.....	158
Figure 6.14: Map showing the percentage of red-coloured deposits in the Naskapi Member.....	159
Figure 6.15: Meters of the Naskapi Member with limestone as the dominant lithology (>50%) as logged in drill cuttings by Canstrat™	161
Figure 6.16: Meters of Naskapi Member with shale as the dominant lithology (>50%) as logged in drill cuttings by Canstrat™	162
Figure 6.17: Net to gross map showing the proportion of shale to the total formation.....	163
Figure 6.18: Meters of Naskapi Member with sand as the dominant lithology (>50%) as logged in drill cuttings by Canstrat™	164
Figure 6.19: Meters of the Naskapi Member with siltstone as the dominant lithology (>50%) as logged in drill cuttings by Canstrat™	166
Figure 6.20: Meters of the Naskapi Member with siderite as the dominant lithology (>50%) as logged in drill cuttings by Canstrat™	167
Figure 6.21: Meters of the Naskapi Member with marlstone as the dominant lithology (>50%) as logged in drill cuttings by Canstrat™	168
Figure 6.22: Meters of Naskapi Member with clay as the dominant lithology (>50%) as logged in drill cuttings by Canstrat™	170

Figure 6.23: <i>Canstrat™</i> data indicating if fossil debris is present in the drill cuttings.....	171
Figure 6.24: <i>Canstrat™</i> logs upscaled to a 60-layer Naskapi model with layers measuring 2 – 3 meters each using a sequential indicator simulation and is an aggregated proportional quality assurance map.....	172
Figure 6.25: Map showing the percentage of diagenetic calcite cement found in the cuttings samples as analyzed by <i>Canstrat™</i>	173
Figure 6.26: Meters of the Naskapi Member with total oil staining (sum of good, medium, and questionable) as logged by <i>Canstrat™</i>	175
Figure 6.27: Meters of the Naskapi Member with questionable oil stain as logged by <i>Canstrat™</i>	176
Figure 6.28: Meters of the Naskapi Member with medium oil stain as logged by <i>Canstrat™</i>	177
Figure 6.29: Meters of the Naskapi Member with good oil stain as logged by <i>Canstrat™</i>	178
Figure 6.30: Meters of Naskapi Member silts and sands with 3 – 6 % visual porosity as logged by <i>Canstrat™</i>	180
Figure 6.31: Meters of Naskapi Member silts and sands with 7 – 9 % visual porosity as logged by <i>Canstrat™</i>	181
Figure 6.32: Meters of Naskapi Member silts and sands with 10 – 12 % visual porosity as logged by <i>Canstrat™</i>	182
Figure 6.33: Meters of Naskapi Member silts and sands with 13 – 15% visual porosity as logged by <i>Canstrat™</i>	183
Figure 6.34: Meters of Naskapi Member silts and sands with 16 – 20 % visual porosity as logged by <i>Canstrat™</i>	184
Figure 6.35: Meters of Naskapi Member silts and sands with >20 % visual porosity as logged by <i>Canstrat™</i>	185
Figure 6.36: Meters of Naskapi Member silts and sands with 33 % or maximum possible visual porosity as logged by <i>Canstrat™</i>	186

Figure 6.37: Meters of Naskapi Member that show a summary of all visual porosity estimates as logged by Canstrat™.....	187
Figure 6.38: The Shale volume calculation is the percentage of the total meters of Naskapi Member that is composed of shale, using the gamma ray wireline log to calculate.....	190
Figure 6.39: The map of gamma ray values made in Petrel™, showing the average of gamma ray values using sequential Gaussian simulation.....	191
Figure 6.40: Map of the values from the density log in g/cm ³	192
Figure 6.41: Quality assurance map of the density values.	193
Figure 6.42: Quality assurance map showing average resistivity values using sequential Gaussian simulation.....	194
Figure 6.43: Map of the sonic log values.....	195
Figure 6.44: Quality assurance map of the AC (sonic) logs show the average values.....	196
Figure 6.45: Sonic values modelled in 3D.	197
Figure 6.46: Velocity map calculated from the sonic log values.....	198
Figure 6.47: 3D model of velocity data.....	199
Figure 6.48: Cross section view of a seismic section showing Sable Island C-67, West Venture N-91, and Arcadia J-16 wells, which were used to pick the Naskapi Member and Missisauga Formation tops.....	201
Figure 6.49: Contour map of the Naskapi Member horizon from seismic interpretation of the MegaMerge cube.....	202
Figure 6.50: Contour map of the Missisauga Formation horizon depths from seismic interpretation of the MegaMerge cube.....	203
Figure 6.51: Naskapi Member horizon surface in 3D from seismic interpretation in the MegaMerge cube.....	204
Figure 6.52: 3D image of the Missisauga Formation horizon surface as expressed from seismic interpretation in the MegaMerge cube.....	205

Figure 7.1: TOC, VR, Temperature, and shale volume maps as presented in Chapter 6, shown here to compare to comment on thermal alteration of organic matter in the Naskapi Member.....210

Figure 7.2: Sand content in the study area, with the outline of the Sable Island Delta.....212

Abstract

The fluvial-deltaic successions of the Cretaceous Logan Canyon Formation in the Sable Subbasin, offshore Nova Scotia, have been one of the main sources of hydrocarbon production for decades. The distal and laterally equivalent strata of the Logan Canyon Formation (Aptian – Albian) are transgressive shale sequences within the sand-rich successions, appearing to correspond to global oceanic anoxic events (OAEs). The Aptian Naskapi Member of the Logan Canyon Formation is one of these shale sequences, and the focus of this study. The distal Cretaceous/Jurassic shale section offshore Nova Scotia is considered source rock, although it is uncertain whether there are sufficient concentrations of strata with elevated total organic carbon (TOC) values to form the continuous fluid phase necessary for effective hydrocarbon generation and migration. When comparing existing levels of TOC from the Scotian Basin with those from OAEs elsewhere, the Cretaceous Naskapi Member exhibits lower levels of organic matter.

List of Abbreviations Used

C_{org} – Organic carbon

DST – Drill Stem Test

OAE – Oceanic Anoxic Event

PFA – Play Fairway Analysis

TOC – Total Organic Carbon

VR – Vitrinite Reflectance

Glossary

Abysal – The deepest region of the ocean, greater than 2000 m depth where fine grained sediments fall out of suspension at a slow rate and the depositional environment has very low energy, is cold, and lacks sunlight.

Accommodation space – The volume of space available for sediments to be deposited, which is a function of eustasy, subsidence and sedimentation rate.

Active margin – The boundary of two colliding continental and oceanic lithospheric plates, which include subduction zones, colliding continental plates, or spreading centers created during continental rifting.

Aggradation – Occurs during periods where sediment supply and accommodation space are in balance. Sediment layers are deposited on top of each other and build up vertically.

Allochthonous – Deposits are found in a place different from where they were formed. Movement could be by gravity flow, landslides, or fault movements.

Anoxic – The absence of free oxygen in the environment.

Autochthonous – Deposits remain in the place that they were formed and have not been transported.

Bitumen – Bitumen refers to the portion of naturally occurring inflammable organic matter extractable from rock using organic solvents and is solid, odiferous and brown or black in colour. Kerogen, as it is subjected to increased burial and heating, will yield bitumen, then liquid hydrocarbons followed by gas. Asphalt and mineral wax are types of bitumen.

Carbon flux – The rate of exchange of carbon between the atmosphere and carbon reservoirs, or 'sinks', which occur on land through biota and soil, and the oceans at the surface, biota and the deep ocean.

Chronostratigraphic horizons – Those horizons which were deposited at the same time. Also known as coeval horizons.

Coeval horizons – Those horizons which were deposited at the same time. Also known as chronostratigraphic horizons.

Coriolis effect – Coriolis effect deflects surface waters to the right of flow in the Northern Hemisphere, and to the left of flow in the Southern Hemisphere due to the earth's rotation with intensity increasing with distance from the equator.

Critical moment – The beginning of a viable petroleum system, where source rock is buried at the maximum depth where it has the greatest likelihood of being entrapped and preserved.

Deterministic – A kriging algorithm which will always give the same result with the same input data and where grid cells between two datapoints will be evenly smoothly contoured.

Effective Source Rock – Rock which contains organic matter and is producing in sufficient economic quantities.

Epibathyl – Deep marine region.

Eustasy – Refers to the variation in global sea levels resulting from changes in the volume of ocean basins due to tectonic plate movements, and from climatic changes affecting the amount of water stored in glaciers and icecaps.

Euxinic – Refers to sulfidic anoxic water conditions, which are depleted of oxygen and rich in sulfide (hydrogen sulfide). Euxinic water bodies are stratified with an oxic, highly productive, thin upper layer and an anoxic, sulfidic, bottom layer. A modern-day example would be the Black Sea.

Facies – Defined as coeval sediments which are spatially segregated deposited in a certain depositional environment or by a specific mechanism.

Guyot – An underwater volcanic seamount or table mount at least 200 m below the water surface.

Hadley Cell – Atmospheric circulation in the low latitudes, from the equator to 30 degrees north or south.

Isochron – A line of equal distance in two-way travel time between two seismic surfaces.

Isopach – A line of the equal true thickness of an interval perpendicular to the bedding plane.

Isochore – A line of equal vertical thickness of an interval.

Kerogen – Part of naturally occurring, solid, organic matter, which cannot be extracted by organic solvents. It is found in source rock and made from terrestrial woody plant material or marine algae and has a higher molecular weight than bitumen. As kerogen is

subject to heating and burial, hydrocarbons are produced in the order of: bitumen, heavy oil, liquid hydrocarbons, and gas.

- Type I kerogen is algal/amorphous kerogen (oil prone);
- Type II is mixed terrestrial and marine sourced (waxy oil prone); and
- Type III is woody terrestrial material (gas prone); and
- Type IV is a non-productive hydrocarbon, made of residual kerogen, dead carbon or inertinite.

Litholog – A graphical representation of the lithology of logged intervals in a well, where cuttings samples are taken every 5 meters (10 feet in old wells) and described for rock type, grain size, texture, colour and other parameters observed.

Lithostratigraphic horizon picks – Based on the rock properties of a formation, regardless of the age. Lithostratigraphic picks are not necessarily coeval.

Neritic – A marine zone found between low tide and the continental shelf edge down to a depth of approximately 200 m. Neritic marine organisms live in this zone with exposure to moderate sunlight.

Oceanic Anoxic Events (OAE's) – These are brief periods of time (approximately $<10^6$ years) where marine oxygen is very low (anoxic) resulting in organic-rich laminar black shales with carbon excursions and little evidence of biologic activity.

Oligotrophic – Unproductive, very low primary productivity, due to a low level of nutrients, but a high level of oxygen.

Paleorheology – History of flow.

Passive margin – A margin such as offshore east coast of North America, or the Gulf Coast. There may be fault blocks of sediments that have slumped and show rotation. After a significant period of time has passed and the continents move away from the spreading center, the margin becomes passive.

pCO₂ – Oceanography term referring to the partial pressure of carbon dioxide in the ocean surface waters.

Petroleum system - Components and processes required to generate and store hydrocarbons, which include mature source rock, a migration path, a reservoir rock, a trap, and an effective seal. The timing of generation, migration and accumulation details are required, and is usually displayed in a events chart with the x axis showing time and the y axis showing the components and processes.

Petroleum system modeling - Modelling of a sedimentary basin showing the components necessary to form petroleum, including source rock, reservoir rock, trap,

seal, and the timing of their formation. A 3D model of geological, geophysical and engineering data is formed and reveal if petroleum is present and how much is trapped. These models can aid in exploration, predict pore pressure and are used to plan well and field development, find sweet spots and shale gas deposits. It is viewed on a large scale, unlike reservoir simulation which is on a smaller scale.

Potential Source Rock – Rock which contains sufficient organic matter, which if subjected to heat and pressure, could generate and expel hydrocarbons.

Prodelta – The part of the delta that is below the depth of wave action, which extends beyond the delta front and slopes down into the basin.

Pyrolysis – Geochemical analysis whereby a rock sample is heated in an inert gas under controlled conditions to the point of generating hydrocarbons in order to assess its source rock potential, its TOC values, thermal maturity, and the quality of hydrocarbons it could generate. During pyrolysis, large HC molecules are broken down into smaller ones.

Regression – Sea level drops and the shoreline moves basinward.

Relic Source Rock – Rock which was generating and expelling hydrocarbons but stopped prior to using up its supply of organic matter, due to thermal cooling.

Source Rock – Defined as a rock (shale or limestone usually) with sufficient organic matter (1% or more organic matter and .5% TOC or more) to generate and expel hydrocarbons through biogenic or thermal processes. Source rocks of a marine origin are oil-prone, and terrestrial source rocks are gas-prone as a rule. In reservoirs of shale gas, the source rock is also the reservoir rock.

Spent Source Rock – Rock which has become overmature or does not have sufficient organic matter left so is unable to generate or expel hydrocarbons.

Spline – A mathematic term for connecting data points with a smooth line. The variable lambda in the algorithm controls the direction and curvature of the line which does not necessarily pass through all data points but is affected by their location.

Stochastic – Stochastic algorithms use a random element added to the input data, with that each time the algorithm is applied, a different result will be seen. This is more realistic, as it factors in variability, rather than applying a smooth even contour between data points.

Total Organic Carbon (TOC) – Refers to the concentration of organic matter in a source rock expressed as weight percent of organic carbon. 0.5% of TOC by weight percent is

the minimum required to be classed as an effective source rock. 2% is considered minimum for a shale gas reservoir.

Transgression – Where sea level rises, and the shoreline migrates landward.

Acknowledgements

Many thanks to Professor Grant Wach, the Basin and Reservoir Lab at Dalhousie University, Dr. Ricardo Silva, and the *Source Rock and Geochemistry of the Central Atlantic Margins* consortium for providing a place for me to research this project. Also, the help from my committee members, David E. Brown and Bill Richards, was invaluable, along with their input in the reviewing process. Neil Watson graciously contributed much advice on petrophysics. Proof-reading and academic suggestions from Dr. Mryka Hall-Beyer were extremely helpful. Additional proofreading and lifelong friendship from Kimberley Freeman-Unterganschnigg and Gail Swystun-Abbi was much appreciated. Assistance from Trudy Lewis, Kallen Rutledge, and Kristie McVicar in the Basin and Reservoir Lab, and Norma Keeping, Ann Bannon and Darlene van de Rijt in the Earth Sciences office has been most helpful. Special thanks to Lauren Morris for her thorough editing during the final preparation of the thesis. Camaraderie and friendship from fellow graduate students were much appreciated, especially from Carlos Wong, Taylor Campbell, Charlie Carlisle, Natasha Morrison, Kenn Martyns-Yellowe and Carla Skinner.

Petrel™ software was donated to Dalhousie University, Professor Wach, principal investigator, by Schlumberger, and lithological data was donated by Canstrat™ (Canadian Stratigraphic Services (2000) Ltd.). Software tutoring and geological discussions were kindly provided by Bill Richards, and consultation regarding lithological summary data was generously provided by Ros Zajac of Danic-Geo Consulting Ltd., Calgary.

Heartfelt thanks to Dr. P.S. Simony and the late Dr. L.V. Hills, who willingly gave me references to pursue my studies at Dalhousie, many years after working for them at the University of Calgary. I am also thankful for employers who in the past have facilitated my learning and mentored me in the machinations of the industry.

Last, but not least, I could not have accomplished this without the encouragement and support of my husband Dave Hargreaves and daughters Holly and Stephanie. I am forever thankful for the encouragement my late father, Salomon Flury, who introduced me to the energy industry and encouraged me to pursue a career in science.

Chapter 1: Introduction

1.1 Overview

The Sable Subbasin is the main depocenter in the Scotian Basin, offshore Nova Scotia, Canada. Virtually all known oil and gas production, discoveries, and shows within this Subbasin have been made in the fluvial-deltaic sequences of the Dawson Canyon (Upper Cretaceous), Logan Canyon (Lower Cretaceous), the Missisauga (Lower Cretaceous and Upper Jurassic) and the MicMac (Upper Jurassic) formations. Source rocks for these hydrocarbon accumulations are interpreted, via aromatic biomarker fingerprinting, to be Upper Jurassic Verrill Canyon Formation shales (Mukhopadhyay, 2012). However, largely because of contamination from drilling fluids, Fowler (2016) commented that determining the source rocks of known hydrocarbon accumulations in the Sable Subbasin is difficult, and there is still not an unequivocal source rock correlation. This leads to speculation on the possible existence of Cretaceous organic-rich intervals and potential source rocks, for example as seen in the Play Fairway Analysis (Beicip-Franlab, 2011) where the Naskapi Member is considered a minor source rock.

Oceanic anoxic events (OAE's) were episodes of widespread marine anoxia where large amounts of organic carbon were created, buried, and preserved on the sea floor beneath oxygen-poor bottom waters which lacked significant sea water circulation (Turgeon and Creasor, 2008). Organic-rich shales have been noted as abundant in early and mid-Cretaceous deposits from the deep North Atlantic (Summerhayes, 1987, Trabucho-Alexandre et al., 2010). The Aptian Naskapi Member is correlative with the Early Aptian laminated organic mudstones (LOMs) in the Tethys region and in Western Europe, including the Selli Level (Chavez et al., 2016).

In the Scotian Basin, the Early Cretaceous was typified by the fluvial-deltaic deposits of the Missisauga and Logan Canyon formations with the Late Cretaceous typified by largely transgressive shales of the Dawson Canyon Formation, and the chalky Wyandot Formation (Wade and MacLean, 1990). Sediments of the Sable Delta were deposited during a time of rapid subsidence with high sediment supply transgressing

from east of the Abenaki Bank from the Upper Jurassic Oxfordian through to the Upper Cretaceous (Wade and MacLean, 1990).

The Logan Canyon Formation contains four members: in ascending order, Naskapi, Cree, Sable, and Marmora. Two of these are major transgressive shale tongues; the Naskapi as the basal unit, and the Sable near the top (Wade and MacLean, 1990; Deptuck and Kendall, 2012). The Naskapi separates the sand-rich strata of the Missisauga Formation and the Logan Canyon Formation Cree Member (Wade and MacLean, 1990). Primarily composed of varicoloured shale ranging from yellowish-brown to green-grey and reddish-brown, it is interbedded with sand and silt layers and thickens seaward, while northwards, the Naskapi becomes sandier (Wade and MacLean, 1990). Examination of microfossils indicates tidal flat to marginal marine depositional environment, thus indicating a transgressive phase within the sands of the Sable Delta (Wade and MacLean, 1990).

Pe-Piper and Piper (2004) proposed the cause of elevated sea level and Naskapi Member deposition was due to dextral strike-slip movement along the Cobequid – Chedabucto fault extending west to east across mainland Nova Scotia and across the southwest Grand Banks of Newfoundland. This dextral motion caused extension in the Laurentian Subbasin resulting in a marked, rapid subsidence on the Scotian Margin and a reduction in sediment supply during the Aptian. An uplift in the early Paleozoic Meguma Terrane south of the fault during deposition of the Aptian Naskapi Member disrupted drainage systems and decreased the amount of sediment deposited in the Scotian Basin with sediments diverted to the Fundy Basin, and beyond. As a result, the sedimentation rate of the Naskapi is lower compared to the rest of the Logan Canyon Formation (Piper et al., 2011; Chavez et al., 2016). The Naskapi Member transgression could therefore have been a result of tectonic allocyclic action rather than autocyclic sedimentary processes.

Climate models for the mid-Cretaceous point to a thermohaline circulation that was stronger globally than present today (Trabucho-Alexandre et al., 2010). Estuarine circulation of intermediate depth ocean waters flowing eastward into the North Atlantic

Basin through the central American seaway brought productive waters to the euphotic zone, which encouraged organic-rich sediment deposition in the North Atlantic. An estuarine circulation combined with upwelling of subsurface waters can create a nutrient trap of organic-rich deposits, and the resulting high production and high deposition rate can create anoxic conditions in bottom waters producing an Oceanic Anoxic Event (OAE). However, in times of high sea level, current reversals can occur affecting organic-rich deposition in basins (Trabucho-Alexandre et al., 2010). A sea-level highstand can affect accumulation of marine organic matter in bottom sediments and result in the entrapment of clastic material near coastal areas and dilute the richness of organic matter (Trabucho-Alexandre et al., 2010). Thus, the high delta-derived sediment load which was focused in the Sable Subbasin during the Cretaceous would have served to dilute the amount of organic matter deposited with entrapped clastics during the Naskapi sea level highstand. As well, variations in the direction, strength, and productivity of ocean currents to the area would have affected the abundance of organically rich deposits.

Identifying the extent of potential source rocks and organic-rich intervals, if any, for the Cretaceous would potentially aid future petroleum exploration in the Scotian Basin, and is addressed here by mapping the seismic and lithological characteristics, total organic carbon content, and vitrinite reflectance values of the most significant Cretaceous shale, the transgressive Aptian Naskapi Member of the Logan Canyon Formation.

1.2 Importance of Study

The Source Rock and Geochemistry of the Central Atlantic Margins consortium, led by Professor Grant D. Wach and Dr. Ricardo L. Silva of the Basin and Reservoir Lab at Dalhousie University as the principal investigators, was formed to determine known, probable, and possible source rocks in basins offshore Nova Scotia, Newfoundland, Labrador, and Ireland (Silva et al., 2015). This has been achieved by re-evaluating existing data, integrating these data with time equivalent analog source data from the

eastern Atlantic Margin, and augmenting the existing databases comprising source rock and oceanic anoxic event data.

Recent research undertaken by the Offshore Energy Research Association of Nova Scotia (OERA) and the Nova Scotia Department of Energy and Mines (NSDEM) concluded that strata in the Sable Subbasin's Cretaceous succession does not exhibit sufficient total organic carbon to constitute source rock (unlike the underlying Jurassic section which is interpreted to have sourced the existing and depleted resource) (Beicip-Franlab, 2016). Determining and understanding the reasons for this enables a better understanding of the subbasin and aids in effectively de-risking petroleum exploration. The current study aims primarily to develop hypotheses to explain this unexpected finding.

1.3 Area of Study

The area of study for this thesis is the Sable Subbasin on the Scotian Shelf, offshore Nova Scotia. The following figures 1.1 – 1.3 outline the major geographical components of the study area. Wells included in the study are in the Sable Subbasin and adjacent subbasins and structural elements.

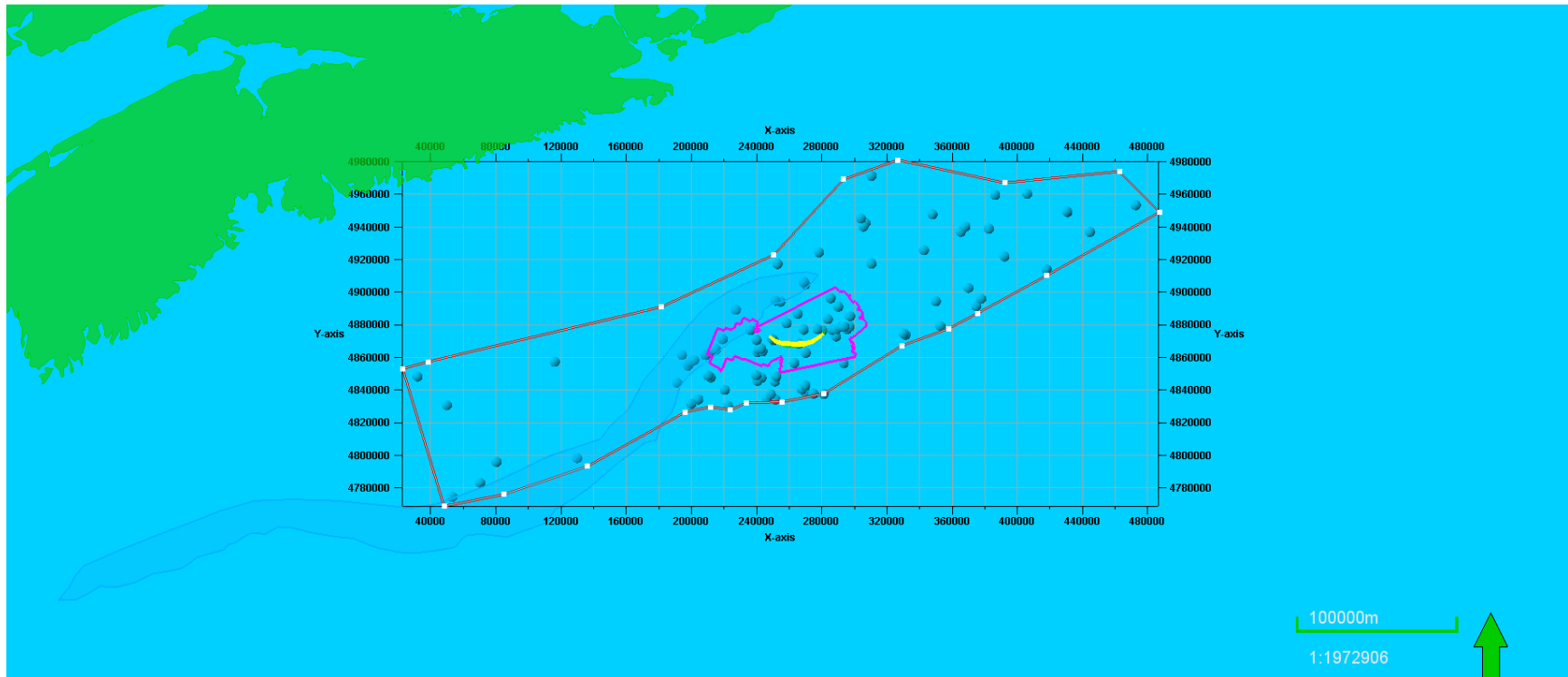


Figure 1.1: Area of study, Scotian Basin, offshore Nova Scotia. The outer grey polygon indicates the main area of study. The violet outline shows the extent of the seismic data used in this study (referred to as the ExxonMobil MegaMerge cube), inside of which is Sable Island (yellow crescent). The coastline of Nova Scotia is in the northwest corner (green, top left). The location of the Late Jurassic Abenaki carbonate Bank is indicated by the shaded blue snake-like shape trending southwest to northeast ending near Sable Island.

1.4 Primary Research Objectives and Methods

The primary objectives is to investigate the Naskapi Member to find:

- a) the stratigraphy, sedimentology, and diagenesis as interpreted from wireline, litholog, and seismic survey data in the study area,
- b) the extent of organic-rich intervals and/or potential source rocks,
- c) the oceanic and atmospheric conditions in the Cretaceous paleo Atlantic which may have affected the deposition and accumulation of organic-rich deposits in the Scotian Basin, and
- d) compare and/or contrast with Cretaceous organic-rich intervals and anoxic events found in other circum-Atlantic Ocean basins.

The following methods were used to fulfill the primary research objectives:

- 1) Literature review of recent research in Cretaceous ocean current modeling and sedimentation rates for the Scotian Basin.
- 2) Retrieval and analysis of available wireline data from wireline logs and lithostratigraphic data from analysis of drill cuttings and cores.
- 3) Creation of isochore maps showing the shale distribution.
- 4) Mapping of potential source intervals as determined by the Delta Log R (Passey) method.
- 5) Maps and models of the existing lithological attributes as identified from cuttings and core descriptions.
- 6) A series of cross sections combining lithology and wireline log data.
- 7) Models from seismic interpretations of the Naskapi Member horizon (top and base).
- 8) Comparison of total organic carbon levels in the Scotian Basin strata to known total organic carbon levels preserved in other basins in the paleo-Atlantic Ocean.

1.5 Thesis Questions

- a) What are the geometrical, lithological, petrophysical, organic, seismic, thermal, and pressure characteristics of the transgressive Naskapi Member as seen on the Scotian Shelf, offshore Nova Scotia? After examining these characteristics, could the Naskapi Member be interpreted as a viable source rock?
- b) Recent research by the Offshore Energy Research Association of Nova Scotia (OERA) and the Nova Scotia Department of Energy and Mines (NSDEM) as presented in their Play Fairway Analysis (2016) concludes that the Naskapi Member does not constitute a viable source rock. Therefore, why does the Naskapi Shale Member of the Logan Canyon Formation not exhibit sufficient levels of preserved organic matter, or share characteristics from oceanic anoxic events seen elsewhere in Cretaceous strata from other circum-Atlantic basins?

1.6 Hypothesis

The Scotian Basin did not accumulate or preserve significant amounts of organic-rich shale necessary to create effective regional source rock during the Cretaceous (Aptian) global oceanic anoxic events, as is seen elsewhere, due to:

- a) A high delta-derived sediment load focused in the Sable Subbasin during the Cretaceous that resulted in high dilution of organic matter by entrapped clastic material.
- b) The direction and strength of the ocean current regime during that time was not conducive for sufficient preservation of organic matter.

1.7 Thesis Format

Chapter 1 introduces the study area and outline of the main thesis questions, hypotheses, methods, and objectives. Chapter 2 covers the regional geological setting and specifics regarding the Cretaceous Period in this area, including sea level, volcanism, sedimentation, and formation descriptions from the study area. Chapter 3 examines characteristics of past and present ocean currents relevant to this study. Chapter 4

outlines source rocks, including the definition of the carbon cycle, total organic carbon, and kerogen, as well as a section on coeval organic-rich intervals found elsewhere in the paleo Atlantic Ocean. This is concluded with a discussion of oceanic anoxic events, their causes, and attributes. Chapter 5 describes methods and techniques used in this study, such as cross sections, cuttings examinations, wireline logging techniques, shale volume determination, sedimentation rates, sequence stratigraphy and modeling. Chapter 6 outlines the results, with supporting data, maps and cross sections presented in the figures, tables, and appendices. Chapter 7 provides the summary and discussion, and finally Chapter 8 is the conclusions and recommendations for further work.

Chapter 2: Geological Setting

2.1 Introduction

The Scotian Margin, offshore Nova Scotia, covers an area of approximately 300,000 km² on the eastern flank of the Appalachian Orogen. Starting in the Middle Triassic, rifting and sedimentation on the Scotian Margin was initiated in response to the breakup of Pangea as North America separated from Africa and created the Equatorial Atlantic Gateway (Wagner, 2002), exhibiting features of the opening phase of a Wilson cycle.

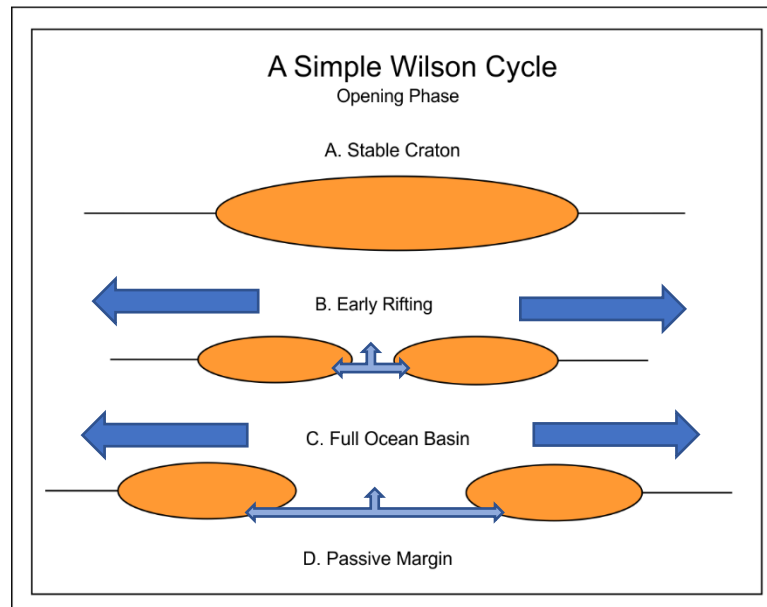


Figure 2.1: A simple Wilson cycle opening phase as seen in the proto-Central-Atlantic (Hargreaves, modified after SEPM Strata).

Initially, during the Middle to Late Triassic rift phase, red beds and evaporites dominated (Wade and MacLean, 1990). These were followed in the succeeding post-rift/drift phase by clastic progradational sequences interspersed with carbonate deposition (Wade and MacLean, 1990). Increasing amounts of sediments were shed from the distal rift flanks and advanced towards the rift margin and formation of the Sable Delta. As the margin matured the depositional environment changed from a deltaic shallow marine clastic shelf to an estuarine shallow marine clastic shelf, and finally to an open marine outer shelf which occurred when the passive margin stage was reached.

The succession demonstrates, in time as well as over space, influences of global events, which link climate with geochemical environments, as well as the progression of the tectonic conditions as the area transitioned from a rift to passive margin.

2.2 Regional Geology and Tectonics

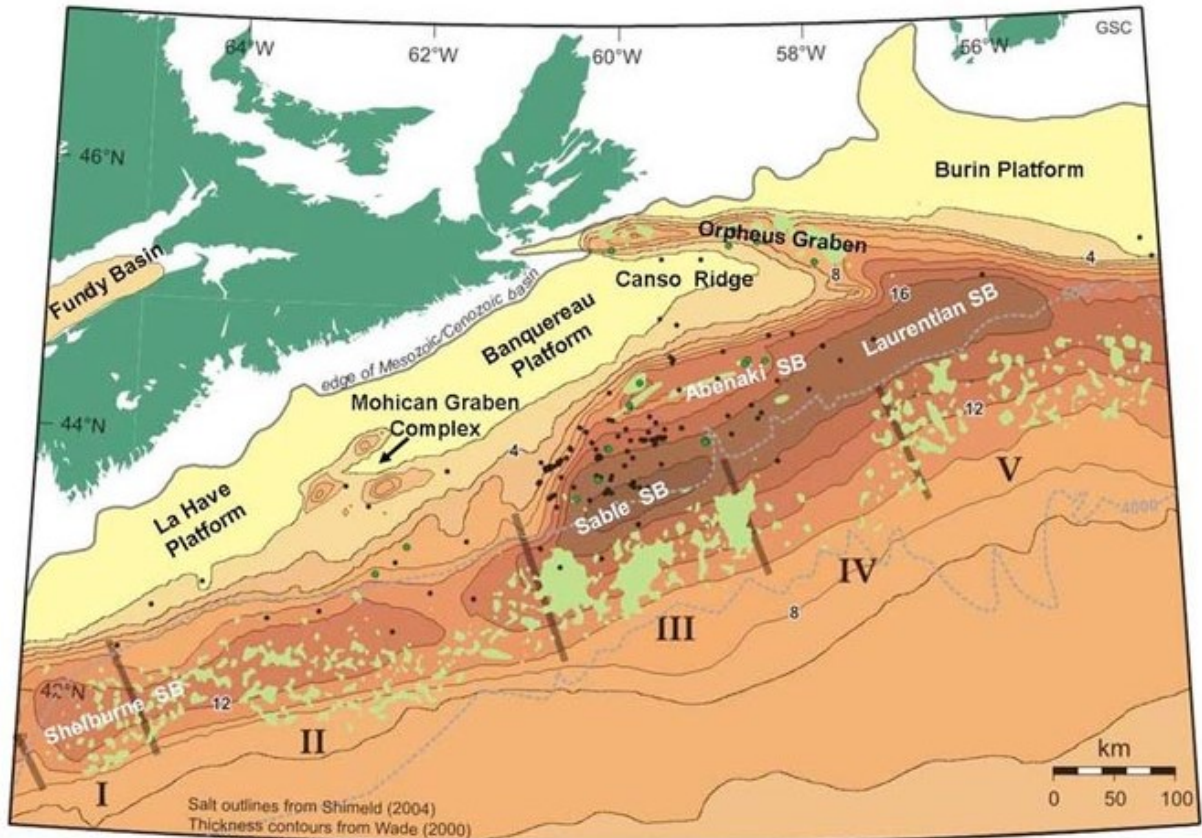


Figure 2.2: Basins on the Scotian Margin. This map shows the geographical area, depositional subbasins (SB), and major structural elements of the Scotian Basin. Roman numerals define distinctive salt tectonic regions. The location of the seismic study area is centered in the Sable Subbasin (OETR, 2011).

After the Late Triassic rift phase deposition of red beds and evaporites and continental breakup, in the Early Jurassic the region became tectonically stable with the formation of platforms and local depocentres (Figure 2.2). All were bounded by oceanic fractures zones perpendicular to the mid-ocean ridge that extended landward (Welsink et al., 1990). By the Middle Jurassic (ca. 180 Ma) post-rift thermal subsidence was well underway (Bowman, 2010). Along the rift/shelf margin the Abenaki Formation

carbonate bank began to form above a structural hinge line between the La Have Platform and Sable Subbasin. The long-lived Abenaki carbonate complex is subdivided into the Scaterie, Misaine, and Baccaro members, each representing a distinct paleoenvironment and depositional facies. The structural hinge line marks the landward limit of maximum tectonic extension where an increased basement depth is seen due to thermal subsidence (sag) as newly created oceanic basement moved away from the spreading centre.

By the end of the Jurassic, three major deltas, the Sable, Laurentian, and to a lesser extent, the Shelburne, were well established depositing siliciclastic material into depocenters seaward of the basin hinge line. The Abenaki carbonate complex was coeval with but eventually terminated and overlain by the Mic Mac Formation's fluvial-deltaic sediments. Throughout the Early Cretaceous deltaic facies reached their maxima as represented by the extensive and thick deposits of the Missisauga Formation's siliciclastics and were transitioning into the upper Early Cretaceous Logan Canyon Formation. The Late Cretaceous saw increasing global sea levels (Haq et al., 1987) and the resultant deposition of marls, chinks and marine shales of the Dawson Canyon and Wyandot formations on the shelf and slope of offshore Nova Scotia (McIver, 1972; Jansa and Wade, 1975; Mosher et al., 2010).

2.3 Stratigraphy of the Scotian Shelf

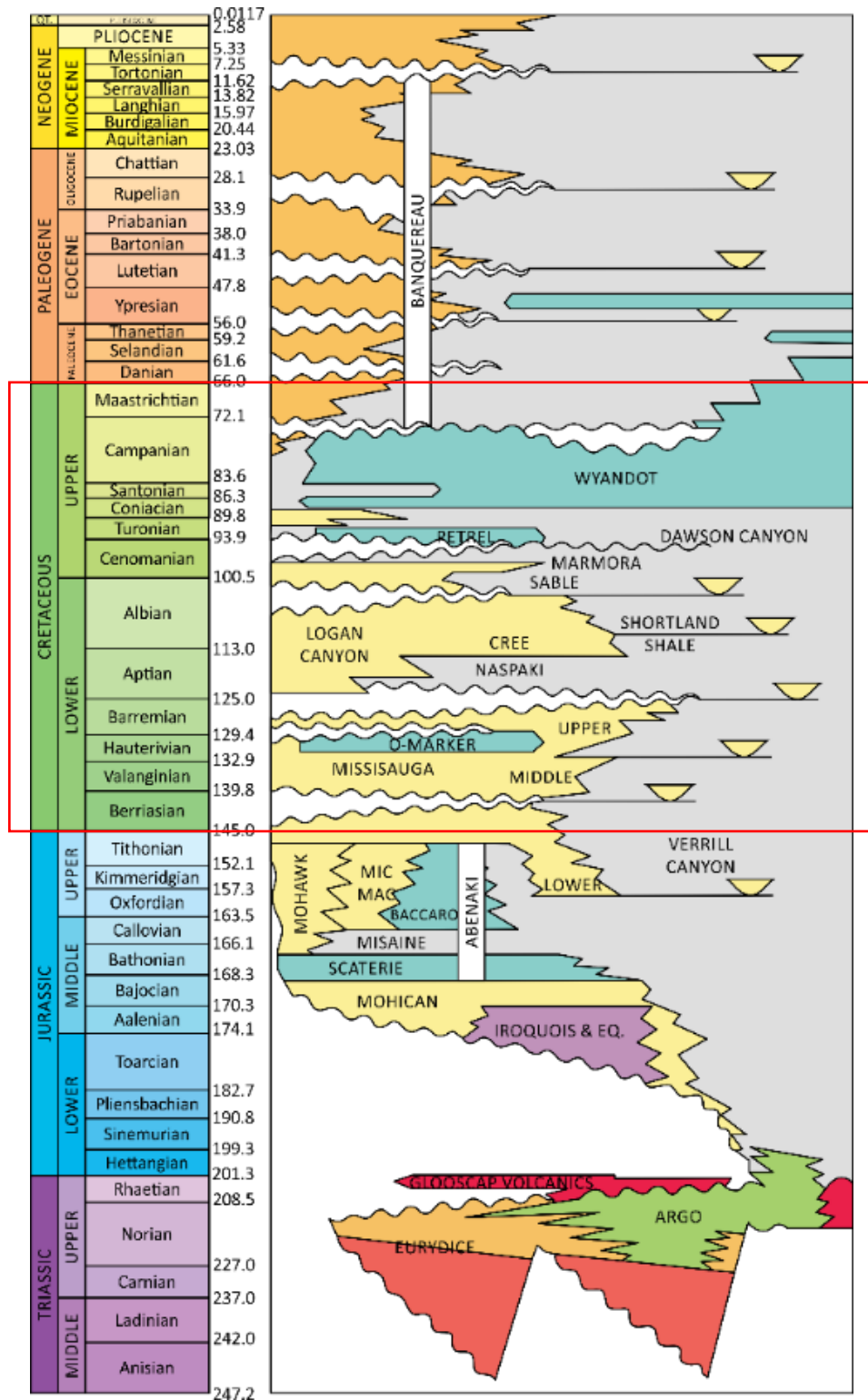


Figure 2.3: Generalized chronostratigraphic chart of the Scotian Basin (OETR, 2011). Lithostratigraphic units in the Cretaceous from 145 to 66 Ma (Gradstein et al., 2005), interpretations are after Weston et al. (2012). The red box is the interval investigated for this study.

2.4 Cretaceous Period

The Cretaceous Period was a time of extreme global warming with a greenhouse climate. The earth was mostly ice-free, with an absence of permanent polar ice caps (Wagner, 2002). Greenhouse conditions with CO₂ levels three to twelve times higher than levels in pre-industrial atmospheric conditions were thought to exist (Berner, 1994; Hay et al., 1999; Wagner, 2002). Tropical plants grew in polar regions, with dinosaurs, turtles, and crocodiles in existence north of the Arctic Circle. It was estimated that the North Pole was twenty degrees C° warmer than today (Schlanger and Jenkins, 1976).

Antarctica was located over the South Pole by this time and was thought to have ephemeral ice sheets during the Late Cretaceous (Matthews and Poore, 1980; Miller et al., 2003; Hay, 2008; Cloetingh and Haq, 2015). However, it is thought that the equator to pole temperature gradients were reduced and measured much less than in present day (Wagner, 2002) due to the absence of permanent ice caps throughout the bulk of the Cretaceous.



Figure 2.4: Late Cretaceous schematic of the geography, topography, and bathymetry of the world after the breakup of Pangea. Dark blue represents deep water, pale blue shallow water, and greens/browns the land masses. The configuration shows Africa and South America have rifted with a narrow ocean separating them. The proto-Caribbean Seaway is open with only a shallow water barrier permitting flow of nutrient-rich waters from the Pacific. The northern proto-Atlantic Ocean is located between the equator and 30+ degrees north latitude, thus in a tropical environment. The red "x" indicates the approximate location of the study area at about 94 Ma (Scotese, 2003).

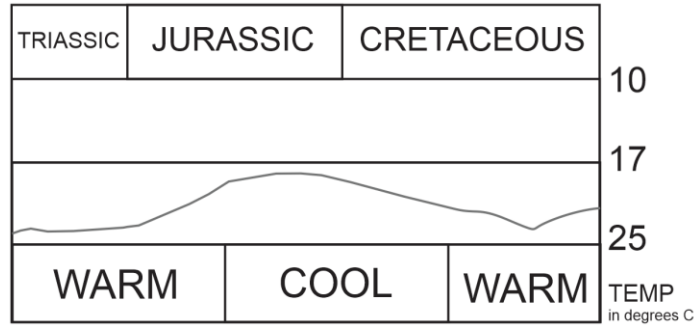


Figure 2.5: General climatic paleotemperature during the Triassic, Jurassic, and Cretaceous periods (after Scotese 2003: <http://www.scotese.com/climate.htm>). The Middle Jurassic into Early Cretaceous was relatively cool, only warming during the Aptian.

After a cool interval in the Early Cretaceous, there was warming lasting until the late Albian, followed by cooling in the Cenomanian and warming in the Turonian. Cooling again occurred from the Santonian to the Campanian with warming in the late Campanian (Frakes, 1999). During the Aptian, the Cretaceous marine paleotemperatures were estimated to be between 25° C at the equator to approximately 15° C at 30° latitude north globally (Frakes, 1999).

2.4.1 Cretaceous Sea Level

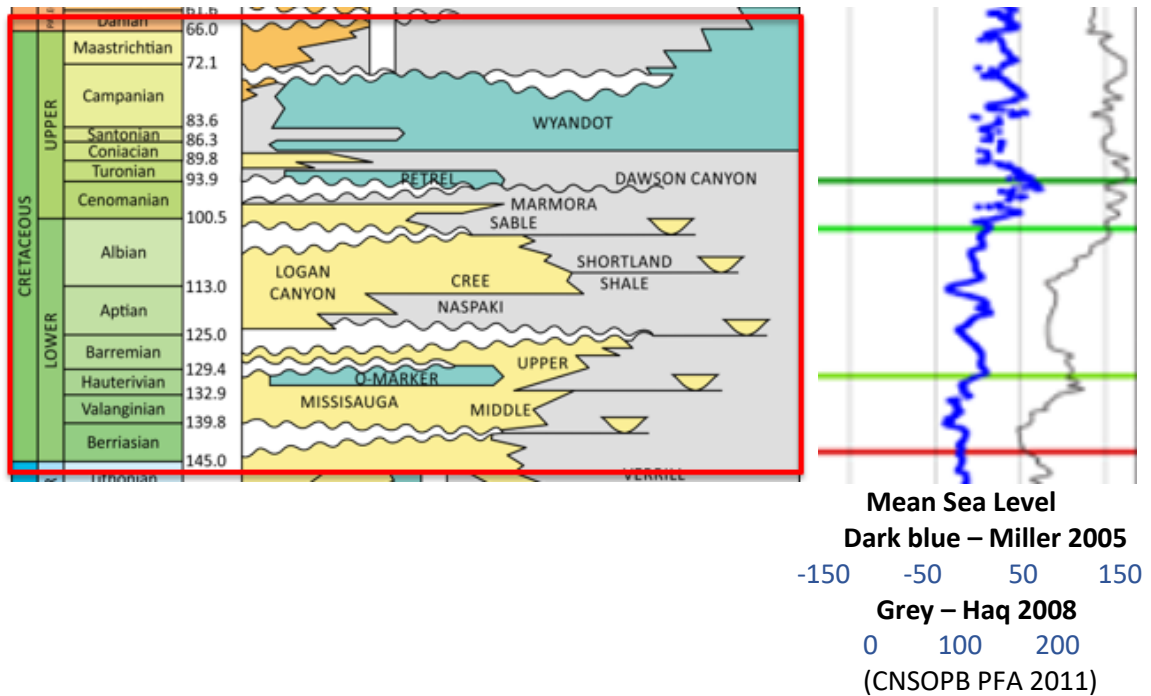


Figure 2.6: Chronostratigraphic chart of the Cretaceous Period from 145 – 66 Ma (OETR, 2011). On the right are the corresponding sea level estimates of Miller et al (2005; dark blue) and Haq (2008; grey) and their corresponding water depths.

Sea level in the Cretaceous was higher than at present day, with a low during the Early Cretaceous and the peak in the late mid-Cretaceous (Cloetingh and Haq, 2015). The Cenomanian-Turonian was considered to have the highest Cretaceous sea level measuring 170 – 250 metres above present-day levels.

2.4.1.1 The Effect of Volcanism on Sea Level

The Cretaceous was a time of high rates of oceanic volcanism (Coffin and Eldholm, 1994; Ito and Clift, 1998). Enhanced volcanic activity (Scotese et al., 1988; Larson, 1991 a, b) contributed to the Cretaceous greenhouse conditions (Huber et al., 2002; Jenkyns et al., 2004) which in turn contributed to a long-term sea level rise (Miller et al., 2005; Mueller et al., 2008).

The elevated level of volcanism was associated with an unstable upper mantle, which resulted in the rifting and the breakup of Pangea (Skogseid et al., 2000; Zeigler and Cloetingh, 2004). Rifting in the North Atlantic was initiated in the Middle Triassic, through the Jurassic, and continued during the Cretaceous in southern Pangea between Africa and South America. High amounts of oceanic crust were produced at spreading ridges, resulting in high rates of water expulsion from the mantle (Cloetingh and Haq, 2015). At subduction zones, large amounts of water were captured and absorbed. On a global scale, during the late Early and late mid-Cretaceous, a net gain in water levels is interpreted as indicating higher rates of water expelled from the mantle at spreading centers compared to amounts being entrapped at subduction zones (Cloetingh and Haq, 2015).

Due to the volcanic activity at the mid-ocean ridge, the production of ocean crust and its associated water expulsion, is thought to have added 225-250 metres to sea level in the Cretaceous (Conrad, 2013). Sections of the Cretaceous sea floor are still in existence making it possible to reconstruct, image and model the Cretaceous mantle (Mueller et al., 2008; Liu et al., 2008; Cloetingh and Haq, 2015).

2.4.1.2 Water Sequestration on Land

Water sequestration onto land occurs where seawater is transferred to continental areas where it is then recorded in the sedimentary record, such as during an ice age where water is stored as land-based ice. Water sequestration onto land allows this history to be stored in the sedimentary record, where it is captured as a global signal for large events. Glacial episodes are recorded for the Late Ordovician – Early Silurian, Late Devonian, Carboniferous (Mississippian – Pennsylvanian), Permian, Late Paleogene – Neogene, and ice cover over both poles in the late Neogene (Deynoux et al., 1994). However, in the Late Cretaceous, it is suspected that there were ephemeral Antarctic (over the south polar paleo-location) glacial episodes (Matthews and Poore, 1980; Stoll and Schrag, 2000; Cloetingh and Haq, 2015).

Water is also sequestered during ocean/deep mantle exchanges. It is subducted along with hydrated minerals into the deep mantle over millions of years (Conrad, 2013) and released by degassing from the mantle into the deep ocean along spreading ridges. This system is thought to be in balance over time scales of ten million years or more. In times of high oceanic crust production such as occurred in the Late Cretaceous, there would be a net gain of water released into the oceans. The system would be in balance again later, when increased subduction would occur and create a net loss for oceanic water volume (Haq, 2014; Cloetingh and Haq, 2015).

2.4.1.3 Deglaciation and Isostatic Rebound

During times of deglaciation, as ice receded, the isostatic rebound of the continents occurred on a scale of tens to hundreds of years. This can be distinguished from post-deglacial response, such as mass redistribution and vertical displacement on continental margins, which occurred on the time scale of thousands to hundreds of thousands of years. This results in regional anomalies rather than global anomalies seen along a margin (Cloetingh and Haq, 2015).

Modeling of glacial isostatic adjustments (GIAs) shows that rebound and the subsequent viscous mantle flow under these deglaciated areas occur within thousands

and hundreds of thousands of years (Mitrovica and Peltier, 1991; Lambeck et al., 1998). These GIAs depend upon how far they are from the ice sheet and are thought to reach equilibrium after 100,000 years post-glacially (Cloetingh and Haq, 2015).

The variability in the rate of oceanic crust formation at the mid-ocean ridges affected the volume of the ridges and therefore the eustatic sea level changes on longer time scales of ten million years or more (Pitman III and Golovchenko, 1983; Dewey and Pitman, 1997). The ridge volume from the Cretaceous to today has been modeled (Kominz, 1984; Rowley, 2002) and it has been found that there has been a slowing of 60 – 80 % in the spreading rate since the Late Cretaceous resulting in a lower ridge volume (Mueller et al., 2008; Becker et al., 2009; Cloetingh and Haq, 2015).

2.5 Cretaceous Formations

In the Scotian Basin, the major Cretaceous geological formations comprise of the Early Cretaceous Missisauga Formation followed by the Logan Canyon Formation, coeval basin sediments of the Verrill Canyon Formation. During the Late Cretaceous (Santonian to Maastrichtian) on the open marine outer shelf, chalks and marls of the Wyandot Formation were laid down.

The provenance of the Missisauga and the Logan Canyon formation sediments was Devonian to Permian age sedimentary rocks from New England and the Maritime Provinces and older metamorphic rocks from Newfoundland and Labrador (Pe-Piper and Piper, 2004; Pe-Piper and MacKay, 2006). The Shelburne, Sable, Abenaki, Laurentian, and South Whale subbasins, all located outboard of the basin hinge line on the Scotian Shelf, have accumulated approximately 12 kilometres of Mesozoic and Cenozoic sediments with a maximum of 18 kilometres estimated for the Sable Subbasin (Wade and MacLean, 1990) (Figure 2.2).

2.5.1 Aptian Stage

The age ranges for the Aptian vary considerably depending on the time scale used for defining the interval (Wach, 1991). Harland et al suggests the Aptian Stage extends from 124.5 Ma to 112.0 Ma with a duration of 12.5 Ma. Table 2.1 illustrates the differing opinions of proposed time scales. There have been differing opinions on the age range of the Aptian Stage proposed.

Table 2.1: *Aptian stage age range estimations from various studies 1961 to 2018.*

APTIAN STAGE AGE RANGES		
Author	Year	Age Range
Kulp	1961	125-120 Ma
Kent and Gradstein	1985	119-113 Ma
Graham et al	1990	124.5-112 Ma
Gradstein et al	1995	121-112.2 Ma
Odin	1996	114-108 Ma
GTS	2004	125-112 Ma
CNSOPB/OETR PFA	2011	125-112 Ma
GSA	2018	125-113 Ma

Potassium/Argon (K/Ar) and Rubidium/Strontium (Rb/Sr) ratio dating methods are less reliable than $^{40}\text{Ar}/^{39}\text{Ar}$ and Uranium - Lead (U/Pb) ratios (Villeneuve, 2004; Mattinson, 2013). Radiometric dating is considered to have an accuracy of +/- 0.1% using present day methods that equates to an accuracy of +/- 100,000 years over 100 Ma (Miall, 2016).

2.5.2 Naskapi Member

The Aptian Naskapi Member is the focus of this study, incorporating data from logged intervals to create maps, cross-sections, and seismic interpretations with the results presented in Chapter 6.

Age: Aptian

Age Range (Ma): 125 – 114 (145.5 – 99.6)

Type Section (Well): Cree E-35

Interval (m-TVD): 2377 – 2551 (NRCAN, 2009) or 2582 – 2408 (Wade and MacLean, 1990)

The Naskapi Member of the Logan Canyon Formation consists of varicoloured, fissile, carbonaceous, and dolomitic transgressive shales, ranging in colour from yellowish-brown to green-grey and reddish-brown with interbedded silts and sands, along with some basalt flows and volcanoclastic beds in the northeast Scotian Shelf region (Wade and MacLean, 1990). The member was deposited under tidal flat to marginal marine conditions and distally thickened to marine shales (Wade and MacLean, 1990; NRCan 2009).

It is traditionally considered a transgressive shale member overlying the massive fluvial-deltaic sandstones of the Missisauga Formation and underlying the interbedded fluvial-estuarine sandstones and shales of the formation's Cree Member (Wade and MacLean, 1990). The Naskapi becomes sandier in the more inboard Abenaki Subbasin and above the Canso Ridge (Wade and MacLean, 1990; NRCan, 2009).

Pe-Piper and Piper (2004) proposed that the rise in sea level, which is reflected in the Naskapi strata depositional facies, was due to dextral strike-slip movement along the Cobequid – Chedabucto Fault Zone (CCFZ) extending from mainland Nova Scotia to the southwest Grand Banks of Newfoundland. This dextral motion caused extension in the bounding Laurentian Subbasin and linked events seen in the regions adjacent to this fault system. An unconformity in the mid-Cretaceous (Aptian) is observed on seismic profiles onshore Nova Scotia in the Chaswood Formation. Volcanics (extrusive) in the Orpheus Graben may be related to a marked, rapid subsidence on the Scotian Margin during the mid-Late Cretaceous. In the Albian to Cenomanian, another unconformity is present in the southwest Grand Banks of Newfoundland. Motion along this fault may explain these unconformities, volcanism in the Orpheus Graben, and the rapid subsidence seen along the Scotian Margin (Pe-Piper and Piper, 2004).



Figure 2.7: This photo illustrates variability in lithology of the Naskapi Member, observed in conventional core from Sable C-67 (left), and Grand Pre G-08 (centre and right) wells. Grey shales are inter-bedded with red shales, red silts, and show scouring and bioturbation, as well as cross-beds. The colour is predominantly light grey. Sandstone sections are porous but lack oil stain in the Grand Pre core. The Naskapi here does not show any evidence of OAEs. The arrow indicates the core upsection direction.

2.5.3 Other Cretaceous and Cenozoic Formations

The following section briefly describes the lithologies and major characteristics of the main Cenozoic and Cretaceous formations in the Scotian Basin. The age ranges are taken from the chronostratigraphic chart (Gradstein et al., 2005; CNSOPB, 2011), and where the Lexicon of Canadian Geological Names (Natural Resources Canada – NRCAN Weblex online, 2009) ages differ, they are listed in parentheses. Type sections and reference sections, if known, are included with the interval measured in metres True Vertical Depth (m-TVD).

2.5.3.1 Banquereau Formation

Age: Late Cretaceous (Campanian) to Tertiary (Pliocene)

Age Range (Ma): 100.5 – 2.6 (99.6 – 1.806)

Type Section (Well): Sable C-67

Interval (m-TVD): 165 – 1355

The formation's lithology is comprised of mudstones, and lesser quantities of sandstones and siltstones. In the Scotian Basin, the Banquereau conformably overlies the Upper Cretaceous Wyandot Formation, and unconformably overlies the Dawson Canyon where the Wyandot is absent. The thickness ranges from zero to greater than

1500 metres in the Sable Subbasin. Jansa and Wade (1975) and Wade and MacLean (1990) note a few major unconformities in the Banquereau Formation on the outer slope and upper shelf deposits, which are most likely due to changes in sea level (NRCan, 2009).

2.5.3.2 Wyandot Formation

Age: Coniacian - Campanian
Age Range (Ma): 87 – 74 (99.6 – 65.5)
Type Section (Well): Mic Mac H-86
Interval (m-TVD): 18 – 806
Reference Section (Well): Dauntless D-35
Interval (m-TVD): 1433 – 1830

The Wyandot covers much of the Scotian Basin (Jansa and Wade, 1975). It is dominated by light grey to white chalk composed of coccoliths, which are interlayered with calcareous mudstones and marlstones. Deposition was in deep water on the then-paleoshelf in the outer neritic to upper bathyal zones (McIver, 1972) and thickens eastward from 50 metres on the La Have Platform to 400 metres in the Dauntless D-35 well (Wade and McLean, 1990; McIver 1972, NRCan, 2009).

2.5.3.3 Petrel Member

Age: Late Cenomanian - Turonian
Age Range (Ma): 94 – 90 (99.6 – 65.5)
Type Section (Well): Gannet O-54
Interval (m-TVD): 1585 – 1665

The Petrel Member of the Dawson Canyon Formation is a transgressive light grey micro- to cryptocrystalline series of limestones and marlstones with glauconite and sandstone stringers (Jansa and Wade, 1975). It reflects a change in ocean circulation patterns to warmer water. On the Scotian Shelf, the thickness ranges from 0 metres in the west to 85 metres in the east and appears as a strong regional seismic marker (Deptuck, 2003; NRCan, 2009).

2.5.3.4 Dawson Canyon Formation

Age: Mid-Cenomanian – Mid Coniacian
Age Range (Ma): 96 – 87.5 (99.6 – 65.5)
Type Section (Well): Missisauga H-54
Interval (m-TVD): 1017 – 1288

The Dawson Canyon Formation consists of grey-green, fine-grained, argillaceous siltstones and silty shales, with occasional sandstone beds. It is interpreted to have been deposited in an open marine shelf environment during a transgressive period (Jansa and Wade, 1975) when the sediment load of major rivers flowing into the Scotian Basin was dominated by silts and clays (Jansa and Wade, 1975). The lower Dawson Canyon was deposited in an inner neritic setting, grading to an outer neritic setting moving up-section (Ascoli, 1976; NRCan, 2009).

2.5.3.5 Logan Canyon Formation

Age: Early Aptian – Early or Late Cenomanian (Wade and McLean 1990)
Age Range (Ma): 124 – 104
Type Section (Well): Cree E-35
Interval (m-TVD): 1472.5 – 2582

The Logan Canyon Formation is composed of alternating thick shale and sandstone intervals were deposited near shore (NRCan, 2009). These strata grade to distal shales informally termed the 'Shortland Shale' (Jansa and Wade, 1975). The formation broadly covers the Scotian Basin, with thicker shales of 2000 metres in the Abenaki and Sable subbasins varying to 170 metres on the La Have Platform (NRCan, 2009).

The four members of the Logan Canyon are the Marmora, Sable, Cree, and Naskapi (NRCan, 2009).

2.5.3.6 Marmora Member

Age: Early Cenomanian
Age Range (Ma): 97 – 99
Type Section (Well): N/A
Interval (m-TVD): N/A

The Marmorata Member is comprised of thin, fining-upward sandstone intervals interpreted to have been deposited in a marginal marine to an outer shelf setting (Wade and MacLean, 1990; NRCan, 2009).

2.5.3.7 Sable Member

Age: Late Albian – Early Cenomanian
Age Range (Ma): 103 – 99
Type Section (Well): Cree E-35
Interval (m-TVD): 1674 – 1748

The Sable Member is represented by fissile yellowish-brown to green-grey marine shales with some thin sandstone and siltstone beds. It was deposited in deep water during a rapid transgression (McIver, 1972; Jansa and Wade, 1975; NRCan, 2009).

2.5.3.8 Shortland Shale

Age: Albian
Age Range (Ma): 113 – 102 (100.5 – 145)
Type Section (Well): N/A
Interval (m-TVD): N/A

The Shortland Shale informally refers to the coeval offshore basinal counterpart of the Logan Canyon Formation (see 2.5.2.5) (Wade and MacLean, 1990) and is also referred to as the distal basinal facies of the Logan Canyon Formation (Jansa and Wade, 1975; NRCan, 2009).

2.5.3.9 Cree Member

Age: Late Aptian – Late Albian
Age Range (Ma): 115 – 99.6
Type Section (Well): Cree E-35
Interval (m-TVD): 1805 – 2408

The Cree Member is the thickest of the formation's members and composed of channel, estuarine, and shallow marine sandstones interbedded with medium to dark

grey shales and siltstones. It is thickest in the Abenaki and Sable subbasins (NRCan, 2009). It is interpreted to have been deposited under transgressive tidal flat to marginal marine conditions (Wade and MacLean, 1990; NRCan, 2009).

2.5.3.10 Missisauga Formation – Upper Member

Age: Barremian – Early Aptian

Age Range (Ma): 128 – 122

Type Section (Well): Missisauga H-54 (up-dip facies)

Interval (m-TVD): 0 – 3000

Reference Section (Well): Southwest Banquereau F-34

Interval (m-TVD): 3918 – 4980

The Upper Missisauga consists of thick, massive, stacked channel sandstones with minor thin argillaceous shale and siltstone beds, with rare thin limestones. The sandstones are coarse-grained and highly porous with basal conglomerates. The unit is interpreted to represent a regressive, highly active progradational deltaic facies (NRCan, 2009) with the up-dip facies deposited in an alluvial plain setting. The feeder system for the entire formation was a large river system draining the northeastern region of the Canadian Shield during the Cretaceous (Wade and McLean, 1990; NRCan, 2009).

2.5.3.11 O-Marker

Age: Barremian

Age Range (Ma): 126 – 128

Type Section (Well): N/A

Interval (m-TVD): N/A

The O-Marker is the informal name of an oolitic limestone/limey sandstone interval present in the Upper Missisauga Formation. It is up to 122 metres thick and broadly distributed across most of the Sable Basin and thus is a very useful regional seismic marker (Jansa and Wade, 1975). It was deposited during a minor transgression amidst a major regressive phase (NRCan, 2009) and divides the Missisauga Upper and Middle members (Wade and MacLean, 1990).

2.5.3.12 Missisauga Formation – Middle Member

Age: Valanginian - Barremian

Age Range (Ma): 140 - 128

Type Section (Well): Missisauga H-54

Interval (m-TVD): 2740 – 3537

Type Section (Well): Cree-E-35 (Down-dip facies)

Interval (m-TVD): 2551 – 3719

The Middle Missisauga is described as a series of stacked, thick, clean, fine to coarse grained sandstones, which are poorly to moderately sorted with variable porosities (NRCan, 2009) deposited in a lower delta plain, to an inner neritic setting (Wade and MacLean, 1990; NRCan, 2009).

2.5.3.13 Missisauga Formation – Lower Member

Age: Late Jurassic - Early Cretaceous (Kimmeridgian –Berriasian)

Age Range (Ma): 155 – 140

Type Section (Well): Venture H-22

Interval (m-TVD): 4149 – 5100

The Lower Missisauga contains fine- to coarse- and pebbly-grained, coarsening upwards sandstone intervals, with minor thin limestone and some interspersed grey marine clay intervals deposited under delta front to prodelta conditions from a large river system (Wade and MacLean, 1990; NRCan, 2009). The Lower Member is found only in the Sable Subbasin (Wade and MacLean, 1990).

2.5.3.14 Verrill Canyon Formation

Age: Middle Jurassic – Early Cretaceous (Bajocian – Barremian)

Age Range (Ma): 171 – 125 (175.6 – 99.6)

Type Section (Well): Oneida O-25

Interval (m-TVD): 2858 – 2498

The Verrill Canyon Formation is the coeval, distal basinal equivalent of the Abenaki, Missisauga, and Logan Canyon formations. Its lithology is dominated by medium grey to brown, calcareous, fissile, silty shales with thin siliceous sandstones, along with mica, pyrite, and some glauconite mineral constituents. These strata are

interpreted to be prodelta, distal shelf and slope deposits representing neritic to epibathyal environments (Given, 1977). It ranges in thickness from 300 metres in the southwest, to 900 metres in the northeast of the Scotian Basin though is considerably thicker alongside the deep-water Scotian Slope (Jansa and Wade, 1975; NRCan, 2009).

2.5.3.15 Abenaki Formation

Age: Middle Jurassic – Early Cretaceous (Callovian-Berriasian – Valanginian)

Age Range (Ma): 166.1 – 132.9 (175.6 – 99.6)

Type Section (Well): Oneida O-25

Interval (m-TVD): 2858 – 3821

The Abenaki Formation is a carbonate platformal succession formed along the Scotian Basin's hinge line margin. It is 10 to 40 kilometres wide paralleling the shelf edge along the LaHave Platform on the Scotian Shelf. There are four members in the Abenaki representing different depositional settings. The basal Scatarie Member is made of bioclastic limestones and occasional dolostones deposited on an open, high energy, and well-oxygenated shelf. The Scatarie is conformably overlain by neritic, partly glauconitic Misaine Member highstand shales deposited in a marginal marine environment. The Baccaro Member is the thickest member composed of massive oolitic and bioclastic (reefal) carbonates deposited in a humid tropical, wet-dry climate, in a shallow marine to inner to outer neritic setting. The Artimon Member is a thin, deeper water transgressive sequence of algal limestone and calcareous shales (Wade and MacLean, 1990; NRCan, 2009).

The chronostratigraphic column for the Scotian Basin (Gradstein et al., 2005) shows the Abenaki as being Jurassic, however NRCan (2009) considers the Abenaki to extend into the earliest Cretaceous (Artimon Member), therefore, it has been included here for completeness.

2.6 Summary

The Cretaceous Period reflects a time of a global greenhouse climate, with low sea levels in the Early Cretaceous peaking in the late mid-Cretaceous. The equator-to-

pole temperature gradients were lower than is seen in the present day, indicating closer temperature values between the equator and at the poles, and it is believed that permanent polar icecaps were not in existence.

High rates of sea floor volcanism and oceanic crust formation due to the breaking apart of Pangea contributed to the greenhouse climate and a high sea level. The increase in sea level during the late Early and late mid-Cretaceous is partly due to higher amounts of water being expelled from the mantle at spreading centers compared to water being entrapped at subduction zones.

By the Early Cretaceous, the Scotian Margin was a subsiding passive margin due to thermal subsidence whereby the seafloor cooled and became denser away from the spreading centre (thermal sag). This contributed to alteration of the ocean circulation patterns which in turn changed the pattern of sedimentary and geochemical facies deposition. Increasing sea level through the mid Upper Cretaceous resulted in deposition of marls, chinks and marine shales of the Dawson Canyon and Wyandot formations on the shelf and slope offshore Nova Scotia. A major shift occurred in the Late Cretaceous when the deep-water circulation direction changed from an east-west equator-parallel circulation to a north-south pole-ward circulation, resulting in heat transfer from the low to high latitudes.

The Missisauga and Logan Canyon formations were deposited in the Cretaceous, with sediments sourced from Devonian to Permian age rocks from regions of present-day New England and the Maritime Provinces. The Naskapi Member of the Logan Canyon Formation was deposited under tidal flat to marginal marine conditions, thickening seaward, and is a transgressive shale which overlies the massive deltaic sandstones of the Missisauga Formation. Pe-Piper and Piper (2004) proposed that the increased water level during the mid Late Cretaceous was due to dextral strike-slip movement along the Cobequid – Chedabucto fault causing extension in the Laurentian Subbasin, which in turn caused rapid subsidence on the Scotian Basin during the time the Naskapi Member was deposited. The scenario of dextral strike-slip movement allows for motion along the fault and helps to explain the Aptian unconformities seen in

the (slightly younger) onshore Chaswood Formation and the volcanics of the Orpheus Graben, and the rapid subsidence seen along the Scotian Margin which resulted in the deposition of the Naskapi Member.

Chapter 3: Ocean Circulation

This chapter will begin with outlining present-day processes, for application to paleoclimate conditions. These concepts have much relevant to ocean circulation and productivity which took place in the past.

Oceans are critical in understanding global paleoclimate systems as they moderate seasonal temperatures and transport heat between the equator and the poles. Winds alter ocean surface circulation and the location of divergent (or upwelling), and convergent (or downwelling) zones, as well as the density of water masses and the interchange of heat and moisture between water and air, all which affect intermediate and deep-water flow (Poulsen et al. 1999).

The following chapter outlines necessary information and concepts regarding ocean water movement, how it affects the transfer of nutrients in the ocean, and the resulting productivity of biota, the deposition of which contributes to organic-rich sediments. Organic-rich sediments, and zones of anoxia (which can be part of a worldwide occurrence of Cretaceous Oceanic Anoxic events – OAEs) are discussed in Chapter 4. This basic overview of oceanographic concepts helps elucidate the understanding of offshore deposition of source rocks and the accumulation and preservation potential of sediments rich in organic matter.

3.1 Ocean Water Movement

Several factors are involved in creating ocean currents including the Coriolis Effect, Ekman transport and the ocean basin configuration. This summary has been largely sourced from the NASA (National Aeronautics and Space Act) website, which offers a sound basic outline of ocean water movement for those without prior oceanographic knowledge (NASA, 2017).

3.1.1 Coriolis Effect

Wind passing over the ocean surface moves the water by frictional drag at a rate of about 2% of the wind speed. The Coriolis Effect deflects surface waters to the right of

flow in the Northern Hemisphere, and to the left of flow in the Southern Hemisphere due to the earth's rotation with intensity increasing with distance from the equator. The thin surface layer also shifts the water beneath it, like moving a deck of cards, with the effect that each successive layer moves, resulting in a change in direction of water movement with depth (NASA, 2017).

Air currents flowing between 30° north and 30° south latitudes, known as the Tradewinds, create average wind directions which in present day are from northeast to southwest between the equator and 30° north, and southeast to northwest between the equator and 30° south latitudes (Figure 3.1). In the absence of continents, ocean currents would flow from east to west near the equator, and west to east in the area between the equator and 30° north and 30° south. However, continents interrupt these zones creating circular rotations called gyres. In the northern hemisphere these circulate clockwise and in the southern hemisphere counterclockwise. On continental shelves these large-scale currents vary due to localized and/or regional influences. They can be weather or tidally dominated and vary in their intensity (Trabucho-Alexandre, 2015).

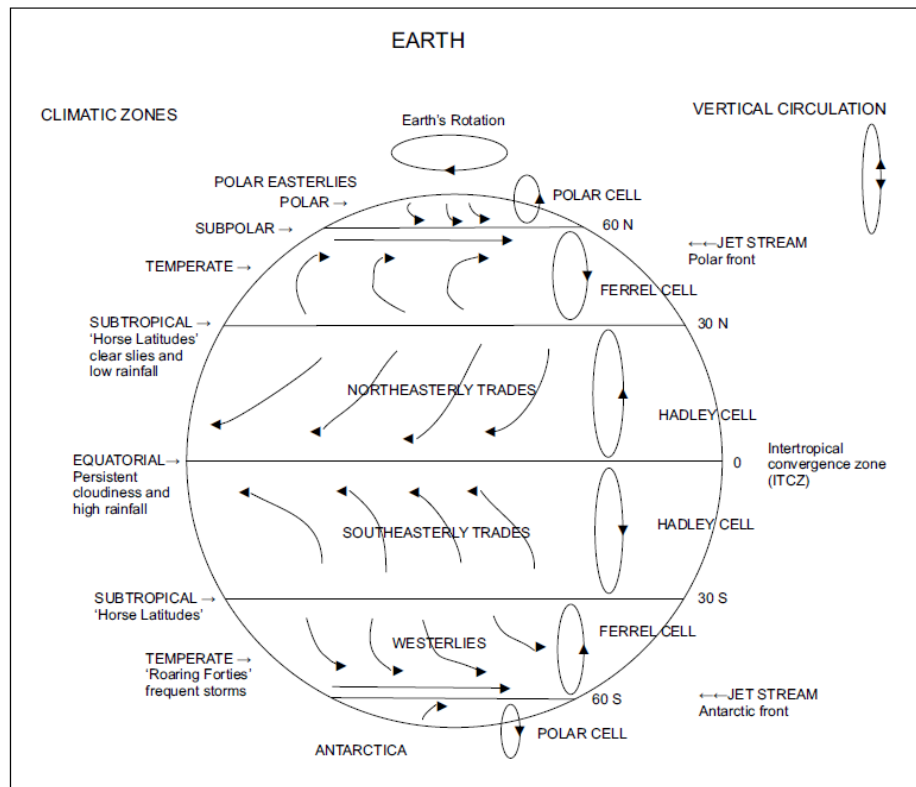


Figure 3.1: Global winds and relationship to latitudes (Showman, 2009).

3.1.2 Ekman Transport

Surface water moves at an angle of 45 degrees from the direction of wind motion to the right or left (depending on the hemisphere) and each layer (with increasing depth in the water column) moves further to the right or left, but at a slower speed than the layer above. The direction of water movement therefore changes with depth, with net water transport being 90 degrees to the right or left at a depth of between 100 – 150 metres. At this depth, water is moving very slowly at about 4% of the surface water speed (which is approximately 2% of the wind speed) and is the basal limit of the wind's influence on ocean movement (NASA, 2017). This net transport of water due to wind interacting with surface water is known as Ekman transport (NASA, 2017).

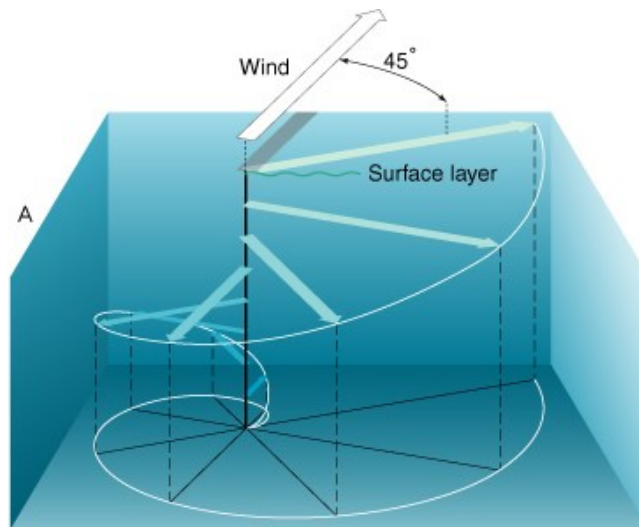


Figure 3.2: *The Ekman spiral. This process is modeled in three dimensions by using vectors to demonstrate the speed and direction of water movement due to wind at surface. The vector directions move to the right or left with depth and the vector lengths (indicating speed) become shorter with depth (NASA, 2017). Shallow water depth will interfere with this ideal situation as the angle of surface water movement will be less than 45 degrees. Also, surface water can accumulate in areas due to bathymetry, resulting in a higher water surface level. This will create a water pressure gradient which results in water movement called geostrophic flow (NASA, 2017).*

3.1.3 Meridional Overturning Circulation

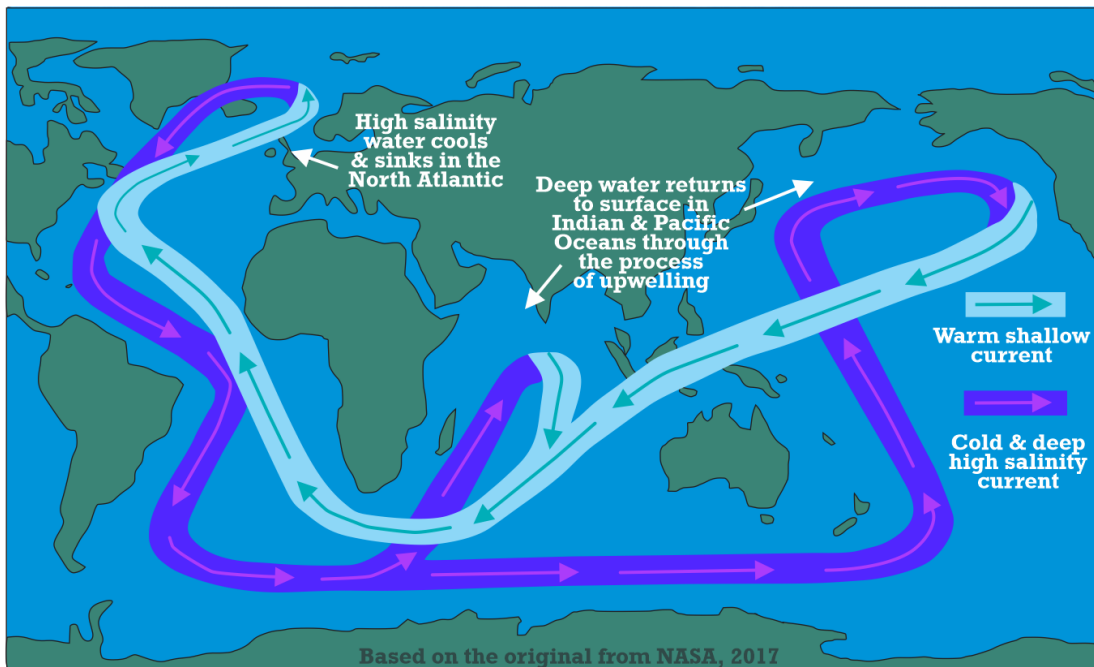


Figure 3.3: Chart showing the present-day meridional overturning circulation (original chart from NASA, 2017). The light blue ribbon shows the warm shallow current (Gulf Stream) which flows from the Caribbean northeast to the UK past this study's area of interest, where the high salinity water becomes denser, cools and sinks returning south as shown by the purple ribbon, eventually circling, and cooling the Antarctic region.

The global oceanic conveyor belt, or the meridional overturning circulation, combines the ocean surface water flow with the deep mass thermohaline circulation to transport heat and salt. Water differs in density due to temperature and salinity. Cold salty water is denser and sinks, as it does in the present-day North Atlantic, and this process initiates what is called thermohaline circulation, which is critical to the meridional overturning circulation (NASA, 2017).

In the present day, warm surface waters from the Caribbean and Florida flow into the Gulf Stream and head northeastward becoming more saline as warm tropical air evaporates surface water. As the Gulf Stream flows into the Northern Atlantic, the waters are cooled by cold Arctic winds from Canada and Greenland, where evaporation and the formation of sea ice contribute to the cold saline North Atlantic Deep Water (NADW) current. This current then sinks and flows south along the continental slope of North and South America to Antarctica, where it joins other currents circulating eastward as the Antarctic Circumpolar Current (see Figure 3.3); from there it flows north

into the Pacific and Indian Ocean basins. The cold bottom waters slowly rise and mix with overlying warmer waters at a rate of a few meters per year. Warmer surface waters then flow westward across the Pacific and Indian oceans around Africa and back into the Southern and Northern Atlantic oceans where the cycle repeats itself (NASA, 2017).

The meridional overturning circulation can be altered by temperature or salinity changes as it takes place in only 1% of the ocean's surface region (NASA, 2017). For example, if higher salinity surface water decreases in salinity, due to an influx of fresh water from melting polar ice, the lesser volume of saline waters will sink into the deep and discourage the formation and flow of deep ocean water masses. This happened during what is known as the Little Ice Age between 1400 and 1850 CE (NASA, 2017) as well as during the earlier Younger Dryas period, 12,900 – 11,600 years ago. At that time, blockages holding Glacial Lake Agassiz (over the Great Lakes region) collapsed releasing huge volumes of fresh water into the North Atlantic via the St. Lawrence River. This resulted in a decreased volume of saltwater sinking into the deep-water mass, which halted the thermohaline circulation and resulted in a temporary return of the ice age for approximately 1000 years (NASA, 2017).

3.1.4 Ocean Circulation and Temperature Gradients

By the Early Cretaceous, the Scotian Margin was a subsiding passive margin, largely due to thermal subsidence, whereby newly created oceanic crust cooled and became denser away from the spreading centre. This altered the ocean circulation pattern resulting in changes in the sedimentary and geochemical facies deposition in conjugate (and adjacent) ocean basins (e.g. Wagner, 2002; Hay, 1995; Hay, 1996; Wagner and Pletsch, 1999; Pletsch et al., 2001). Through the mid Upper Cretaceous, increasing global sea levels (Haq et al., 1987) saw the deposition of marls, chalks and marine shales of the Dawson Canyon and Wyandot formations on the shelf and slope of offshore Nova Scotia (MacIver, 1972; Jansa and Wade, 1975; Mosher et al., 2010). This was largely due to a shift in deep-water ocean circulation in the Late Cretaceous (Wagner, 2002), where the direction changed from an east-west equator-parallel

circulation to a north-south polar-ward circulation. This circulation change occurred as the Atlantic Ocean extended southward due to the rifting between Africa and South America, resulting in heat transfer from the low to high latitudes (Hay, 1995; Wagner, 2002).

In present day, the temperature gradient between the equator and poles is about 60° C, however in the Cretaceous it was approximately 30° C (Hay and DeConto, 1999). The smaller temperature gradient was most likely due to slower winds and ocean currents and a warmer temperature at the poles; however, salinity differences could also have contributed. Increased water vapor in the air would have changed the atmospheric pressure differences, and the resulting increased evaporation and precipitation would have created much greater salinity contrasts in the oceans (Hay and DeConto, 1999). Movement of atmosphere and ocean water serves to transport energy from warmer low latitudes to cooler high latitudes to overcome the radiation imbalance (Hay and DeConto, 1999). Variations in oceanic heat transport are most likely due to deep ocean circulation changes (Poulsen et al., 1999). Seaways moving water between high and low latitudes serve to reduce the equator to pole temperature gradient, perhaps as much as 15° C, causing changes in climate, which in turn can produce low latitude warm saline bottom waters resulting in tropical cooling (Poulsen et al., 1999).

3.1.5 $\delta^{18}\text{O}$ and Salinity

Evaporation and continental runoff can affect the isotope $\delta^{18}\text{O}$ value of surface water (Frakes, 1999). A change in salinity of 3 ppt (parts per thousand), found in near-shore shallow water, is required to alter the temperature of sea water by 4 degrees or the oxygen isotope $\delta^{18}\text{O}$ value by 1 per millilitre (expressed as ‰, parts per thousand) (Frakes, 1999). Lower temperature gradients, as proposed for the Cretaceous, can possibly be explained by ocean heat transport as previously explained, and the increased partial pressure of CO_2 and other greenhouse gases during the warmer climate in the Cretaceous. Cooler temperatures during the Late Cretaceous could reflect ocean heat transport to higher latitudes and the loss of CO_2 from the atmosphere.

Atmospheric drawdowns of CO₂ would occur during oceanic anoxic events where burial rates of oxygen isotope $\delta^{18}\text{O}$ values were very high, such as during the Aptian, Albian and Cenomanian, when shelf carbonate accumulation decreased and atmospheric CO₂ was absorbed into seawater (Frakes, 1999).

3.2 Ocean Layers

There are three main horizontal zones in the ocean, which are based on water density and separated by gravitational forces (Figure 3.4). They are the mixed layer, pycnocline, and deep layer.

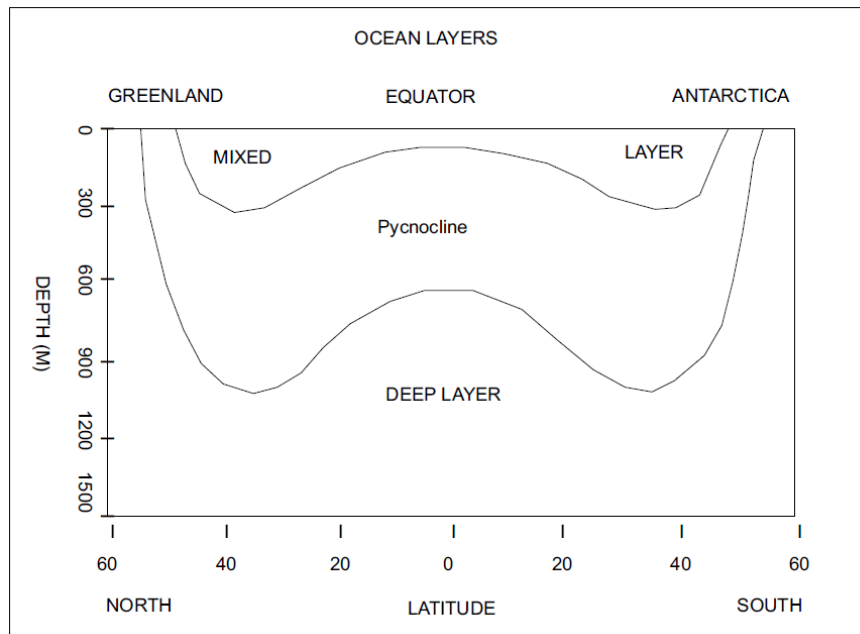


Figure 3.4: Ocean layers profile – Greenland to Antarctica longitudinal transect (after the American Meteorological Society, 2005). The upper mixed surface has variable thickness depending on the temperature and winds.

The upper mixed surface has variable thickness depending on the temperature and winds. The mixed surface layer occurs in the top one hundred metres of water above the pycnocline, and is uniformly dense, but its thickness can change due to winds and temperature. Strong surface currents can penetrate deeper to several hundred metres (American Meteorological Society DataStreme Ocean, NASA 2017).

Below the mixed layer, the pycnocline extends from about 500 – 1000 metres, and is a porous layer through which kinetic energy moves from the surface layer into the deep-water layer. In the pycnocline, the water density changes rapidly with depth. Cold, salty water is denser than fresh, warm water and sinks. The pycnocline is stable and serves to act as a barrier to vertical ocean motion which suppresses mixing. Storms temporarily disrupt the stability. If the temperature declines with depth and causes an additional increase in density with depth, the pycnocline is also a thermocline. But if an increase in salinity is the dominant cause of the increase in density with depth, it is called a halocline.

3.2.1 Depth of Sediment Disturbance

Nearshore, ocean current velocities are generally 5-20 cm/s from between 70 and 140 metres in depth during fair weather (Trabucho-Alexandre, 2015; Hickey, 1997) with the depth increasing during cyclones. The water movement determines the depth to which sediments can be disturbed, and this can be as much as 200 metres with 300-500 cm/s water velocities (Komar, 1972; Trabucho-Alexandre, 2015). Eddies in the deep ocean can also occur and increase the current speeds up to 300 times (Hollister et al. 1984; Trabucho-Alexandre 2015). Current velocities required to erode sediment in the ocean range from 5-15 cm/s for calcareous ooze, to 7-20 cm/s for settled sediment or even 30-100 cm/s for some clays (Southard et al., 1971; Lonsdale and Southard, 1974; Trabucho-Alexandre, 2015).

3.3 Upwelling and Downwelling Currents

Alternating wind patterns affect surface water circulation due to changes in Ekman transport and the resulting changes to the location of Ekman divergence (upwelling) and convergence (downwelling) zones (Poulsen et al., 1999). The occurrence of upwelling and downwelling ocean currents affects both the temperature of the sea surface waters and the amount of organic matter productivity. Changing surface

temperatures and precipitation patterns also affect intermediate and deep ocean circulation (Poulsen et al., 1999).

3.3.1 Upwelling

Upwelling zones show high productivity resulting in organic-rich sediments because they permit nutrient-rich water from a 100-200 metre depth to be brought to surface. Upwelling waters which originate in the deep layer below the pycnocline will be colder than the surface waters that are replaced. Cool, deep waters are rich in nutrients such as nitrogen and phosphate compounds, which are required for phytoplankton growth. When the nutrients reach sunlight in the photic (euphotic) zone, rapid growth in the phytoplankton population occurs.

Nutrients are transferred from the photic (euphotic) zone as organisms die and descend through the water column, causing nutrient values to increase with depth. However, due to the thermocline and overturning circulation patterns, nutrients are brought to the surface again in upwelling zones and the cycle repeats (Trabucho-Alexandre et al., 2010). Productive fishing zones are found in areas of coastal upwelling, where cold nutrient rich waters are brought to the surface.

In regions where wind direction, the Coriolis Effect, and Ekman transport move surface waters away from the coastline, deep water wells up from below. Upwelling is most common along the eastern sides of ocean basins (western coasts) when winds blow from the poles, causing Ekman transport of surface water away from the shore. In the present day, upwelling occurs on the west coast of South America (Peru and Chile) and southwestern Africa where transport is away from the shoreline. Upwelling occurs at the equator as the winds change directions in that region, and the Coriolis Effect is weak to nonexistent. Surface water goes north or south depending on the hemisphere (or position relative to the seasonal Inter Tropical Convergence Zone (ITCZ)), leaving water to upwell at the equator.

There is also some upwelling along the eastern coasts (western basin), but this is minimal due to western boundary currents. Note that relatively little upwelling occurs

along the western coasts of Europe and North America due to continental configurations. (NASA, 2017).

3.3.2 Downwelling

In regions where wind direction, the Coriolis Effect and Ekman transport move surface waters towards the coastline, downwelling occurs. Water piles up near the coastline and is forced downwards. In zones of coastal downwelling, the surface layer of warm, nutrient deficient water becomes denser and sinks, reducing biological productivity.

3.4 Tectonics

During the breakup of Pangea, rifting in the Triassic and Jurassic created the continental margins of what is now northwest Africa, eastern North America, southern North America and northern South America (James, 2005). The Yucatan rifted from South America at approximately 140 Ma (Burke, 1988).

North America rifted away from South America during the Jurassic, however, South America remained attached to what is now Africa (James, 2005). While the North Atlantic opening was well underway by 140 Ma, the South Atlantic opened later, just prior to 120 Ma. South America began to separate from Africa by rifting to the west (James, 2005). The South Atlantic opening was long and narrow, with the narrowest seaway likely having higher than average salinity. In the Cretaceous the flow of two large rivers, the Amazon and the Zaire, was to the Pacific and the Indian Oceans respectively. The present-day configuration has both flowing into the Southern Atlantic, which did not take effect until the Miocene (Hay et al., 1999).

The syn-rift phase of continental breakup can last hundreds of millions of years, and is followed by a post-rift phase, during which tectonic subsidence does not necessarily follow a steady decrease with time (Unternehrl et al., 2010; Cloetingh and Ziegler, 2007; Dupre et al., 2007; Bertotti and Gouza, 2012).

3.4.1 Central American Seaway

During the mid-Cretaceous the Central American Seaway through the Panama Strait area was thought to be open connecting the Pacific Ocean to the Atlantic Ocean (Hay et al., 1999; Trabucho-Alexandre et al., 2010) as seen in Figure 3.5, where the centre figure shows the open seaway allowing water flow from west to east. The Caribbean Plate migration and creation of the associated island arc did not occur until the Late Cretaceous (Alexandre et al., 2010; Utsunomiya et al., 2007). During the Early Cretaceous, a deep passage from the central Atlantic through to the Pacific was not open, as it was blocked by northern Central America blocks and the Caribbean Plate (Hay et al., 1999). The earliest opening between North and Central America was about 100 Ma.

During the mid-Cretaceous, as Pangea broke apart, it is thought that Pacific intermediate-depth water began to flow into the Central (North) Atlantic (Trabucho-Alexandre et al., 2010). The Caribbean Plate moved eastward between the gap, and it is thought that a collision with the Bahama Platform and South Florida in the Late Cretaceous halted its eastward movement (Hay and Wold, 1996; Hay et al., 1999). In the Late Cretaceous, deep passages appeared which connected the western Tethys with the Central Atlantic, and the South Atlantic connected with the Indian Ocean through a southerly route (Hay et al., 1999).

3.4.2 Cretaceous Ocean Circulation Models

During the post-rift phase of the proto-Atlantic mid ocean ridge, ocean circulation was affected by sea levels, intraplate deformation (warping), vertical motion of sea water, and lithosphere-mantle interaction. Lithosphere-mantle interaction depends on thermal age, deformation, and flow (rheology) of the lithosphere, making it difficult to model (Cloetingh et al., 1985; Cloetingh et al., 2013). The closure of major gateways connecting open sea areas also affected ocean circulation patterns in the same way that the continental configuration affects present-day currents (Cloetingh and Haq, 2015).

Inherited continental topography affected sea level changes, glacial isostatic adjustment, dynamic topography (differences in surface elevation in the ocean), mantle-lithosphere interaction, oceanic crust production rate variations, plate reorganization, and plate deformation, which in turn was overwritten by ensuing climate effects, glaciations, and deglaciations, all affecting the sea level (Cloetingh and Haq, 2015). Continental flooding data and volume estimates for ocean ridges were first used to determine a eustatic curve for the Cretaceous (Pitman III and Golovchenko, 1983; Ronov, 1994) and the overall curve is still valid even with recent advances in modeling (Cloetingh and Haq, 2015) (Figure 2.6).

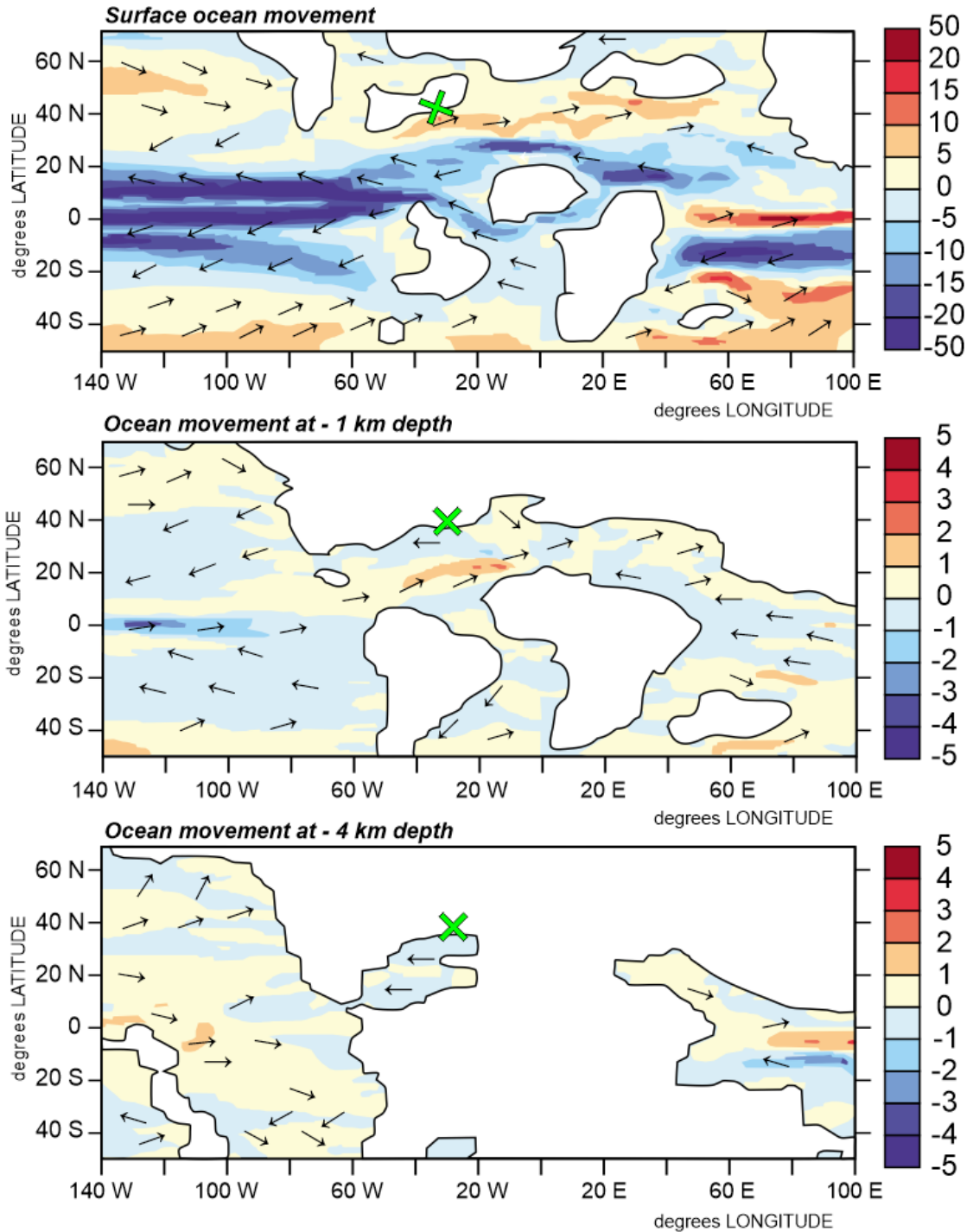


Figure 3.5: Model of the mean velocity vectors of surface waters (top) and at 4 km subsurface (bottom) in cm s^{-1} . The green 'X' in each plate indicates the approximate position of present-day Nova Scotia. Arrows indicate the direction of movement. The surface water extent is much greater than the extent at a 4 km depth. At surface there is connectivity between the Pacific and Atlantic Oceans, however with depth it is much reduced. An estuarine circulation pattern brings nutrients from the volcanic and submarine igneous events in the Pacific favoring the deposition of organic-rich sediments (Modified from Trabucho-Alexandre et al., 2010).

Paleogeography and winds established the estuarine circulation pattern in the mid-Cretaceous (the pattern of circulation that is established where saline ocean waters meet incoming fresh waters via rivers and/or estuaries), which also encouraged upwelling on the south edge of the North Atlantic that was observed in the model (Figure 3.6). Winds blowing parallel to the coastline would lead to Ekman upwelling (Trabucho-Alexandre et al., 2010).

Authors such as Summerhayes (1981), and Thierstein and Berger (1978) have suggested an estuarine circulation of ocean water (that which occurs near river mouths where fresh water meets saline marine conditions) could be the process by which the organic matter is deposited in the North Atlantic in the mid-Cretaceous (Alexandre et al., 2010). Meyer and Kump (2008) and Ridgwell et al. (2007) have put forward a biogeochemical cycling model for the oceans during the Cretaceous, which show a phosphate trapping mechanism for the North Atlantic and also the western Tethys oceans (Alexandre et al., 2010). Alexandre et al. (2010) reports that Meyer and Kump (2008) indicated that stagnant oceans do not lead to euxinia (anoxia, or oxygen depletion) and point to an estuarine circulation pattern which resulted in black shale deposits. Alexandre et al. (2010) show that there is a connection between Pacific large igneous provinces (LIPs) and their supply of nutrient-rich waters, and the flow of intermediate water from the Pacific into the Atlantic, and the resulting OAEs (Trabucho-Alexandre et al., 2010).

3.4.3 Upwelling and Downwelling Zones in Circulation Models

Ekman-introduced upwelling is found within horizontal ocean circulation. Surface and intermediate waters flow in opposite directions (as seen in the top and middle maps of Figure 3.5) resulting in nutrients also shifting horizontally, and the total amount of nutrients showing an increase in the direction of the subsurface flow (Brongersma-Saunders, 1971; Redfield et al., 1963; Alexandre et al., 2015). This direction is eastward in the mid Atlantic during the mid Cretaceous (Trabucho-Alexandre et al., 2010).

Results from the model indicate that a global thermohaline ocean circulation in the Cretaceous was stronger than that which occurs today. The model shows two large vertical circulation cells in the Pacific Ocean (Figures 3.5 and 3.6). The present-day meridional circulation in the North Atlantic (Figure 3.2) is connected to the South Atlantic and connects two polar areas, but during the Cretaceous the model shows that the circulation pattern was a narrow latitudinal ocean connecting the former Tethys region with the Atlantic, and both regions were tropical (Trabucho-Alexandre et al., 2010).

This paleo-trans-equatorial seaway had a strong zonal circulation which was overturning and was dominant in the southern region of the North Atlantic (Alexandre et al., 2010) from approximately 10 – 30 degrees north of the equator. Details of the model show that surface water moved westward from the Atlantic Ocean to the Pacific Ocean, while at intermediate depths, around 1000 metres, water moved eastward from the Pacific to the Atlantic in an estuarine circulation pattern. The basins in the North Atlantic, which received Pacific water at intermediate levels, would be productive when the nutrients reached the euphotic zone, or the upper 80 metres of the ocean (Alexandre et al., 2010). Upwelling zones are seen in the model in the Pacific near the equator, the south margin of the North Atlantic, and the Eastern Tethys. The upwelling zones correspond with mid-Cretaceous black shale deposits (Alexandre et al., 2010).

Paleogeography affected the thermohaline circulation, where the North Atlantic in the mid-Cretaceous ran parallel to the direction of flow of the trade winds, and where a gateway downwind (the Central American Seaway) had surface water that was circulated east to west, and subsurface water which flowed west to east into the Pacific. Water laden with nutrients from the Pacific upwelled (Alexandre et al., 2010). However, water saturation of O₂ is 20% lower at 15 degrees C than at 0° C (Huber et al., 2002; Pedersen and Calvert, 1990; Alexandre et al., 2010) so it is thought that oxygen depletion was occurring.

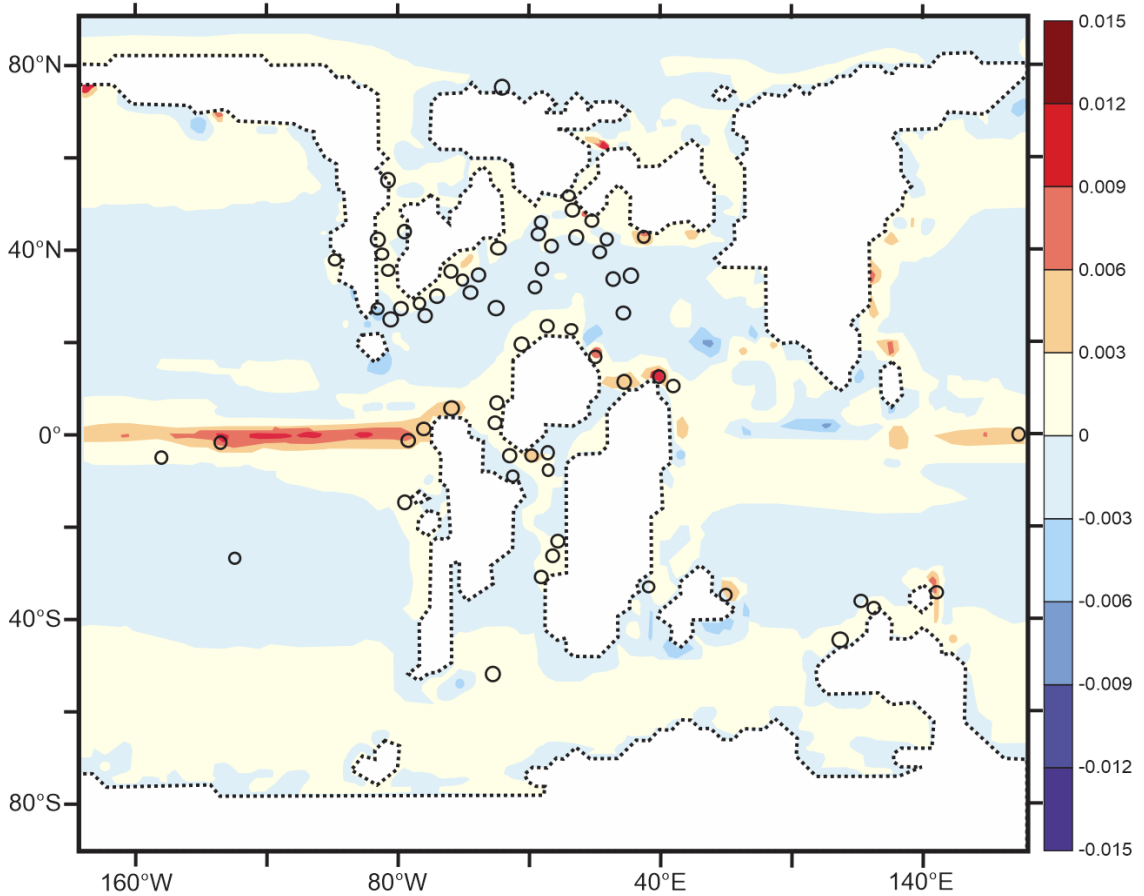


Figure 3.6: This figure of the Cretaceous continental configurations is a model by Trabucho-Alexandre which clearly shows the areas where the average vertical velocity points to areas of upwelling (positive velocity), with the strongest shown in orange/red colours at the equator (a divergence zone) and in the South paleo-Atlantic (approximately +25 degrees N), which is most likely in the area where La Luna Formation was deposited. Known black shale deposits are indicated with black circles. A pale orange area is seen in the paleo-Scotian Basin which would indicate a moderate amount of upwelling, but not as significant as than seen elsewhere (Modified from Trabucho – Alexandre et al., 2010).

Winds and tides drive the overturning of the circulation in the oceans today and likely also in the Cretaceous (Ledwell et al., 2000). Alexandre et al. (2010), from analyzing models, proposed that the thermohaline circulation was similar or higher than present day (Otto-Bliesner et al., 2002), and this agrees with the absence of anoxic sediments in the deep Pacific in the Cretaceous (Heezen et al., 1973; Trabucho-Alexandre et al., 2010).

3.5 Summary

The deposition of organic matter is influenced by ocean currents, wind currents and the availability of nutrients. Volcanic activity in the Pacific Ocean, and in the proto-Atlantic Ocean due to rifting, contributed nutrients to the ocean water. The ocean circulation of the proto-Atlantic was oriented east-west, eventually changing to a north-south circulation after the opening of the southern proto-Atlantic. The opening of the Caribbean Seaway allowed nutrient-rich waters to migrate from the Pacific in a west to east direction.

An abundance of nutrients fosters production of organic matter in the ocean water. In zones of upwelling, production of organic matter is abundant. Zones of upwelling are enhanced by winds, and modelling shows rich upwelling areas in the ICTZ zone at the equator, as well as the area that is present-day offshore northern South America. The basins in the North Atlantic, which received the Pacific water rich in nutrients at intermediate levels, would be productive when the nutrients reached the euphotic zone, or the upper 80 metres of the ocean (Alexandre et al., 2010). Upwelling zones are seen in the model in the Pacific near the equator, and in the south margin of the North Atlantic, as well as in the Eastern Tethys. The upwelling zones correspond with mid-Cretaceous black shale deposits (Alexandre et al., 2010).

In the areas of highest productivity, oceanic anoxic events were possible. Organic matter deposits on ocean floors would initially exhibit bioturbation, however with very high productivity, oxygen levels would deplete, biota would die, and subsequent deposits would be anoxic. Without bioturbation, laminated black shale deposits would prevail and mark these oceanic anoxic events.

Chapter 4: Organic- Rich Deposits in the Proto-North Atlantic Ocean

4.1 Introduction

When exploring for oil and gas deposits, determining the presence of an organic-rich source rock is of great importance. It must be determined whether the rock in question has the potential to produce hydrocarbons, or if the hydrocarbons have already been generated and migrated elsewhere (Law, 1999). Source rocks are organic-rich shales and lime-mudstones (Passey et al., 1990), which, when subjected to sufficient heat and pressure will generate petroleum. Understanding the organic geochemical nature of source rocks and their depositional history helps to define their potential for petroleum generation (Huang et al., 1996).

This chapter will cover the fundamentals of organic matter and various factors that influence its occurrence, and its role in source rock formation. Following that, the occurrence of oceanic anoxic events and their characteristics will be reviewed, with a summary of the most significant zones of Cretaceous age in the proto-Atlantic Ocean which have proven to be effective source rocks.

4.2 Source Rock Characteristics

The four main types of source rocks can be defined as follows:

- Potential source rock – that which has enough organic matter, which if subjected to heat and pressure, could generate and expel hydrocarbons.
- Effective source rock – that which contains organic matter and is producing hydrocarbons at present.
- Relic effective source rock – that which was generating and expelling hydrocarbons but stopped prior to using up its supply of organic matter due to thermal cooling.
- Spent source rock – that which has become mature or does not have sufficient organic matter left so it is unable to generate or expel hydrocarbons.

Source rocks can be characterized by the quantity of its organic material, as determined by a measure of its total organic carbon (TOC), and the quality of the

source rock by identifying the type of kerogen involved. TOC and kerogen depend on the depositional setting, while the thermal maturity of the source rock is a result of its tectonic and structural history (Law, 1999).

4.2.1 Source Rock and Oil and Gas Deposits

The deposits of oil and gas found worldwide are relatively young; 70% of oil and gas deposits were generated from the Coniacian onward and 50% from the Oligocene onward (Klemme and Ulmishek, 1991). In their summary table of worldwide source rock areas, Klemme and Ulmishek (1991) mention the Upper Jurassic source rocks of the Kimmeridgian clays and marine siliceous shales found for North Sea and Greenland Sea deposits. The Upper Neocomian – Aptian lacustrine and marine shales, and the Turonian marine shales are named as Middle Cretaceous source rocks for South Atlantic rift basins.

The middle Cretaceous stratigraphic intervals worldwide host source rocks which hold 29% of the world's reserves of oil and gas (Klemme and Ulmishek, 1991). Factors which control the distribution, geochemistry and effectiveness of the source rocks are age, paleolatitude, structural setting and biota (Klemme and Ulmishek, 1991). Although the Cretaceous provided 29% of the world's generated petroleum it only provided 20% of the world's trapped petroleum (Klemme and Ulmishek, 1991).

Source rocks with Type III kerogen are more abundant than Type I or II, with Type II mostly found in the Tethyan seaway. Along the easterly part of the north American marine shelf, the structural type for source rock is classified as a half-sag or linear sag over a single rift. Worldwide, 71% of the effective Cretaceous source rocks are structurally defined as linear sags (Klemme and Ulmishek, 1991). According to the study by Klemme and Ulmishek (1991), of the 29% of the worldwide source rocks that were created in the Mid Cretaceous, 61% of them produce oil and 10% produce gas generated from kerogen types I and II, and 4% of them produce oil and 25% produce gas generated from kerogen Type II and coal.

Diversity and abundance of the source rocks worldwide was on the increase through the Phanerozoic. Most likely, as life evolved, increased organic matter supply contributed to this (Klemme and Ulmishek, 1991).

4.3 Petroleum System Events and Processes

The four main events components of a petroleum system are:

- a) organic-rich potential source rock
- b) reservoir rock
- c) seal rock
- d) overburden, which serves to bury and heat the organic matter.

Subsequent processes that are necessary are the formation of effective traps and the generation, migration, and accumulation of hydrocarbons. Preservation of these events is required as well. The critical moment is defined as the point approximately half-way through the sequence of events when peak hydrocarbon generation occurs (Al-Hajeri, 2009).

Figure 4.1 shows the components and processes of the petroleum system events found offshore Nova Scotia as published in the Play Fairway Analysis (OETR, 2011). Potential source rocks in the Scotian Basin are noted sporadically from the Jurassic through to the mid-Cretaceous, with the Aptian source rock being the youngest organic-rich deposit of interest. Preservation of this source rock is uncertain (OETR, 2011).

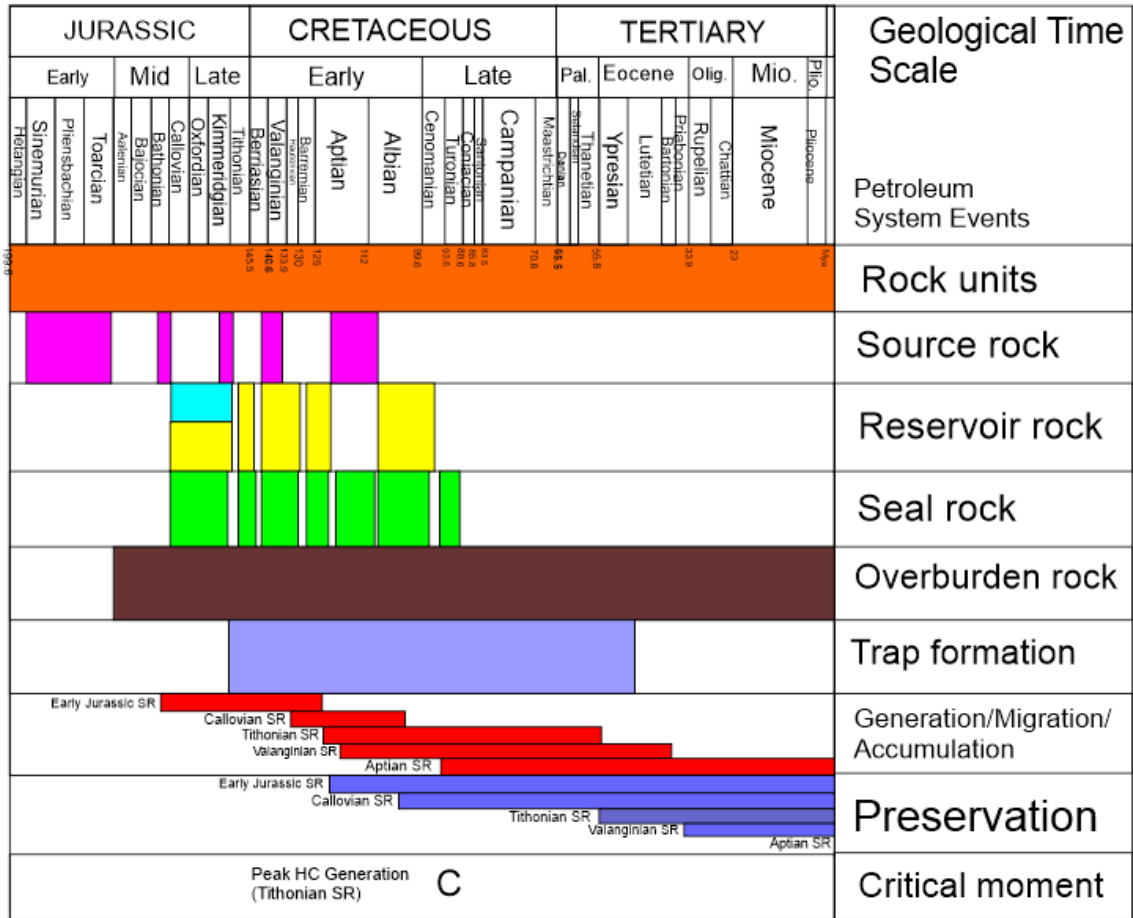


Figure 4.1: Petroleum systems event chart for the Scotian Basin, offshore Nova Scotia (Beicip-Franlab, 2011). The sequence of deposition of source rock, reservoir rock, and overlying rock, which serves to seal the reservoir rock, and overburden, which aids in heating the underlying source rock to generate hydrocarbons is shown. The processes that follow are trap formation and the subsequent hydrocarbon generation, migration, and accumulation into those traps, followed by preservation. The critical moment is defined as approximately halfway through the entire process (after Al-Hajeri et al., 2009). Aptian source rock is seen to have generated, migrated and accumulated however it was not preserved according to this chart of petroleum systems events. In fact, the best-preserved source rocks appear to be from the Early Jurassic (OERA, 2011).

4.4 Organic Matter

Organic matter is material of a biological origin that can decay. At present day, production of organic matter in the oceans of the world is about 50 billion tons a year, but most of this (99%+) is broken down due to oxidation, microbial activity in the water column or bottom sediments, or chemical changes in the water column. The result is that only .01 - .001% of the organic matter originally produced is available to be preserved in sediments.

4.4.1 Organic Facies

The study of facies rich in organic matter is used to predict the likelihood of hydrocarbon source rocks forming in certain depositional environments, and to predict lateral variations in quality (Powell, 1987; Tyson and Funnell, 1990). Palynofacies refers to the specific assemblage of insoluble particulate organic plant matter (spores and pollen) that is left from a rock sample, after the matrix has been dissolved by HCl and HF acids (Tyson, 1995; Powell et al., 1990). This provides information on the age of the rock, depositional environment, and association with a particular type of hydrocarbon that would be expelled from the resulting source rock (Tyson and Funnell, 1990).

There are also structural controls on organic-rich facies. Klemme and Ulmishek, define structural forms such as platforms, circular sags, linear sags, rifts, foredeeps, half sags and deltas (1991). They conclude that in the mid-Cretaceous, the main effective source rock deposit mechanism occurred in linear and circular sags. Linear sags are elongated low areas overlying single rifts with low angle sloping limbs, while circular sags are larger and overlie branching rift systems or basaltic areas.

4.4.2 The Carbon Cycle Overview

The carbon cycle defines the two-way flow of carbon on the planet. The cycle occurs naturally and is driven by biological, physical and chemical reservoirs or 'sinks' which occur on land through biota and soil, and in the oceans between surface waters, biota and the deep ocean. Carbon is released to the atmosphere through forest fires, volcanic eruptions, ruminant livestock, and the burning of fossil fuels.

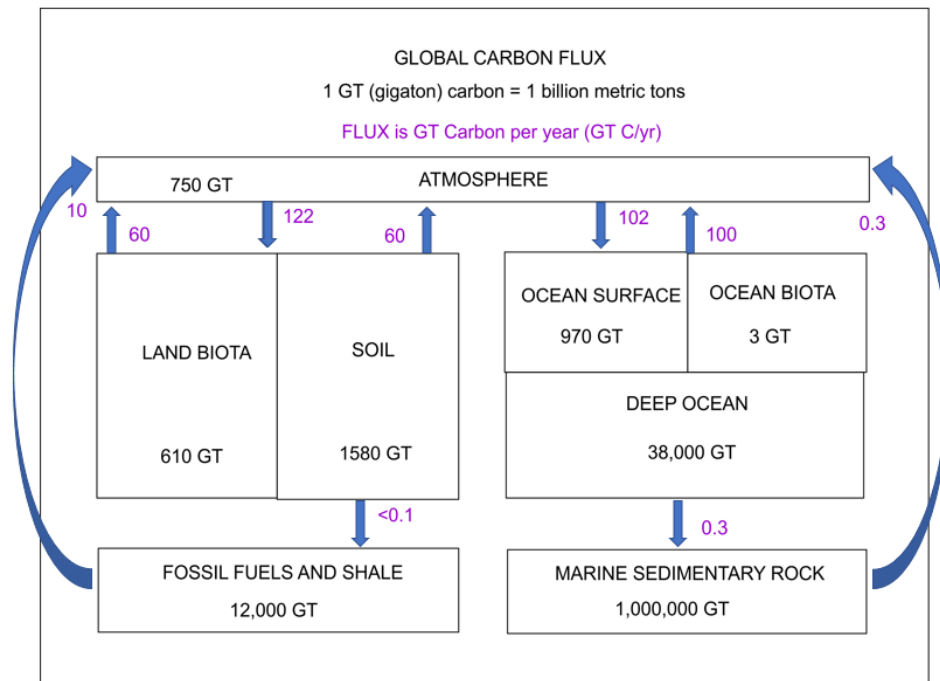


Figure 4.2: Schematic outlining present day carbon flux (after Cornell, 2016). The violet numbers indicate the carbon flux per year in gigatons and the black numbers indicate the amount of carbon held (United States Department of Energy (USDOE) 2017). **Note on use of ton (SI) vs. tonne (metric). The British ton is referred to as a long ton weighing 2240 pounds, and the American ton is referred to as a short ton which weighs 2000 pounds or 907.18 kg. The metric tonne weighs 1000 kilograms, or 2204.62 pounds. The data from this table is from the USDOE (USDOE, 2017) and is therefore using the American ton measurement.

A carbon cycle can be viewed as slow, from 10s to 100s of thousands of years or more, or fast, for example daily or yearly. A slow carbon cycle operates on a long-term cycle of chemical weathering where atmospheric CO₂ is absorbed, such as during erosion, fluvial transport of organic matter to the oceans, subduction of carbonate rocks, and release of CO₂ gases through volcanic activity. Contrastingly, a fast carbon cycle involves the photosynthesis of plants and the respiration of animals. Water, CO₂, and sunlight help plants produce oxygen and carbohydrate molecules as food for animals, who in turn consume plants and animals and inhale oxygen, and whose exhalations produce CO₂ (Sorkhabi, 2016).

4.4.3 Kerogen

Kerogen, or fossil organic matter, is the naturally occurring solid organic matter in source rocks, which is insoluble in common organic solvents and alkaline solutions

(Tissot and Welte, 1984) and can yield hydrocarbons upon heating. The amount and type of kerogen determines if the source rock is gas- or oil-prone (Law, 1999).

Typical organic constituents of kerogen are algae and woody plant material.

Four types of kerogen are classified:

- Type I: Alginite and amorphous kerogen – algal bodies and other algal-derived debris and/or marine plankton - highly likely to generate oil.
- Type II: Amorphous kerogen and Liptinite (a coal term - formerly Exinite) - mixture of terrestrial spores, pollen, leaf and plant material, and marine planktonic material - can generate waxy oil.
- Type III: Vitrinite - woody terrestrial source material - typically generates gas.
- Type IV: Inertinite – woody debris – no hydrocarbon potential.

Types of Kerogen and their Hydrocarbon Potential				
Environment	Kerogen Type	Kerogen Form	Origin	HC Potential
Aquatic	I	Alginite	Algal bodies	Oil
		Amorphous Kerogen	Structureless debris of algal origin	
	II		Structureless planktonic material primarily of marine origin	
Terrestrial	II	Exinite	Skins of spores and pollen, cuticle of leaves and herbaceous plants	
	III	Vitrinite	Fibrous and woody plant fragments and structureless colloidal humic matter	Gas, some oil
				Mainly gas
	IV	Inertinite	Oxidized, recycled woody debris	None

Figure 4.3: Types of Kerogen and their potential for generating hydrocarbons (after Schlumberger Limited, 2015).

The Logan Canyon Formation sediments present in wells in the Scotian Basin contain organic matter with kerogen that is of largely terrestrial type III origin (Bujack et al., 1980; Wade and MacLean, 1990). Deposits from the lower member of the Missisauga Formation may be correlatable with the rich, oil-prone Jurassic Kimmeridgian source rocks found in the Grand Banks (Wade and MacLean, 1990).

4.4.4 Total Organic Carbon

A measurement of the amount of total organic carbon (TOC) in a sample is used to determine if it can be classified as a source rock (Law, 1999). TOC quantifies the concentration of organic matter in a source rock expressed as weight %, which is the percentage of TOC compared to the total weight of the sample (Schlumberger, 2015).

The average TOC value for all shales is 0.8% wt%, while TOC for source rock shales is 2.2 wt%. By comparison, the average for calcareous shale source rocks is 1.8 wt%, and for carbonate source rocks is 0.7 wt%. The average for all source rocks across the board is 1.8 wt% (Law, 1999).

4.4.4.1 Rock Eval Pyrolysis and Kerogen

To determine a shale sample's total organic carbon (TOC), the rocks are analyzed using the "Rock Eval Pyrolysis" method. During pyrolysis, 100 mg samples are heated, without oxygen present, from 300° C to 550° C in the presence of helium (Peters, 1986). The resulting amounts of oil and/or gas are used to rate the potential of a rock to generate petroleum and its thermal maturity (Peters, 1986). Further detail will be described in Chapter 5 "Methods".

4.4.4.1.1 van Krevelen and Pseudo van Krevelen

Plots

The van Krevelen diagram was originally used to classify coals (van Krevelen and Schuyer, 1957). Figure 4.4 shows the plot of Atomic Oxygen/Carbon (O/C) ratios on the X-axis versus Atomic Hydrogen/Carbon (H/C) ratios on the Y-axis (Tissot et al., 1974;

Tissot et al., 1980). Values of atomic ratios of H/C are typically in the range of 0 to 2, and range of the atomic ratio of O/C would be in the range of 0 to 1 (Kim et al., 2003).

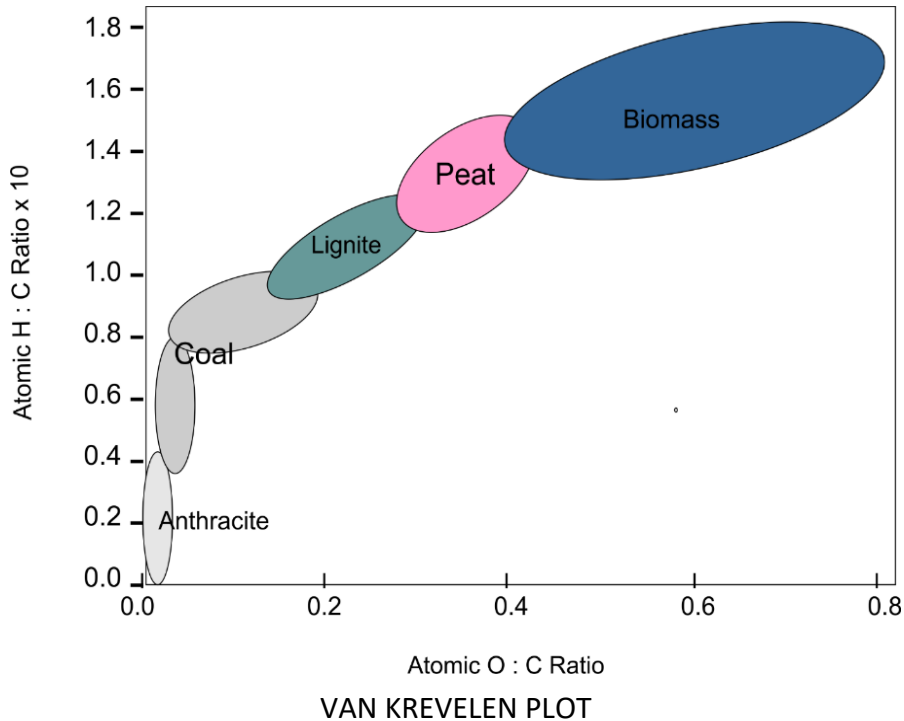


Figure 4.4: Van Krevelen Diagram. Coal determination using the van Krevelen diagram (van Krevelen and Schuyer, 1957). The van Krevelen diagram shows the plot of Atomic O/C ratios on the X-axis versus Atomic H/C ratios on the Y-axis (Tissot et al., 1974; Tissot et al., 1980) and was originally used to classify coals. Values of atomic ratios of H/C are typically in the range of 0 to 2, and range of the atomic ratio of O/C would be in the range of 0 to 1 (after Kim et al., 2003).

For kerogen determinations, a pseudo-Van Krevelen diagram (Figure 4.5) is used to display Rock Eval Pyrolysis data from a Pyrogram. A flame ionization detector (FID) is used to create a Pyrogram to display the results of the test, giving values of TOC, HI (Hydrogen Index), OI (Oxygen Index), S1, S2, S3 values and T_{max} (maximum temperature reached). These measurements indicate the source rock potential of the samples. A value of total organic carbon above 0.5 wt.% (weight percent) is the minimum for an effective source rock, 0.5 to 1% is fair quality, 1-2% is good, and over 2% is very good (Peters, 1986).

These plots show kerogens typed as I, II, III and IV, or very oil-prone, oil-prone, gas-prone and inert respectively. Inert kerogen contains almost no hydrogen (Schlumberger Limited, 2015) and therefore plots very low on the Y-axis. As kerogen is subjected to heat and pressure, bitumen, heavy oil, liquid hydrocarbons, and natural gas

(methane and light hydrocarbons) are produced in that order (Tissot and Welte, 1984; Schlumberger Limited, 2015).

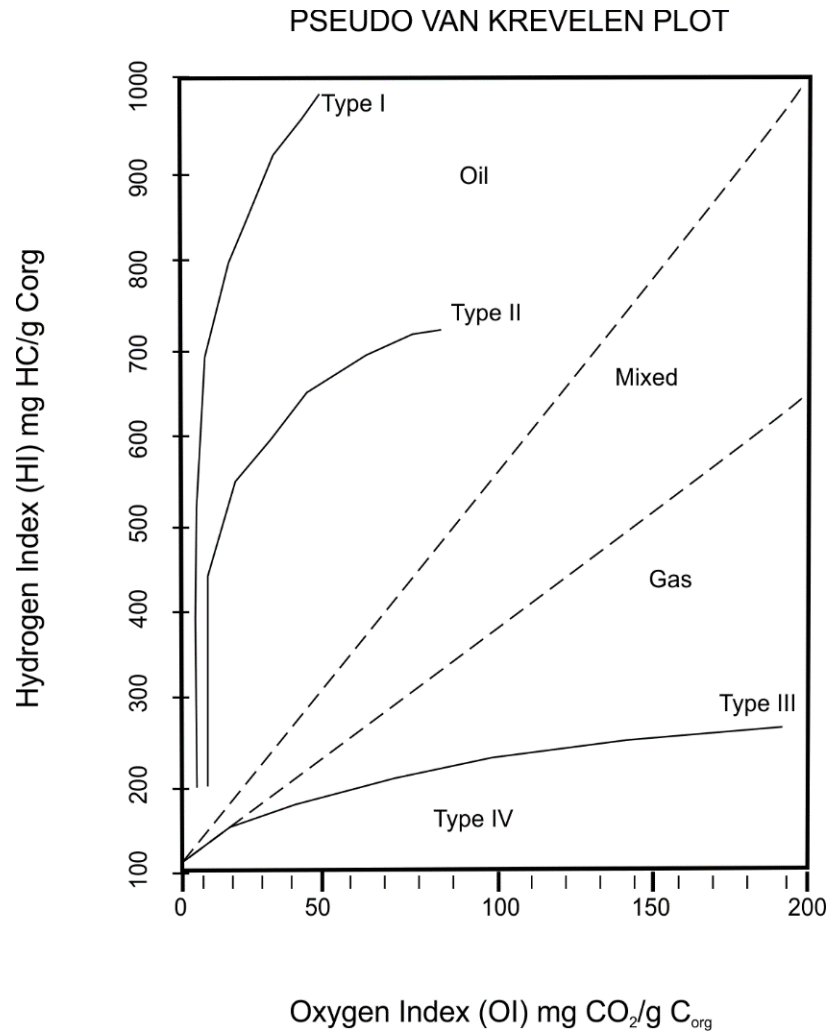


Figure 4.5: Pseudo Van Krevelen diagram showing data plotted from a Pyrogram (from Rock Eval Pyrolysis), which plots the Oxygen Index (OI) in mg CO₂/g C_{org}, on the X-axis versus the Hydrogen Index (HI) in mg HC/g TOC on the Y-axis. Values for the X-axis range from 0 to 200 and on the Y-axis from 0 to 1000. From these plots, the type of Kerogen is classified, and indications are made whether the sample is oil- or gas- prone.

Type I = oil prone, lacustrine with abundant H

Type II = oil/gas prone, marine, moderate H.

Type III = gas prone, terrestrial, minimal H.

Type IV = vitrinite, terrestrial, no H.

(Law, 1999)

Kerogen type III and coal are less effective for petroleum generation than kerogen types I and II on a per area basis (Klemme and Ulmishek, 1991) from studies

based on geochemistry. Type I and II kerogens are oil-prone, and type III and coal are gas-prone (Klemme and Ulmishek, 1991).

4.4.5 Climate

The optimal setting for source rock deposition is a warm climate with high humidity at low to middle latitudes along with tropical rainforests feeding onto a continental shelf which is home to a reef system (Grunau, 1983; Klemme and Ulmishek, 1991).

Klemme and Ulmishek's 1991 study found that two thirds of source rocks in the world were deposited between the paleoequator and 45 degrees paleolatitude. Deposition of black shales is generally associated with high amounts of blue-green algae (cyanobacteria) and green algae, with higher bio-productivity than is seen in winter in the higher latitudes.

The lower occurrence of seasonal water overturn in the stagnant ocean regions favours the deposition and preservation of organic matter from latitudes 0-45 degrees in subtropical and tropical waters. Tropical rainforests have very high productivity on land, but organic matter is usually not preserved as the occurrence of decomposition in that climate is also very high. In higher latitudes, peat bogs are a more common site for preservation of organic matter (Klemme and Ulmishek, 1991).

The climate in the Mesozoic was warmer than present, therefore it was possible for black shales, rich in kerogen types I and II to be deposited at higher than usual paleolatitudes from the Late Jurassic onwards. During the Mesozoic, areas with Type III kerogen and coal were located at high paleolatitudes (Klemme and Ulmishek, 1991). The effectiveness of the source rocks deposited from 0 to 45 degrees paleolatitude, with kerogen types I and II, is much greater than the areal extent of the source rocks. Kerogen types I and II found at paleolatitudes greater than 45 degrees, and kerogen types III and for coal, at both low and high paleolatitudes, have source rock with a much lower effectiveness compared to the areal extent (Klemme and Ulmishek, 1991). This

effectiveness is due to the high-quality reservoirs that are provided by carbonate reefs and siliciclastic reservoirs seen at low paleolatitudes (Klemme and Ulmishek, 1991).

Klemme and Ulmishek conclude that black shale facies were often found together with type II kerogen and reefal reservoir rocks with evaporites as seals, and this often resulted in large accumulations of oil and gas. Such effective petroleum systems are found less with type III kerogen and coal with siliciclastic reservoir rocks and associated seals (Klemme and Ulmishek, 1991).

The effectiveness of source rocks with type III kerogen and coal does not vary much due to structural limitations. However, for type II kerogen, the associated black shale facies were almost exclusively deposited under anoxic or dysoxic conditions since the late Paleozoic. This would often happen on platforms and in circular or linear sags, occasionally in rifts and foredeeps, but rarely in half sags and deltas (Klemme and Ulmishek, 1991).

4.4.5.1 Milankovitch Cycles

Milankovitch astronomical orbital-forcing cycles have affected climate on earth throughout time. Milutin Milankovitch (1879 – 1958) was a Serbian astrophysicist who noticed orbital variations in the eccentricity of the earth's orbit, its axial tilt, and axial precession (wobble), which resulted in a cyclical variation of solar radiation reaching the earth's surface. As a result, the climatic patterns were affected which he thought regulated the pattern of ice advances and retreats (NASA, 2017).

Milankovitch created a mathematical model which calculated differences in latitude and their corresponding differences in the earth's surface temperature for 600,000 years prior to the year 1800. To tie this into the history of ice ages, he chose to model the changes at 65 degrees north latitude where ice sheets were currently in existence. Cooler summers could reduce summer snowmelt, resulting in ice sheet growth changes that could be measured.

In 1976, a study published in the journal *Science* examined deep-sea sediment cores and found that Milankovitch's theory corresponds to periods of climate change (Hays et al., 1976).

4.4.6 Organic-Rich Shale

Organic-rich shales have been noted as abundant in early and mid-Cretaceous deposits from the deep North Atlantic (Summerhayes, 1987; Trabucho-Alexandre et al., 2010), particularly in the Valanginian-Barremian (Blake-Bahama Formation), the Aptian-Cenomanian (Hatteras Formation) and to a lesser extent, the Turonian-Santonian (Plantagenet Formation) (Summerhayes, 1987). The supply rate of organic matter in the eastern and western North Atlantic was similar, though increasing in the east during the Cenomanian and later Cretaceous times, with terrestrial organic matter dominating in the western North Atlantic (Summerhayes, 1987).

Early in the Valanginian, through to the Coniacian there were increased levels of organic matter in the Atlantic (Summerhayes, 1987). This period was favorable due to a higher level of accumulation of organic matter on both sides of the North Atlantic. Productivity rates were higher and burial rates favored preservation. During the Cenomanian, it is thought that a change in deep ocean circulation resulted in upwelling of nutrients from deep water in the North Atlantic, so that sediments from the Cenomanian-Turonian boundary show a large productivity event at this time (Summerhayes, 1987).

4.4.6.1 Black Shale

Black shale is defined as shale with an organic matter content greater than 0.5% (Trabucho-Alexandre, 2015). Black, dark green and dark grey sediments containing greater than 1% total organic carbon (TOC) are evident in deep sea North Atlantic drill cores (Summerhayes, 1987). These black shales can be good source rock for petroleum systems where they have undergone burial to sufficient depth to be heated to the point of maturity (Summerhayes, 1987).

Lithologically, these black shale deposits range in colour from black, dark green or dark grey layers with higher amounts of organic matter, to lighter green or grey marly layers with lesser amounts of organic matter. The lighter green interbedded shales are lower in organic matter and show bioturbation, indicating deposition under oxygenated conditions favorable to benthic macrofauna. The black shale and dark grey marl deposits are finely laminated, which points to deposition under anoxic conditions, where benthic macrofauna have died off due to anoxia (Demaison and Moore, 1980; Summerhayes, 1987).

4.4.7 Sedimentation Rate

By the Albian (post-Aptian) the North Atlantic Ocean had a preserved record of black shale deposition. The globally observed levels of elevated organic matter during the Cenomanian-Turonian are seen in North Atlantic deposits (Summerhayes, 1987). The proto-Atlantic was by then approximately 3000 kilometres wide extending east-west with connectivity to the Tethys on the eastern side, and on the west, the Pacific (Barron et al., 1995; Hofman et al., 1999). The mid-ocean ridge further divided the ocean into subbasins at an estimated depth of 2200 metres in the south and becoming shallower to the north (Hofman et al., 1999) with a maximum ocean depth of 5000 metres (Tucholke and Vogt, 1979; Hofman et al., 1999).

On a global scale, the mid-Cretaceous sediments from the Aptian to Turonian were deposited during a marine transgression which reached its peak during the Turonian (Klemme and Ulmishek, 1991). High levels of sedimentation plus high levels of productivity combined to create ideal conditions for excellent source rock (Bohacs et al., 2005). A simple formula is:

$$\text{Organic matter enrichment} = \text{Production} - (\text{Destruction} + \text{Dilution})$$

Equation 4.1: *Organic matter enrichment (Bohacs et al. 2005).*

Enrichment is a function of preservation by burial with optimal sedimentation rates (Bohacs et al., 2005). Therefore, the highest organic matter production rates do

not necessarily result in the highest enrichment. Very high production rates result in dilution of organic matter by a high amount of biogenic material and often exhibit a high amount of siliceous material, which results in cherts and porcellanites (Bohacs et al., 2005). Good preservation conditions along with moderate primary production can result in significant concentrations of organic matter (Bohacs et al., 2005).

The distribution of organic matter may be more a function of sedimentation rate than abundance (Muller and Seuss, 1979; Summerhayes, 1981). Similarities are seen on both east and west sides of the Atlantic. High sedimentation rates occur in the Early Cenomanian, Early to mid-Albian, Early Aptian, and the Hauterivian to Late Valanginian. Lower sedimentation rates are seen in the Late Cenomanian, Late Albian, mid to Late Aptian, Late Hauterivian to Barremian and Berriasian to Early Valanginian. This points to the sedimentation rate being related to tectonostratigraphic events and sea level changes that would produce coordinated results on both sides of the Atlantic. Therefore, it is suggested that high sedimentation rates correlate to the fall in sea level during the Late Aptian and Early Cenomanian, which are followed by low sedimentation rates as sea levels rise (Summerhayes, 1987).

The average sedimentation rate for the Albian-age Naskapi Member was 10-15 m/Ma, which was significantly slower accumulation as compared to 40-60 m/Ma for the Upper Missisauga Formation (Wade and MacLean, 1990; Ogg et al., 2012; Chavez et al., 2018).

Summerhayes (1987) observed that the areas with highest sedimentation rates also had the highest amount of organic matter, and bottom waters were suboxic to anoxic intermittently, which also helped to preserve organic matter.

The S_{TOC} for black shales is proportional to the sedimentation rate (Summerhayes, 1987; Arthur et al, 1984). An explanation for this is that during deposition, the water at the sea floor was anoxic or suboxic, preserving greater amounts of organic matter (Summerhayes, 1987). S_{TOC} increases with an increase in sedimentation rate due to higher preservation of organic matter as it is buried faster, without sufficient time for much biodegradation from benthic megafauna (Muller and

Seuss, 1979; Summerhayes, 1987). S_{TOC} peaks in the Early Albian and Late Cenomanian correspond to sea level transgressions and positive excursions of the $\delta^{13}\text{C}$ stable isotope curve (Summerhayes, 1987).

4.4.7.1 Preservation of Organic Matter

Preservation of organic matter can be further defined. Benthic megafauna requires oxygen supplies to live. Therefore, in areas where well-oxygenated bottom waters have low sedimentation rates, these organisms have time and opportunity to consume and biodegrade the organic matter. The result is a low TOC, as well as evidence of bioturbation in the shale sediments.

Conversely, in zones that are anoxic and with a high sedimentation rate, biotic megafauna is not present in great numbers, as they require oxygen to live, so the organic matter is rich, dark, and of a higher TOC value. In these areas the shale deposition is laminar with little evidence of bioturbation (Summerhayes, 1987).

4.4.7.2 Terrigenous Sediments

The terrigenous sediments and muds sources from river systems with organic content that would contribute to the accumulation of type III kerogen, tend to remain close to shore and not advance seaward. Suspended sediments in the deeper ocean tend to be reworked sediment due to older sediments being disturbed by organisms and/or ocean current movements rather than coming from more recent river-borne sediments (Trabucho-Alexandre, 2015).

On the west side of the Atlantic, the high amount of terrigenous organic material was due to humid climates with high levels of runoff producing a large supply of terrigenous land plant debris available to be deposited (Summerhayes, 1987). The terrigenous organic material would be deposited near shore and distributed to the distal shales by turbidity currents (Robertson and Bliefnick, 1983; Summerhayes, 1987). On the eastern side of the Atlantic, a drier climate produced less terrigenous organic matter, and more amorphous, or marine, organic matter. The rate of accumulation of

amorphous material is similar in the east and west, with the west having more abundant terrigenous organic material supply (Summerhayes, 1987).

4.4.7.3 Productivity

A well developed and very poorly oxygenated minimum zone existed in the North Atlantic during periods in the Cretaceous (Summerhayes, 1987). However, the high amount of TOC was not only a function of anoxia during deposition, but also a function of productivity. High productivity could also result in high TOC and low biodegradation as a result of existing populations of benthic megafauna, which was due to a large supply of organic matter accumulating on the ocean floor. Accompanied by a high sedimentation rate, rapid burial would cause preservation of the material (Summerhayes, 1987).

Summerhayes (1987) also comments on the anoxic conditions being prolonged without any vertical circulation of ocean waters. The North Atlantic did not have any cold oxygenated waters available to sink to degrade the anoxic conditions, and there was little contribution from Pacific waters. Any vertical mixing would be due to water with a higher salinity sinking, and as mentioned previously, such water would be produced in shallow marginal waters. A simple model would have a higher amount of evaporation in turn creating a sink of saline waters and increased oxygenation in deeper water (Summerhayes, 1987). However, if the Cretaceous was a time of high sea level, with fewer shallow evaporating basins, the result would be a lesser amount of saline water supplying oxygenated water to the deep anoxic water bodies.

4.5 Oceanic Anoxic Events

The mid-Cretaceous, from the Barremian to Turonian, includes the time period of study (Aptian) which is one of the six intervals in the Phanerozoic (three of which are in the Cretaceous) that have oceanic anoxic events of note (Trabucho-Alexandre et al., 2010; Klemme and Ulmishek, 1991).

4.5.1 Introduction

Oceanic anoxic events (OAEs) were episodes of widespread marine anoxia where large amounts of organic carbon became buried and preserved within sea floor sediments beneath oxygen-poor bottom waters lacking significant circulation (Turgeon and Creasor, 2008). This section will define oceanic anoxic events, and their characteristics.

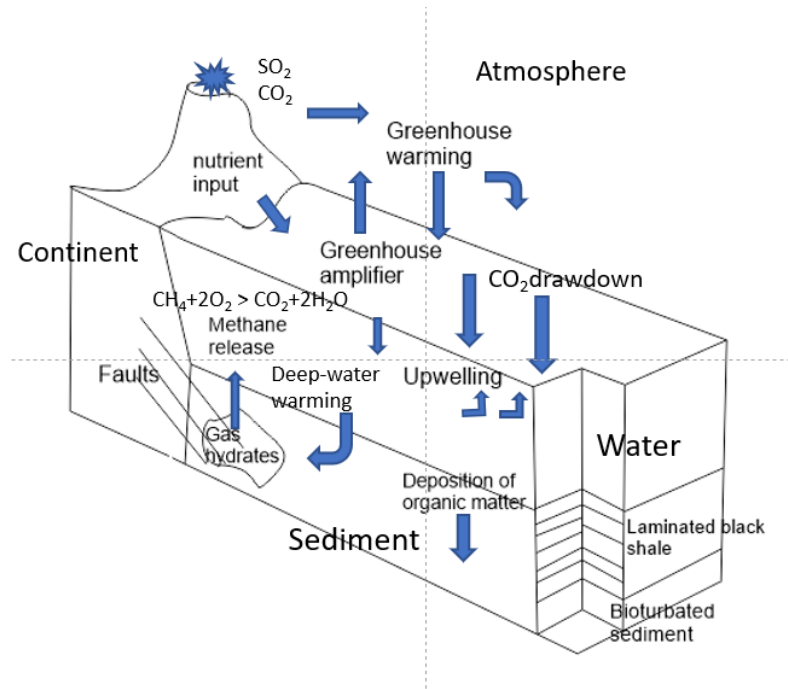


Figure 4.6: Schematic showing the major processes at work during an oceanic anoxic event (OAE). Volcanism emits greenhouse gasses CO₂ and SO₂ which increase warming of the atmosphere and the ocean resulting in deep-water warming. This promotes the release of methane from gas hydrates adding to ocean and atmospheric temperatures. An increase in precipitation on land increases erosion and supply of nutrients into the ocean, promoting growth of plankton in the oceans, and the deposition of organic-rich sediments, initially heavily bioturbated but becoming laminated as anoxia becomes prevalent due to microbes depleting the oxygen (Jenkyns, 2010). Alternating layers of laminated sediments showing deposition and erosion can all be erased by the effects of bioturbation (Hollister and McCave, 1984; Trabucho-Alexandre, 2015).

Oceanic anoxic events are favorable to the deposition of source rocks.

Conditions during oceanic anoxic events include:

- high volcanic activity, adding CO₂ into the atmosphere,
- warm climates which encourage ocean productivity, such as the “greenhouse’ world in the Cretaceous; and

- euxinic or sulfidic waters due to volcanic activity, which supplies nutrients which encourage planktonic productivity, resulting in a high level of organic matter settling to the ocean floor (Sorkhabi, 2016).

The mid-Cretaceous, from the Barremian to the Turonian, was a time of warm climate, with direct evidence in the form of the biogeography of terrestrial plants (Parrish and Spicer, 1988; Fassell and Bralower, 1999) and marine organisms (Mutterlose, 1992; Fassell and Bralower, 1999). Indirect evidence is seen in increased midplate volcanic activity and ridge crests (Schlanger et al., 1981) and atmospheric pCO₂ levels several times our present-day levels (Arthur and Dean, 1986; Fassell and Bralower, 1999). This combined with high eustatic sea levels (Haq et al., 1987; Fassell and Bralower, 1999), led to global warmth without climatic extremes and reduced thermal gradients.

4.5.2 Oceanic Anoxic Event Characteristics

4.5.2.1 Anoxic Conditions

In modern times, anoxic conditions are rare in seas and oceans (Tyson, 1995). However, 10 – 15% of the marine depositional area was covered by anoxic source rock facies during the major OAEs in the late Paleozoic and Mesozoic (Tyson, 1995).

When organic matter breaks down, it combines with oxygen and produces carbon dioxide and oxygen molecules, the opposite of photosynthesis. Oxygen helps produce organic matter but also destroys it. An anoxic environment (where O₂ is < 0.2 mL/L) occurs in lakes with thermal stratification of warm over cold water. It also occurs in near-shore basins which are cut off from the open ocean, where differences in salinity occur. For example, light, fresher water lies above heavy, saline water. Also, in low latitude oceans, below the photic zone (the zone where light penetrates, from 200 – 1500metres depth), colder, deeper water wells up and this means that this area tends to be anoxic (Tyson, 1995).

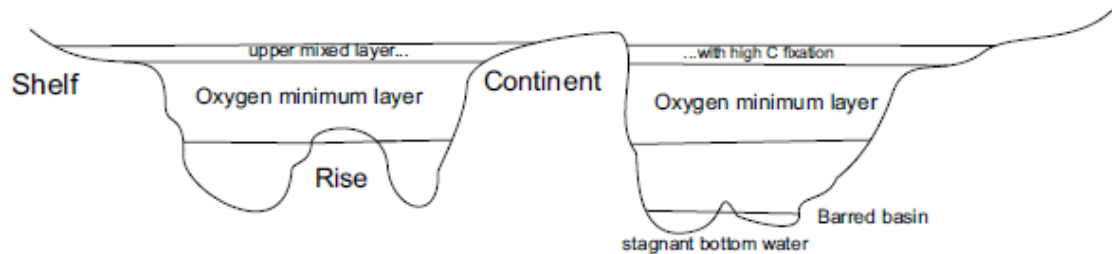


Figure 4.7: Ocean stratification during an oceanic anoxic event. The oxygen-minimum layer is extensive and deep, extending down to the top of high plateaus on ocean shelves and plateaus. Several types of organic-rich deposits accumulate on a) oceanic shelves, b) oceanic rise areas, and c) barred basin accumulations such as are seen in the Atlantic basins, where abundant terrestrial plant matter accumulated due to river runoff and turbidity currents (after Schlanger and Jenkyns, 1976).

4.5.2.2 Biolimiting Nutrients

Characteristics of oceanic anoxic events include discrete organic-rich intervals with carbon isotope excursions, and significant amounts of biolimiting nutrients such as nitrogen, phosphorus, and silica, that are necessary for life in the oceans. If they increase, marine productivity increases. If they decrease, marine productivity decreases, or becomes limited (Trabucho-Alexandre et al., 2010).

Productivity is a function of nutrient supply in the euphotic zone, and the availability of light and zooplankton. Nutrient supply made available through upwelling and mixing of waters (Trabucho-Alexandre et al., 2010) is responsible for approximately three quarters of the current productivity in the present-day oceans (Piper and Calvert, 2009). The nutrients are then subject to downwelling in the water column as particles sink (Trabucho-Alexandre et al., 2010).

4.5.2.3 Positive δ^{13} Excursions

Oceanic Anoxic Events are characterized by dark or black shales rich in organic matter and exhibiting positive δ^{13} excursions, along with a disappearance or dissolution of microfossils.

Carbon isotope excursions are associated with OAEs in the Mesozoic and hyperthermals in the Cenozoic, and their record is recorded in lacustrine and marine shales. An example of a hyperthermal is the Paleocene-Eocene Thermal Maximum

(Trabucho-Alexandre, 2015). Estimations on the durations of these events are inconclusive (Sageman et al., 2006; McArthur et al., 2008; Suan et al., 2008; Dickens, 2011; Zeebe et al., 2014; Trabucho-Alexandre, 2015).

In these organic-rich sequences, carbon excursions are seen within stratigraphic intervals of less than 1 Ma duration (Gale et al., 1993; Schlanger and Jenkyns, 1976; Scholle and Arthur, 1980; Trabucho-Alexandre et al., 2010). Their character can be described as having locally higher marine organic matter of 10-20% TOC and geochemical anomalies (Brumsack, 1980; Leckie et al., 2002; Scholle and Arthur, 1980; Trabucho-Alexandre et al., 2010). They are also confined to interbasinal and interoceanic settings rather than a global extent (Trabucho-Alexandre et al., 2010) because locally the organic matter may not be deposited or preserved. However, the isotopic signal is global and worldwide (Trabucho-Alexandre et al., 2010).

In the South Atlantic and proto-Indian oceans, organic-rich sediments from the mid-Cretaceous are from mid-water depths (500-2500 m) with oxygen minimal conditions (Trabucho-Alexandre et al., 2010; Van Andel et al., 1977; Thurow et al., 1992) and coevally deposited in deeper parts of the basins (Thiede and Van Andel, 1977; Thurow et al., 1992, Trabucho-Alexandre et al., 2010). Black shales will show a lower positive reading of $\delta^{13}\text{C}_{\text{org}}$ that indicates a kerogen quality with a higher amount of marine-derived organic matter (Hofman et al., 1999).

By the Late Albian, the North Atlantic was separated into two subbasins near the mid-Atlantic Ridge. On the southeastern side, anoxic conditions prevailed, however the north-western side was characterized by dis-aerobic mid-water and sub-oxic to oxic deep-water conditions (Hofman et al., 1999).

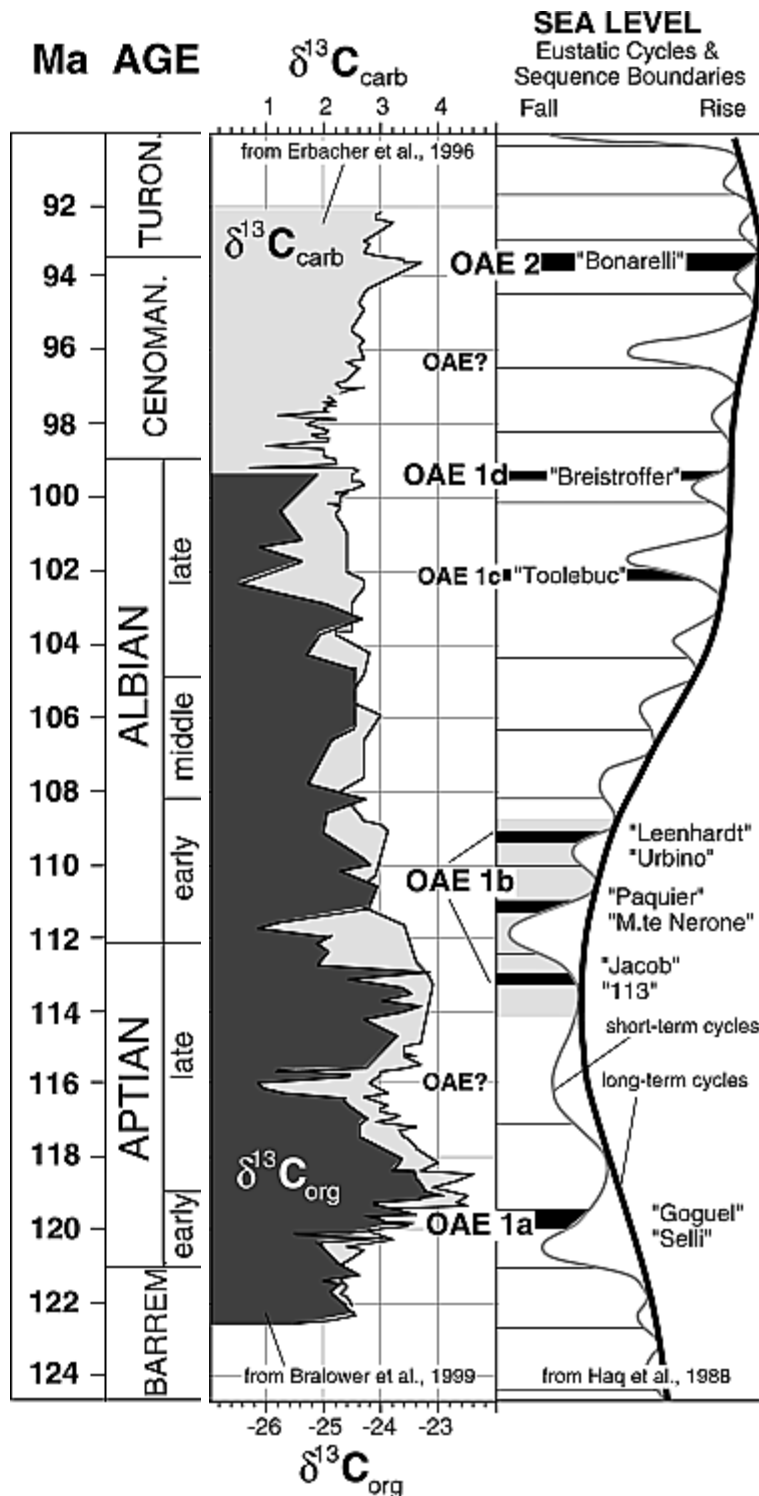


Figure 4.8: Carbon Isotope ($\delta^{13}C_{org}$) and sea level curves from the Barremian through the Aptian, Albian, Cenomanian, and Turonian of the Cretaceous Period. Oceanic anoxic events (OAEs) are associated with positive $\delta^{13}C$ excursions and labelled from 1a-2 (Leckie et al, 2002).

There was a worldwide Late Aptian – Early Albian positive $\delta^{18}O$ value excursion (equivalent to OAE 1b) in marine carbonates seen in planktonic foraminifera as well as

continental concretions in Australia, recording changes in the global carbon budget (Ferguson and Gregory, 1999). The meteoric waters from southeast Australia follow those of the global climate signals from the Aptian to Albian, showing an increase in temperature by 10 degrees C through the Aptian and peaking in the Late Albian (Ferguson and Gregory, 1999).

Tropical temperatures are interpreted to have been cooler than expected under greenhouse conditions, cooling from the Middle to Late Cretaceous, as interpreted from oxygen isotope studies of planktonic foraminifera (Crowley, 1991). The reduced temperature gradient from equator to pole (Poulsen et al., 1999) was due to increased oceanic heat transport towards the poles during this time (Barron et al., 1981; Barron and Washington, 1985; Schneider et al., 1985; Poulsen et al., 1999).

4.5.2.4 Paleogeography

Oceanic anoxic events (OAEs) occur when a certain paleogeography is combined with changes in either ocean circulation and/or available nutrient supply (Trabucho-Alexandre et al., 2010). It is debated whether organic-rich sediments are mostly due to enhanced productivity or to anoxia (Demaison and Moore, 1980; Pedersen and Calvert, 1990; Trabucho-Alexandre et al., 2010). Some enhanced level productivity is needed to create the organic-rich sediments in the first place; however, the ultimate level of total organic carbon (TOC) is dependent on the rate of sedimentation (Trabucho-Alexandre et al., 2010; Tyson, 2001).

4.5.2.5 Pyrite and Other Minerals

Pyrite formation in sediments depends on the oxygen level in the atmosphere and the sulfate concentration found in seawater. The factors involved are the amount of organic matter and its supply rate, the amount of sulfate dissolved, and the amount of detrital iron minerals available. In normal marine sediments, where sufficient dissolved sulfate and iron minerals are available, the supply of organic matter is the main control on the formation of pyrite. However, in freshwater sediments where there is insufficient

sulfate, pyrite formation is low (Berner, 1983). As a sidenote, in this way, one can determine if a shale is a marine shale or an organic-rich freshwater shale.

In marine shales, where the marine conditions are euxinic (where a combination of anoxic and sulfidic conditions exist), enough H₂S is produced to make the main control the amount of reactive iron minerals available (Berner, 1983).

Other minerals, which can be associated with organic-rich black shales are glauconite, pyrite, chamosite and phosphate (carbonate fluorapatite) (Jenkyns, 1980). Ca-Mn-Fe-Mg carbonates in Cenomanian and lower Toarcian in the Alpine-Mediterranean area are important, because today we find those minerals in the salinity-stratified stagnant centre of the Baltic Sea in black phosphatic and organic-rich muds (Jenkyns, 1980). Some dolomite and siderite occurrences could contain manganese. Barite, adjacent to organic-rich deposits, can also be of significance and is seen in Cretaceous deposits of Israel and Western Australia.

Some geochemical indicators of paleoproductivity are the presence of Barium, Cadmium and Phosphorus (Schmitz, 1987; Dymond et al., 1992; Villamil et al., 1999).

Anoxic water conditions can leave indicators in the sediment record and have done so in Deep Sea Drilling Project (DSDP) cores of Albian age; for example Site 369A Core 41 (Hofman et al., 1999). Anoxia favours the reduction of Mn oxides to Mn²⁺ which results in a reduced flux of Mn-oxides into the sediments (Calvert and Pedersen, 1996; Hofman et al., 1999). Depletion of manganese and siderophile element enrichment is indicative of anoxic bottom waters (Hofman et al., 1999). Another indicator is the size of framboidal pyrites, which will range from 2.9-3.5 µm when formed in an anoxic water mass (Hofman et al., 1999). Sulfur/carbonate ratios can indicate anoxic bottom water conditions as well as sulfur content which is independent of organic carbon content. The availability of reactive iron controls the fixation of sulfur instead of labile organic matter (Raiswell and Berner, 1985; Leventhal, 1983; Dean and Arthur, 1989; Hofman et al., 1999). Anoxia in the photic zone can also be indicated where black shale and brown-green marlstone deposits have aryl isoprenoids derived from photosynthetic green-

sulfur-bacteria (*Chlorobiaceae*), which need concurrent light and anoxia to exist (Hofman et al., 1997; Hofman et al., 1999).

Cycles of organic-rich black shale layers alternating with carbonate-rich layers show where the organic-rich layers exhibit low CaCO₃ (less than 20 weight %), low Si/Al ratio (less than 3.6), low Ti/Al ratio (less than .05), low Mg/Al ratio (less than .4), and higher TOC (greater than 5 weight %), Hydrogen Index (HI greater than 350), and low Mn/Al ratios (less than 30 x 10⁴) e.g., DSDP Site 369A Core 41 (Hofman et al., 1999).

4.5.2.6 Marine Transgressions

Marine organic-rich sediments often occur together with transgressive sea levels (Arthur and Sageman, 2005; Parrish and Curtis, 1982). In the Paleozoic, the Lower Ordovician, Mid Silurian, and Upper Devonian deposits of the pelagic black shale facies correlate with high sea levels from interglacial periods (Jenkyns, 1980). In the Mesozoic, the Early Toarcian saw deposition over northern Europe of bituminous black shales and is regarded as a product of the Jurassic OAE (Jenkyns, 1980).

A rising sea level facilitates movement of terrigenous organic matter oceanward, and the increase in shelf area from this transgression stimulates the production of marine plankton, and as the marine biota consumes and processes this increased amount of organic matter, oxygen is used up in the marine muds. A condition of anoxia then prevails (Jenkyns, 1980). Characteristic facies during this time include glauconitic sandstones and phosphatic chalks (Jenkyns, 1980).

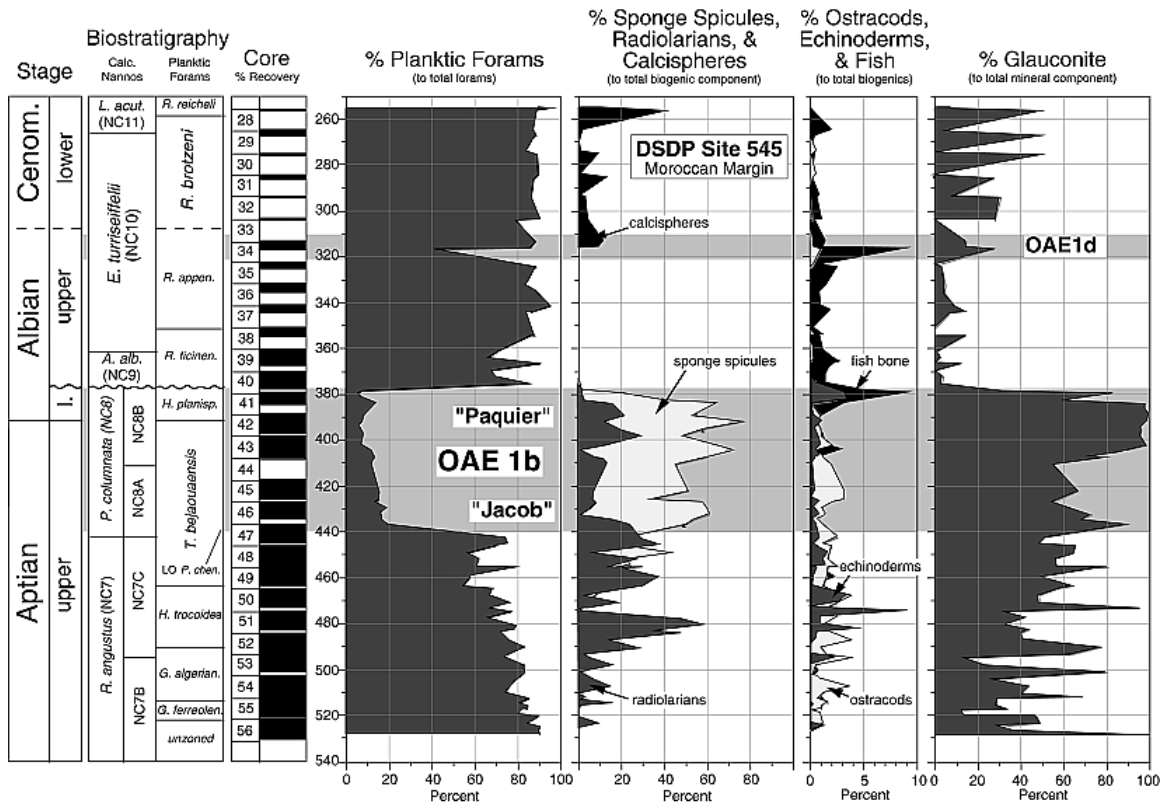


Figure 4.9: Fossil and mineral constituent alteration patterns during the Upper Aptian-Lower Albian OAE 1b event. In the Upper Albian, there is a sharp decrease in the percentage of planktic forams, and an increase in the percentage of sponge spicules with a decrease in the number of radiolarians. Also noticeable is the increase in glauconite (Leckie et al, 2002).

4.5.2.7 Thermohaline Circulation

Changes in thermo-haline circulation indicate that more nutrients are available in the upper ocean due to upwelling and runoff, which lead to more ocean productivity (Arthur and Schlanger, 1979). The warm, wet climate during the Cretaceous, with abundant CO₂ introduced into the atmosphere from volcanic activity, a high sea level due to the lack of polar ice, and abundant plant life, together facilitated a high degree of weathering. This allowed abundant nutrients, particularly nitrates and phosphates, to enter the oceans. Phytoplankton became very abundant in the upper ocean, which resulted in a thick layer of black organic-rich shale deposited in the deep ocean. This became an abundant source of nutrients for the microbes living in the seafloor muds, and their intense activity resulted in reduced oxygen on the seafloor (Leckie et al., 2002). This resulted in the deepening of the oxygen minimum zone down to abyssal depth (Arthur and Schlanger, 1979). Increased preservation also occurred as the

increase in surface water temperatures and runoff lead to decreased bottom water formation and elevated carbon burial.

The organic matter deposited in these anoxic events is either carbon of marine planktonic origin, or, plants of terrestrial origin, which was formed as the transgressive shallow seas covered the forested coastal plains.

4.5.2.7.1 Neodymium Isotopes

Neodymium isotopes can be identified and quantified, indicating the source and path of water masses. In the mid-Cretaceous at the Demerara Rise, a change is seen where low background values of neodymium isotopes change to values seen in the Pacific (MacLeod et al., 2008), and the Atlantic DSDP Site 1050 shows a value change from a Pacific signature in OAE2 change to an Atlantic/Tethyan value in the Late Cretaceous (MacLeod et al., 2008). This points to a source and circulation change for intermediate water during the mid-Cretaceous (Trabucho-Alexandre et al., 2010).

4.5.2.8 Igneous and Volcanic Rocks

4.5.2.8.1 Basalts

Hydrothermal alteration of basalts on Pacific oceanic plateaus would release Fe and trace metals (such as Cd, Cu, Ni, and Zn) that affect productivity by trace metal limitation of nitrogen fixation. They also show micronutrients where they are used by phytoplankton in the euphotic zone (the top 80 metres). This transport would have been made easier by a lower seawater pH (Liu and Millero, 2002) which was due to both atmospheric and seawater increases in CO₂ which was due to submarine volcanism.

In the North Atlantic, there is a decrease in the amount of trace metals moving eastward, and it is at its lowest close to Europe (Orth et al., 1993). There is also a trend from west to east for the onset of organic matter deposition in relation to the carbon isotope excursion.

4.5.2.8.2 Submarine Volcanoes

Mantle-lithosphere interaction affects sea floor topography and sea level variations in time frames greater than 5 million years (Cloetingh and Haq, 2015). Both mantle upwelling and downwelling, and the occurrence of continental crust over-riding a subduction zone, can affect long-term sea level variations (Cloetingh and Haq, 2015).

Evidence of a pulse of activity by submarine volcanoes in the Pacific was noted in the mid-Cretaceous (Larson, 1991a; Schlanger et al., 1981) and was called a super-plume episode. This episode may be correlated with the extremely long normal magnetic polarity noted in sediments (Larson, 1991b), and perhaps caused very high sea levels in combination with increasing CO₂ levels which created high paleotemperatures.

4.5.2.8.3 Large Igneous Provinces

Events known as large igneous provinces (LIPs) occur when large volumes of magma erupt over a large area in a relatively short time interval of 10⁴ to 10⁶ years. They are a result of thermal activity in the mantle allowing for the transfer of magma in regions with a thin, attenuated and/or rifted crust (Jones et al., 2016), however they are not necessarily correlated with regional plate tectonics (Coffin and Eldholm, 1994). Submarine LIPs manifest as basinal flood basalts, seamounts, oceanic plateaus, and submerged ocean ridges (Neal et al., 1997; Greene et al., 2008, Jones et al., 2016) which can affect basin volume and sea level. Plume emplacement enables the creation of 'superswells' where sea level increases and then is followed by subsidence (Cloetingh and Haq, 2015).

The emplacement of large igneous provinces (LIPs) occurred in the Early Cretaceous, producing the Shatsky Rise (137-131 Ma), the Ontong-Java and Manihiki Plateaus, (122-90 Ma) in the Pacific (Ito and Clift, 1998), and the Deccan Traps area of the Indian Ocean in the Late Cretaceous (Courtilot et al., 1986). This affected the volume of the world's oceans (Cloetingh and Haq, 2015). Elevated bathymetry at the ocean ridges due to the high spreading rate, along with emplacement of these large

igneous provinces, at least partly explains the high sea levels. However, high delivery of sediment into the ocean can increase subsidence in the basins (Conrad, 2013).

There is evidence for, and association of, oceanic anoxic events with marine basalt LIP emplacement (Sinton and Duncan, 1997; Kerr, 1998; Jones et al., 2016). Large igneous province emplacements could contribute to oceanic anoxic events, in that they increase the amount of nutrients available together with an increasing level of CO₂, causing an increase in primary productivity in the oceans. The result could be anoxia (Bralower et al., 1997; Erba, 1994; Kerr, 1998; Tarduno et al., 1991; Trabucho-Alexandre et al., 2010), however this is not proven (Trabucho-Alexandre et al., 2010). The main problem with the hypothesis is that most of the large igneous provinces are in the Pacific, proto-Indian Ocean and South Atlantic, but most of the organic-rich sediments are in the North Atlantic Ocean and the Tethys ocean remnants (Trabucho-Alexandre et al., 2010).

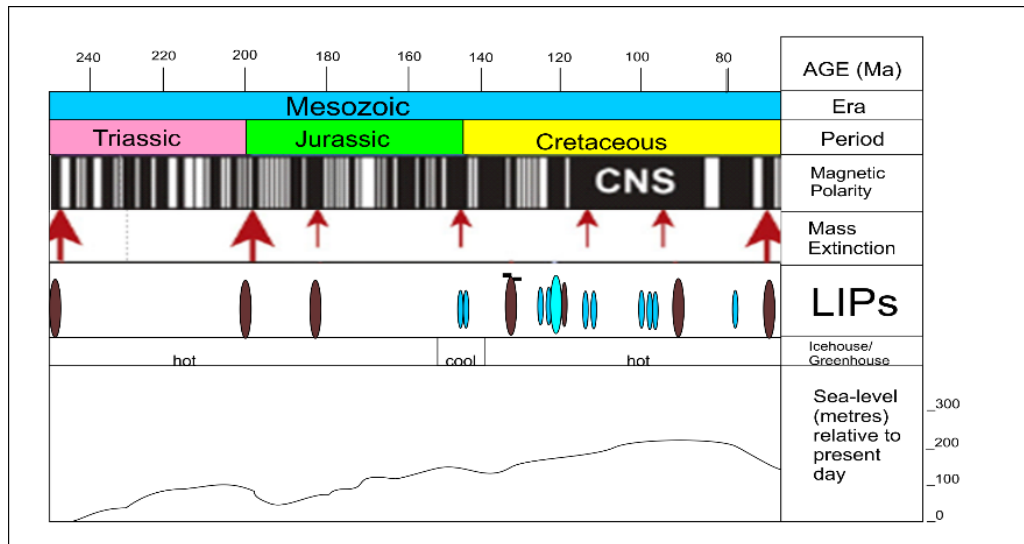


Figure 4.10: This chart shows the Mesozoic with red arrows indicating the main extinction events, grey-blue shadings indicating the emplacement of large igneous provinces (LIPs) on oceanic plateaus, and dark red shadings for continental flood basalts. Magnetic polarity is also shown with the Cretaceous Normal Superchron (CNS) highlighted as a long stable time of normal polarity. There were a significant number of submarine LIPs during the Cretaceous, more than any time in the earth's recorded history (Jones et al., 2016).

4.5.2.9 Strength of Lithosphere

Generally, continental cratons reflect a strong lithosphere; mountain belts and oceanic spreading centers point to a weak lithosphere (Cloetingh and Haq, 2015). The

strength of the lithosphere determines its loading capacity with respect to ice and/or sediment loading. Weaker areas are more susceptible to upwelling of the mantle, intra-plate deformation and vertical motion on old fault lines or zones of weakness (Cloetingh and Haq, 2015). Stresses weaken plates and make them prone to plume emplacements, which would cause an initial uplift, which if on the ocean floor, a swelling would occur, followed by subsidence as the plume weakened (Cloetingh and Haq, 2015). There is a link between a strong lithosphere and higher continental topography and a weaker lithosphere and lower topography, leading to areas that are prone to ocean flooding (Burov, 2010; Francois et al., 2013).

The Cretaceous lithosphere in general was weaker and therefore prone to oceanic flooding because there was high oceanic crustal production as well as continental breakup occurring as the proto-Atlantic widened. In addition, ocean water volumes were higher due to the high mantle expulsion rates of water by degassing from the volcanic activity associated with seafloor spreading (Cloetingh and Haq, 2015). The paleo-rheology, or flow history, during the Cretaceous varies, but the lithosphere became more rigid, and therefore stronger, near the end of the Cretaceous.

Cloetingh and Haq (2015) point out that volcanic rift margins are prone to plume emplacement, and these emplacements can lead to vertical motion through inherited vertical structures. In the Early Cretaceous, the lithosphere was thermally rejuvenated, followed by a period when it aged and cooled. Cloetingh and Haq propose that over the long term, this increased plate rigidity, which allowed the plates to tolerate loading, and flexural widening in the post-rift phase, resulted in plate reorganization affecting lithospheric stress fields, and intraplate deformation caused vertical motion over large areas. At the same time as the northern Atlantic was rifting, the African plate was also showing differential motions in the rift basins (Cloetingh and Haq, 2015).

4.6 Cretaceous Oceanic Anoxic Events

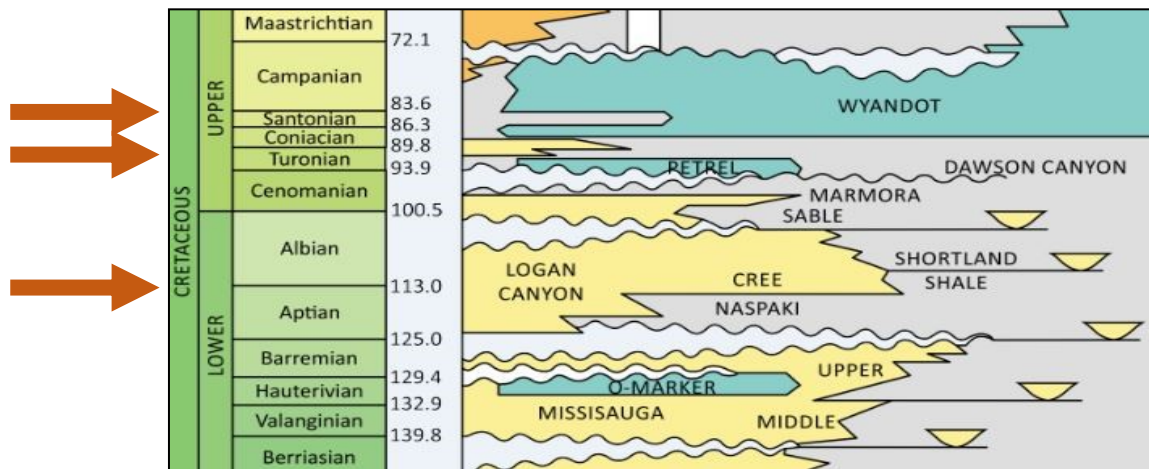


Figure 4.11: Stratigraphy of the Scotian Basin during the Cretaceous Period, 65.5-145.5 Ma, from Figure 2.3. Arrows show the notable Cretaceous Oceanic Anoxic Events, deposits of which have been found worldwide from the Late Barremian to Albian, the Cenomanian to Turonian, and the Coniacian to Santonian.

During the Barremian-Albian and Cenomanian-Turonian, and to a lesser degree the Coniacian-Santonian stages of the Cretaceous, organic-rich sediments were deposited on a global scale (Schlanger and Jenkyns, 1976; Jenkyns, 1980). The widespread extent of these deposits indicates a global Oceanic Anoxic Event (OAE) resulting from two major factors; a Late Cretaceous transgression that increased the volume and number of shallow seas which resulted in increased organic carbon, and a climate which reduced the amount of cold oxygenated bottom water in the world's oceans (Schlanger and Jenkyns, 1976).

Table 4.1: *Oceanic anoxic events of the Cretaceous (Cronin, 2010; Paleoclimates; Columbia University Press; Schlanger and Jenkyns, 1976; Jenkyns, 1980; Arthur et al., 1987; Bralower et al., 1994; Leckie et al., 2002; Takashima et al., 2006; OAE2; Meyers and Sagerman, 2007; ETH Swiss Federal Institute of Technology Zurich).*

CRETACEOUS OCEANIC ANOXIC EVENTS

OAE	Stage	Age	Name
OAE3	Coniacian - Santonian	86	
OAE2	Cenomanian - Turonian Boundary	93	Bonarelli
OAE 1d	Late Albian	99	Breistoffer
OAE 1c	Late Albian	102	Toolebuc
OAE1b	Late Aptian - Early Albian	109 - 113	Leenhardt - Urbino Paquier Monte Nerone Jacob - 113
OAE 1a	Early Aptian	120	Goguel, Selli
Weissert	Valanginian - Hauterivian	132	Weissert

Oxygen-rich bottom waters were restricted from areas of sediment deposition by the new ocean ridges and bathymetric sills during the initial rifting phase of the Atlantic (Kaneps, 1976). Changes in salt-water circulation meant that more nutrients became available due to upwelling and runoff leading to more ocean productivity, which in turn resulted in deepening of the oxygen minimum zone down to abyssal depth. Concurrently, increased preservation occurred as the increase in surface water temperatures and runoff led to decreased bottom water formation and elevated carbon burial.

Cretaceous organic-rich deposits exhibit cyclicity. They show evidence of alternating organic-rich and organic-poor levels, particularly of Late Barremian through Aptian and Albian age on land in the Apennines and Southern and Maritime Alps, and in the Atlantic Ocean sediments of Aptian to Turonian age (Jenkyns, 1980). This cyclicity could be a result of times of anoxia due to salinity stratification (Jenkyns, 1980), which has been viewed as a cause of anoxia, where dense, high-saline brines from evaporitic lagoons or restricted ocean basins are injected into an area where subsequent organic-rich anoxic deposits of mud and shale are found (Jenkyns, 1980). Aptian brines from the new shallow South Atlantic shelf were thought to move into the Central Atlantic and

contribute to anoxic deposits on the abyssal plain (Jenkyns, 1980). In this way, seafloor spreading events contribute to OAE formation (Jenkyns, 1980). Although the spilling of saline waters can result in cyclic deposits in anaerobic basins, this is not a cause of OAEs (Jenkyns, 1980).

Thin bituminous deposits less than a few meters are generally of a discontinuous nature (Jenkyns, 1980). It is thought that organic deposits are favoured mostly in basin hollows. The rate of accumulation of organic carbon is related to the bulk sedimentary rate, so that ash falls, or turbidity currents may result in a discontinuous deposit of organic material (Jenkyns, 1980). Bituminous deposits tend to be higher in deposits of chert- or carbonate-replaced radiolarians that could be due to high productivity of radiolarians, or a preference for preserving siliceous over carbonate microfossils (Jenkyns, 1980).

Oxygen deficiency happens when demand exceeds supply which is determined by hydrographic and/or oceanographic processes. Lignin-rich woody organic matter does not consume a high level of oxygen however decomposing organic matter has the highest demand for oxygen (Cruz and Gabriel, 1974; Tyson, 1995).

Oceanic thermohaline circulation provides oxygen to the deep ocean. Demand for oxygen by marine organic matter and biota increases as oxygen becomes less abundant. There is a higher chance for oxygen depletion on the ocean shelf rather than in the deep ocean due to the higher productivity found there. Deep-water anoxia can occur if the supply of well oxygenated bottom water is reduced, as the level of primary productivity in deep water is naturally quite low. Surface water can be dense due to evaporation or cooling or through having travelled a long way beneath highly productive water (Tyson, 1995).

4.7 Proto-Atlantic Aptian Organic-Rich Deposits

The formations of organic-rich deposits in the Aptian proto-Atlantic consist broadly of a series of limestones to clastics cycles. The sequence in time as well as over space show influences of both world-wide events, linking climate with geochemical

environments and the progression of the tectonic conditions as the area transitioned from rift margin to passive margin (Trabucho-Alexandre et al., 2010).

Enhanced productivity due to the nutrients available from volcanic activity contributed to deposition of significant amounts of organic carbon as did increased preservation in many ocean basins worldwide including the North Atlantic, Western Tethys, South Atlantic, and proto-Indian Ocean, and are seen as dark, organic-rich, carbonate-free 'black shales' (Bralower et al., 1994; Schlanger et al., 1987; Trabucho-Alexandre et al., 2010).

In the present day, oceans are well-oxygenated (Tyson, 1995) however Klemme and Ulmishek (1991) consider 10-15% of oceans in the Late Paleozoic and Mesozoic to have exhibited anoxic conditions, due to the presence of large tracts of upper shelf and slope areas. Tyson (1995) estimates, after accounting for shallow shelf facies to be less likely to be preserved than basinal facies, that there was a 2-4-fold increase of anoxic deposits as compared to what is seen today.

Anoxic black shale facies were deposited during the Late Devonian to Mid Cretaceous (from 377.4-88.5 Ma), with a peak from the Late Cenomanian to Early Turonian around 90.4 Ma (Tyson, 1995). It is thought that at that time sea level was 255 meters higher than today at a maximum and that an organic-rich facies was deposited over half of the shelf area (Haq et al., 1987; Arthur et al., 1987; Tyson, 1995). Schlanger and Jenkyns (1976) and Arthur et al. (1987) propose that the shelf area then was twice as large as today, and if the 50% coverage by anoxic waters is correct this would result in an extreme maximum of thirty-two times the area of deposition and twenty-five times the shelf area compared to conditions today (Tyson, 1995). Other significant areas of anoxic oceanic deposits are the La Luna Formation in Venezuela and Columbia, and the Garau-Kaxhdumi Formation in Iraq and Iran, both dating from the Mid Cretaceous (Tyson, 1995).

The composition and maturity of organic matter within the Cretaceous black shale sequences have been studied in several DSDP sites in the Atlantic Ocean, and worldwide, which were cored between 1968 and 1983. Black, dark green, or dark grey

sediments with greater than 1% TOC were reported as widespread in Cretaceous sediments. These are also considered to be potential source rocks providing that they were buried sufficiently to become mature (Summerhayes, 1987).



Figure 4.12: Configuration of the continental areas during the Cretaceous (Cenomanian-Albian) time at approximately 100 Ma +/- 10 Ma. The black regions have organic carbon-rich marine sediments of Aptian – Albian or Cenomanian age. The circles are wells from the Deep-Sea Drilling Project (DSDP) which contain Early to mid-Cretaceous sediments. The circles filled in black represent dark, organic-rich marine sediments, whereas the open circles have none (modified from Arthur and Schlanger, 1979; Fischer and Arthur, 1977). Figure after Smith et al., 1973.

Of interest is that 63% of the world’s giant oilfields are within Mesozoic reef reservoirs, which are stratigraphically linked to basinal black shale source rocks (Arthur and Schlanger, 1979).

Geochemical studies have shown there is a distinct difference between the southern and northern North Atlantic. In the south abundant marine organics are preserved with up to 45% TOC (average = 10%), whereas in the north, it is mostly terrestrially sourced organic matter deposited by turbidites interbedded with dark pelagic mudstone containing marine organic matter with TOC’s of 26% (average = 5-6 %) (Summerhayes, 1981; Tissot et al., 1980; Forster et al., 2007; Kuypers et al., 2004; Trabucho-Alexandre et al., 2010).

4.7.1 Metals in Organic Matter

As discussed previously, evidence suggests that during the Aptian to Santonian, organic matter accumulation in marine sediments was significant globally (Arthur et al., 1987; Davis et al., 1999). Concentrations of metals within source rocks and hence in oils can make oil refining difficult. Importantly, metal ratios found in oils can be used to correlate oil to source rock relationships (Davis et al., 1999). Furthermore, specific depositional environments can be indicated by the presence of certain trace metals and ratios (Davis et al., 1999).

High concentrations of Ni, V, and Zn in black shales can point to regional oceanographic conditions causing these trace metal enrichments (Davis et al., 1999). Organic-rich marine muds often contain a suite of trace metals which include Cu, Mo, Ni, V and Zn (Desborough and Poole, 1983; Brumsack, 1980; Dean et al., 1984; Davis et al., 1999).

Organic matter enrichment and trace metals interact via biogeochemical pathways such as bioaccumulation, where organisms incorporate nutrients or essential metals; adsorption of metals on organic particles as they settle; complexation of metals by organic ligands; and metal sulfide precipitation in organic-rich sediments which are experiencing bacterial sulfate reduction (Davis et al., 1999). Chemical weathering and erosion of continental rock, oceanic crust leaching at hydrothermal sites, and devitrification of volcanic ash allow metal ions to enter ocean water (Davis et al., 1999).

4.7.2 Oxygen Isotope Data

Paleotemperatures can be estimated from oxygen isotope measurements, and it is thought that Cretaceous global ice coverage was minimal such that the $\delta^{18}\text{O}_w$ value would be -1%. The oxygen isotope level in seawater is affected by the balances of evaporation and precipitation, which affects the salinity, and by the transport of vapor. The paleo-salinity is the most uncertain factor. A large part of the Cretaceous ocean was located in the subtropics, and therefore the salinity gradients would be higher between the low and high latitudes. Small differences in paleo-salinity can indicate large

temperature differences, with a 1‰ of $\delta^{18}\text{O}_c$ difference equates to 4° degrees C difference. Based on $\delta^{18}\text{O}_w$ – salinity relationships for subtropical ocean basins, the relationships between temperature, salinity and $\delta^{18}\text{O}_c$ for mid Cretaceous evaporitic ocean basins have been calculated assuming that Hadley cells which control the evaporation – precipitation balance were in the same position as in modern oceans today (Fassell and Bralower, 1999).

4.7.3 Note on Fossil Assemblages and Thermal Gradients in Black Shale

Sediment samples containing a high diversity of fossil assemblages are thought to represent a stable, oligotrophic oceanic environment and not one of high fertility or with high nutrient levels (Fisher and Hay., 1999).

Sediments with a high level of organic carbon can be associated with areas of high fertility, although the preservation of high amounts of organic carbon is not solely dependent on high productivity (Fisher and Hay., 1999). High fertility is usually attributed to upwelling (Fisher and Hay., 1999).

Low thermal gradients promote slow deep-water circulation and the deposition of organic-rich sediments in anoxic, oxygen-poor deep-water (e.g. Arthur and Schlanger, 1979). DSDP project site 305, as studied by Douglas and Savin (1975), points to the Aptian and Albian having the highest sea surface temperatures (SSTs) in the last 120 My (Barron, 1983; Huber et al., 1995) with temperatures estimated between 26° and 32° C in the tropical ocean (0°-30°N).

Stable isotope data for the Albian shows 16° C for high latitude (approximately 60°S) in the Albian sediments at DSDP Site 511 (Huber et al., 1995; Fassell and Bralower, 1999).

The Aptian through the Albian period had sea temperatures of 26-32 degrees C as determined from analyses of DSDP sites 305 cores (Douglas and Savin, 1975), and are believed to have been the warmest sea temperatures in the past 120 My. (Barron, 1983; Huber et al., 1995; Fassell and Bralower, 1999).

Low thermal gradients resulted in slow deep-water circulation which encouraged the deposition of organic-rich deposits in anoxic deep ocean settings (Fassell and Bralower, 1999).

Where diagenetic alteration has occurred, the $\delta^{18}\text{O}$ and $\delta^{13}\text{C}$ values are likely to be more negative (Fassell and Bralower, 1999).

Aptian samples from DSDP sites 417 and 418 contain secondary calcite in the foram specimens examined (Fassell and Bralower, 1999).

In terms of coccolithophores found in surface sediments, low diversity, high dominance floras in an inner shelf setting, and moderate to high diversity and lower dominance floras in a middle and outer shelf setting occur today in the South China Sea. It is concluded that the low diversity of the inner shelf is due to the high salinity levels of approximately 30 ppt. Some modern species of coccolithophores have high salinity tolerances (Fassell and Bralower, 1999) but most thrive well at normal salinity levels.

Rhythmic bedding cycles are interpreted to reflect Milankovitch cycles. They are coupled cycles expressing changing redox conditions and marine organic matter productivity, carbonate and biogenic silica productivity cycles, as well as carbonate compensation cycles. These can be diluted near shore by clastic dilution and changes in sediment supply (Hofman et al., 1999).

Albian-Aptian strata in the DSDP sites noted above are thought to represent an undisturbed sediment deposition record with little disturbance by events such as turbidity currents which occur nearer to shore (Hofman et al., 1999).

More arid periods favour carbonate cycle production and more humid periods indicate increased ocean fertility from upwelling or from nutrients supplied from continental runoff, high organic matter production and an extension of the oxygen minimum zones and the deposition of organic-rich shales. (Hofman et al., 1999).

4.7.4 Tethyan Organic-Rich Deposits

From the Aptian through the Maastrichtian, the European and Adriatic tectonic plates are interpreted to have moved north by 5-7 degrees latitude (Voigt et al., 1999),

as the northern reef line moves southward relatively from the Aptian Helvetic shelf to southern Spain by the Maastrichtian. At the end of the early Aptian, a thick shallow water carbonate platform was well established with coral-stromatoporoid and rudist bioconstructions along the north edge of the Tethyan Sea (Voigt et al., 1999). This continued until the Early Aptian, after which there was a facies change from carbonate platform to phosphate-rich, terrigenous, nutrient-dense deposits due to a high rate of continental weathering to greenhouse conditions (Föllmi, 1989; Föllmi et al., 1994; Voigt et al., 1999). Reduced sedimentation from the late Early Aptian to the Cenomanian was followed by pelagic sediments from the Turonian onward (Voigt et al., 1999). A lagoonal circulation pattern combined with a warm climate at lower latitudes (tropic and subtropic) promotes carbonate platform development and is characterized by warm temperatures and low nutrient supply (Voigt et al., 1999). If precipitation and runoff exceed evaporation, fresh-water influx dominates, and an estuarine circulation occurs in shallow water areas close to shore. The salinity decreases and the surface water density becomes lighter such that the circulation pattern changes to estuarine. At midlatitudes, an increased humidity favours continental weathering and therefore increases terrigenous sedimentation and corresponding nutrient supply to the ocean. The influx eutrophic nutrient levels in the water and reduces carbonate production and drowns carbonate platforms as the facies changes to a siliciclastic one. Increased sediment supply reduces the amount of sunlight reaching the reef platforms due to increased turbidity, and this has a detrimental effect on the health of the reefal organisms (Voigt, 1999).

Nutrients entering the southern North Atlantic ocean were trapped in that region and then transported eastward towards the Tethys. Upwelling occurred before reaching there, so the Tethys region has fewer organic-rich deposits than are found in the NW Europe epicontinental sea.

Cenomanian (post-Albian) sediments have organic-lean pelagic marls and chalks, which are associated with increased carbonate production (coccolithophores) which

point to oligotrophic, or low nutrient/ high oxygen surface waters (Trabucho-Alexandre et al., 2010).

4.7.5 Carbonate Cycles

During the mid-Cretaceous, orbital variations were thought to often drive deep sea anoxia (Herbert et al., 1999; Schwarzacher and Fisher, 1982). Carbonate-marl cycles reflect fluctuating paleoenvironments of carbonate variations and varying dilution by terrigenous material (Herbert et al., 1999). The flux of carbonate and terrigenous supply was driven by the amplitude of precessional (axial wobble) forcing (Herbert et al., 1999). Carbonate variation is thought to represent climate change due to the earth's precessional cycles which have a mean repeat cycle of 22 thousand years (ky) and a median repeat cycle of 24 ky. Studies done in the Late Cretaceous of the South Atlantic show sedimentation rates varied in proportion to the amplitude of carbonate variation, resulting in periods of higher climatic variance that were also periods of higher average deposition rate (Herbert et al., 1999).

A study of Late Cretaceous South Atlantic drill holes done by Herbert et al. (1999) indicates carbonate content variations at 20 ky cycles. Furthermore, they suggest that precessional cycles of 100, 400 and 2400 ky can be correlated between drill holes. They based their study on the energy of the amplitude signal rather than the average percentage of carbonate material present. The variation pattern can be linked between drill hole sites by the precessional driver. Surface temperature and ocean salinity levels can affect the production of calcareous plankton and also create humid conditions in continental source areas (Herbert et al., 1999).

Seawater is corrosive and acts as a control on deep sea sediment removal due to the chemical properties of seawater, which vary due to depth (Trabucho-Alexandre, 2015). Distinct changes in the flow rate of bottom waters and chemistry are associated with gaps in the marine sediment record (Trabucho-Alexandre, 2015). Productivity of surface waters controls the organic-rich content in sediment supply and areas underneath zones of low productivity will not have deposition, especially where the

ocean floor is deeper than the calcite compensation depth (CCD) (Trabucho-Alexandre, 2015). The calcite compensation depth is that below which the supply rate of calcite is less than the rate that it is dissolved, so that calcite is not preserved.

4.8 Proto-Atlantic Regions of Interest

Several regions of the proto-Atlantic are notable in having organic-rich deposits of Cretaceous age. Some have proven oil and gas reserves. The following is mention of some of the more important regions, such as Trinidad, Morocco, Georges Bank offshore Massachusetts, the Demerara Rise, offshore Angola and other regions in the South Atlantic Ocean with black shale deposits.

4.8.1 Trinidad

The Gauthier and Naparima Hill Formations are proven source rocks deposited in the Upper Cretaceous between 99.6 and approximately 64 Ma (Rodrigues, 1993; Persad et al., 1993). They are composed of blue-grey siliceous mudstones (argillites) which are organic-rich, interbedded with shale and shaly limestone (Kugler, 1959) and they are from the deep-water open marine outer shelf and slope environments. The kerogen is type II with vitrinite reflectance values comprising 0.56-2% (Summa et al., 2003). Thomas (2014) classifies the Gautier Formation as oil and gas prone with TOC ranging from 0.5-7% and the Naparima Hill Formation as oil prone with TOC from 0.2-8%.

Gibson et al. (2004) attribute this source rock deposit to high nutrient levels and excessive fluvial runoff which enhanced the preservation of organic matter due to deep marine slopes overloading and slumping forming turbidite deposits, and to rising sea levels creating muddy sediments which work to rapidly trap plankton. During the Lower Cretaceous, the Cuche Formation was deposited from 145.5-99.6 Ma and is classified as a potential source rock (Rodrigues, 1993; Persad et al, 1993).

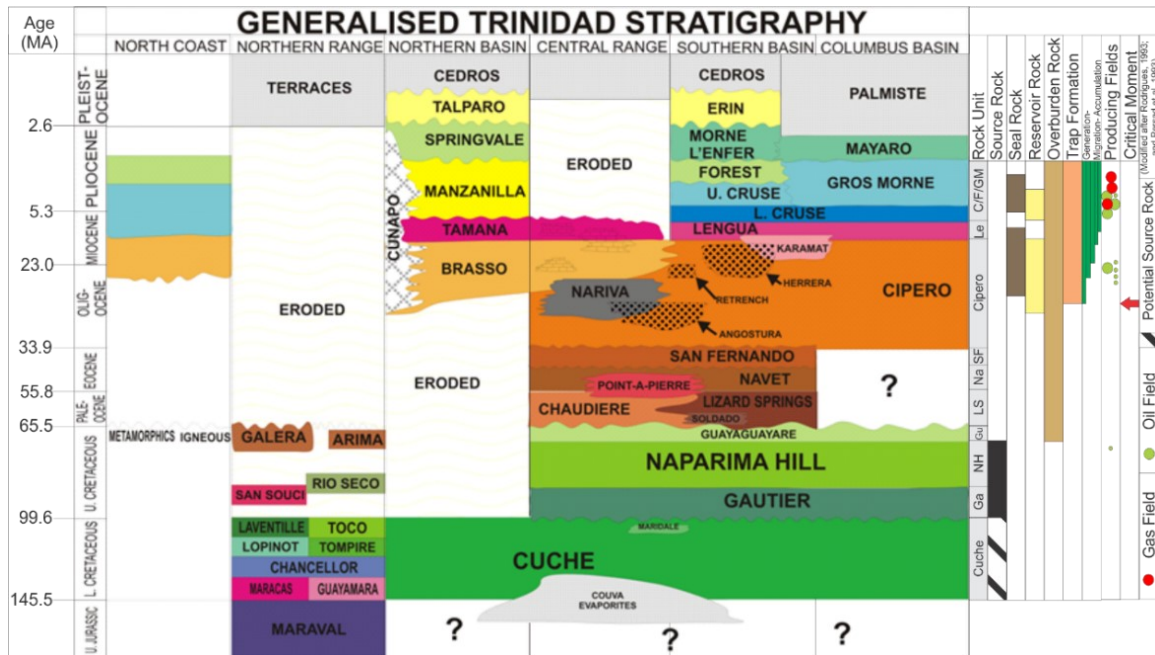


Figure 4.13: Generalized Trinidadian Stratigraphy. From about 85–65 Ma the Naparima Hill Formation accumulated and is oil prone with TOC from 0.2–8% and is considered to be a source rock, along with the underlying Gautier Formation and possibly the Cucche Formation as well (Field Guide, Trinidad Field School 2016, Dalhousie University).

4.8.2 Morocco

Ancient Morocco and Nova Scotia were adjacent to each other prior to the initial stages of continental breakup and three main stages can be identified in both areas: pre-rift, syn-rift and post-rift (Pique et al., 1998). Gondwana, Laurentia and the Baltic cratons collided during the Late Paleozoic after which post-orogenic collapse led to rifting following a Permian age extensional regime. This created horsts and grabens with bounding normal faults trending from NE-SW to ENE-WSW, both newly created and reactivated pre-existing faults. Straddling the Triassic-Jurassic boundary (199–197 Ma), syn-rift phase, voluminous plateau basalts were extruded within and bounding the central rift axis. This circum-Atlantic region extends from Nova Scotia, northeastern USA, northeast Brazil, and northwest Africa and is known as CAMP (Central Atlantic Magmatic Province) and was a precursor to final rifting and formation of true oceanic crust in the new Atlantic (Manspeizer et al., 1978). This event was likely a significant factor in causing the End-Triassic Extinction (ETE) event (Dal Corso et al., 2014). The CAMP basalts covered (or in some cases (Morocco) interfingered with) the salt deposits

which were laid down in the shallow water that flowed east into the new Atlantic from the Tethys Ocean.

The post-rift stage began as active rifting ceased in the Early Jurassic with full development of a passive margin by the Early Cretaceous (Redfern et al., 2017). During the Middle and Late Jurassic extensive carbonate reef complexes were developed along the basin hinge line margins of Nova Scotia and Morocco (Tari et al., 2012). By the Early Cretaceous these reefs died out and were covered by advancing mixed siliciclastic deposits. Specific to Morocco, in the Late Cretaceous the African plate rotated counterclockwise and collided with the Eurasian plate and initiated the Alpine deformation.

Early Cretaceous sediments of the Essaouira-Agadir Basin (EAB) crop out along the Atlantic Coast in a belt 100 km wide by 150 km long. West of the EAB is the Atlas Gulf. In the Jurassic, carbonate platforms formed offshore of Northwest Africa (Jansa and Wiedemann, 1982; Tari et al., 2012). During the Early Cretaceous into the Cenozoic, tectonic-driven inversion and uplift occurred due to the Atlasic and Alpine orogenies (Beauchamp et al., 1999) and salt tectonics (Tari and Jabour, 2013). This inversion and uplift resulted in the deposition of Cretaceous sediments in the same setting as offshore Nova Scotia; above sea level on the Moroccan side but well below sea level and covered by Cenozoic sediments offshore Nova Scotia.

4.8.2.1 Moroccan Cretaceous Stratigraphy

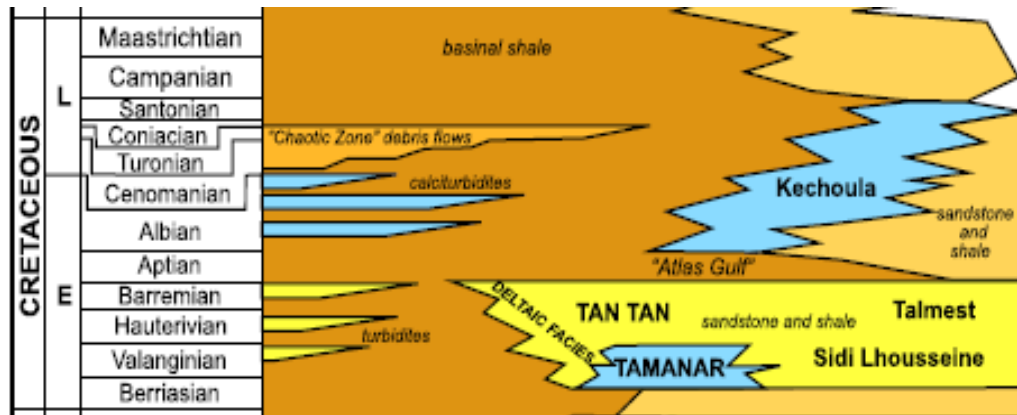


Figure 4.14: Offshore Moroccan Cretaceous stratigraphy. This succession reveals an Albian basalinal shale deposit – “Atlas Gulf” – that would be age-equivalent to the Naskapi Member offshore Nova Scotia (Redfern et al, 2017; North Africa Research Group (NARG), 2017).

Early Cretaceous stratigraphy comprises shallow westward dipping shelf deposits laid down over the Jurassic to Early Cretaceous Berriasian carbonate ramps. West of the EAB in the Atlas Gulf, the deposits are mud dominated with some discrete, coarse clastics. Carbonate production decreases during the Cretaceous. The shale thickens westward and thins eastward, pinching out as it onlaps on the coastal deposits (Rey et al, 1988). It also thins due to salt diapir structures.

Late Early to Late Cretaceous sediments contain black shale deposits that were deposited in deeper basins at low latitudes and have source rock potential. Multiple oceanic anoxic events occurred during this time (Jenkyns, 1980; Arthur et al., 1988). The OAE2 which occurred during the Late Cenomanian to the Early Turonian has been the most documented of the OAEs (Schlanger and Jenkyns, 1976). The OAE2 is characterized by black shale and a positive carbonate isotope δ^{13} excursion which is regional and global in extent and corresponds to a rapid sea level transgression.

There are two main formations in the Moroccan Aptian: the Bouzergoun and the Tamzergout formations. The Bouzergoun is composed of thick shelf muds with minor sandstone layers at the base interlayered with thickening and coarsening-upwards shallow marine and deltaic and fluvial deposits. There are green to red mudstones with interbedded sandstones, sandy limestones with marine fauna. The top of the formation

contains oyster beds and is diachronous being early Lower to early Upper Aptian in age (from the base of the *Deshayesites forbesi* zone to the lower *Colombiceras tableri* zone) (Rey et al., 1988).

The Tamzergout Formation consists of fossiliferous blue-grey marls and grey limestone shelf deposits with a regional unconformity defining its top (Rey et al., 1988).

The Albian Oued Tidzi Formation consists of marlstone along with some green marls with distinctive small pyritic ammonites interlayered with marly limestones and sandy dolomites (Rey et al., 1988). The blue Aptian marls change to green Albian marls rich in bioclastic debris.

4.8.2.2 Moroccan Sequence Stratigraphy

The lowest Bouzergoun Formation was deposited in the Late Barremian during a late highstand (HST) (Rey et al, 1988) as a deltaic deposit prograding succession towards the shelf edge. Moving upwards the deposits indicate a forced regression with distinct sequence boundaries marked by sharp based shoreface sand deposits seen distally showing the marine erosive regressive surface. Incised valleys are filled with fluvial to marginal marine deposits.

In the Aptian, a transgression dominates with a maximum flooding surface (MFS) seen in the *P. dechauxi* zone and a sequence boundary in the hiatus from early to late Aptian. The Tamzergout Formation points to continued flooding (Rey et al, 1988).

By Albian times, accommodation space continued to increase with continued sea level rise, and marls of the Oued Tidzi Formation were laid over the Tamzergout Formation and landward the shallow marine limestone of the Kechoula Formation became established (Rey at al, 1988).

4.8.3 Georges Bank

The Georges Bank Basin is an extension of the Scotian Basin, and underlies the offshore Georges Bank. It was created due to a post-rift sag in the continental platform (Wade and MacLean, 1990).

The basin's Barremian to Cenomanian age organic-rich interval is the Hatteras Formation (Poag, 1982; Jansa et al, 1979) and is equivalent to the Logan Canyon and Missisauga formations (Figure 4.17) (Trabucho-Alexandre et al., 2010).

The lithology is shales and marls of various colours, laminated black carbon rich, organic mudstone alternating with red marls and mudstones with little organic matter. (Trabucho-Alexandre et al., 2010)

Sequences which show alternating black shales and green or red marls in Kuypers et al. 2004, are thought to be orbitally forced productivity variations shown alternating rhythmically.

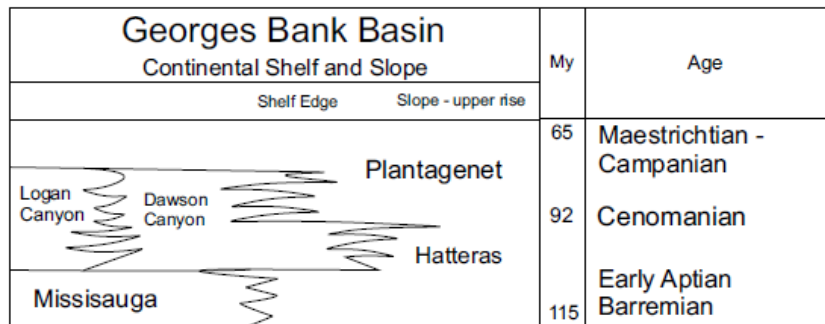


Figure 4.15: Correlation of lithostratigraphic units in the Georges Bank Basin, offshore eastern USA (Massachusetts area). The age boundaries are different than what is used in the more recent stratigraphic chart of the CNSOPB (2011) (Beicip-Franlab, 2011) and the OERA (2016) (Beicip-Franlab, 2016). The Hatteras Formation as defined ranges in age from 115-92 and the (upper) Missisauga from 115-100 Ma. This is equivalent to the Logan Canyon Formation's Naskapi Member as noted on the OERA (PFA) 2016 (Beicip-Franlab, 2016) stratigraphic chart, which occurs from approximately 122-113 Ma and the upper Missisauga occurs from 126-122 Ma. From Poag, (1982) and Jansa et al., (1979).

4.8.4 La Luna Formation – Venezuela

The La Luna Formation is a thermally mature calcareous formation containing source rock that was deposited in an anoxic marine environment under reducing conditions (Escobar et al., 2012). Its lithology is primarily organic-rich black limestones

and shales and is considered the main source rock for the Marcelina Formation (Cogella Group) reservoir rocks (Escobar et al., 2011). Figure 4.18 shows the generalized stratigraphic column for the Alturitas oilfield.

Cretaceous	Late	Mito Juan	Siltstones
		Colon	Gray shales
		La Luna ●	Organic matter-rich Black limestones and shales
	Early	Cogello Group ■	Biomicrotic limestones, shales and sandstones
		Rio Negro	Coarse-grained arkosic and fine-grained sandstones

Figure 4.16: Generalized stratigraphic column of the Alturitas oilfield in Venezuela (after Escobar et al., 2012). The black circle indicates La Luna source rock, and the black square indicates the Cogello Group reservoir rock which is stratigraphically lower. The prolific La Luna source rock is identified as Late Cretaceous in age.

Studies have shown that hydrocarbons were generated, expelled, and migrated during a single pulse, and have not been significantly biodegraded. Major faults that surround the Alturitas field allowed the vertical migration of hydrocarbons from the deeper La Luna Formation to accumulate in the offset and structurally higher Marcelina Formation (Escobar et al., 2012).

Lower Albian-Coniacian organic-rich shales, which are the main source rocks of northern South America, are associated with periods of significant upwelling (Villamil et al., 1999). From Late Jurassic to Cretaceous, a significant facies change occurred in the southern proto-Atlantic in Venezuela and Colombia. The deposition of the original passive margin offshore Venezuela and Trinidad ceased in conjunction with the Cretaceous global sea level rise. This is accompanied by an increase in upwelling and productivity which was possibly due to the northward movement of the South American Plate (Villamil et al., 1999). The Aptian (Hauterivian-Lower Albian) deposits comprise marine siliciclastics and carbonate platforms (Villamil et al., 1999). The Upper Albian was, however, the time that the organic-rich shales alternated with limestones and comprises the major source rock found in northern South America, namely the Villeta Group in south and central Colombia, the La Luna Formation in northern Colombia and

western Venezuela, and the Querecual Formation in Eastern Venezuela (Villamil et al. 1999). The Late Aptian – Early Albian saw primarily shallow water carbonate facies succeeded by predominantly shales by the Middle to Late Albian (Villamil et al., 1999).

The TOC values in the Columbia-Venezuela region strata were highest in the Upper Albian and again in the Lower Turonian strata (Villamil et al., 1999). The conclusions that Villamil et al. reached in their 1999 work was that the increased upwelling occurred when the northern margin of South America was south of the equator, Ekman transport from westward blowing winds pushed surface water south to the continent promoting downwelling and the associated low productivity. As the northern edge of South America moved north and crossed the equator, Ekman transport then began to move surface waters away from the continent resulting in upwelling (Villamil et al., 1999). The result was a facies change from – in ascending order – a clastic-dominated system, changing to carbonate platforms, followed by organic-rich shales interbedded with limestones, and finally in the Santonian-Campanian, chert and phosphates depositions (Villamil et al., 1999).

4.8.5 Eastern Equatorial Atlantic

Upper Cretaceous black shale deposits in offshore West Africa were created by the tectono-sedimentary evolution of the Deep Ivoirian Basin located north of the Cote d'Ivoire-Ghana transform fault margin. Included in these deposits are sediments from the last two of the three Cretaceous OAEs: the Turonian OAE 2 and the Coniacian-Santonian OAE 3 (Wagner and Pletsch, 2001). The OAE3 is considered to have good source rock potential with 17% TOC and kerogen type I/II (Wagner and Pletsch, 2001).

4.8.6 Eastern Pacific – Costa Rica

The Loma Chumico Formation of the late Cenomanian-Campanian deposited in the Tempisque Basin of Costa Rica contains cherts, siliceous shales, volcanic ash/tuffs/glass and volcanoclastic sandstone and contains both organic-rich (5-15% average up to 33% TOC) and organic-lean (<1%) facies. Deposition occurred in a mid-

shelf to outer slope setting near an active subaerial island arc (Erlich et al., 1996). Upwelling and volcanism controlled the nutrient supply productivity in the region. Silica injected volcanically caused pulses of radiolarian, dinoflagellate and diatom 'blooms' and are thought to have expanded the OMZ (oxygen minimum zone) and therefore helped to preserve organic matter.

During the Cenomanian-Campanian time, ocean-wide anoxia was unlikely. Deposition of organic-rich rocks occurred during the latest Santonian-earliest Campanian in Costa Rica and the central Caribbean (Erlich et al., 1996). Earlier, the Jurassic-Mid-Late Cretaceous ophiolite complex basalts formed in an island arc setting (Erlich et al., 1996).

4.8.7 Demerara Rise

A study by Hofman and Wagner (2011) analyzed data from the Ocean Drilling Program (ODP) site 1261 on the Demerara Rise. The borehole is in the western tropical region of the Atlantic Ocean offshore South America and the section studied was a black shale of Coniacian to Santonian age. A comparison was made of a similar unit from the eastern tropical region offshore Africa at ODP site 959. Both these sites were in the Intertropical Convergence Zone (ITCZ) in the tropical Cretaceous Atlantic Ocean.

Studies on these two black shale deposits showed similar repetitive sedimentation patterns deposited under the tropical upward portion of Hadley cells caused by shifts in the ITCZ, pointing to orbitally controlled geochemical cycles. Tropical South America had anoxic bottom waters at the Demerara Rise, alternating between anoxic non-sulfidic and euxinic conditions. The organic carbon burial is due to a variable upwelling system whose intensity was affected by the strength of the Northeast Trade Winds. Variable upwelling with a high level of runoff from the South American continent caused the anoxic bottom waters to vary between anoxic non-sulfidic and euxinic conditions. On the African side, however, the continental climate was more humid with the sea varying between oxic and euxinic conditions. Hofman and Wagner (2011) concluded that black shale sedimentation was largely controlled by atmospheric

circulation from trade winds and monsoonal precipitation, and occurred due to restricted ocean circulation between the regions. High volumes of fluvial runoff created high primary production making the western Cretaceous Atlantic anoxic over long time periods, which in turn ultimately created hydrocarbon-producing black shale deposits. Black shale deposits across the tropical Cretaceous Atlantic were thus connected by atmospheric processes operating over large distances (Hofman and Wagner, 2011).

4.8.8 Offshore Angola

DSDP wells were examined by Hartwig et al. (2012) to evaluate the source rock potential of Aptian, Albian, and Turonian aged samples. They included DSDP sites 364 offshore Angola, borehole 530A north of the Walvis Ridge offshore Namibia, and borehole 361 offshore South Africa. Aptian and Albian aged intervals from borehole 365 were identified as the best examples of high-quality kerogen with sapropelic shales, with type II kerogen and type IIS kerogen which could generate low wax oils and low gas/oil ratio (GOR) sulfur-rich oils. Type III kerogen in silty sandstones had gas condensate potential. In these wells, the Aptian-aged black shale source rock kerogen is thought to have the most potential in the region (Hartwig et al., 2012).

4.8.9 Other South Atlantic Cretaceous Black Shale Deposits

Three other regions with notable black shale deposits are worth mentioning briefly from elsewhere in the proto-Atlantic.

Deposits are found offshore Brazil in the South Atlantic (Mello et al., 1988; Davison, 1999), with oils from these Aptian source rocks being rich in sulfur (Mello et al., 1988) In the Lower Congo and Angola basins offshore of southern Africa (Coward et al., 1999; Beglinger et al., 2012) the variability in kerogen stability is significant in lower Cretaceous organic-rich shales (Burwood, 1999).

Also, in the Orange and Bredasdorp basins offshore southern Africa (Jungslager, 1999; van der Spuy, 2003), the main source rock is Lower Cretaceous lacustrine and Lower to Upper Cretaceous marine black shales.

4.9 Summary

Source rocks with type III kerogen are more abundant than type I or II. Type II is mostly found in the Tethyan seaway. Along the east North American marine shelf, the margin's structural type is classified as a half-sag or linear sag over a single rift. Worldwide, 71% of the effective Cretaceous source rocks are structurally defined as occurring in linear sags.

Although the Cretaceous provided 29% of the world's generated petroleum it only provides 20% of the world's trapped petroleum. Diversity and abundance of the source rocks worldwide was on the increase through the Phanerozoic. Most likely, as life evolved, increased organic matter supply contributed to this.

A common hypothesis is that due to paleogeography and changes in the ocean circulation, the nutrient supply in the proto-North Atlantic was altered. Organic-rich sediments occurred where there was an upwelling of nutrients which lead to high productivity of organisms that proliferated being fed by these nutrients, and therefore created rich deposits of organic matter.

A hypothesis is that the mid-Cretaceous in the North Atlantic region was a nutrient trap as a result of ocean circulation patterns bringing waters from the Pacific Ocean. Submarine igneous events in the Pacific Ocean produced nutrient-rich seawater which was circulated to the North Atlantic where it subsequently welled up and enhanced marine productivity.

Nutrient trap creation results in high productivity, and high deposition of organic-rich sediments. High total organic carbon (TOC) and the deposition of high metal element levels lead to anoxic conditions in the bottom sediments and caused enrichments of redox sensitive elements such as cadmium (Cd), copper (Cu), nickel (Ni), zinc (Zn), molybdenum (Mo), uranium (U), and vanadium (V).

There is discussion about whether an increase in organic material comes from increased production or increased preservation through anoxia. Increased production is due to more nutrients from upwelling and runoff from the adjacent landmasses. This increases productivity, which in turn deepens the oxygen minimum zone to abyssal

depths. Increased preservation of organic matter happens where an increase in surface water temperature and increased runoff from adjacent landmass cause decreased bottom water formation and an elevated carbon burial.

There is a distinction between black shales found in the southern North Atlantic where abundant marine organics are preserved (up to 45% TOC with average 10%), and the northern North Atlantic which contains mostly terrestrially sourced organic matter deposited by turbidites interbedded with dark pelagic mudstone (TOCs of 26% with an average of 5-6 %). Of note in the southern North Atlantic, organic-rich black shale deposits of largely Aptian-Albian and Cenomanian age resulted in source rocks which charged significant hydrocarbon reservoirs. Examples are the Loma Chumico Formation of the late Cenomanian-Campanian in the Tempisque Basin of Costa Rica; the La Luna Formation in Venezuela composed of primarily organic-rich black limestones; the Deep Ivoirian Basin offshore west Africa with 17% TOC; the Naparima Hill Formation in Trinidad which is oil-prone with TOCs from 0.2 to 8%; and the Hatteras Formation in the Georges Bank Basin, where the TOC of sediments ranges from approximately 2 to 10%.

The mid-Cretaceous time has been termed a nutrient trap period with organic-rich sequences containing discrete, highly organic-rich layers, and significant carbon isotope ($\delta^{13}\text{C}_{\text{org}}$) excursions. This is believed to be due to nutrients supplied by hydrothermal alteration of submarine basalts from the Pacific Ocean and proto-Indian Ocean, which are biolimiting.

Data from the Deep Sea Drilling Program (DSDP) demonstrated that there is not a continuous record of deposition in the deep ocean, and that over the 125 Ma since the Atlantic Ocean formed, only half is recorded in the sedimentary column indicating that erosion occurred.

Black shale and OAEs are not truly global as they are missing from the deep Pacific, and the global ocean meridional overturning circulation fostered the recycling of N, P, Si, Cd, Cu, Zn, and Ni from the surface. Without this they would have downwelled to deeper waters and circulated throughout other oceans, then upwelled where they

were brought to the surface. The result would be enhanced productivity, high fertility, and deposition of organic-rich sediments.

To be classified as an oceanic anoxic event, the black shales must be seen not only in the shelf deposits but pelagic deposits as well. In marine settings, biological growth, or primary productivity, increases due to elevated temperatures and an increase in atmospheric CO₂. CO₂ is fixed as organic matter as well as inorganic carbon in calcite. Oceanic anoxic events can be triggered by a volcanic pulse. The response of the oceanic anoxic event lags the CO₂ pulse by approximately 23,000 years.

It is thought that widespread anoxia is the main control during the mid-Cretaceous, as the volume of organic-rich sediments accumulated in Cretaceous sediments is lower than is seen today in modern oceans where high productivity occurs. The widespread accumulation of organic carbon-rich sediments as well as metal-rich sediments was probably enhanced by reduced dilution of marine sediment by terrigenous clastics. The Mid Cretaceous maximum sea level high stand would have reduced the exposed land/sea floor ratio. Assuming the terrigenous sediment supply remained constant, its supply to a given unit of sea floor would be greatly reduced and result in the reduced dilution of marine sediment.

Deposition of organic carbon-rich sediments occurred during the Aptian Selli Event, the Aptian/Albian Boundary Event, and the Cenomanian Bonarelli Event. Two other major events were in the Santonian, where the largest foraminiferal turnover occurred, and the major extinction event at the end of the Cretaceous. All five events indicate that increased upwelling caused and upper water column disruption.

Chapter 5: Data and Methods

The following data and methods were used in this study and are outlined in this chapter.

5.1 Data Examined

The digital data set incorporated in this thesis is comprised of:

- a. Public domain wireline log data provided digitally by DivestoCo to Dalhousie University available through the Basin and Reservoir Lab (BARL).
- b. Digital lithology data provided by Canadian Stratigraphic Services (2000) Ltd. (Canstrat™) to Dalhousie University made available through the BARL.
- c. Geochemical, maturation, and temperature analyses summarized from multiple company and Geological Survey of Canada (GSC) reports: publicly available digitally in the online NRCan (Natural Resources Canada) BASIN Database.
- d. Drilling data, formation tops, pressures, test results, biostratigraphy similarly available in the NRCan BASIN data base.
- e. Well reports and wireline log PDFs publicly available from the Canada-Nova Scotia Offshore Petroleum Board' online Data Management Centre (CNSOPB-DMC).
- f. 3D seismic data cube (ExxonMobil Sable MegaMerge) made available and used with permission to Dalhousie by Sable Offshore Energy (with restrictions on publication).

5.2 Workflow for Compiling and Interpreting Data

Almost all the well data noted above is available digitally, either as continuous logs (e.g. wireline logs such as gamma, resistivity, and density), discrete logs (e.g. Canstrat™ logs where properties such as lithology have integer values), or point data sets (e.g. geochemical analyses such as TOC or VR). With these data it is possible to use 3D modeling techniques and extract 2D maps, once a geocellular framework has been established and populated.

This was accomplished by using Petrel™ software, a copy of which was donated to Dalhousie University Basin and Reservoir Lab (BARL) courtesy of Schlumberger. This program makes it possible to create shelf wide maps of individual properties and attributes which can be examined for characteristics potentially diagnostic of source rocks. The workflow is summarized in Figure 5.1.

Firstly, the Top and Base Naskapi Member horizons were correlated at XX wells, and then a geocellular depth model was constructed with XX layers – at 2m vertical intervals.

Total Organic Carbon (TOC), vitrinite reflectance (VR) data, and temperature data from the BASIN database were extracted. Canstrat™ LAS 2.0 file data, and the MegaMerge seismic cube were loaded into Petrel™. From this information, a cross section was built from all wells that had complete wireline log data through the Naskapi Member (gamma ray – GR, resistivity – R, and neutron – N), as well as complete Canstrat™ well data. Wells with only partial coverage were excluded. From the cross section, the tops of the Naskapi and Missisauga (i.e. the base of the Naskapi) horizons were selected. TOC, VR, and temperature data were extracted where available for the defined Naskapi interval. Using Petrel™, spreadsheets of these data were loaded and mapped.

Canstrat™ data spreadsheets were also inputted and mapped. Geophysical logs (gamma ray, density and neutron logs) were mapped in Petrel™. Using the MegaMerge seismic data, well ties were made with all wells within the polygon, and Naskapi and Missisauga horizons were picked and mapped in 3-dimensions.

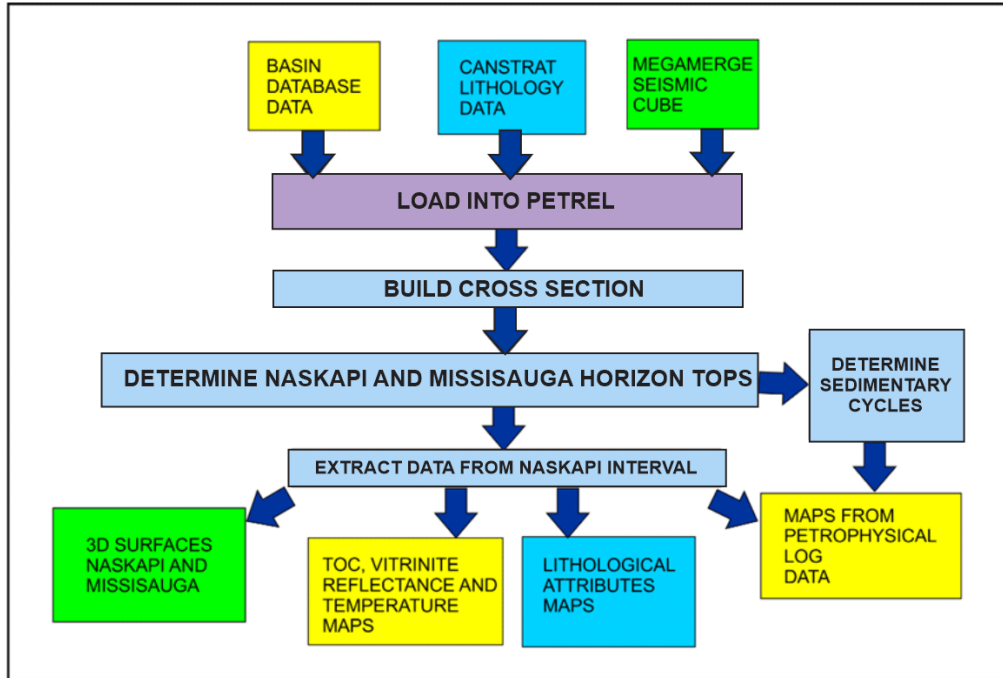


Figure 5.1: Flow chart outlining workflow with available data.

5.3 Cuttings Examination

Wells are drilled by a bit at the end of a metal drill string, which is rotated and cuts downward through the rock using mud as a lubricant that under pressure is ejected through nozzles at the bit, and together hydraulically fractures the formation lithologies. Mud is circulated down the middle of the pipe and returns up the annulus, or the area between the outside of the pipe and the borehole, carrying particles cut out of the hole. These particles are referred to as cuttings. A cuttings sample is taken from the mud as it passes through the shale shaker at specific intervals, usually 5-10 metres. The lag time between drilling and emerging at the surface is estimated via mud volume / pump volume estimates or directly via carbide lag tests. A bucket of mud is captured, and a representative handful of cuttings is removed, bagged, and labeled. To label cuttings for depth, estimations are made for the depth down the hole, and a lag time is calculated from when the cuttings are drilled until the time those cuttings return to surface with the drilling mud.

At the well site, the cuttings are examined in conjunction with electrical logs from tools behind the drill bit and rate of penetration (ROP) curves to interpret which

depth and shows questionable oil stain at 9250 ft. Porosity grades in Column 4 indicate increasing porosity as bars move to the left. Column 5 shows the subsurface lithology in 10 foot intervals colour coded for different rock types. Wireline logs are included for comparison (left of the lithology column is the Gamma Ray log and right of the column is the Sonic log). Column 6 indicates grain size with increasing bars to the right. Column 7 shows rounding where a indicates sub-angular and r indicates sub-rounded. Sorting is shown in Column 8 where M indicates medium-sorted and W indicates well sorted. Framework numbers in Column 9 show the higher the number the higher the ratio of framework to filler (e.g. a clean sandstone with good porosity would be a 10, and a shale would be a 0). Word abbreviations describe the samples and their contents, and the C- letter-number combinations on the far right of Column 10 indicate diagenesis such as type and percentage of cementation between grains (e.g. C-1 would indicate 10% calcite cement and S-1 would indicate 10% silica cement) (Canstrat™ dataset, 1974 – Dalhousie University).

The Canstrat™ cuttings data are compiled in a strip-log format showing depth with cuttings described at 10 feet (prior to 1977) or 5-metre (post-1977) intervals. The following attributes are noted: major rock type and percent, grain size, rounding and sorting of clastic grains, accessory rock types and percentages, visual porosity type and percentage, oil staining, fluorescence, mineral occurrence, and fossil type and percentage. Also, framework is noted, which is the ratio of grains, such as clasts, fossils, pebbles, or nodules, to matrix. On a scale of 1 to 10, a high framework number would correspond to a clean sand, and a low one would indicate pure mudstone or claystone.

Cuttings were examined from collections stored in government repositories, made publicly available after a defined period of confidentiality. Canstrat™ geologists examining the cuttings were specially trained to bring consistency and a high level of detail to the cuttings descriptions. The dataset is consistent and reliable for use in regional studies.

Beginning in 1968, the lithologs were digitally coded into ascii *.dat files, where the attributes were converted to an alpha-numeric code. In 2007 these files were converted to LAS 2.0 files. For the purposes of this study, LAS files were imported into Petrel™. Canadian Stratigraphic Services (2000) Ltd. donated the lithology logs and LAS files from 284 well locations from the East Coast of Canada offshore area to Dalhousie University Department of Earth Sciences in 2012. 90 of the 105 wells in the study area were logged by Canstrat™ and available as LAS 2.0 files.

Canstrat™ lithological descriptions can have a high level of detail with up to 241 separate characteristics being described. For the purposes of this study, focus has been

on the following characteristics: rock type, colour, visual porosity, oil staining, grain size, and cementation type and amount.

5.3.1.1 Rock Type

There may be several distinct lithologies apparent in one cuttings sample. The most abundant type is regarded as the main lithology and the percentage can be estimated. The second most abundant lithology will be logged as minor or accessory lithology.

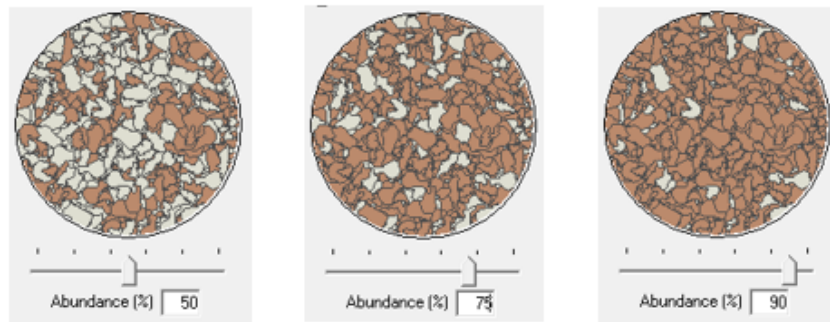


Figure 5.3: Example of percentage values (50%, 75% and 90%) of major lithological constituent of cuttings sample. If a sample contains 50% or more clasts of a particular lithology, that lithology is considered to be the main lithology in the Canstrat™ database (courtesy of HRH Geological Services, Aberdeen, Scotland).

Rock types are also assigned a colour that provides a visual cue when viewing cross sections. See Figure 5.4.

Code	Name	Parent	Background	Lines	Pattern
1	igenous basic 1		Green	Black	Green
2	igneous acidic 2		Green	Black	Green
3	metamorphic 3		Olive	Black	Olive
4	volcanic 4		Light Green	Black	Light Green
5	5		Light Blue	Black	Light Blue
6	6		Light Blue	Black	Light Blue
7	7		Light Blue	Black	Light Blue
8	siderite 8		Light Blue	Black	Light Blue
9	glacial 9		Light Blue	Black	Light Blue
10	10		Light Blue	Black	Light Blue
11	11		Light Blue	Black	Light Blue
12	cgl_12		Magenta	Black	Magenta
13	brc_13		Magenta	Black	Magenta
14	14		Light Blue	Black	Light Blue
15	15		Light Blue	Black	Light Blue
16	16		Light Blue	Black	Light Blue
17	ss_17		Orange	Black	Orange
18	silt_18		Yellow	Black	Yellow
19	cly_19		Grey	Black	Grey
20	sh_20		Grey	Black	Grey
21	21		Light Blue	Black	Light Blue
22	bentonite_22		Brown	Black	Brown
23	23		Light Blue	Black	Light Blue
24	coal_24		Black	Black	Black
25	25		Light Blue	Black	Light Blue
26	marl_26		Blue	Black	Blue
27	lst_27		Blue	Black	Blue
28	lst_27		Blue	Black	Blue
29	28		Light Blue	Black	Light Blue
30	dol_30		Purple	Black	Purple
U	UNDEF		Grey	Black	Grey

Figure 5.4. Canstrat™ colour coding of rock types. Canstrat™ uses industry standards for easy recognition of rock types when viewing logs and cross sections. These colours have been used for this study (Chart from Petrel™, 2017).

5.3.1.2 Rock Colour

Colour is an important indicator of rock type, and can point to provenance of grains, environment of deposition, and conditions affecting the rock post-deposition. The main lithologies are assigned their default colour for display purposes, however shales and clays, which are typically grey, are also coloured to indicate their true appearance. Colours noted on Canstrat™ logs for shales and clays are green, red, purple, brown, and varicoloured. Up to two hues are coded per depth interval (e.g. blue - green) and saturation (light, dark, medium).

The depositional environment of a rock, and subsequent diagenesis can affect the colour of a sample. The oxidation – reduction balance of the sediments is important. Reduced sediments appear green or greenish-grey, due to carbon with an organic origin, and Fe²⁺ sulfides. Small localized reducing environments which form around a decaying organism, can appear as splotches of green or greenish-grey colour. On the other hand, oxidized sediments can contain oxidized Fe³⁺ compounds such as limonite and hematite, and appear red, brown, or yellow (Miall, 2016).

Clastics generally reflect the colour of their detrital components, for example quartz rich sediments will appear white or pale grey, sediments with feldspathic grains will appear pink, and lithic rocks with an argillaceous, shaly matrix will appear dark grey (Miall, 2016).

5.3.1.3 Visual Porosity

Visual porosity percentage and type is noted from the main lithology grains, such as inter-granular porosity in clastics, inter-crystalline porosity in carbonates, or evidence of leaching or vugs. If loose calcite or quartz crystals are seen at the bottom of the sample tray, this points to crystal growth inside a vuggy, porous rock. Presence of kaolinite, a clay mineral, indicates earthy porosity. Fractured grains indicate porosity from faulting or other tectonic events.

5.3.1.4 Oil Stain

Oil stain is qualitatively noted as good, questionable, or dead. Dead oil stain can indicate that oil passed through the rock. In addition, Canstrat™ methodology involves placing a small sample of cuttings on a spot plate, adding several drops of xylene to separate any hydrocarbons contained therein, and inspection under a fluoroscope. Streaming hydrocarbons in the xylene is referred to as ‘cut’. Observed cut or fluorescence is noted.

5.3.1.5 Grain Size

Grain size of clastic materials are measured using the Wentworth scale to describe sizes such as clay, silt, sand, and pebble.

Grain size along with other criteria rounding of grains is noted, indicating angular, sub-angular, sub-rounded, and well rounded. The degree of rounding indicates the amount of movement and grain-to-grain impacting that the grain has been subject to.

Sorting of grains is classified ranging from poor to well sorted. This can indicate the environment of deposition at the time of burial. For example, a high-energy shoreface sand would tend to be well rounded and well sorted.

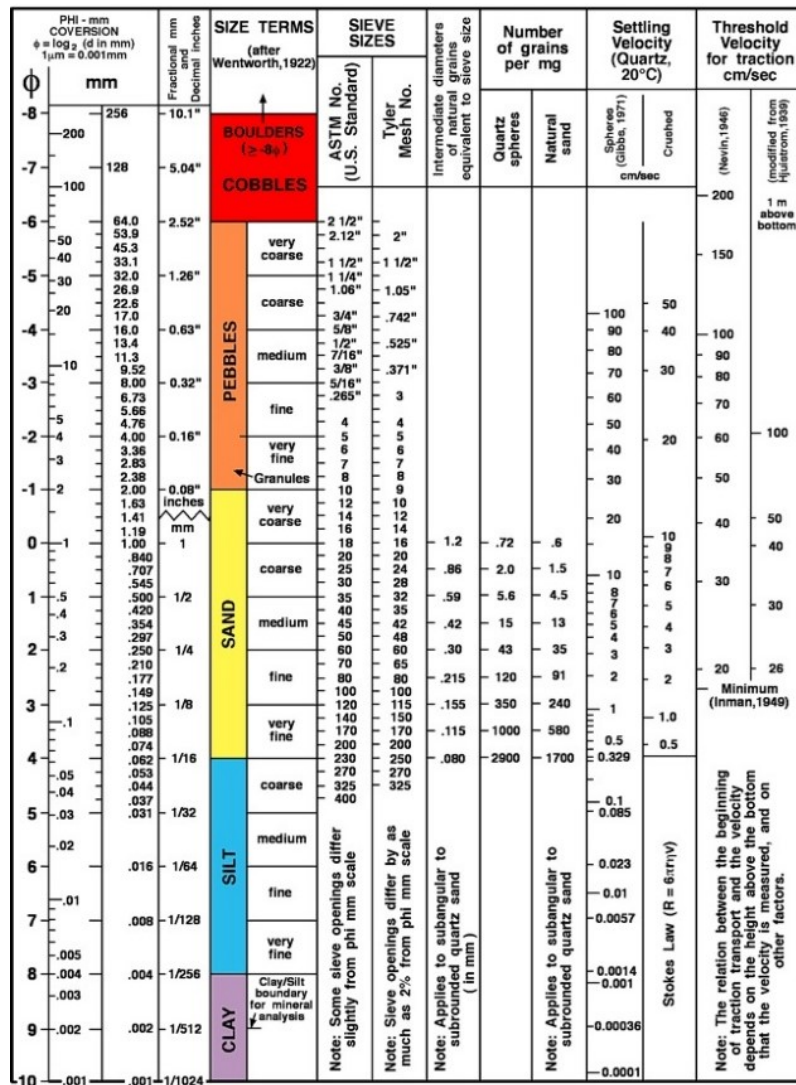


Figure 5.5: U.S. Wentworth scale of grain size estimation (Geological Survey Open-File Report 2006-1195).

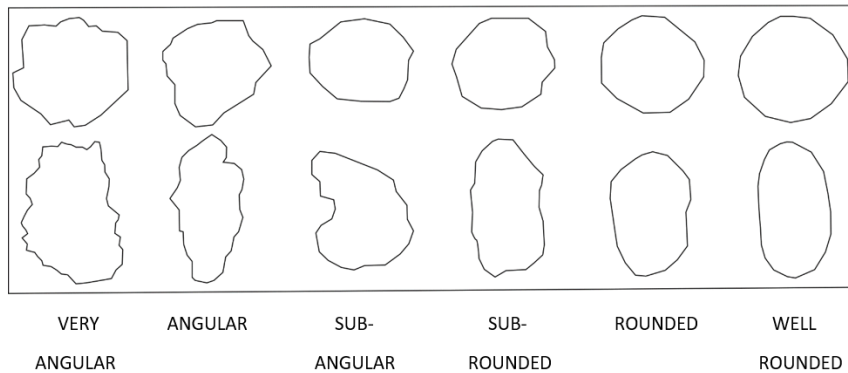


Figure 5.6: Grain roundness and angularity comparison (after Powers, 1953). Roundness indicates that the grain has travelled a significant distance, enough to round and smooth its surfaces. Angular grains point to the grain remaining closer to its source.

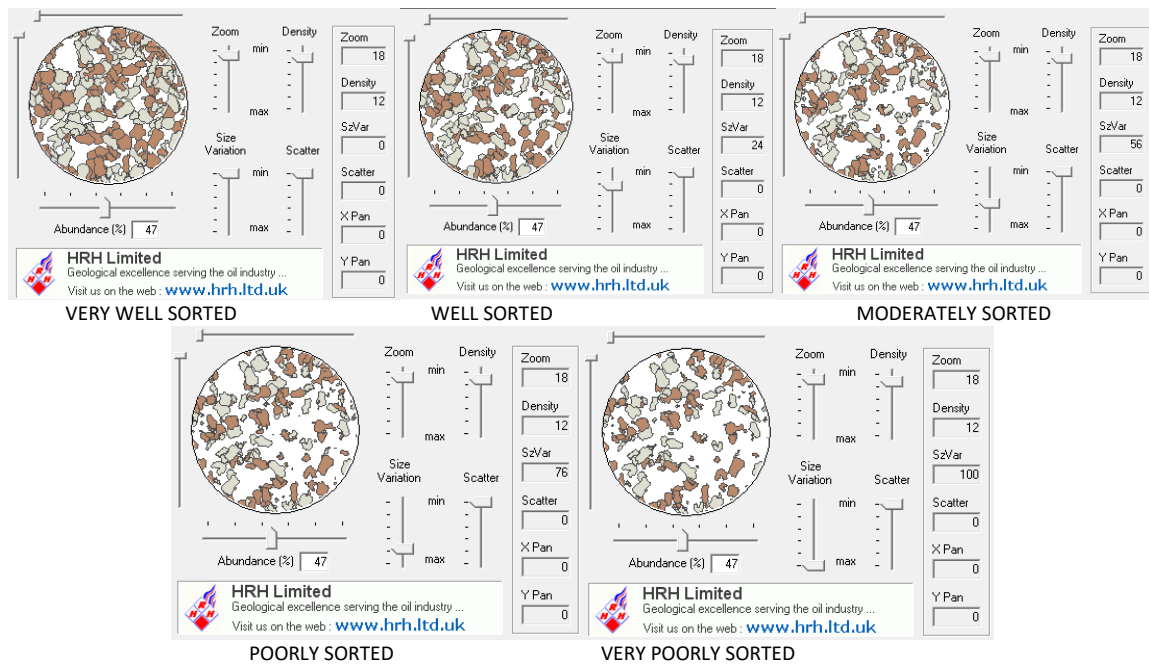


Figure 5.7: Grain sorting comparator (courtesy of HRH Limited, Aberdeen, UK). The sorting of a sediment refers to the variance in grain size found in that sediment. A poorly sorted sample with a large variance of grain size indicates low energy environment during and post deposition. A well sorted sample indicates a higher energy environment where significant water or wind action moved the grains around and winnowed out the finer material. This results in the coarser material sorted by size and is dependant on the strength of the water or air movement and its ability to move grains of a certain mass. The stronger the current of air or water, the heavier the grain that can be transported.

5.3.1.6 Cementation

Diagenesis, which refers to any changes that have occurred to the sediments or sedimentary rocks after deposition, is noted and includes alteration by waters or

formation fluids that pass through the rock. Some examples are as waters containing magnesium pass through a limestone, dolomitization occurs, or as silica-rich fluids flow through sediments, chert nodules can form. This process can also be referred to as metasomatism, or actions by fluids from igneous or metamorphic sources. Iron-rich fluids can deposit siderite, pyrite, or ironstone nodules. Water flow can convert (rehydrate) anhydrite deposits to gypsum; or conversely, gypsum can convert to anhydrite if dehydrated. Canstrat™ classifies these cementation types (factors) along with a number indicating the percentage (usually 1 or 2 meaning 10 or 20%).

S factor – silica cement

C factor – calcite cement

M factor – metasomatism

A factor – anhydrite cement

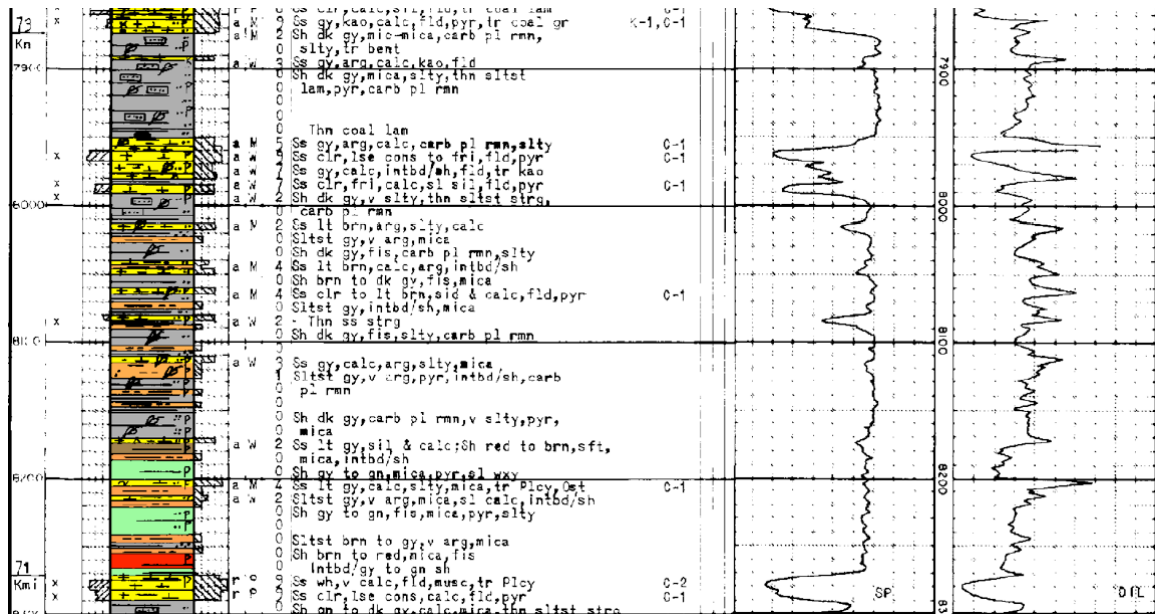


Figure 5.8: Canstrat™ log number EC39 (Sable Island E-48) showing an example of annotation, colour coding and shorthand including diagenesis annotation for cements. C-1 refers to 10% calcite cement for the interval at 7980 ft. S-1 refers to 10% silica cement for the interval at 7870 ft.

5.3.2 Canstrat™ Coding

The collection of Canstrat™ lithology logs were coded by the firm into an ASCII format beginning in 1968 enabling computer data analysis, a novelty for that era. Figure 5.9 shows an example of this.

```

E 2641 43-53-06 059-51-41MMOBIL SOUTH SABLE B-44 KB 416M52075
E 2642 88-03-27 88-07-08 GAS WELL 300B444400059450 8850 52075
E 2648 YB 8850
E 2648 TOP 8850
E 2648 K 14395
E 2648 KNY 14395
E 2648 KDC 15420
E 2648 KPL 16020
E 2648 KLO 17110
E 2648 KN 28510
E 2648 KMI 30515
E 2648 J 42455
E 2648 JMC 42455
E 2648 JVC 49800
E 2648 BOT 52075
E 2647 8850 8900C7M01 B JY1LY1IY1 GL%M%F
E 2647 8900 8965C5M03 B JY1LY3IY1%F2 GL%M
E 2647 8965 8975I5202 B JY1LY1AR3%B1 GL
E 2647 8975 9055C5M03 B JY3LY1IY1 GL%F%M
E 2647 9055 9070I5202 B JY1LY1AR3%B1 GL
E 2647 9070 9090C5M04 B JY3LY1IY1%F1 GL%M
E 2647 9090 9100I5202 B JY1LY1AR3%B1 GL
E 2647 9100 9135C5M03 B JY3LY1IY1 GL%F%M
E 2647 9135 9145J5405BG SL1LY1CY1CS1IY1 2WGG
E 2647 9145 9200C6M02 B JY2LY1IY1 GL%F%M
E 2647 9200 9255C5M03 B JY3LY1IY1 GL%F%M
E 2647 9255 9295I5202 B JY2LY1AR1S51 GL F
E 2647 9295 9350C6M03 B JY2LY1IY1%F1 GL%M
E 2647 9350 9377C5M02 B JY2LY1IY1I51 GL%M%F
E 2647 9377 9395S7M01 B JY1LY1IY1 GL

```

Figure 5.9: Canstrat™ log coded in ASCII format. For the well South Sable B-44, location information is coded in the first two rows, followed by 13 rows of formation top names (abbreviated) and depths. Thereafter, each interval with differing lithology is coded with depth information, lithology colour, accessory rock types, grain size, mineral content, porosity, and percentage etc. This data format was developed in 1968 for rudimentary mapping, and subsequently converted to LAS 2.0 format in 2005 to be used with modern mapping software.

All attributes described on a Canstrat™ log were represented by either a letter or a number. In 2007, the ASCII data was converted to a LAS 2.0 format, from which the user can export summary reports of the lithology. The reports summarize, by formation name, the meters of a formation which exhibit an attribute such as rock type, colour, visual porosity, oil staining, grain size or cementation type and amount.

<pre> E 2647 9135 9145J5405BG SL1LY1CY1CS1IY1 2WGG East Coast well 264, lith code, 913.5 – 914.5 ft depth, 50% sand, 10% siliceous, 10% limey, 10% clay, 10% claystone stringers, 10% silty, subrounded, well sorted, glauconite grains present. E 2647 9145 9200C6M02 B JY2LY1IY1 GL%F%M East Coast well 264, lith code, 914.5 – 920 ft., clay 60%, sandy 20%, limey 10%, silty 10%, glauconite, fossiliferous, micaceous </pre>

Figure 5.10: An example in detail of a line of lithology interval coding from Figure 5.9. Letters and numbers refer specifically to an attribute type and each number refers to a percentage or amount.

considerably. The geologist logging the samples is aided by comparing their logged lithotypes with available wireline logs and rate of penetration curves.

The Canstrat™ geologists who logged the samples were very well trained, but as with any task, human error is possible; description of attributes can be at times subjective. The coding of the logs into ASCII data, and the conversion of ASCII to LAS 2.0 files are also subject to transcription error.

5.3.4 Lithology Logs from Natural Resources Canada BASIN

Database

The Canstrat™ offshore Nova Scotia database was generated well over twenty years ago, with very few logged wells being added in the past fifteen years. Approximately twenty-five well log studies from newer wells are available to view and download from the CNSOPB-DMC and NRCAN BASIN database for the area of interest. An attempt to code these wells using the Canstrat™ coding method was carried out. Ultimately, those data were not added to the Canstrat™ data used in map generation for this project. The consistency of data generation could not be assumed to be of the same quality as that of the Canstrat™ data set. The well logs from the CNSOPB files and NRCAN database were of varying quality with logged samples showing differing levels of detail, and thus were not comparable to the Canstrat™ equivalent.

5.4 Wireline Log Data



Figure 5.12: Log sample from the Mississauga H-54 well through a section showing the Naskapi Member. The unit is bounded by black dashed lines and combines wireline logs (from left to right): gamma ray, sonic, density and deep resistivity) with lithologs that clearly highlight the yellow sand and grey shale intervals.

After a well is drilled, logging is done by introducing various pieces of equipment, known as tools, down the wellbore that record data while drawing the tool back up the hole. These data are shown on a graph, referred to as a “wireline log” where down-hole measured depth is displayed on the y-axis and the wireline log units of measurement displayed on the x-axis.

For the purposes of this paper, four types of wireline logs were used to create cross sections and maps of the subsurface in the study area. Also, these four log types, when used together, allow one to measure the “ Δ log R” values, which can indicate if source rocks/hydrocarbons are present in the subsurface (Schlumberger Limited, 2015).

5.4.1 Gamma Ray Logs

Gamma ray logs are used to correlate rock formations, calculate shale volume, and identify lithologies. The tool measures the naturally occurring radioactivity of the rock that was drilled through. The gamma ray measurement (gAPI, Gamma Units of API) increases with increasing shale/clay amounts (Schlumberger Limited, 2015).

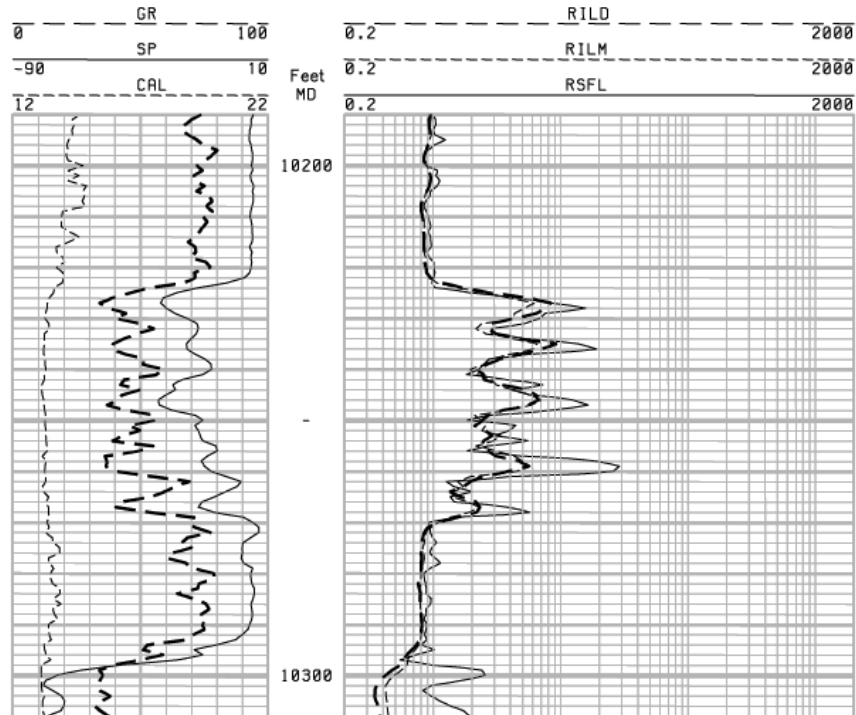


Figure 5.13: Sample of a Gamma Ray log. The GR curve is in the left-hand column, with the large-dashed line the gamma ray trace with the scale ranging from 0 to 100 gAPI. Shale is indicated from 10190-10220 m, and from 10270-10292 m where the gamma ray reading is approximately 70 API. Sandstone is seen from 10222-10268 m approximately with a gamma ray reading of 40-50 API (Krygowski, 2003).

Shales are radioactive because radioactive potassium is a common component in the clays therein. Also, the cation exchange capacity of clay causes them to absorb radioactive uranium and thorium. Thus, shales have the highest gamma ray readings, which are measured in API (American Petroleum Institute) units of radioactivity. The standard for this measurement is based on an artificially radioactive concrete block at the University of Houston, TX, which is defined to have a radioactivity of 200 API units, which is approximately twice the radioactivity of a typical shale.

Sandstones and carbonates, which generally have a low clay or shale content, will therefore have low gamma ray readings. It is possible for a low-gamma-radioactivity sandstone to have a high radioactivity measurement if it contains clasts composed high-radioactivity potassium feldspars, glauconite, or mica minerals (Asquith and Krygowski, 2004)

5.4.2 Resistivity Logs

The first wireline log ever run was a resistivity log in 1919 by Conrad Schlumberger (Rider and Kennedy, 2011). The resistivity log measures the electrical resistivity of the formation fluids and the rock matrix that contains them. The higher the resistivity, the less the rock conducts electricity.

Most rock materials are effective insulators (non-conductors) meaning their resistivity is high. However, porous spaces in the rock can contain water which conducts electricity, so a rock formation that is porous with salt water will have a lower resistivity. If it contains hydrocarbons, or fresh water, resistivity will be higher than for salt but lower than the rock itself.

Formation waters are usually saline, with salinity increasing with depth. Sea water is on average 35,000 ppm NaCl and formation waters can vary from 2,000 ppm to 300,000 ppm (Rider and Kennedy, 2011). The electric current is conducted by ions such as Na⁺ or Cl⁻.

Hydrocarbons have measurable resistivity and conductivity, however they are covalent compounds, not ionic compounds like salt, so will not carry electrical current as easily, and therefore have higher resistivity than saline water. An immature source rock, which is defined as a rock where the total organic carbon has not been converted to hydrocarbons by increased burial depth, will have lower resistivity than a source rock, or rock containing mature hydrocarbons (Asquith and Krygowski, 2004).

In porous rocks, this difference in resistivity is used to estimate hydrocarbon volumes when the water saturation is calculated from the resistivity logs (Rider and Kennedy, 2011). A rock with high resistivity values can therefore indicate a porous hydrocarbon-bearing rock or a tight (non-porous) formation with low to zero levels of porosity. Resistivity logs give the raw data to calculate water saturation. The following formulas define resistance and resistivity of a cylinder of rock, where r = resistance, ρ = Resistivity, A = area of cross section of rock in m², and L = the length in metres of the rock downhole (core).

r in ohms = Resistance = $L \times \text{Resistivity}/A$

Equation 5.1: *Resistance*

R or ρ in ohm-m = Resistivity = $r \times A/L$

Equation 5.2: *Resistivity*

R or ρ in ohm-m = Resistivity = $1000/\text{conductivity in mS/m}$

R_w = Resistivity of the formation waters

R_o = Resistivity of the rock filled with formation water

$R_o = F \times R_w$ where F is the Formation Factor which varies from rock to rock.

Equation 5.3: *Resistivity R_o*

The formation factor (F) will equal 1 for a 'pure water' where conductivity is unimpeded. F increases as conductivity becomes more difficult if pores are not interconnected. F decreases, but never less than 1, as pores are more interconnected, and permeability increases.

An additional factor that should be considered is that the resistivity or conductivity of formation water is directly dependent on the temperature of the formation that the tool is passing through.

5.4.3 Sonic Logs

The sonic log measures interval transit time (Delta t , Δt) or the time required for a compressional sound wave transmitted from the logging tool down the borehole, to move laterally through the formation and return to the receiver positioned in the tool distant from the generating source. Δt depends on lithology and porosity. The sonic-derived porosity, Φ_s , can be derived through application of the Wylie equation using standard given values for the matrix interval transit time (Δt_{ma}) of the rock type.

$$\Phi_s = \frac{\Delta t_{log} - \Delta t_{ma}}{\Delta t_{fl} - \Delta t_{ma}}$$

Equation 5.4: *Sonic derived porosity Φ_s .*

Φ_s is the sonic-derived porosity, Δt_{ma} is interval transit time of the matrix, Δt_{log} is the interval transit time measured in the formation for the mixture of rock and pore-filling fluids, and Δt_{fl} is the interval transit time of the formation fluid held in porous spaces in the formation. The formation fluid is normally salt water. The transit times are measured in $\mu\text{sec}/\text{ft}$ or $\mu\text{sec}/\text{m}$ (Asquith and Krygowski, 2004). An example of the sonic log is shown in Figure 5.12.

5.4.4 Density Logs

The continuous density log measures the bulk density of the rock, which includes both the rock matrix and fluids enclosed in pore spaces. The bulk density varies depending on the rock type, amount of porosity, and the fluids contained in the pore spaces, which could be water, oil, or gas. The density log both emits and detects gamma rays, thus measuring the density, or the count of the rays which varies with the density of material between the emitter and the detector (Asquith and Krygowski, 2004).

The gamma rays emitted are 662 KeV (kilo electron Volts) from ^{137}Cs (Cesium). They are emitted out a small hole beamed into the formation and attenuated by Compton scattering. The so-called "Compton effect" is an inelastic scattering of a photon from bombardment by an electron resulting in a decrease in energy and therefore an increase in wavelength of the photon. The number of electrons per unit volume in the rock ($\text{electrons}/\text{cm}^3$) is closely related to the rocks common density of g/cm^3 . Of 50 billion rays emitted, only several hundred will be detected.

The density log, like the sonic, can be used to derive porosity. It is reliable, as the precision of the vertical resolution is excellent with an approximate accuracy of $\pm 0.01 \text{ g}/\text{cm}^2$ or ± 0.5 porosity units (Rider and Kennedy, 2011). The tools are calibrated monthly to an aluminum block which measures $2.70 \text{ g}/\text{cm}^3$, or to a magnesium block of $1.738 \text{ g}/\text{cm}^3$. Typical density values for minerals and fluids are listed in Table 5.1 below.

Table 5.1: Density values of minerals, fluids, and hydrocarbons (Rider and Kennedy, 2011; Schlumberger, 1989; Minette, 1996).

DENSITY VALUES

MINERAL OR FLUID	CHEMICAL FORMULA	ρ_b DENSITY g/cm ³	ρ_e ELECTRON DENSITY	ρ DENSITY read on log
Quartz	SiO ₂	2.654	2.65	2.648
Calcite	CaCO ₃	2.71	2.708	2.71
Dolomite	CaCO ₃ MgCO ₃	2.85	2.863	2.85
Halite	NaCl	2.165	2.074	2.032
Gypsum	CaSO ₄ 2H ₂ O	2.32	2.372	2.351
Anhydrite	CaSO ₄	2.96	2.957	2.977
Sylvite	KCl	1.984	1.916	1.863
Coal - bituminous		1.2 - 1.5	1.272 - 1.590	1.173 - 1.514
Coal - anthracite		1.4 - 1.8	1.442 - 1.852	1.355 - 1.796
Fresh Water	H ₂ O	1	1.11	1
Salt Water	H ₂ O with 200,000 ppm NaCl	1.146	1.273	1.135
Oil	n(CH ₂)	0.85	0.97	0.85
Methane	CH ₄	0.000677	0.00084	
Gas	C _{1.1} H _{4.2}	0.000773	0.00096	

Density (ρ or Rho) is measured in grams per cubic centimeter; $\rho = \text{g/cm}^3$, where bulk density is ρ_b or the combination of formation mineralogy plus pore-filling fluids, and matrix density, or ρ_{ma} , is density of the rock portion only. Porosity is a function of rock bulk density and the contributing components of rock and the drilling and formation fluids occupying the pore space that is present. If a formation has hydrocarbons in its interstices, or pore spaces, the density log and the sonic log will show lower values. Hydrocarbons are less dense than salt water and formation fluid (Asquith and Krygowski, 2004). A good analogy for this is to visualize oil floating on water.

$$\% \text{ solid space} = (\rho_b / \rho_{ma}) \times 100$$

Equation 5.5: % Solid Space

$$\Phi = 100 - (\% \text{ solid space})$$

Equation 5.6: Porosity Φ

In a dense formation, fewer electrons reach the detector, and in a less dense formation, more electrons reach the detector. High density has a low count, and low density has a high count, which increases logarithmically. Another type of scattering, called photoelectric absorption is used to generate the Pe log, which is handy to delineate carbonates from clastics. The continuous density log can be combined with a sonic log to create an acoustic impedance log, which is used to model a seismic response. When combined with a neutron log, it can be used to assess potential source rock organic matter. The “Delta log R” method is described in Section 5.4.7 and Figure 5.14.

5.4.5 Neutron Logs

Neutron logs measure neutron count rates, as neutrons are shot into a formation. Neutron porosity units are measured and indicate the formation hydrogen richness. If hydrogen is present in the formation, usually as water, the neutron log will thus give a measure of the amount of porosity that is present (Rider and Kennedy, 2011). This contrasts with density logs that measure a formations bulk density. By using two logs to calculate porosity, the results will be more accurate, for example neutron and density, neutron and sonic, or density and sonic can be used. With three logs, neutron, density and sonic can be used together.

5.4.6 Neutron – Density Logs

The figure bellow shows combinations of logs used together to determine lithology, oil, gas and/or water content.

Table 5.2: *This shows the lithology types and their typical response in three main wireline logs (Krygowski, 2003).*

Responses

<i>Lithology</i>	<i>Porosity</i>	<i>Neutron-Density response</i>	<i>Pe response</i>
Shale	--	Neutron greater than Density by some variable amount depending on the shale composition and depth.	Variable, but about 3.
Limestone	0.05	Neutron and Density values overlay.	About 5.
Limestone	0.15	Neutron and Density values overlay.	About 5.
Dolomite	0.10	Neutron values greater than Density by 12 to 14 porosity units (0.12 to 0.14).	About 3.
Shale	--	<i>As described in the Shale section above.</i>	<i>As above.</i>
Sandstone	0.26	Neutron values less than Density ("crossover") by 6 to 8 porosity units.	2 or slightly less.
Sandstone	0.05	Neutron values less than Density ("crossover") by 6 to 8 porosity units.	2 or slightly less.
Anhydrite	--	Neutron porosity greater than Density by 14 porosity units or more. Neutron porosity near zero.	About 5.
Shale	--	<i>As described in the Shale section above.</i>	<i>As above.</i>
Salt	--	Neutron porosity slightly negative. Density porosity >40 porosity units (bulk density near 2.0). Check the caliper for bad hole and bad density data.	About 4.7.
Shale	--	<i>As described in the Shale section above.</i>	<i>As above.</i>
Coal	--	Responses variable depending on coal composition. High Neutron and Density porosities (low bulk density).	Less than 1.
Shale	--	<i>As described in the Shale section above.</i>	<i>As above.</i>
Limy Dolomite	0.10	Variable response with lithologic mix, but Neutron generally greater than Density.	3 to 5.
Sandy Limestone	0.10	Variable response with lithologic mix, but Neutron generally less than Density.	2 to 3.
Dolomitic Sand	0.10	Highly variable, with Neutron greater or less than Density, depending on the lithologic mix.	2 to 5.
Shale	--	<i>As described in the Shale section above.</i>	<i>As above.</i>

5.4.7 "Delta Log R" Method of Analysis

The resistivity log can provide information on the degree of maturation of organic matter. If the source rock is immature there is no diagnostic signature, but if the organic matter is mature, the resistivity will increase significantly (Rider and Kennedy, 2011).

The Δ Log R process (Passey, 1990) can be used to determine organic richness of an interval. The method requires knowledge of two log types, the sonic (or acoustic) log which measures porosity, and the resistivity log which measures electrical resistance.

To use the Δ Log R method, a shale baseline is created, whereby the interpreter chooses a value on both the resistivity and the sonic logs, which best represents the average value for the shales over an interval in a well. This can be done by superimposing the sonic and resistivity log readings over each other as they pass

through a non-organic shale. The 5080-5140 feet interval in the South Venture O-59 well will serve as an illustrative example (Figure. 5.14). If the rock is in the oil window, meaning that it has been subjected to sufficient burial depth, time, and temperature to produce hydrocarbons from the total organic carbon available, the log resistivity will show an increase in hydrocarbon concentrations above background values. At the same time, the sonic log will show a decrease in transit time (meaning an increase in porosity) with increasing concentrations of hydrocarbons when compared to the baseline established in a nearby non-hydrocarbon-bearing shale. The result is the sonic decreases (AC line moves to the left) and the resistivity increases (ILD – Induction Log Deep – line moves to the right). The cross-over area in red highlights the hydrocarbon response.

The hydrocarbon response signature is seen for both the hydrocarbon-rich source beds and in reservoir rock currently containing hydrocarbon concentrations. By combining the crossover method with existing lithology logs and referring to the gamma ray response, the source rocks can be separated from the reservoir units. In Figure 5.14, the gamma ray moves left in clean sandstones between 5000 and 5030 metres thus indicating there is a hydrocarbon-bearing sand reservoir. Shales that show the hydrocarbon response, as from 4870-4930 m, can be interpreted as source rock.

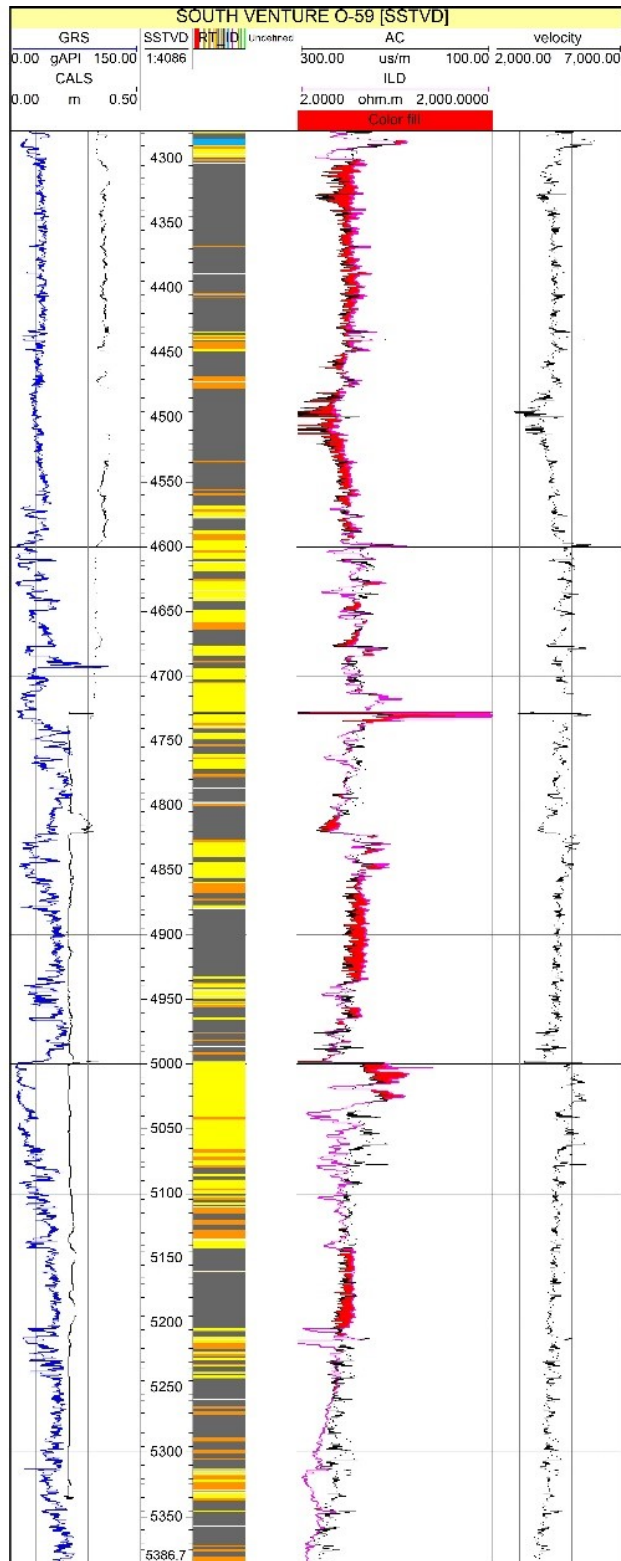


Figure 5.14: An example the Delta Log R method for determining the organic richness of a sandstone and shale succession, South Venture O-59. The Delta Log R method highlights the areas containing hydrocarbons (red), with the shale portion, (e.g. 5150-5200 m) indicating source rocks, and the sand components (e.g. 5000-5030 m) indicate reservoirs. Note that the Sonic is labelled "AC" and Resistivity "ILD".

5.5 Mapping in Petrel™

Petrel™ software, courtesy of Schlumberger, was used to map the datasets for this study. Data from the Canstrat™ LAS 2.0 files were used to create contour maps of the lithology and associated attributes as logged by Canstrat™. Temperature and TOC data are from the NRCan BASIN database and data obtained from wireline logs were mapped in Petrel™ generally as quality assurance maps and used algorithms based on kriging. Following is a brief summary of the methodology and process.

5.5.1 Deterministic and Stochastic Algorithms

Sequential Gaussian simulation is an example of a stochastic algorithm based on kriging and was used in the formation of several of the maps presented in the next chapter. Kriging, or Gaussian process regression, is where interpolation of data uses covariances in the model, not splines, to smooth out differences between data points (Figures 5.15 and 5.16). It is said to give the best linear unbiased prediction of intermediate values. A kriging algorithm uses input data points with a location tag to solve a semi-variance equation with different lag distances. It then plots these points on a semi-variogram and fits various smooth curves to this plot. The software automatically applies quality criteria such as best fit. Then, various descriptive values are derived from the fitted curve, which can be input into further models. Systematically comparing various fits or various subsets of points can characterize and help with uncertainty (personal conversation with M. Hall-Beyer, 2019).

Quality assurance maps are created by Petrel™ using either deterministic or stochastic algorithms. One characteristic of deterministic kriging algorithms is that they will always give the same result with the same input data. On the positive side, it is simple to see why one cell was given a certain value, but on the negative side, if there is very little data, the algorithm will smooth out the values and the uncertainty in areas far from data points is difficult.

Stochastic algorithms, on the other hand, use a random element which is added to the input data, with the result that each time the algorithm is applied a different result

will be seen. This is more realistic, as it factors in variability, rather than applying a smooth even contour between data points.

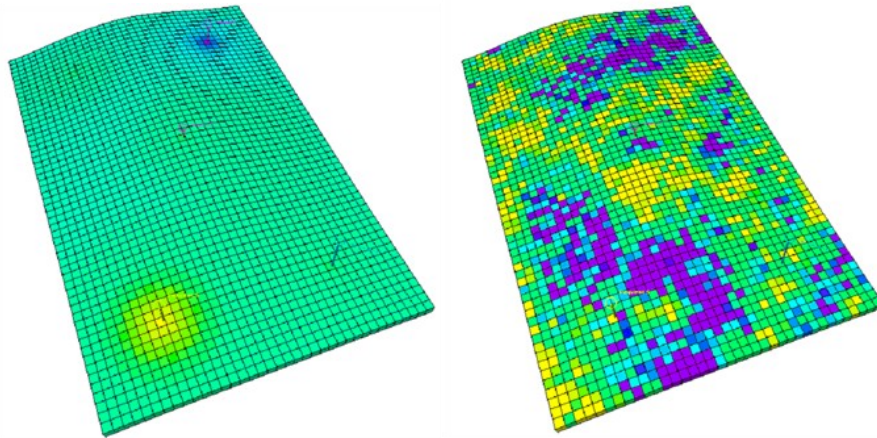


Figure 5.15: Differences between a deterministic algorithm and a stochastic algorithm, where random variability has been factored in. The left-hand grid shows an example of a deterministic algorithm, where the grid cells between the two known datapoints (the yellow and the blue) are evenly and smoothly contoured. The grid on the right is an example with the same two datapoints, but now exhibiting a stochastic algorithm; here, random variability has been factored in. The grid cells in between show variability and uncertainty, and although it is not known if it is 'correct' it stands to be a lot closer to reality than the left-hand grid (images courtesy of Petrel™ V.15 Help Guru).

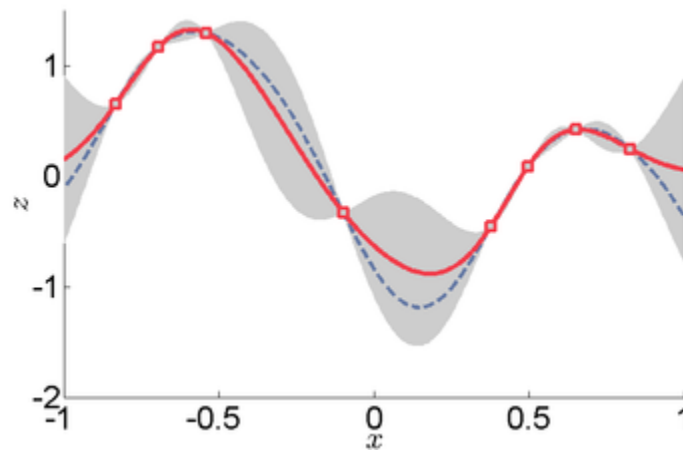


Figure 5.16: Illustrations showing the difference between a spline which smooths out the line between data points in a regular polynomial, and kriging (Gaussian process) which adds in a random seed to give possible outcomes that are seen in the greyed areas. Image courtesy of Petrel™ V.15 Help Guru.

Another Stochastic algorithm, truncated Gaussian simulation, is not chosen in this instance, as it should be used when one is mapping a sequence of facies with a natural transition, such as a progradational fluvial facies, or carbonate facies. Facies are input in

order of occurrence and will always be placed next to each other. In the lithology maps in Chapter 6, deposition systems are mixed and carbonate facies can occur in the fluvial setting, so the Sequential Gaussian simulation was chosen.

5.5.2 Facies Modeling and Petrophysical Modeling

Both facies modeling and petrophysical modeling algorithms can be either Stochastic or Deterministic. However, facies model input data will be discrete such as Constrat™-type lithodata and use sequential indicator simulation. Petrophysical modeling data will be continuous (as in wireline log data) and use the Sequential Gaussian simulation method. Quality assurance maps for discrete properties will be expressed as either thickness (in meters of rock formation) or proportion (percentage of interval or net-to-gross such as net sand/total reservoir thickness) maps of each facies or other discrete value, at each data point. Quality assurance maps for continuous properties will be either thickness of the rock interval with a certain property at a data point, or the average value or a property at each data point.

5.6 Temperature vs. Depth Plots

Temperature increases with depth down the borehole. The geothermal gradient is expressed in the formula:

$$G = \frac{T^{\circ}_{\text{formation}} - T^{\circ}_{\text{surface}}}{\text{Depth}}$$

Equation 5.7: *Geothermal gradient G*

where G is the geothermal gradient, $T^{\circ}_{\text{formation}}$ is the temperature in degrees Celsius of the formation, and $T^{\circ}_{\text{surface}}$ is the temperature in degrees C at surface, which can be either on land or on the sea bottom (Rider and Kennedy, 2011).

A factor affecting the geothermal gradient is the formation's ability to transmit heat, which is referred to as its thermal conductivity. Rocks with high thermal conductivity, such as salt, transmit heat quickly, and have a low thermal gradient, and

rocks with a low thermal gradient, such as shale and coal, transmit heat slowly and will have a high thermal gradient (Rider and Kennedy, 2011).

Other factors that affect the geothermal gradient are circulating fluids, heat flow, and heat produced by the formation itself. Circulating fluids can lower the geothermal gradient even if there is a high shale content, such as new sediments on the Gulf Coast. Heat flow values for a given area vary depending on the type of rock present. For example, in basement igneous rocks the heat flow values are normally higher than in sedimentary rocks due to a higher amount of radioactivity present.

Generally, eastern Canada has a thermal gradient of 22 °C per km, which is low compared to the North Sea with 34.6 °C/km or Western Canada with 31.8 °C/km (Nagihara and Smith, 2008; Rider and Kennedy, 2011).

Temperatures measured in the borehole reflect the mud temperature which is cooler than the formation temperature. Three or four months after drilling, the borehole temperature will reach equilibrium with the formation temperature (Benoit et al., 1980; Rider and Kennedy, 2011). Corrections are often applied to multiple bottom hole temperature (BHT) readings, where the BHT is plotted vs. $\Delta t/t + \Delta t$.

- Δt is the time measured in hours since circulation stopped or is the available time to reach an equilibrium temperature.
- t is the circulation time at TD before logging commenced, or the time that the formation was exposed to the cooler mud.

Temperature anomalies can be caused by sudden influx of formation fluid or hydrocarbons into the drilling mud. Formation fluid could cause a jump in temperature as it is warmer than the drilling mud. Conversely, a gas kick could cause lower (cooler) measurements as it expands and then cools as it enters the borehole. Lost circulation into fractures can also show cooler temperatures (Rider and Kennedy, 2011).

The BHT is useful for assessing a source rock's production potential (Rider and Kennedy, 2011). The time that a source rock is at a certain temperature range can indicate its source rock potential. A hydrocarbon generation curve is created by

extending temperature gradients from the present day back in time and combined with burial depth curves

5.7 Shale Analysis

Shale analysis is of interest in this study as it assists in defining source rock potential. Of particular interest is a shale volume analysis, as well as the amount of total organic carbon, which can be determined by a process called *Rock Eval Pyrolysis*.

5.7.1 Shale Volume Analysis

A contour map of the shale volume is useful. The shale volume is calculated as the percentage of shale content in the cuttings or the ratio of the total amount of shale to the total amount of sample.

5.7.2 Total Organic Carbon

Total organic carbon (TOC) refers to values determined from Rock Eval Pyrolysis tests performed on rock samples. TOC data used in this study were obtained from the online repository of publicly available data from Natural Resources Canada (BASIN database). Summary excel spreadsheets were provided by Paul Lake of the Geological Survey of Canada (NRCan).

5.7.2.1 Rock Eval Pyrolysis

Tests for total organic carbon, using Rock Eval Pyrolysis, are used to rate the potential of a rock to generate petroleum and to put a value on its thermal maturity (Peters, 1986). Compiling measurements of S₂ and total organic carbon and plotting these to calculate the regression equation aid in determining the true average hydrogen index, and measure the adsorption of hydrocarbon by the matrix of the rock, which also indicates the kerogen type (Langford and Blanc-Valleron, 1990). In this way the organic components of the samples are compared, and the potential of hydrocarbon generation can be stated (Langford and Blanc-Valleron, 1990). The resultant reports, called

pyrograms, should be run every 9-18 metres of a section (Peters, 1986), and used along with visual data noted from examining cores and cuttings.

To conduct the analysis, whole rock samples of up to 100 mg in weight are ground up and pyrolyzed at 300^o C for 3 to 4 minutes, after which the temperature is increased at a rate of 25^o C per minute to 550^o C in a helium atmosphere. Cooling follows, resulting in a total time of 20 minutes to analyze each sample (Peters, 1986). This can be done at the wellsite. Treating with acid to dissolve and remove carbonate from the rock sample and heating up to 1000^o C will allow the result to measure only organic carbon and avoid a skew in the data from carbon from carbonate rocks (Peters, 1986; Peters and Simoneit, 1982) and how carbonate carbon and organic carbon are different and how that is determined. Another problem encountered is that mature samples, which have a vitrinite reflectance (R_0) of > 1%, will result in poor TOC results because a T of 600^oC is not high enough to completely burn the sample (Peters, 1986). An overcooked rock with a high graphite content will show high TOC but no pyrolysis data (Peters, 1996).

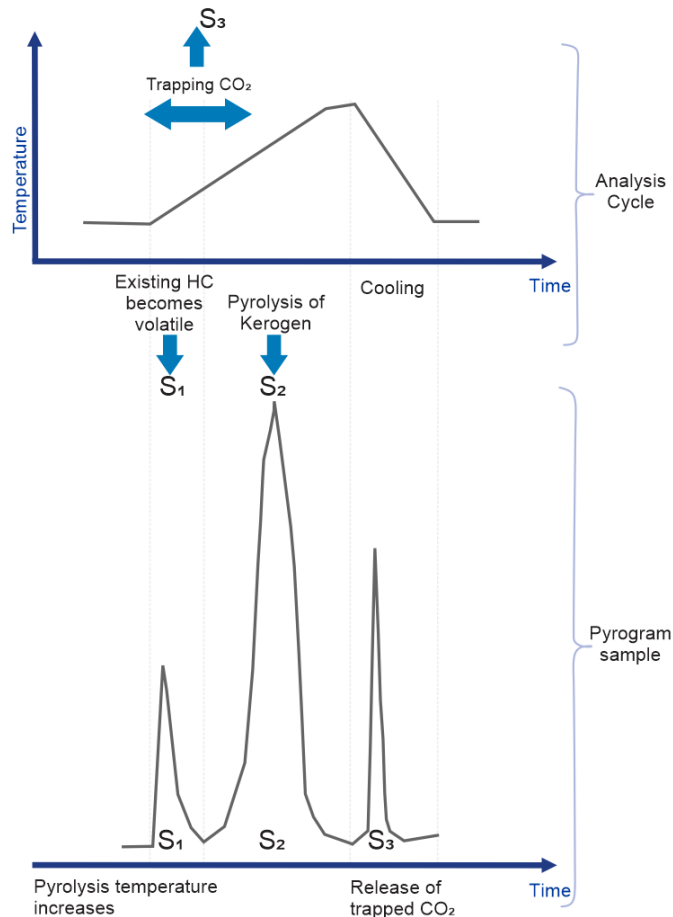


Figure 5.17: Pyrogram showing the change of organic compounds from the rock sample with increasing time and heat. Measurements found during pyrolysis are S1, S2, S3 and T_{max}. The Hydrogen Index and Oxygen Index are calculated (Equations 5.8 and 5.9). After Peters, 1986; AAPG/wiki.

A flame ionization detector (FID) will show results of three essential organic compounds that are generated during the analysis (Figure 6.21). S1 is seen on the first peak, which shows the mg of hydrocarbons which can be thermally distilled per 1 gram of rock. The second (most important) peak shows the S2 value, indicating the mg of hydrocarbons resulting from pyrolytic degradation of the kerogen present per 1 gram of rock (Langford and Blanc-Valleron, 1990). In this analysis, hydrocarbons are deemed any compound containing carbon. The S3 peak value shows the mg of CO₂ resulting from 1 gram of rock as the T moves to 390⁰ C and is determined by thermal conductivity detection or TCD (Peters, 1986).

T_{max} is measured as the temperature at which the greatest amount of hydrocarbons, as seen on the S2 curve, are produced. The HI (Hydrogen index) is

defined as the mg of hydrocarbons, or pyrolyzable organic compounds from the S2 curve compared to the TOC or total organic carbon found in the samples. $HI = (S2/TOC) \times 100$ or the mg of hydrocarbon/g organic carbon = mg HC/g C_{org}. The OI, or oxygen index, is the amount of CO₂ from the S3 curve compared to the TOC (or mg CO₂ / g C_{org}). The production index, or PI, is the ratio of S1 to (S1+S2) (Peters, 1986). Tables 5.3 and 5.4 indicate how TOC, S1, and HI can be used to describe a source rock.

$$HI = \text{Hydrogen Index} = (S2/TOC) \times 100$$

Equation 5.8: *Hydrogen Index*

$$OI = \text{Oxygen Index} = (S3/TOC) \times 100$$

Equation 5.9: *Oxygen Index*

$$PI = \text{Production Index} = S1/S1+S2$$

Equation 5.10: *Production Index*

Table 5.3: *Source rock generative potential using TOC, S1, and HI to describe the quality of a source rock (Peters, 1986).*

SOURCE ROCK Generative Potential

Quantity	TOC weight %	S1 mg HC/g rock	S2 mg HC/g rock
Poor	0 - .5	0 - .5	0 - 2.5
Fair	.5 - 1	.5 - 1	2.5 - 5
Good	1 - 2	1 - 2	5 - 10
Very Good	2+	2+	10+

(after Peters, 1986)

Table 5.4: Table of Hydrogen Index (HI) values and S2/S3 ratios generated from a pyrogram and the resulting hydrocarbon type (after Peters, 1986).

HYDROCARBONS generated from the PYROGRAM

TYPE	HI mg HC/g C _{org}	S2/S3*
Gas	0 - 150	0 - 3
Gas and Oil	150 - 300	3 - 5
Oil	300 +	5+

(after Peters, 1986)

*assumes R₀ = 0.6%

Determining S2 can be come complicated if the matrix retains some of the generated hydrocarbons so that the HI will not show the true ratio of pyrolizable hydrocarbons to organic carbon, and so a correction must be applied (Langford and Blanc-Valleron, 1990).

Table 5.5: Thermal Maturation determination using results from the Pyrogram that can be used to delineate the top and bottom of the oil window in a formation (after Peters, 1986).

THERMAL MATURATION

MATURATION	PI {S1/(S1+S2)}	T _{max} (°C)	R _o (%)
TOP oil window	~ 0.1	~435 - 445*	~0.6
BOTTOM oil window	~0.4	~470	~1.4

(after Peters, 1986)

* T_{max} depends on type of organic matter

Coals show high S2/S3 ratios of >5 and low HI (Hydrogen Index) values of less than 300 mg HC/g TOC. Rock Eval data will be inaccurate if migrated oil and drilling mud additives are present (Peters, 1986). In thermally immature rocks, bimodal S2 peaks and PI values > 0.2 are an indication of contaminated samples (Peters, 1986).

Additional analyses of results include the mapping of regional thermal maturity and the richness of source rocks are useful, as are cross sections showing the correlation

of reservoirs or source rocks between wells. It helps identify regions in a basin where it is likely that petroleum accumulations will be found (Peters, 1986).

5.8 Cross Sections from Formation Tops Picks

5.8.1 Cross Sections from Wireline Log Formation Top Picks

Wireline logs were correlated in Petrel™ along the top and base of the Naskapi Member. Nine cross sections were constructed throughout the study area with the Naskapi horizon tops picked lithostratigraphically giving a two-dimensional view of the subsurface.

Appendix A lists the Canstrat™ wells used in this study. Of 103 wells in the study area, 99 were included in the cross sections which trend from approximately north to south and include all wells with reliable wireline and lithology log data through the Naskapi Member. Appendix H shows maps detailing the location of each section and lists the wells included.

Cross sections were constructed throughout the study area in order to interpret and correlate the top and base of the Naskapi horizon. Wireline logs were correlated in Petrel™ where the Naskapi horizon tops were picked lithostratigraphically. They serve to visualize the subsurface in a two-dimensional view. The picks from the BASIN database were used as a starting point and refined to identify which parts of the wireline logs, Canstrat™ logs and the BASIN database analytical data fell within the Naskapi Member. These refined picks were used to model, map, and interpret the changes in the unit's deposition.

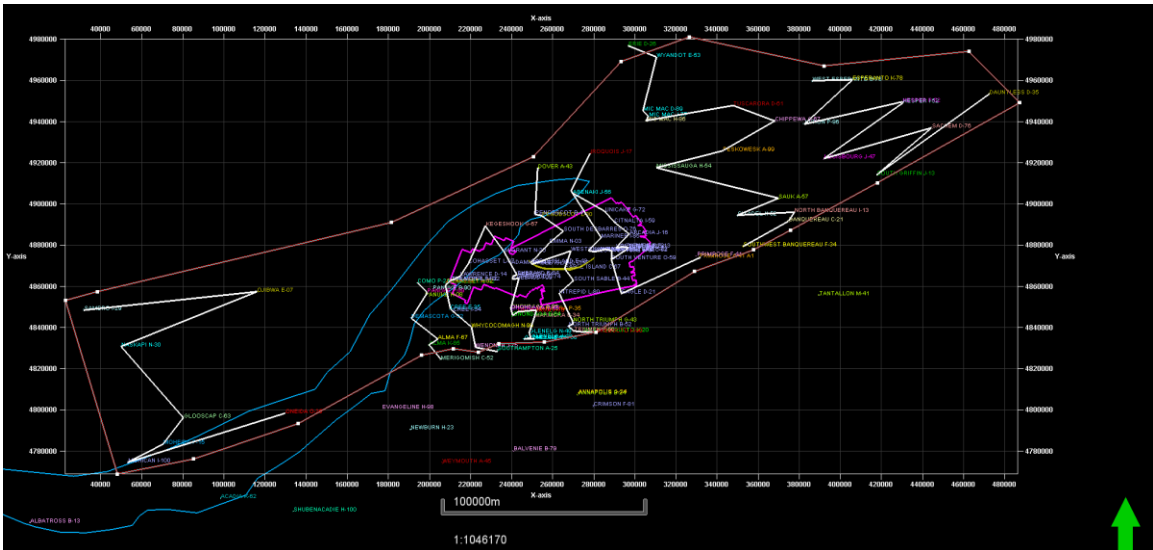


Figure 5.18: Schematic map of the cross sections and locations used in the study. The white lines show the cross sections, and the blue line shows the location of the Abenaki Bank. The pink outlines the location of the MegaMerge 3D cube. The yellow crescent shape is Sable Island.

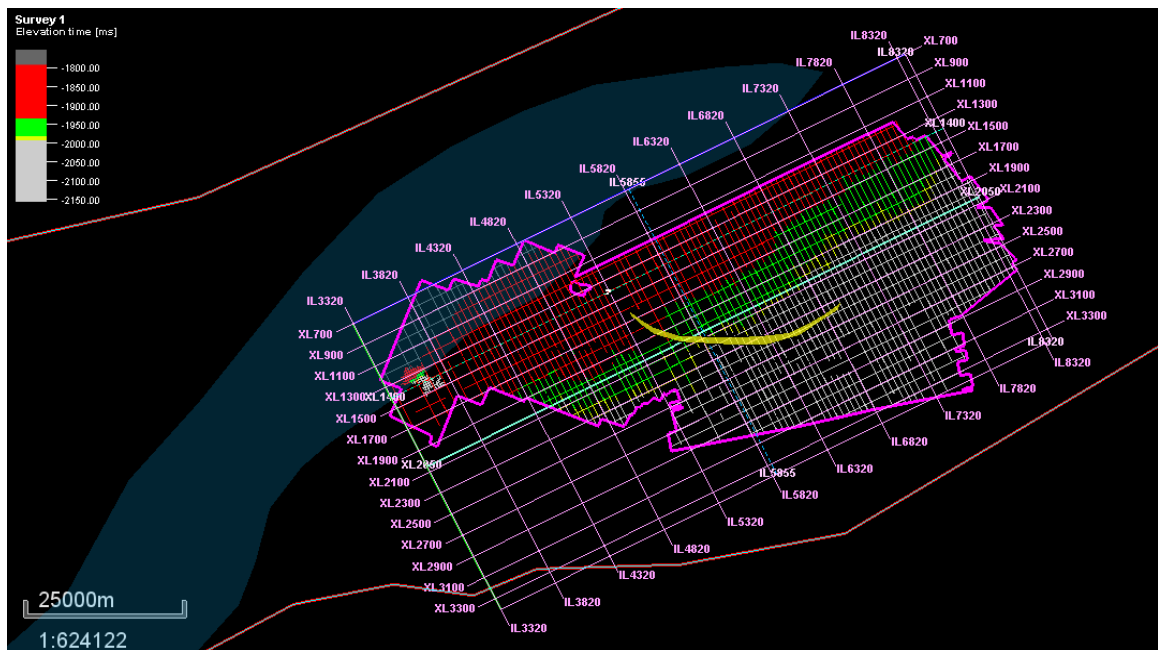


Figure 5.19: Plan view of MegaMerge Cube with a pink outline, and the layout of the seismic lines used in creating 2D and 3D maps of the Naskapi Member and Missisauga Formation tops. Sable Island is indicated by the yellow crescent shape in the middle of the figure.

5.9 Seismic Interpretation

Seismic reflection exploration, or the study of the subsurface using sound wave reflections, is used in petroleum exploration (Denham, 1984). Seismic processing serves to manipulate the raw data to make it easier to interpret and seismic interpretation is

the result of comparing the exact mathematics of seismic data processing with incomplete geological data and known geological principles of the subsurface study area (Denham, 1984).

An acoustic energy source is deployed on the earth's surface or near to it, in the case of offshore studies. Compressional elastic P waves are reflected from the interfaces between rock layers with differing elastic properties. Geophones receive these reflections at equal intervals along a seismic line or line of survey. By using the time required for a wave to travel from the surface to the interface and back to the receiver, if the velocity wave is known, the depth of the interface can be calculated. Seismic interpretation analyzes the results after processing, with respect to the geology of the subsurface (Schlumberger, 2015).

The 3D seismic MegaMerge cube was made available to the Basin and Reservoir Lab at the Dalhousie Department of Earth Science courtesy of ExxonMobil. A total of 500 inline and 270 cross line seismic sections were interpreted at 50 metre increments, which can be seen in Figure 5.19. Petrophysical wells were tied to the seismic sections by loading checkshot data where log data was converted to time data and effectively tied to seismic two-way time (TWT). The tops picks of the Naskapi Member and underlying Missisauga Formation were then recognizable and picked along the seismic lines and mapped in Petrel™.

Chapter 6: Results

The following data sets were used in the study as noted in Chapter 5.

- Public domain wireline log data.
- Canstrat™ digital lithology data.
- Geochemical, maturation, and temperature from the Natural Resources Canada (NRCan) BASIN online data base.
- Drilling data, formation tops, pressures, test results, biostratigraphy similarly available in the Natural Resources Canada (NRCan) BASIN online data base.
- Well reports and wireline log PDFs and LAS-format files publicly available from the Canada-Nova Scotia Offshore Petroleum Board's online Data Management Centre (CNSOPB-DMC).
- 3D seismic data (proprietary ExxonMobil Sable MegaMerge seismic cube).

Accordingly, from these data, the following were created and are presented as results:

1. Nine cross sections running approximately north to south extending across the study area polygon outlining the area of interest from east to west (location maps Figure 5.18 and Appendices H and J).
2. 3D surfaces of the top Naskapi Member and top Missisauga Formation.
3. Maps displaying total organic carbon (TOC), vitrinite reflectance (VR), and temperature.
4. Maps displaying lithological attributes.
5. Maps displaying petrophysical log data.
6. Contour maps of the Naskapi and Missisauga surfaces interpreted from the MegaMerge seismic cube.

6.1 Introduction

Maps were created for the Naskapi interval showing main lithology (deterministic and stochastic), limestone content, shale content, shale proportion to total lithology, sand content, siderite content, marlstone, clay, fossil debris, mineral content, colour, green proportion, red proportion, green shale, calcite cement content,

oil stain (good, medium, questionable), visual porosity from 3 – 33% (specifically 3 – 6%, 7 – 9%, 10 – 12%, 13 – 15%, 16 – 20%) and the maximum possible, approximately 33%, and the sum total.

Continuous log maps from wireline log data were created of the values from density, resistivity, gamma ray, and sonic logs, and maps in the Petrel™ quality assurance format of thickness or proportion of the previously mentioned logs, as well as shale volume (V_{shale}) using the gamma ray log. Using the Delta Log R Method, a table summarizing organic-rich intervals in the Naskapi was made.

3D models of velocity and sonic data were made, with slices showing the position of anomalous data, particularly in the sonic.

The 3D seismic MegaMerge cube was interpreted to show the extent of the Naskapi top and bottom, with the bottom pick being equivalent to the top of the Missisauga formation. 500 inline and 270 cross lines seismic sections were interpreted at 50-meter increments. Maps were made of the Naskapi and Missisauga horizon tops. A 3D map was made of the thickness of the Naskapi Member.

Sedimentation rates of the Naskapi, and cycles of parasequences were postulated. A table listing Cretaceous oceanic anoxic events and organic-rich deposits largely from the proto-Atlantic was compiled. Models of paleo-ocean currents during the Cretaceous were compared to the occurrence of these deposits.

6.2 Cross Sections

The cross sections were created in Petrel™ and incorporated lithology, Canstrat™ logs, gamma ray logs, sonic logs, and resistivity logs. The nine cross sections which were constructed are shown in Appendix H and run from a northerly to southerly direction. Wells with salt domes (Cree I-34, Primrose A-41 A1, and Primrose F-41) were not used because when the Naskapi was deposited, the salt structures were not yet present. Wells in the northeast of the study area without Naskapi shales were not used, (Adventure F-80, Argo F-38, Crow F-52, Eurydice P-36, Fox I-22, Jason C-20 and Hercules G-15).

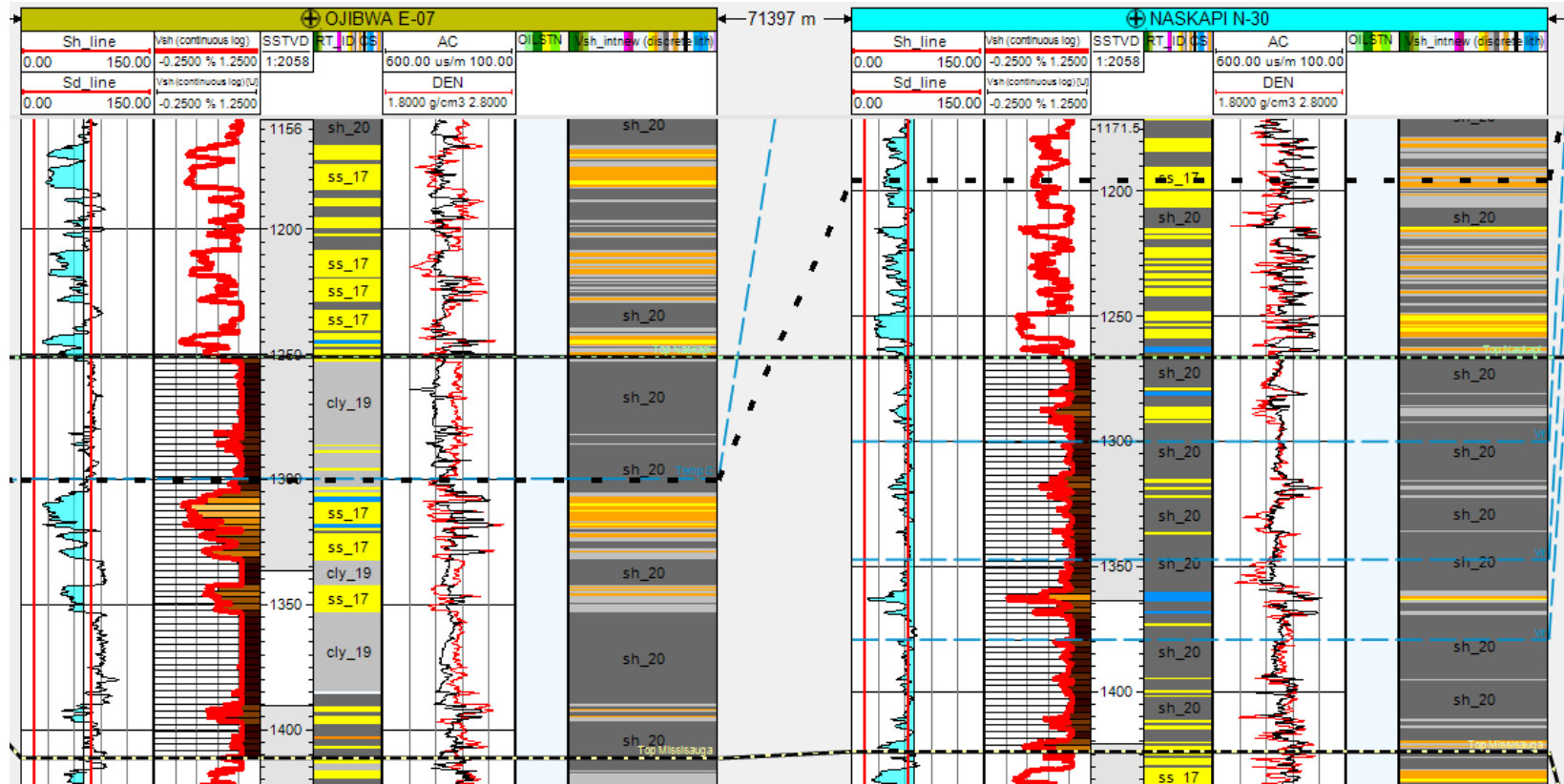


Figure 6.1: Cross section sample through wells Ojibwa E-07 and Naskapi N-30. The cross sections are found in Appendix J.

6.3 Maps (2D and 3D) of the Naskapi Member and the Missisauga Formation

Regional compilation maps of the depths of the Naskapi Member and the Missisauga Formation as determined from the cross sections were made in Petrel™ and are listed in Appendix B.

6.3.1 2D Structure Contour Maps

Structure maps were made in Petrel™ by using horizon tops of the Naskapi Member and Missisauga Formation as determined from cross section picks (See Figure 6.2 and 6.3). Figure 6.2 shows the depth of the top of the Naskapi increasing from 1100 metres landward to 3250 - 3750 metres basinward. Figure 6.3 indicates the depth of the Missisauga extending from about 1250 metres landward, to 3250 – 4000 metres basinward.

6.3.2 3D Maps

The 3D models (Figure 6.4 and 6.5) demonstrate the dip of the formations towards the two notable depressions in the south, near the North Triumph and Chebucto wells, and near the Southwest Banquereau F-34 well.

6.3.3 Isochore Map of Naskapi Vertical Thickness

An isochore map show lines of equal vertical thickness of an interval. The isochore map (Figure 6.6) of the thickness of the Naskapi Member in 2D shows the thickest areas are near the Glooscap, Glenelg, North Triumph and Banquereau wells. The thinnest Naskapi deposit in the study area is just to the northeast of the Sable Delta north of the West Esperanto well.

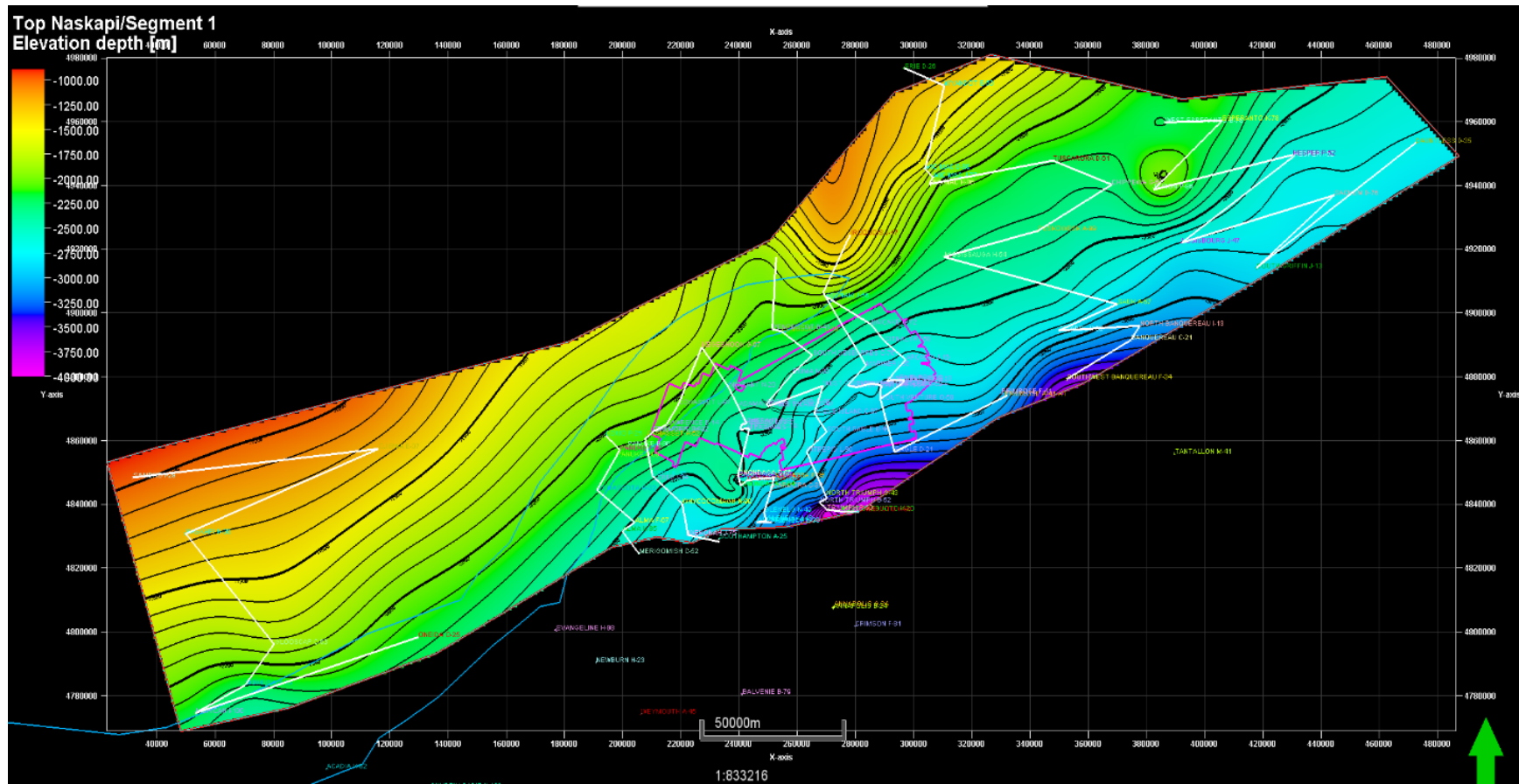


Figure 6.2: Contour map of the top of the Naskapi Member, from lithostratigraphic picks from the cross section of gamma ray, density, sonic and resistivity logs. The Naskapi Member dips deeper basinward. The purple outline shows the location of the MegaMerge seismic cube.

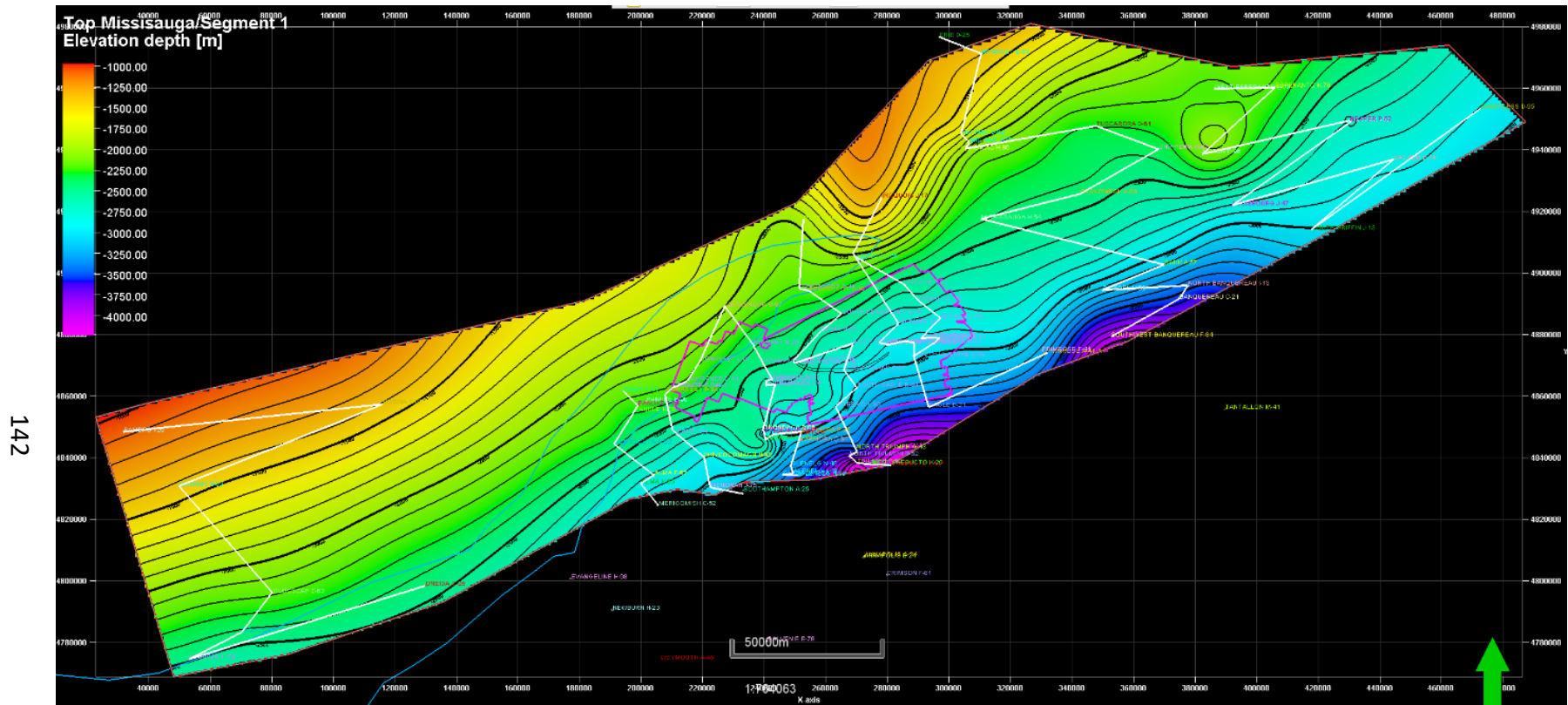


Figure 6.3: Contour map of the top of the Missisauga Formation, from lithostratigraphic picks from the cross section of gamma ray, density, sonic and resistivity logs. The top of the Missisauga dips deeper basinward. The purple outline shows the location of the MegaMerge seismic cube.

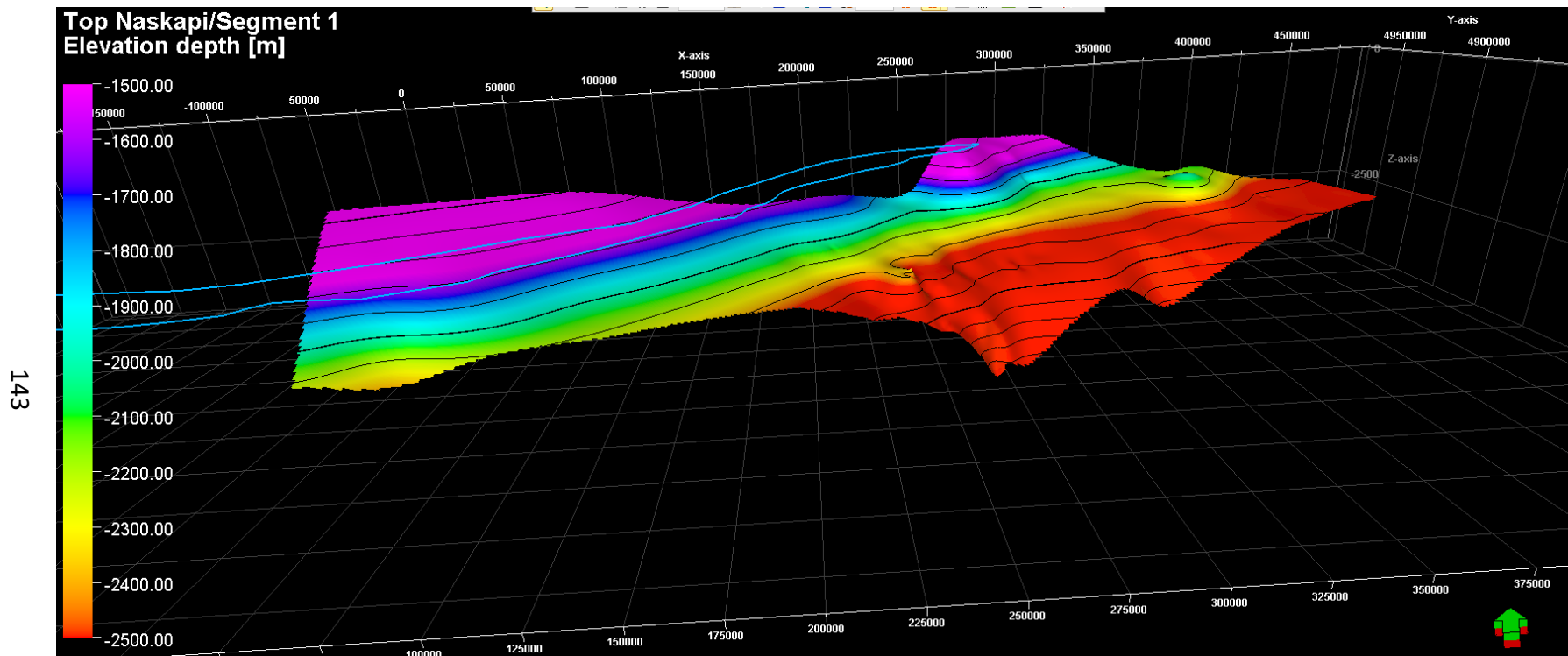


Figure 6.4: 3D model of the top of the Naskapi Member (TVDss m). The depth increases basinward changing from a 1500 metres depth landward to 2900 metres depth basinward in the southeast of the study area. The outlined blue line shows the position of the Abenaki Carbonate Bank.

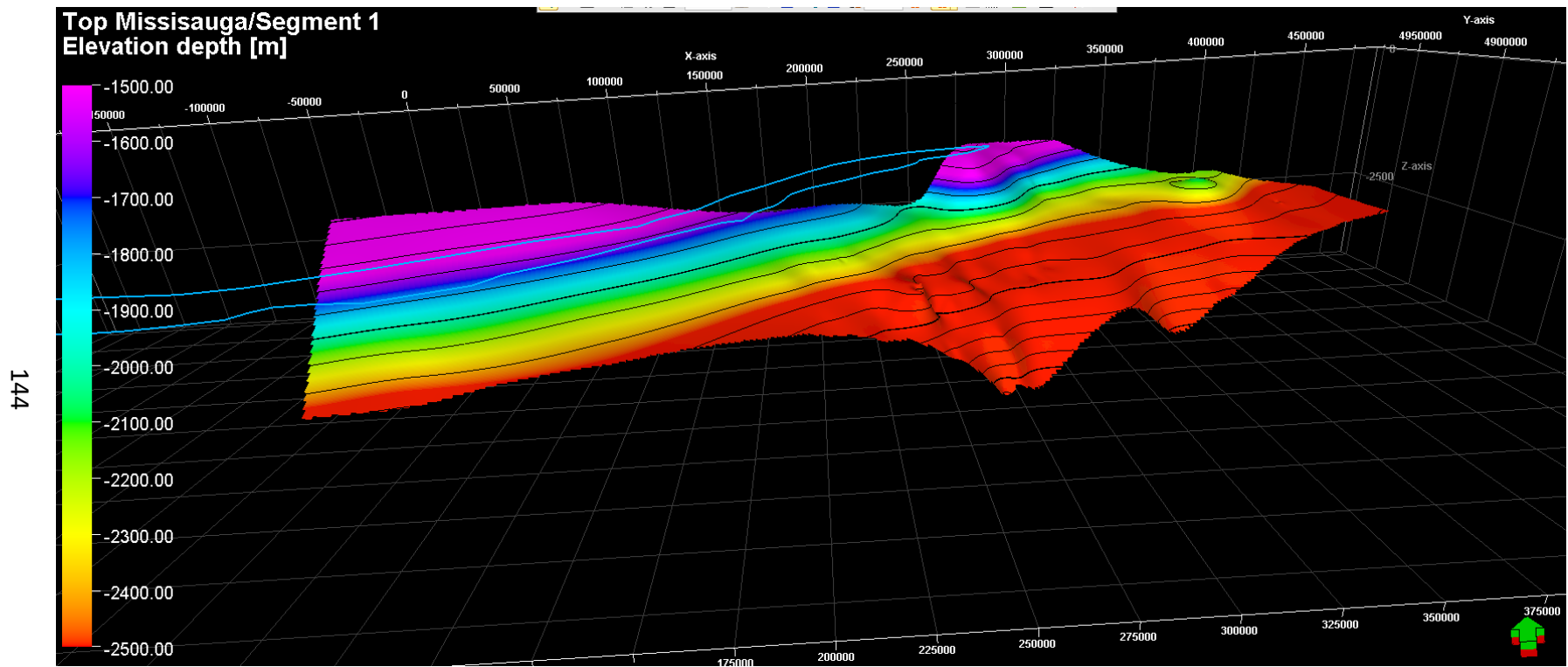


Figure 6.5: This figure shows a 3D model of the depth of the Missisauga Formation (TVDss m), at approximately 1500 m depth landward, extending to a 3600 m depth basinward in the southeast of the study area. The outlined blue line shows the position of the Abenaki Carbonate Bank.

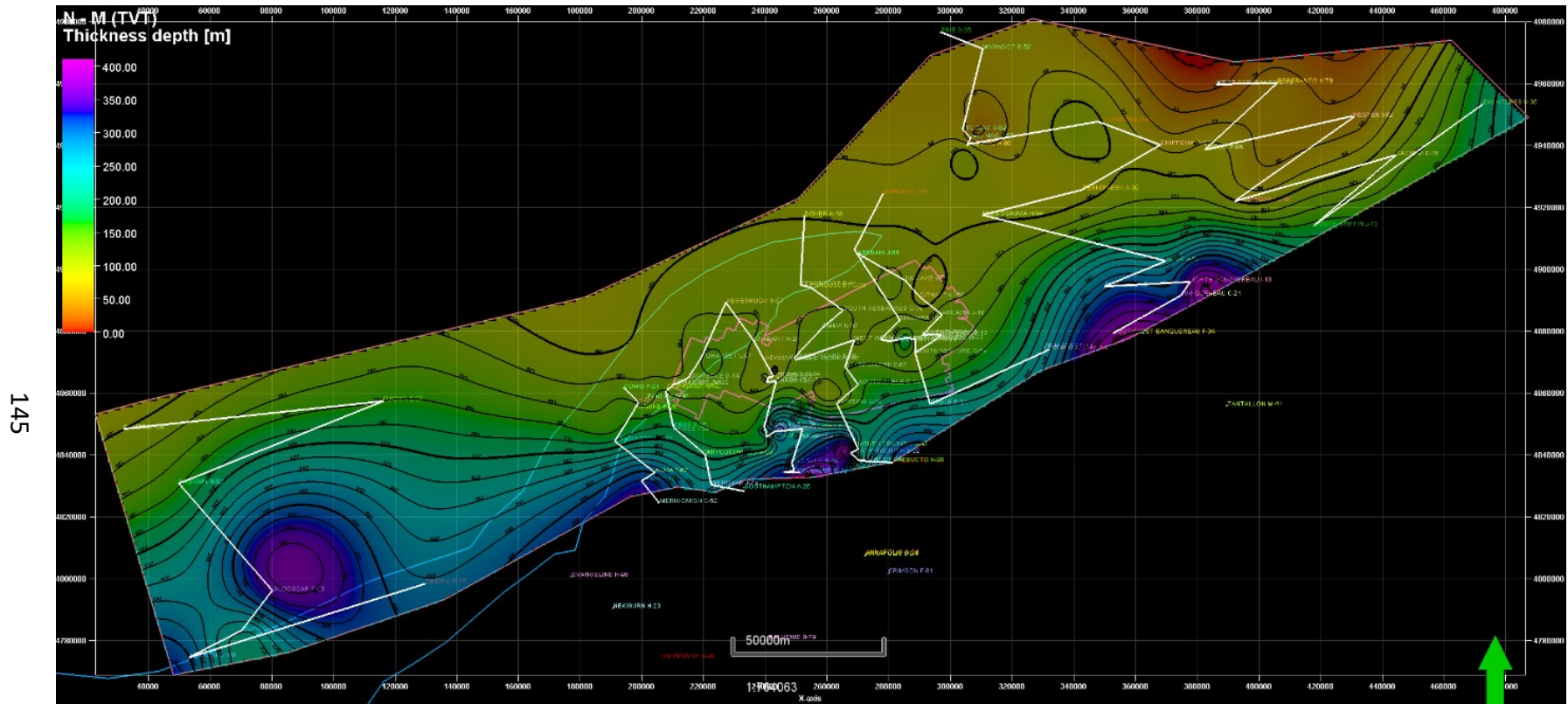


Figure 6.6: Isochore map showing the thickness of the Naskapi Member. It thickens basinward, with the thickest section near the Glooscap, Glenelg, North Triumph and Banquereau wells. The thinnest region is in the northeast near the Sable Delta. The thicker regions in dark blue and purple are localized depocentres with more accommodation space.

6.4 NRCAN BASIN Data Maps

6.4.1 Total Organic Carbon (TOC) Map from Rock Eval Pyrolysis

Data

Data were downloaded from the Natural Resources Canada BASIN Database http://basin.gdr.nrcan.gc.ca/index_e.php available by searching under Wells > Scotian Shelf > Well Name > Geochem > Rock Eval Pyrolysis, and found in the organic carbon column, and plotted in Petrel™. Data used was restricted to the Naskapi Member intervals as defined from the cross sections used in this study. Of the 105 wells in the study area, 37 had total organic carbon values in the Naskapi. Some wells had multiple Rock Eval Pyrolysis studies conducted, in which case the results per depth interval were averaged (see Figure 6.7). The data used are displayed in Appendix G.

The highest amount of TOC occurs in the green-to-yellow-to-red-coloured areas, which are towards the west near the Naskapi N-30 and Mohican I-100 wells, and in the vicinity of the Abenaki J-56, Cree E-35, Southampton A-25, Sauk A-57, Banquereau C-21, and the Panuke and Glenelg wells. The well with the lowest TOC was Kegeshook G-67.

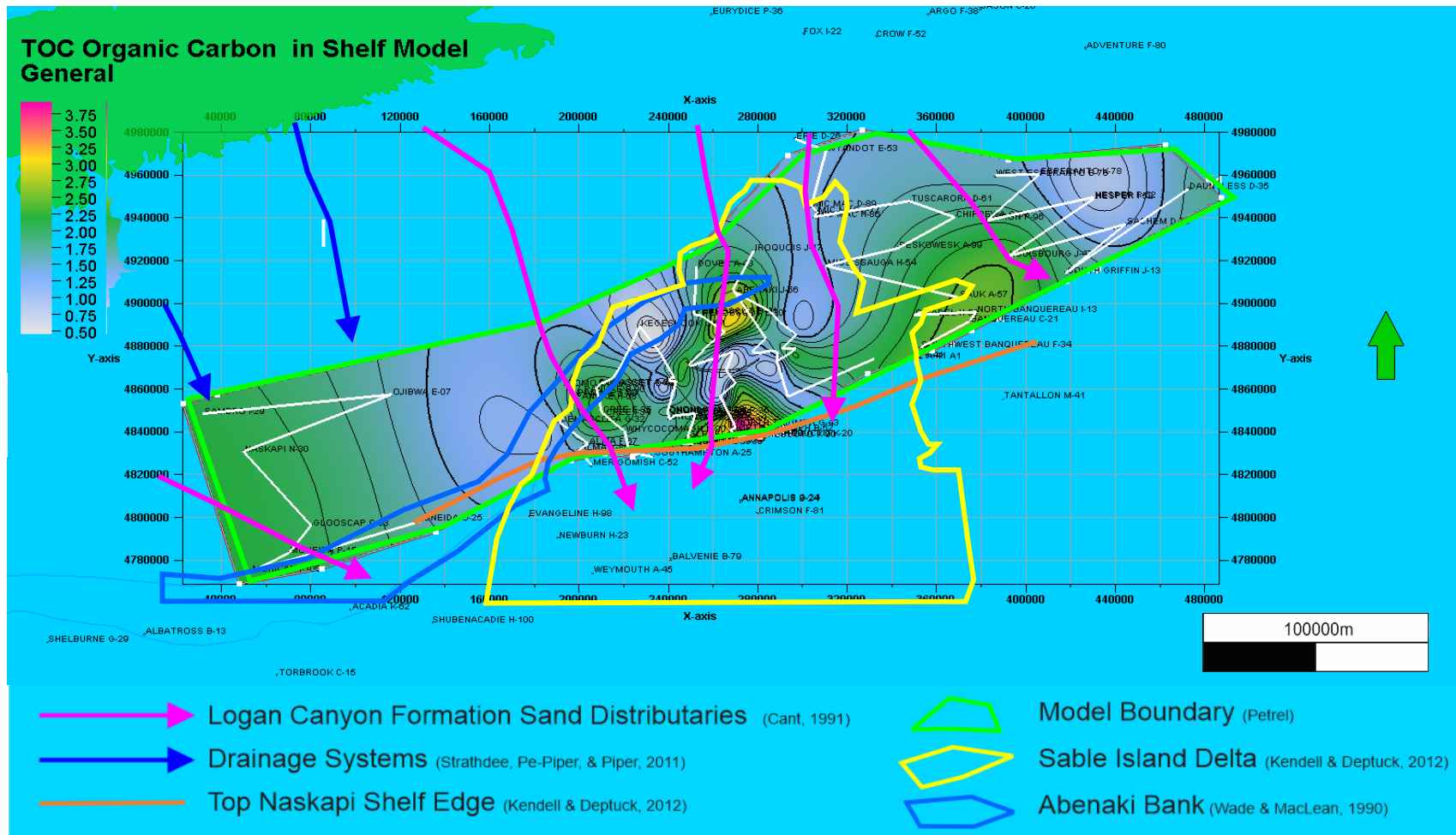


Figure 6.7: Total organic carbon values as determined by GSC data in the Basin Database http://basin.gdr.nrcan.gc.ca/index_e.php limited to the Shelf Model polygon. The highest amount of TOC occurs in the aquamarine-coloured areas, which are towards the west near the Naskapi N-30 and Mohican I-100 wells, and in the vicinity of the Abenaki J-56, Cree E-35, Southampton A-25, Sauk A-57, Banquereau C-21, and the Panuke and Glenelg wells. The well with the lowest TOC was Kegeshook G-67. Perhaps these depocenters with higher TOC could have been smaller subbasins that were confined to some extent during their time of deposition.

6.4.2 Vitrinite Reflectance Map

Data were downloaded from the Natural Resources Canada BASIN Database http://basin.gdr.nrcan.gc.ca/index_e.php and found by searching under Wells > Scotian Shelf > Well Name > Maturity > Well Name > Live Well Name and found in the vitrinite column. Of the 105 wells in the study area, 57 wells had vitrinite reflectance values from the Naskapi intervals as determined from cross-section analysis (Appendix I) that were mapped (see Figure 6.8).

The peak vitrinite reflectance values occur near Southwest Banquereau F-34 and south, as well near Venture B-43. Elevated vitrinite reflectance is seen towards the Naskapi N-30 and Sambro I-29 and the Como P-21 wells on the Naskapi Ridge, and extending from Merigomish C-52, Southampton A-25 and the Triumph wells northeast to Griffin J-13 and Hesper I-52. Low values are near Mohican I-100, Demascota G-32, Penobscot B-41 and L-30, and South Desbarres O-76. Higher vitrinite reflectance measures the thermal maturity of a rock and indicates if the rock could have generated hydrocarbons or could be a source rock. A higher vitrinite reflectance value would indicate that the area had been subjected to higher temperature

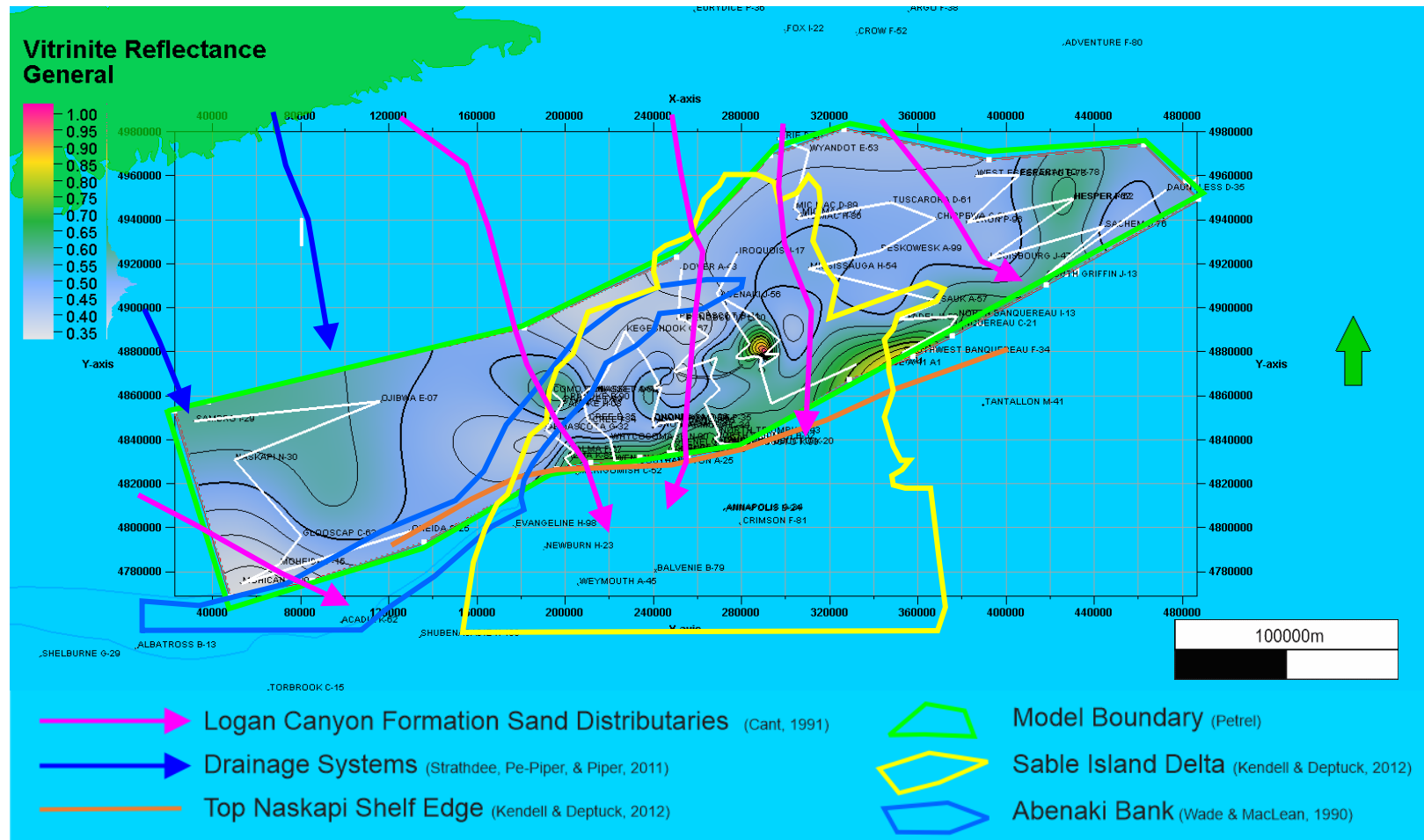


Figure 6.8: Vitrinite reflectance values as determined by GSC data in the Basin Database http://basin.gdr.nrcan.gc.ca/index_e.php. The peak vitrinite reflectance values occur near Southwest Banquereau F-34 and south, as well near Venture B-43. Elevated vitrinite reflectance is seen towards the Naskapi N-30 and Sambre I-29 and the Como P-21 wells on the Naskapi Ridge, and extending from Merigomish C-52, Southampton A-25 and the Triumph wells northeast to South Griffin J-13 and Hesper I-52. Low values are near Mohican I-100, Demascota G-32, Penobscot B-41 and L-30, and Desbarres O-76 wells. Vitrinite reflectance measures the thermal maturity of a rock. Higher values indicate the generation of hydrocarbons within the oil and gas window.

6.4.3 Temperature Map

Data were downloaded from the Natural Resources Canada BASIN Database http://basin.gdr.nrcan.gc.ca/index_e.php and found by searching under Wells > Scotian Shelf > Well Name > Temperature > Well Name > and found in the temperature column. Data used are displayed in Appendix F. Of the 105 wells in the study area, 38 wells had temperature data, but only eight were available with DST temperature data to plot. Log temperature data was not used as those temperatures are generally cooler than the surrounding formation waters. DST temperature readings are more reliable as the drilling muds have had time to normalize with the surrounding formation waters. Peak temperature values are seen in the region of the Chebucto and Triumph wells with temperature decreasing shoreward in an orderly fashion. The coolest regions are north of the Ojibwa E-07 and Sambro I-29 wells. Higher temperatures are also seen through the Sable Island and Citnalta well regions.

6.4.4 Comparison of Temperature and Vitrinite Reflectance Data

Vitrinite reflectance data shows peak values at Southwest Banquereau F-34 and Venture B-43, with mid values near Naskapi N-30, Sambro I-29, Como P-21, Merigomish C-52, Southampton A-25, Triumph P-50, South Griffin J-13, and the Hesper wells, and low values are near Mohican I-100, Demascota G-32, Penobscot B-41 and L-30, and South Desbarres O-76 wells. Temperature data, on the other hand shows peak values near the Chebucto and Triumph wells, with mid-range values near the Citnalta and Sable Island wells, with low values found at the Ojibwa E-07 and Sambro I-29 wells.

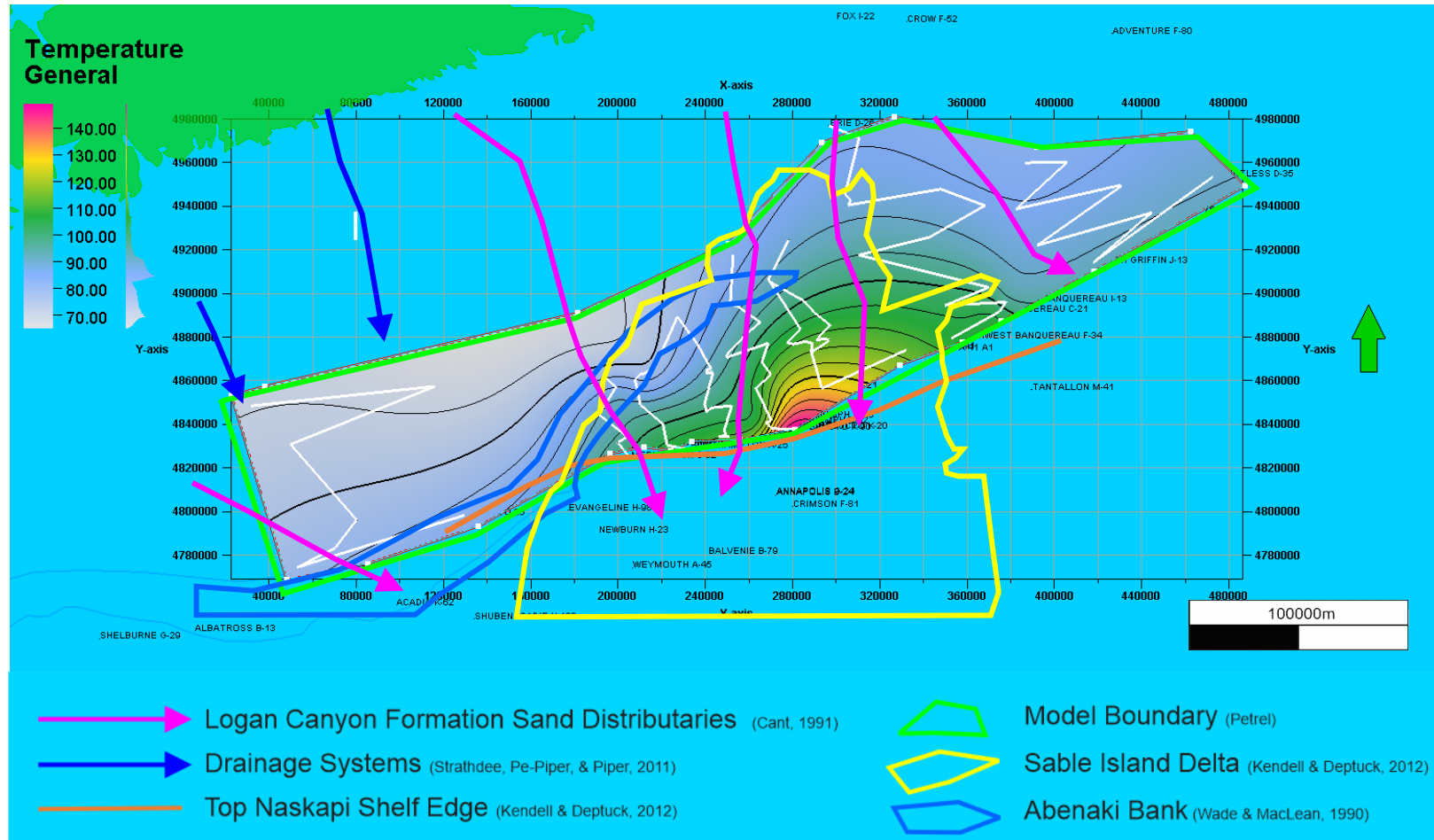


Figure 6.9: Temperature values from DST data as reported to the GSC in the Basin Database http://basin.gdr.nrcan.gc.ca/index_e.php. Peak temperature values are seen in the region of the Chebucto and Triumph fields with temperature decreasing landward, with the coolest regions being north of the Ojibwa E-07 and Sambro I-29 wells. Higher temperatures are also present in the Sable Island and Citnalta well regions. Of the 105 wells in the study area, 38 wells had temperature data, but only eight were available with DST temperature data to plot. Log temperature data was not used as those temperatures are generally cooler than the surrounding formation waters. DST temperature readings are more reliable as the drilling muds have had time to circulate and normalize with the surrounding formation waters.

6.5 Lithological Attribute Maps of the Naskapi Member

Lithological attribute maps were created from wireline and cuttings data for the study area. These maps demonstrate the lithological attributes of the Naskapi Member as logged by Canstrat™.

6.5.1 Dominant Lithology as Stochastic or Deterministic Models

The kriging method used in Petrel™ with the make/edit surface function uses a standard kriging interpolation method. Input data is precise and the program creates a modelled value of the data values where data is absent. Both facies model and petrophysical modeling algorithms can be either Stochastic or Deterministic.

Facies model input data such as Canstrat™-type lithodata is discrete and uses sequential indicator simulation, which is a type of stochastic interpolation. In this simulation, localized highs and lows are generated between the data points with their positions determined by a random number supplied by the software. Petrophysical modeling data such as wireline log data, is continuous (as opposed to discrete) and uses the sequential gaussian simulation method.

Quality assurance maps for discrete properties will use thickness (in meters of rock formation) or proportion (percentage of interval or net-to-gross e.g. net sand/total reservoir thickness) of each facies or discrete value at each data point. Quality assurance maps for continuous properties will use either thickness of the rock interval, or the average value of a certain property at each data point.

As covered in Section 5.5.1, stochastic algorithms use a random element added to the input data, with the result that each time the algorithm is applied, a different result will be seen. Stochastic trend maps help to highlight variability and uncertainty in the data. Figures 6.18 (sand), 6.19 (siltstone), 6.20 (siderite), 6.21 (marlstone), and 6.22 (clay), are made using stochastic algorithms and show the distribution of the dominant lithologies where they are greater than 50%.

To further illustrate this, Figures 6.10 and 6.11 show the difference between deterministic and stochastic algorithms. Figure 6.10 shows an example using a

deterministic algorithm, where the grid cells between the known datapoints (wells) are evenly and smoothly contoured. However, Figure 6.11 is mapped with the same datapoints (wells), but now uses a stochastic algorithm, where random variability has been factored in. The grid cells in between show variability and uncertainty, and although it is not known if it is 'correct' it stands to be a lot closer to reality than the first slide. Each time the map is generated it will be different as it will have a random 'seed' thrown in the algorithm unless otherwise specified (images made in Petrel™ V.15).

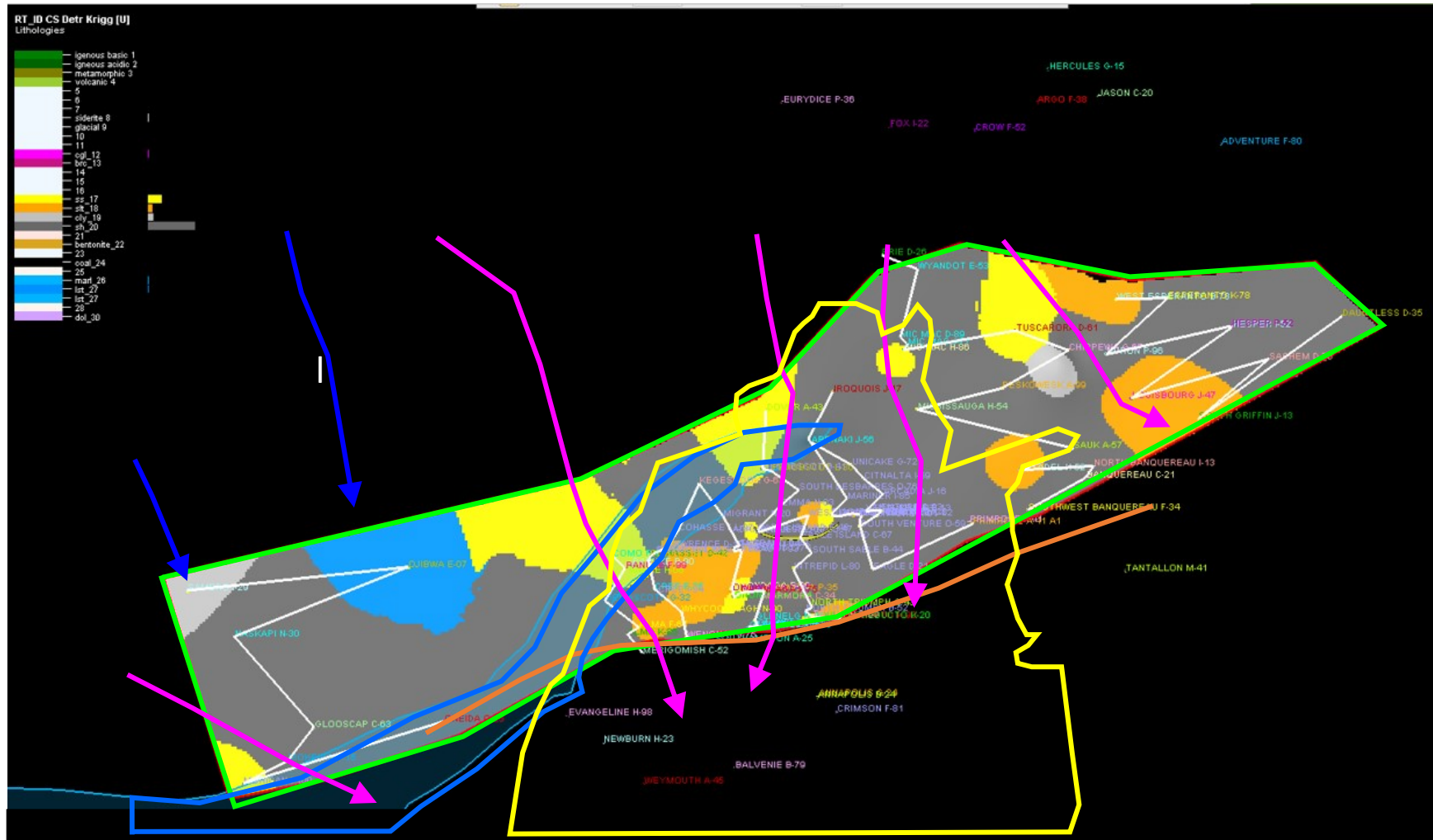


Figure 6.10: This map demonstrates using a deterministic algorithm, where the grid cells between the known datapoints (wells) are evenly and smoothly contoured. Although shale is most common, sands (yellow) are a common grain (>50%) in the Naskapi Member landward closer to delta mouths and silt grains are dominant further from the distributary mouths. Limestone is the dominant lithology in the blue area on the flank of the Abenaki Bank (shaded blue area).

6.5.2 Colour

Figure 6.12 displays colours as indicated by Canstrat™ descriptions from drill cuttings. The colours indicated in the legend display show on the map where that colour is dominant (>50%) for the Naskapi interval. Colours noted are white, cream buff tan, salt and pepper, varicoloured, orange, red, green, brown, and grey. The variation in colour could be due to the different provenance of various sediments with various mineral compositions. Different tributaries are sourced from different areas of the mainland.

Figure 6.12 shows a region of green colour in the Sable Delta area and perhaps indicates glauconite or green shale. A green colour could indicate the presence of glauconite, a potassium iron silicate mineral usually formed in reducing environments. Figure 6.13 and 6.14 are quality assurance maps showing the percentage of green or red coloured deposits in the Naskapi rather than the dominant visible colour.

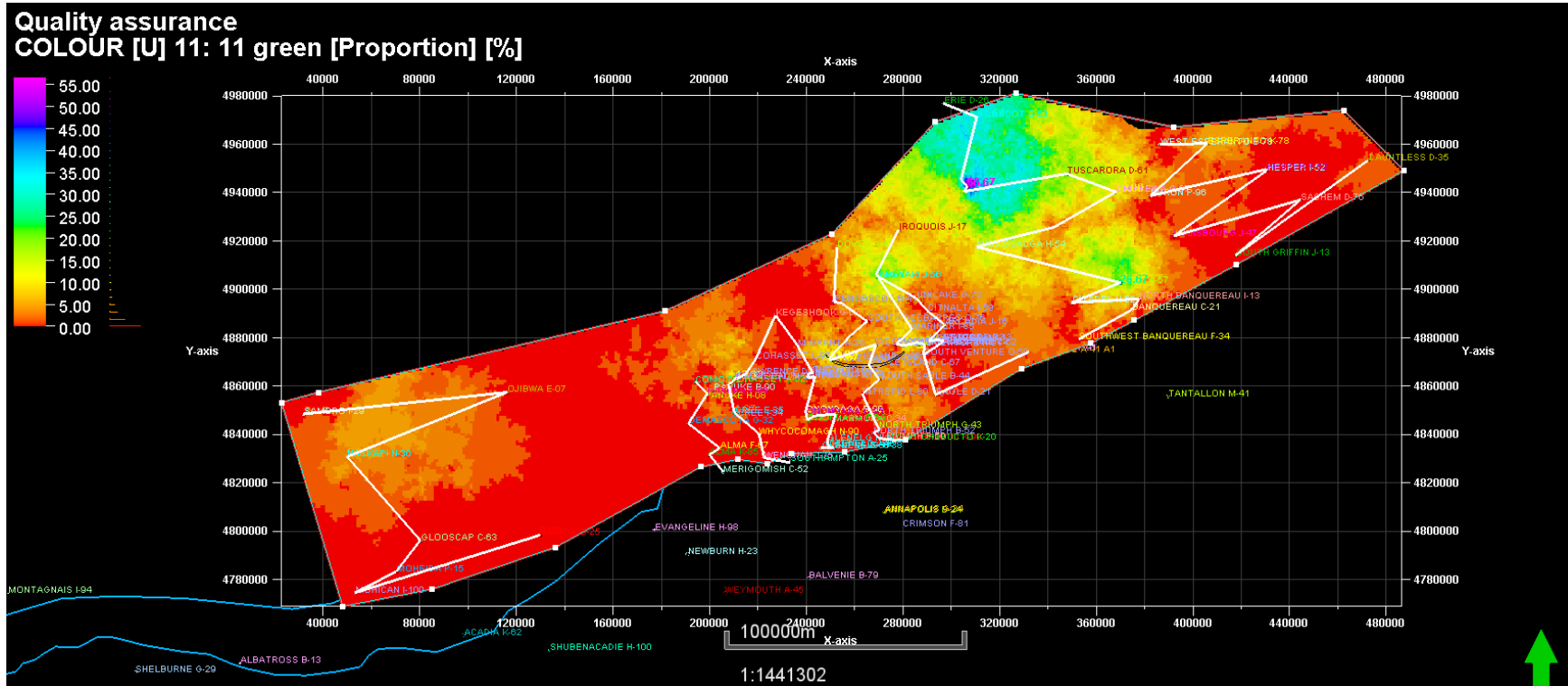


Figure 6.13: Quality assurance map showing the proportion of the colour that is green, with the highest being in the region of the Sable Delta (teal blue/green colour). Areas coloured red show the least percentage of green colour. The variation in colour could be due to the different provenance of various sediments – with different tributaries sourced from different areas of the mainland. A green colour could indicate the presence of glauconite, a potassium iron silicate mineral usually formed in reducing environments. Green shale can occur in reducing conditions, or it can be due to the clay mineral type associated with it such as illite, chlorite, or biotite.

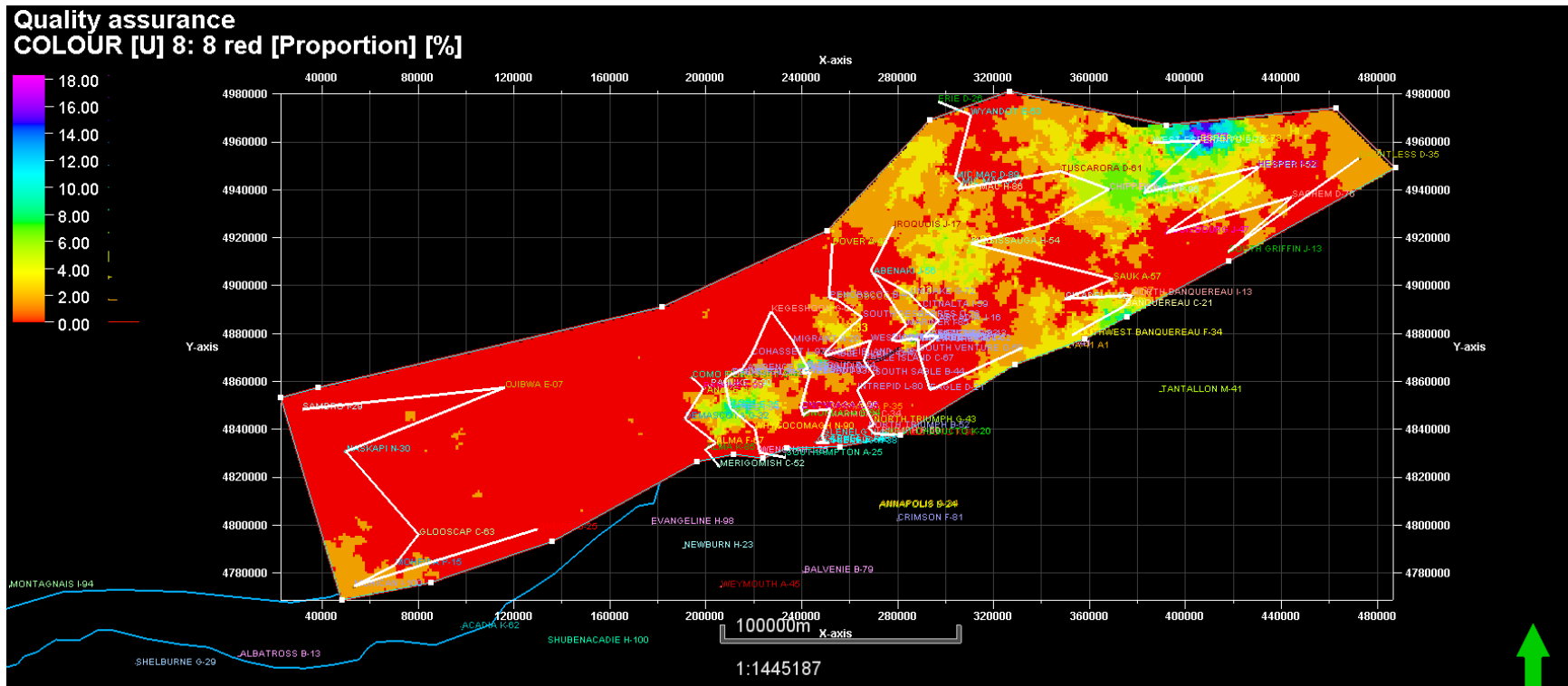


Figure 6.14: This map is showing the proportion of red coloured deposits in the Naskapi Member. The red colour corresponds with the least amount of red colour as indicated on the legend. The provenance of the grains could come from an area with abundant aeolian sediments, eroded volcanics or metamorphic rocks abundant with red minerals.

6.5.3 Limestone Content

Figure 6.15 shows the meters of Naskapi Member with limestone as the dominant lithology (>50%) as logged in drill cuttings by Canstrat™. The higher amount of limestone trends between the Mohican I-100 and Moheida P-15 wells and south of the Abenaki Bank, from where the limestone content is likely sourced.

6.5.4 Shale Content

The shale content of the Naskapi increases basinward. Figure 6.16 shows the meters of Naskapi Member with shale as the dominant lithology (>50%) as logged in drill cuttings by Canstrat™. The thicker shale sections are basinward notably between the Glooscap C-63 and the Banquereau C-21 well areas.

Figure 6.17 is a quality assurance ‘net to gross’ map showing the proportion of shale (rather than sandstone) to the total formation. The lowest proportion of shale is landward in the area where the sandy delta deposits are found, and the highest proportion of shale occurs basinward.

The shale volume in the Naskapi Member is determined to be 40% or less throughout the basin, the exception being thick shale sequences of 80-90% near Merigomish C-52, Oneida O-25, Southampton A-25, South Venture O-59, Southwest Banquereau F-34, and Naskapi N-30.

6.5.5 Sand Content

Figure 6.18 shows the meters of Naskapi Member with sand as the dominant lithology (>50%) as logged in drill cuttings by Canstrat™. Sand is most prevalent landward, to the north of the Wyandot E-53 well, in the region of the Sable Delta.

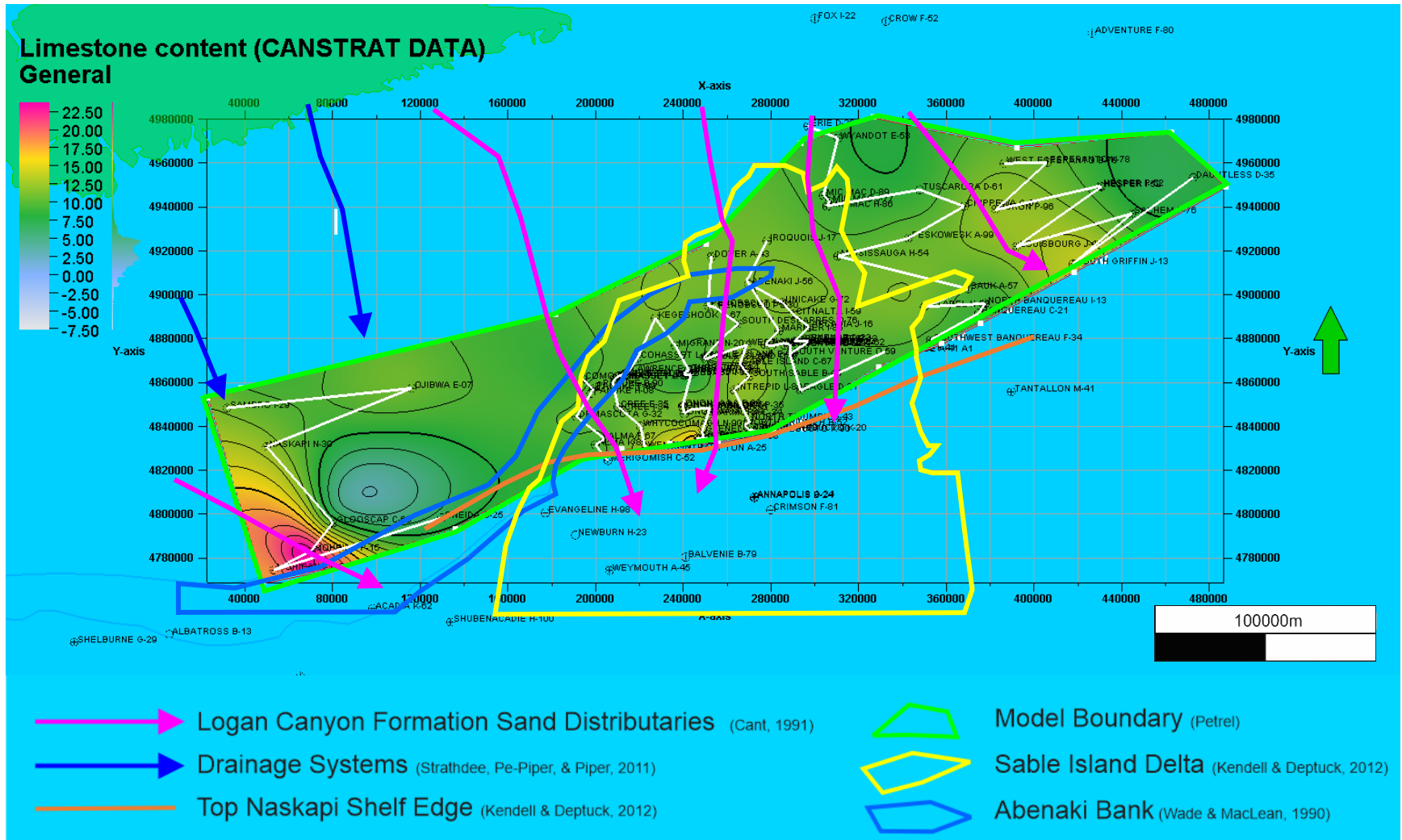


Figure 6.15: Meters of Naskapi Member with limestone as the dominant lithology (>50%) as logged in drill cuttings by Canstrat™. Dominant limestone trends between the Mohican I-100 and Moheida P-15 wells and south of the Abenaki Bank, from where the limestone content is likely sourced.

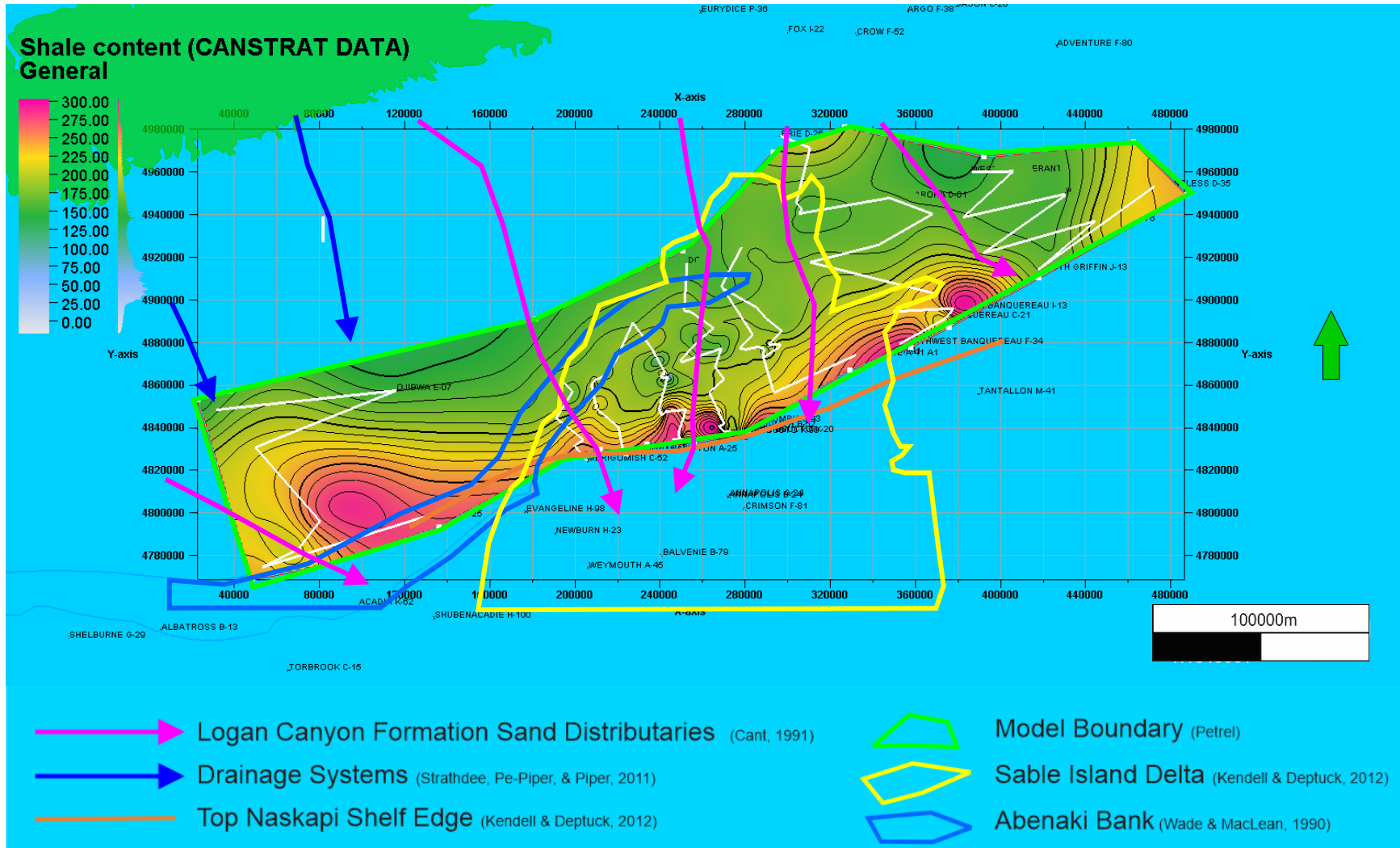


Figure 6.16: Meters of Naskapi Member with shale as the dominant lithology (>50%) as logged in drill cuttings by Canstrat™. The thicker shale sections are basinward notably between Glooscap C-63 and the Banquereau C-21 well areas. The pink concentrations show areas with greater shale content and are likely local depocentres with accommodation space which were protected from erosion.

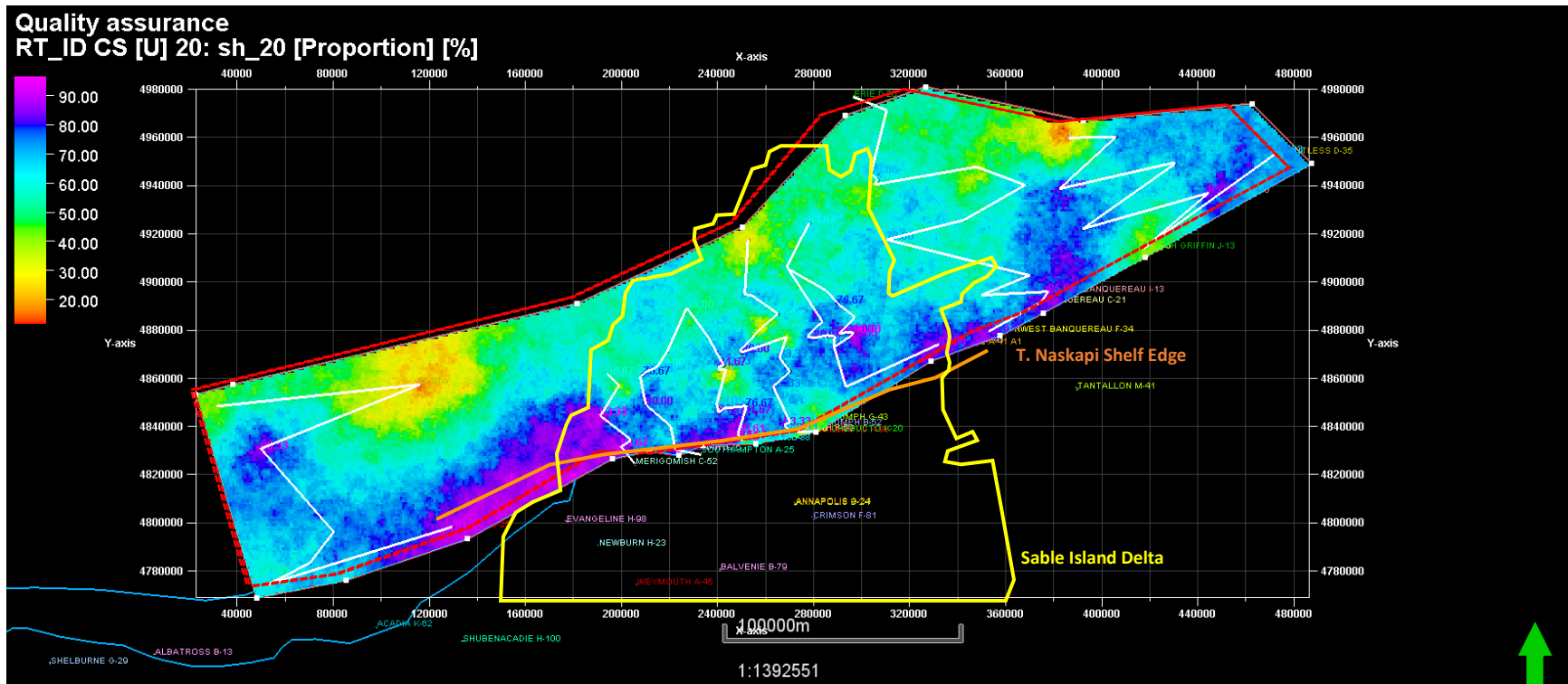


Figure 6.17: Net to gross map showing the proportion of shale to the total formation. The highest proportion of shale is found basinward, seen in purple. The lowest proportion of shale is found landward in the area where distributary clastic deposits dominate.

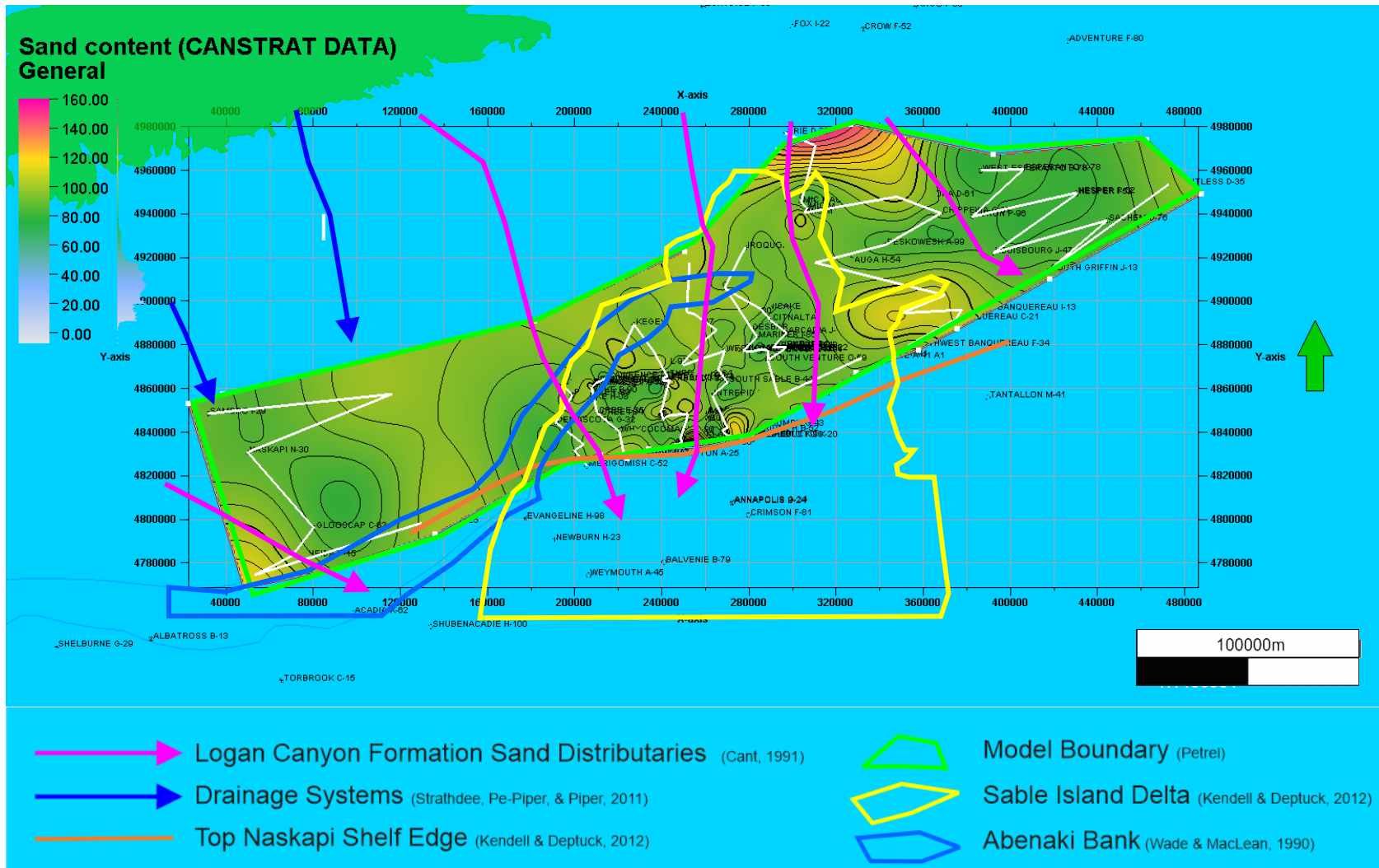


Figure 6.18: Meters of Naskapi Member with sand as the dominant lithology (>50%) as logged in drill cuttings by Canstrat™. Sand is most prevalent landward, nearer to the Sable Delta mouth north of the Wyandot E-53 well. The white lines indicate the location of the cross sections, the Sable Delta is outlined in yellow and the distributaries are as indicated.

6.5.6 Siltstone Content

Figure 6.19 shows the Meters of Naskapi Member with siltstone as the dominant lithology (>50%) as logged in drill cuttings by Canstrat™. Siltstone is found basinward at a distance from the distributary mouths, and peaks in the region of the Glenelg N-49, Southwest Banquereau F-34 and South Griffin J-13 wells.

6.5.7 Siderite Content

Figure 6.20 indicates the meters of Naskapi Member with siderite as the dominant lithology (>50%) as logged in drill cuttings by Canstrat™. A trend towards high siderite content is to the west of the Mohican I-100 and Naskapi N-30 wells. Siderite is an iron carbonate (FeCO_3) which is precipitated in sedimentary rocks in the presence of iron and carbonate. The map shows siderite in areas adjacent to the carbonate Abenaki Bank.

6.5.8 Marlstone Content

Figure 6.21 shows the meters of Naskapi Member with marlstone as the dominant lithology (>50%) as logged in drill cuttings by Canstrat™. Marlstone is defined as a shale where >50% is calcium carbonate-rich with either limestone or dolomite. The highest amount of marlstone noted is in the western part of the study area west of the Demascota G-32 and Como P-21 wells. The highest marlstone content is adjacent to the Abenaki Bank which is likely where the carbonate content was sourced.

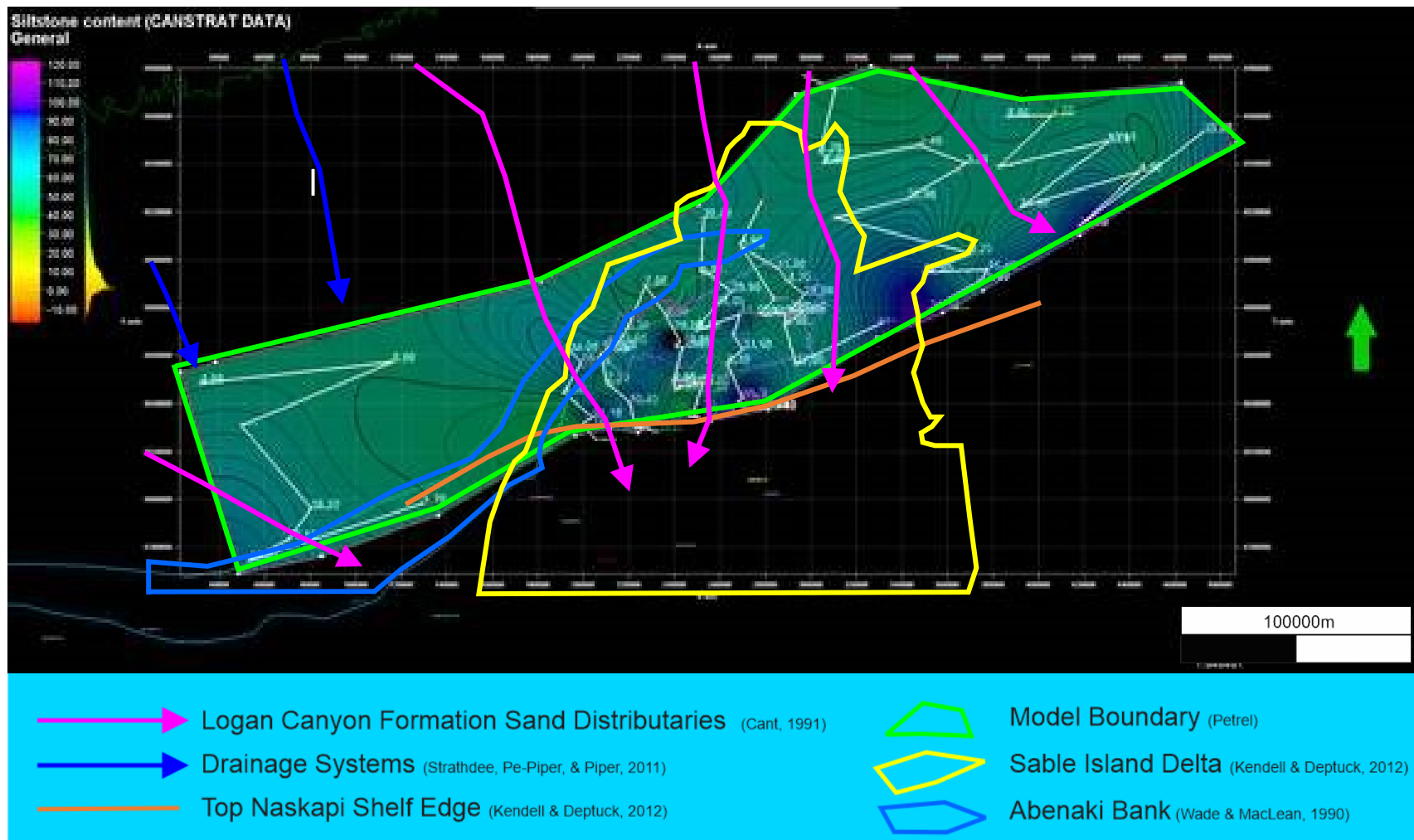


Figure 6.19: Meters of Naskapi Member with siltstone as the dominant lithology (>50%) as logged in drill cuttings by Canstrat™. Siltstone is found basinward at a distance from the distributary mouths, and peaks in the regions of the Glenelg N-49, Southwest Banquereau F-34, and the South Griffin J-13 wells. The white lines indicate the location of the cross sections.

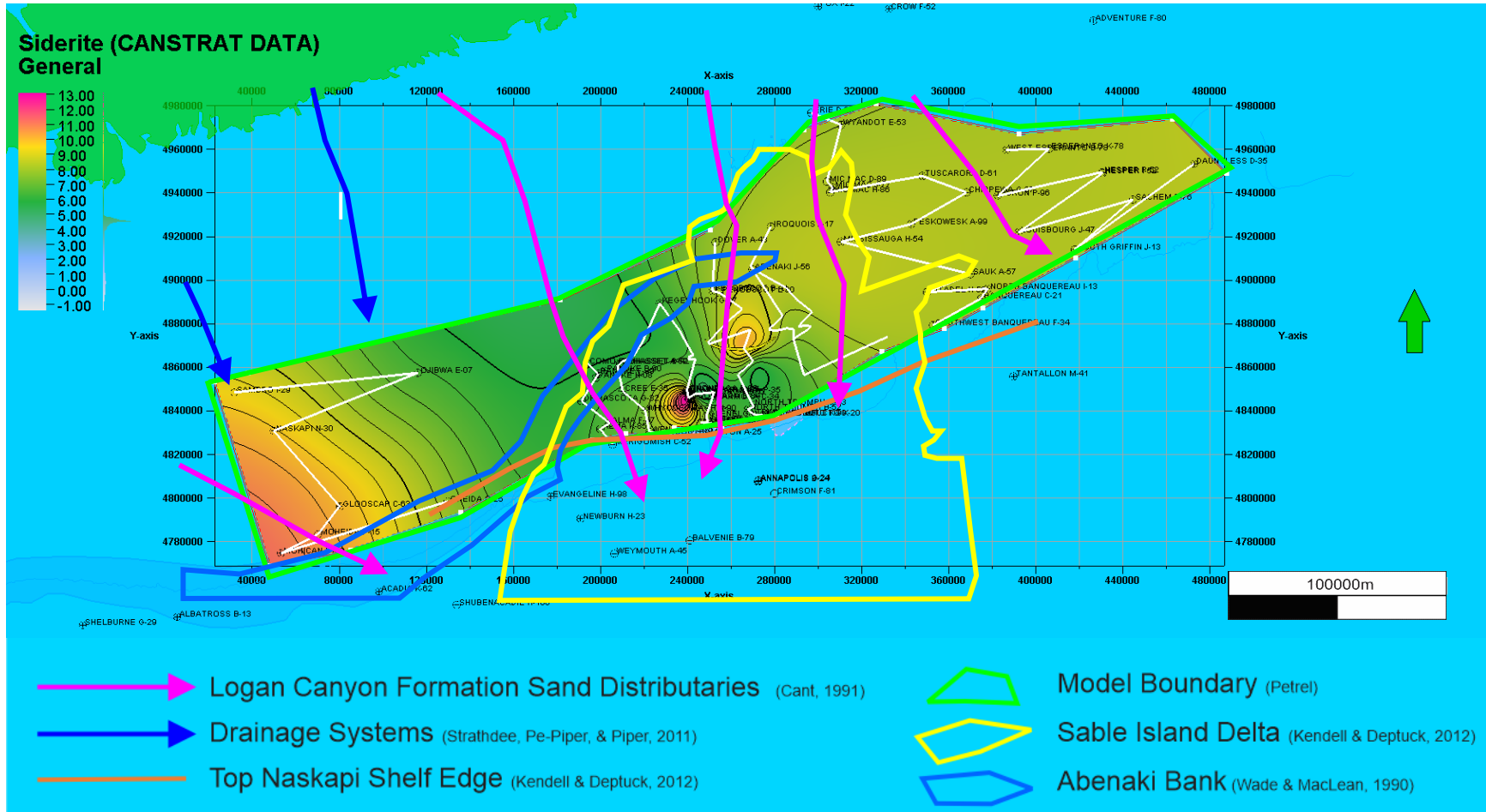


Figure 6.20: Meters of Naskapi Member with siderite as the dominant lithology (>50%) as logged in drill cuttings by Canstrat™. A trend towards high siderite content is to the west of the Mohican I-100 and Naskapi N-30 wells and two ‘bullseyes’ in the Sable Island O-47 and Onondaga E-84 well regions. The white lines indicate the location of the cross sections. Siderite is an iron carbonate (FeCO₃) which is precipitated in sedimentary rocks in the presence of iron and carbonate. The map shows siderite in areas adjacent to the carbonate Abenaki Bank.

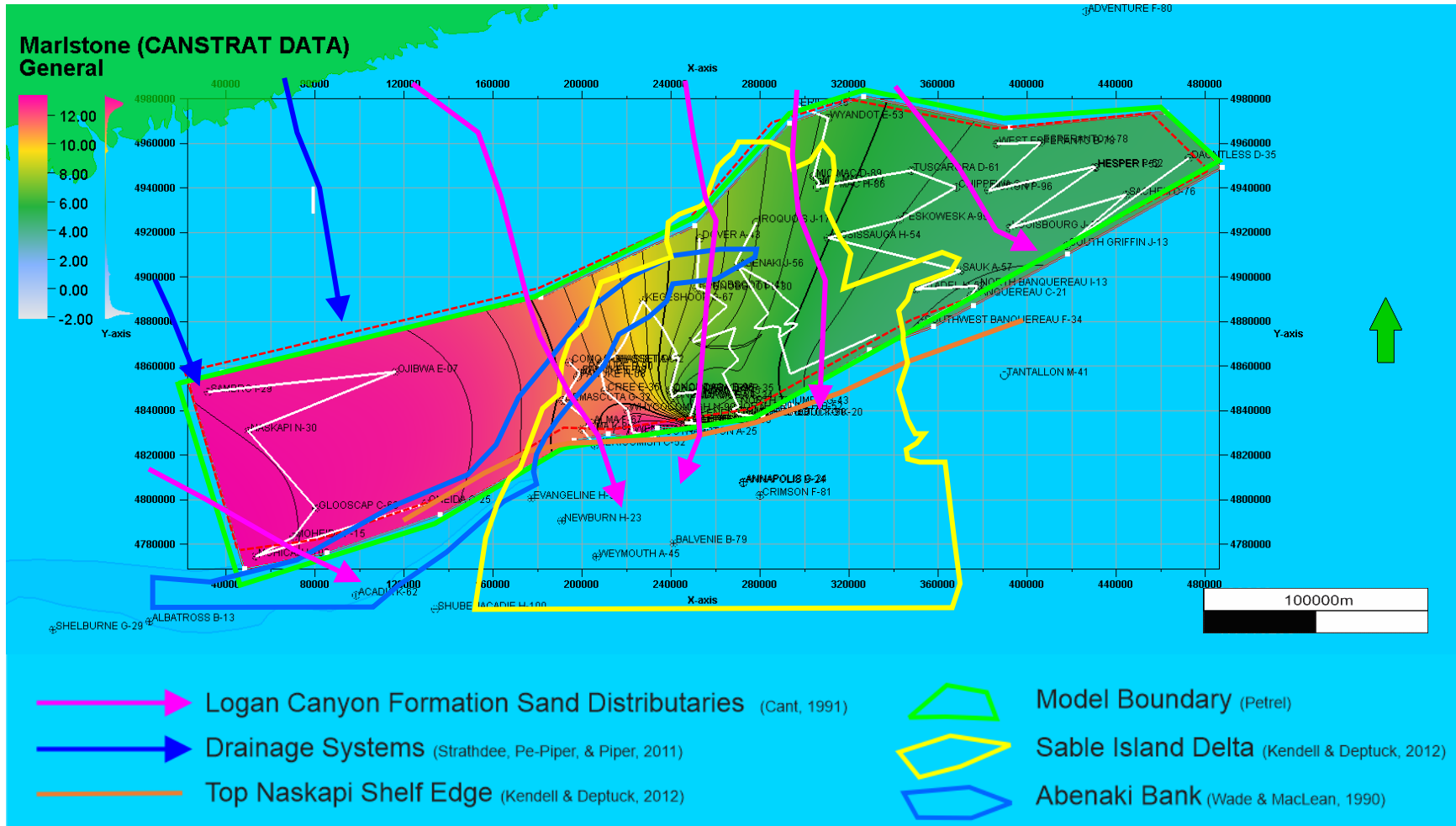


Figure 6.21: Meters of Naskapi Member with marlstone as the dominant lithology (>50%) as logged in drill cuttings by Canstrat™. Marlstone is defined as a shale where >50% is calcium carbonate-rich with either limestone or dolomite. The highest amount of marlstone noted is in the western part of the study area west of the Demascota G-32 and Como P-21 wells, adjacent to the Abenaki Bank, from where the CaCO₃ was likely sourced. The white lines indicate the location of the cross section.

6.5.9 Clay Content

Figure 6.22 shows the meters of Naskapi Member with clay as the dominant lithology (>50%) as logged in drill cuttings by Canstrat™. Clay is dominant in the purple shaded area around the Ojibwa E-07, Glooscap C-63, Mohican I-100, and Moheida P-15 wells. Clay or clay minerals according to the data, are prevalent northwest of the Abenaki Bank area, perhaps indicating an influx of weathered source materials conducive to clay mineral formation.

6.5.10 Fossil Debris Content

Figure 6.23 shows Canstrat™ data where fossil debris is indicated in the cuttings. Light blue areas show fossil material likely shed off the Abenaki bank area outlined in blue.

6.5.11 Green Shale Content

Figure 6.24 shows a map of the meters of green shale in Naskapi Member using Canstrat™ lithology data. The thickest green shale appears in vicinity of the Mohican I-100 and Tuscarora D-61 wells. Green shale can occur due to reducing conditions, or it can be due to the clay mineral type associated with it such as illite, chlorite, or biotite.

6.4.1.12 Calcite Cement Content

Figure 6.25 indicates the amount in percentage of diagenetic calcite cement found in the cuttings samples as analyzed by Canstrat™. The most cemented areas correlate to areas with low porosity in the Naskapi Member (e.g. Figure 6.30 and 6.31) but not areas of maximum porosity. The presence of cement greatly decreases the porosity and permeability of the rock and occurs in previously porous sediments which has been subsequently filled in by supersaturated formation waters. The intrusion of dykes and sills into massive sandstone sequences leads to the widespread formation of carbonate cements (Jones et al., 2016).

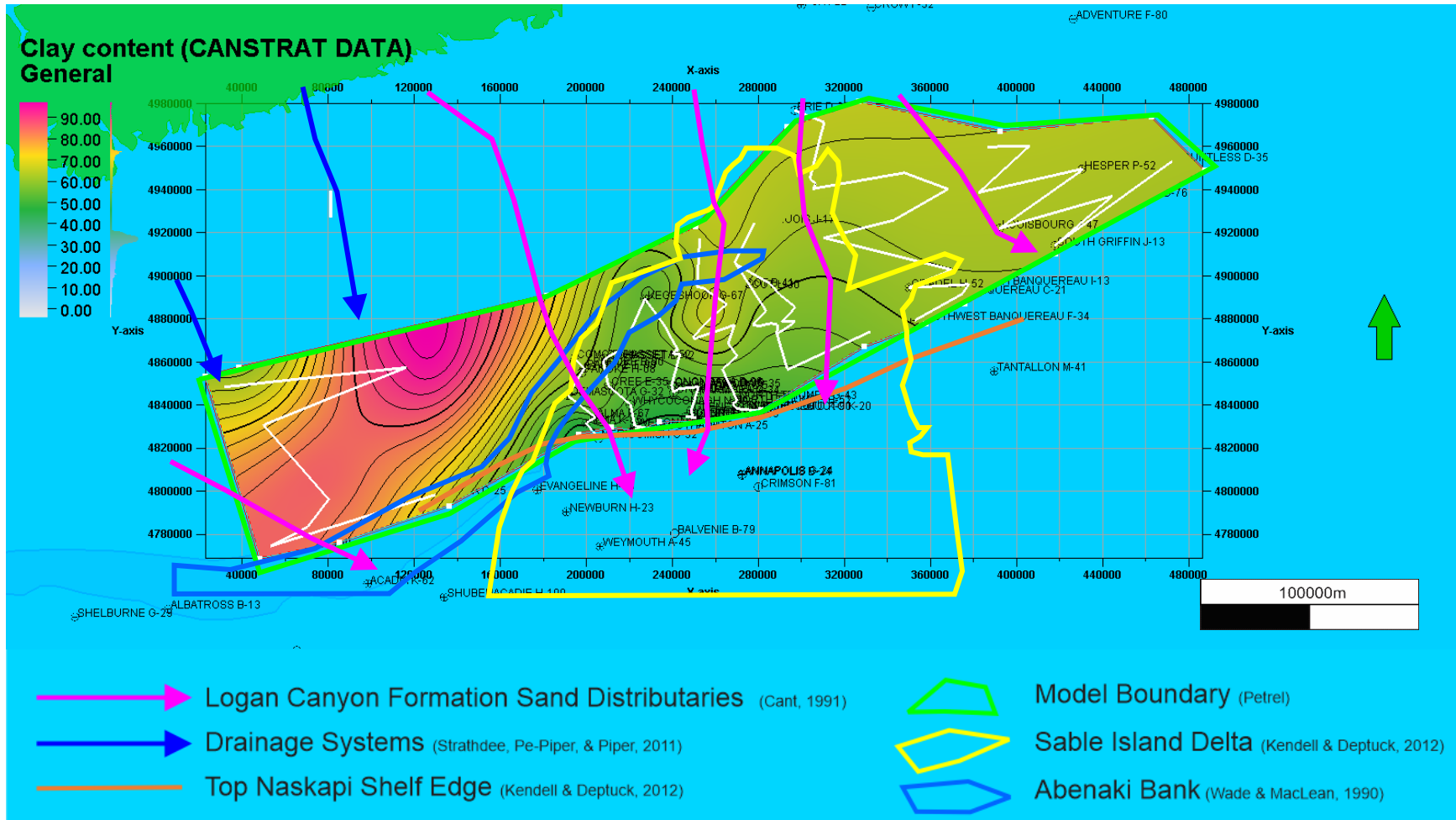


Figure 6.22: Meters of Naskapi Member with clay as the dominant lithology (>50%) as logged in drill cuttings by Canstrat™. Clay is dominant in the purple shaded area around the Ojibwa E-07, Glooscap C-63, Mohican I-100 and Moheida P-15 wells. The white lines indicate the location of the cross sections. Clay or clay minerals according to the data, are found northwest of the Abenaki Bank area, perhaps indicating an influx of weathered source materials conducive to clay mineral formation.

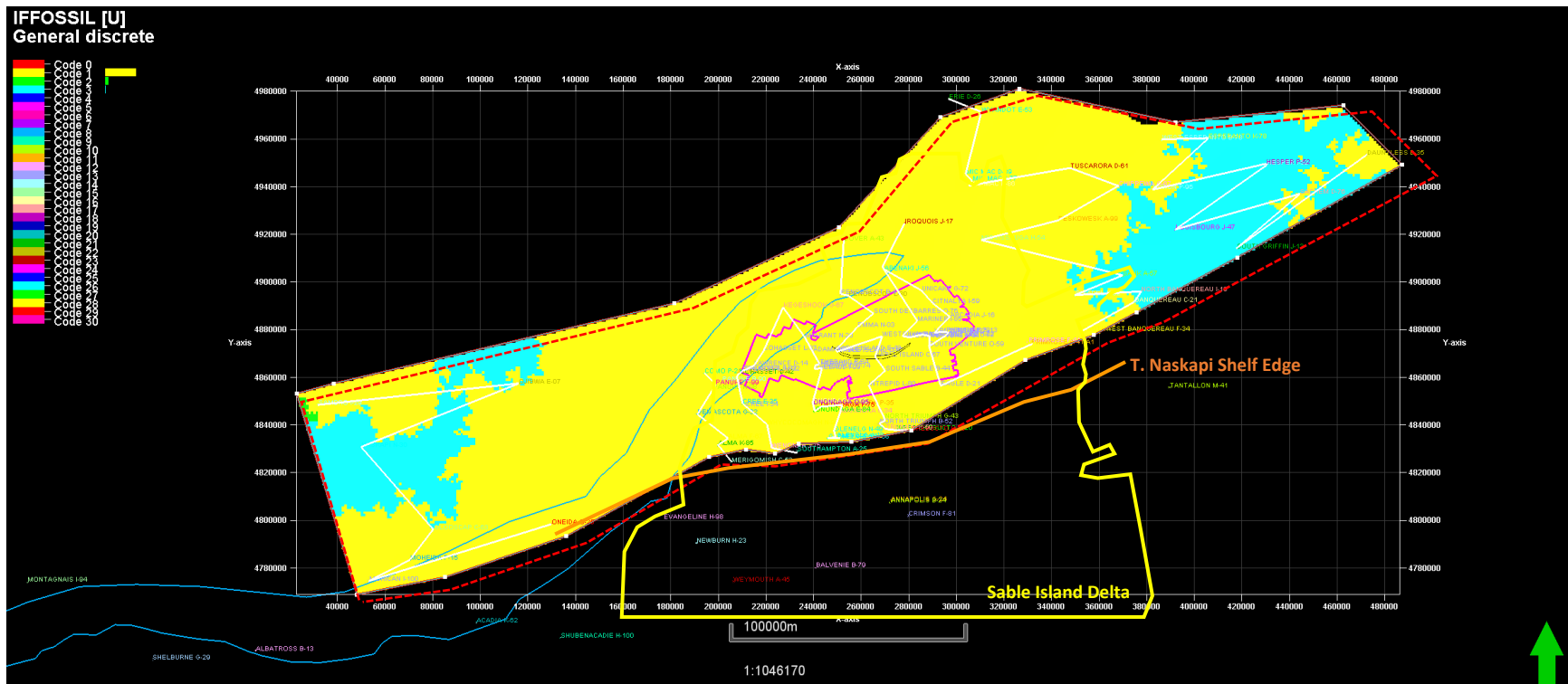


Figure 6.23: Canstrat™ data indicates if fossil debris is found in the drill cuttings. The light blue areas show fossil material likely shed off the Abenaki bank outlined in blue. The white lines indicate the location of the cross sections.

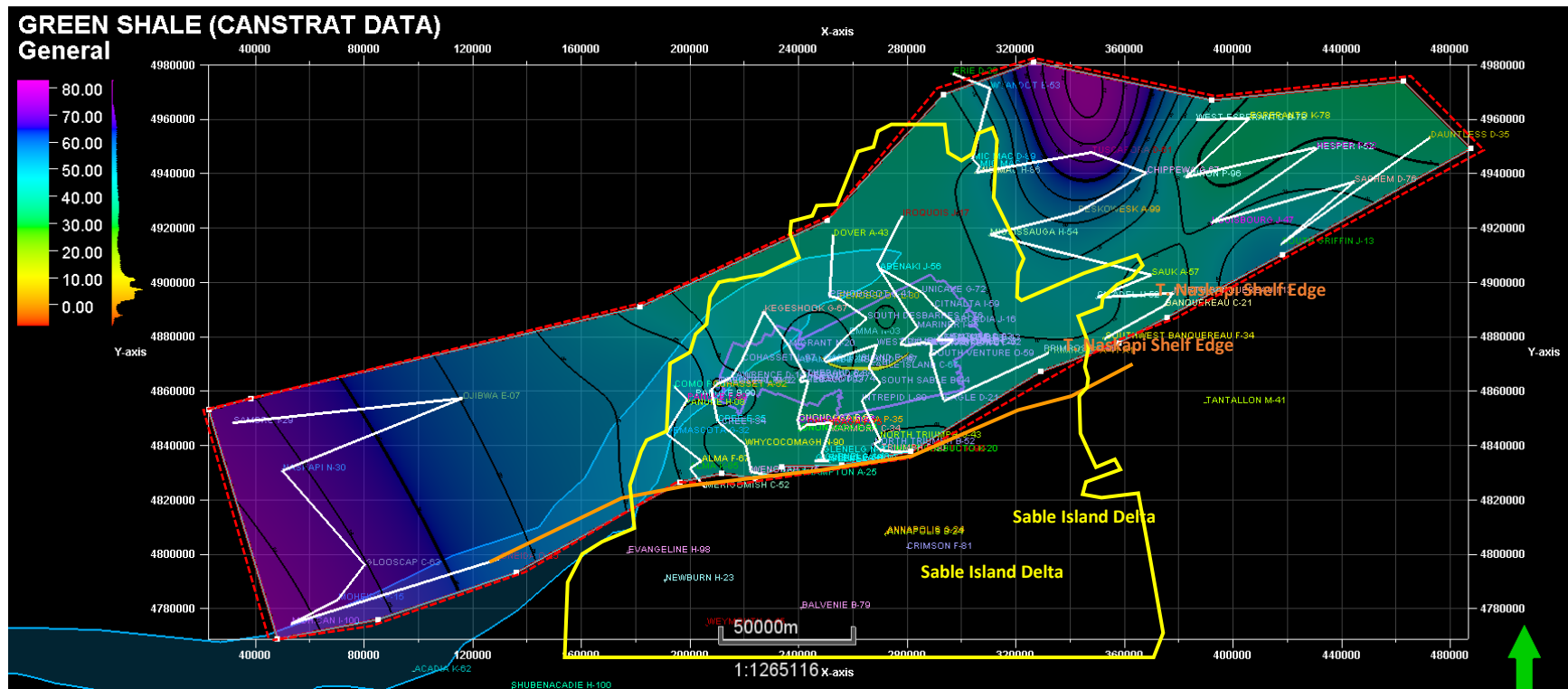


Figure 6.24: Canstrat™ logs upscaled to a 60-layer Naskapi model with layers measuring 2 – 3 metres each using a sequential indicator simulation and is an aggregated proportional quality assurance map. The thickest green shale appears in vicinity of wells Mohican I-100 and Tuscarora D-61. The white lines indicate the location of the cross sections. The data has been propagated using facies modeling. Green shale can occur due to reducing conditions, or it can be due to the clay mineral type associated with it such as illite, chlorite, or biotite.

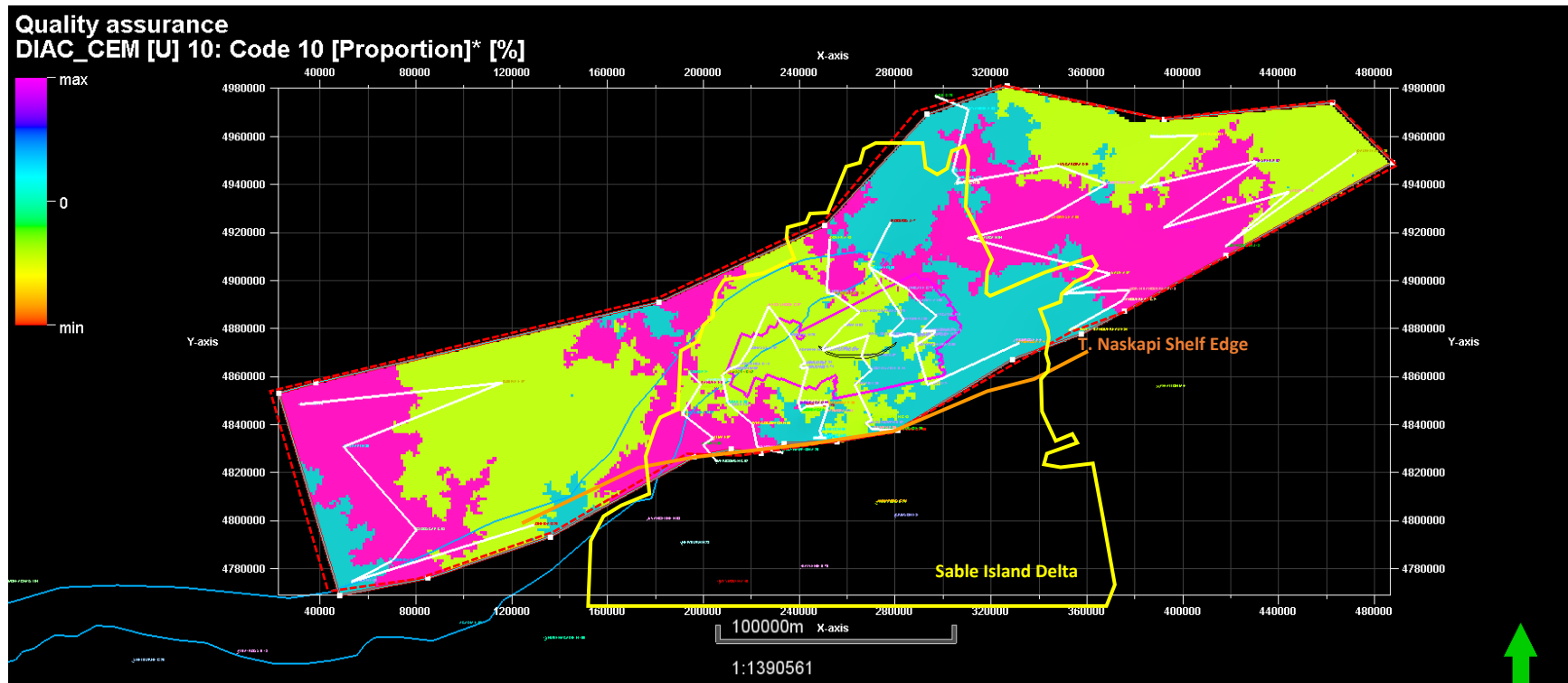


Figure 6.25: This map shows the proportion of diagenetic calcite cement found in the cuttings samples as analyzed by Canstrat™. The white lines indicate the location of the cross sections. Pink and turquoise areas indicate the areas most affected by cement and they correlate to areas with low porosity in the Naskapi Member (e.g. Figure 6.30 and 6.31) but not areas of maximum porosity. The presence of cement greatly decreases the porosity and permeability of the rock and points to previously porous areas deposited in a deltaic setting with larger clasts and subsequently filled in by supersaturated formation waters.

6.5.13 Oil Stain

The maps in Figures 6.26 through 6.29 show the meters of Naskapi Member which contain oil stain, as measured by Canstrat™. Methodology involved putting a small sample of cuttings on a spot plate and adding several drops of xylene to separate any hydrocarbons contained therein. Any cut, or released hydrocarbon, was observed under a fluoroscope and fluorescence was noted.

Figure 6.26 shows the meters of the Naskapi Member with total oil stain (sum of good, medium and questionable) as logged by Canstrat™. Two areas showing the largest amount are in the region of the Mic Mac well group and Missisauga H-54 wells, and south near the Southampton A-25, Annapolis G-24 and Balvenie B-79 wells. Figure 6.27 shows the meters of the Naskapi Member with questionable oil stain. The most questionable staining occurs in the area south of the Southampton A-26 well. Figure 6.28 shows the meters of the Naskapi Member with medium oil stain. The peak of medium staining occurs near the Mic Mac and Missisauga wells. Finally, Figure 6.29 shows the meters of the Naskapi Member with good oil stain. The highest amount noted occurs in the southeast section of the study area.

All grades of oil stain; total, questionable, medium and good, all are seen to have the most stain in the Sable Delta region. In addition, good oil stain is seen to the east of the Sable Delta, suggesting the limits of the delta region could be extended, as deltaic sediments with sufficient porosity and permeability that allowed for the passage of hydrocarbons were deposited there.

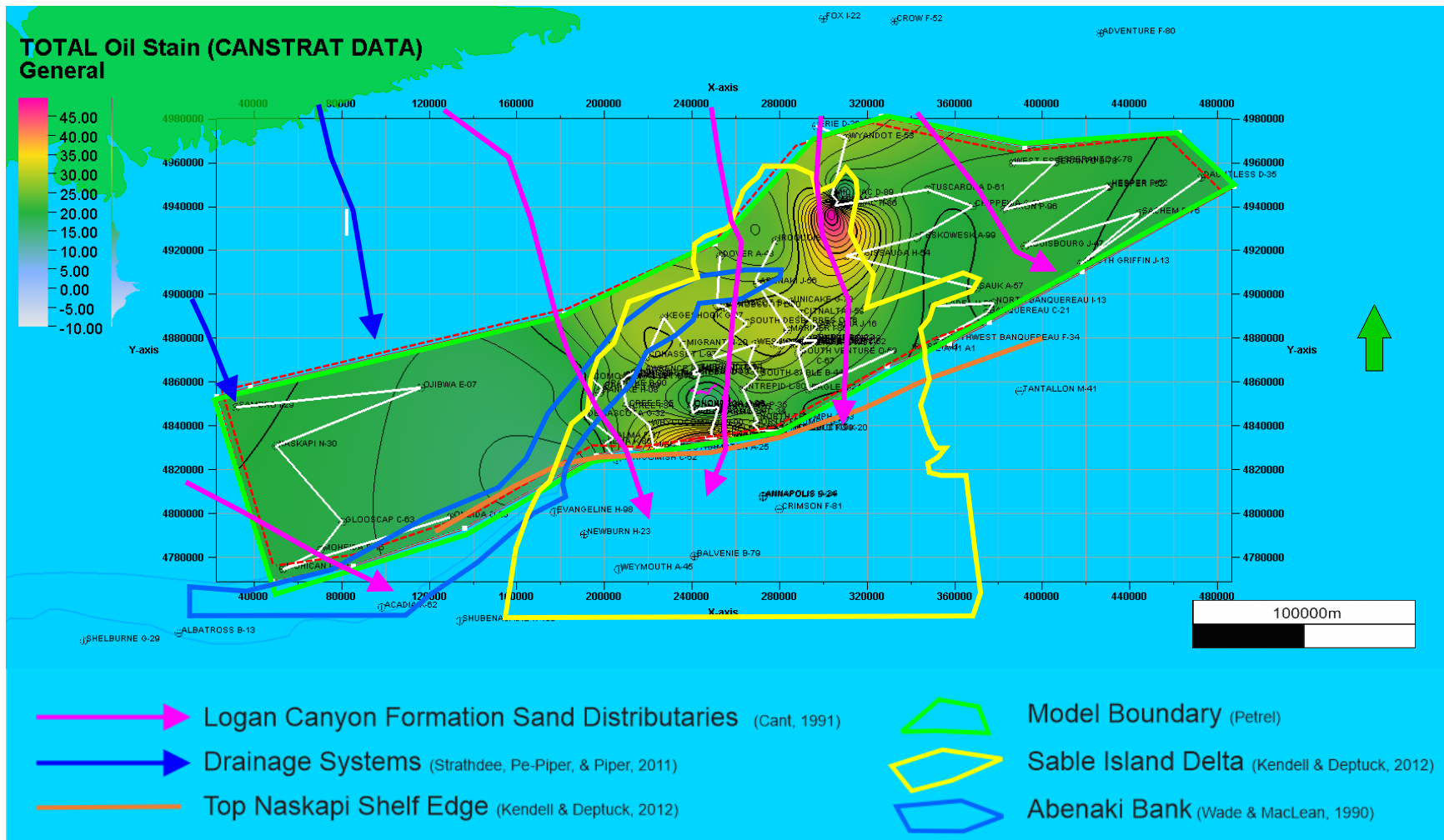


Figure 6.26: Meters of the Naskapi Member with total oil stain (sum of good, medium and questionable) as logged by Canstrat™. Two areas showing the largest amount are in the region of the Mic Mac and Missisauga wells, and south near the Southampton A-25, Annapolis G-24 and Balvenie B-79 wells. The white lines indicate the location of the cross sections. The greatest oil stain correlates well with the Sable Delta area where there would have been more original porosity to allow for the passage of hydrocarbons.

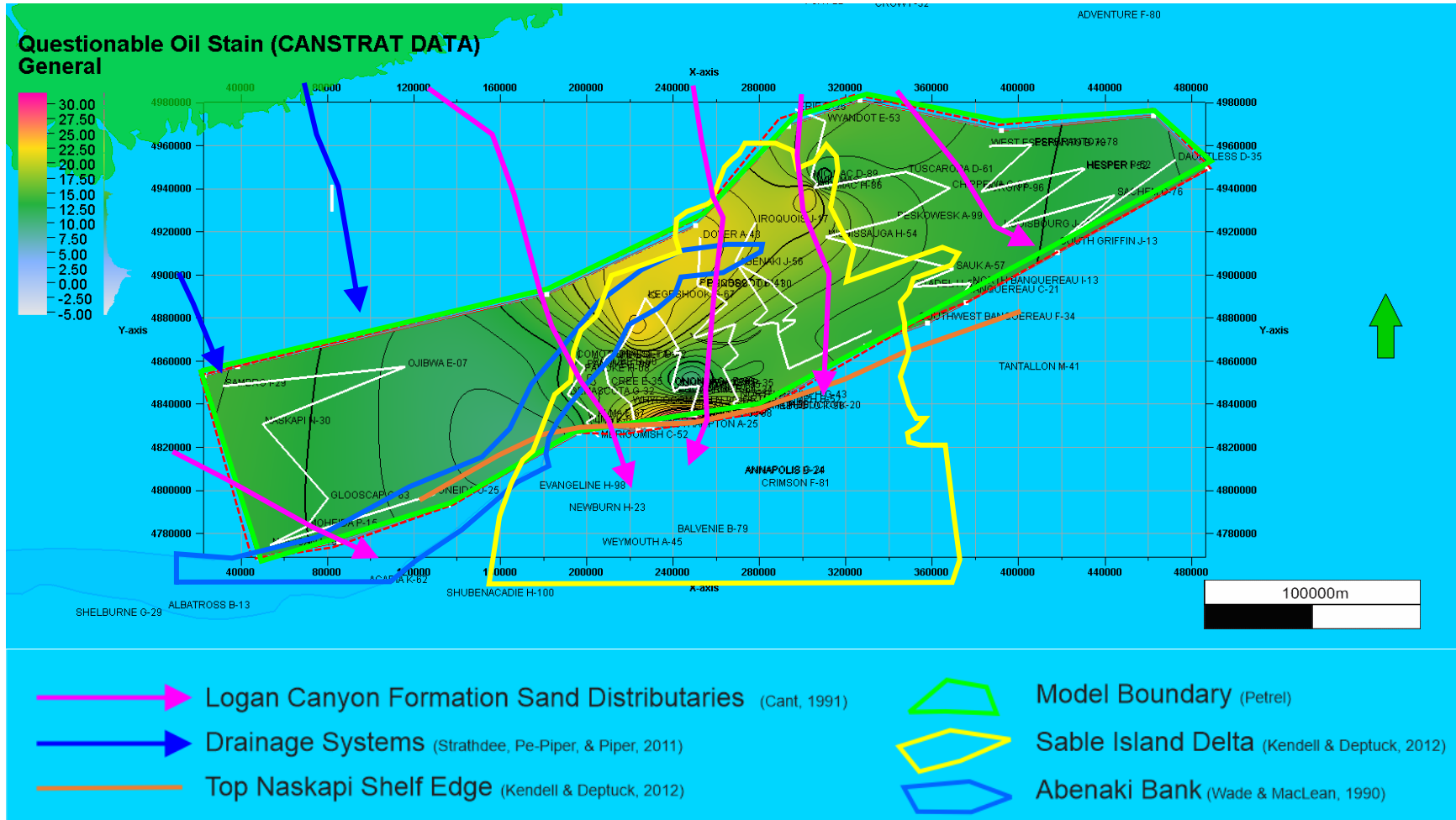


Figure 6.27: Meters of the Naskapi Member with questionable oil stain as logged by Canstrat™. The most questionable staining occurs in the area south of the Southampton A-26 well. The white lines indicate the location of the cross sections. The areas with questionable oil stain correlate with the Sable Delta, where sufficient porosity and permeability would have allowed for passage of hydrocarbons.

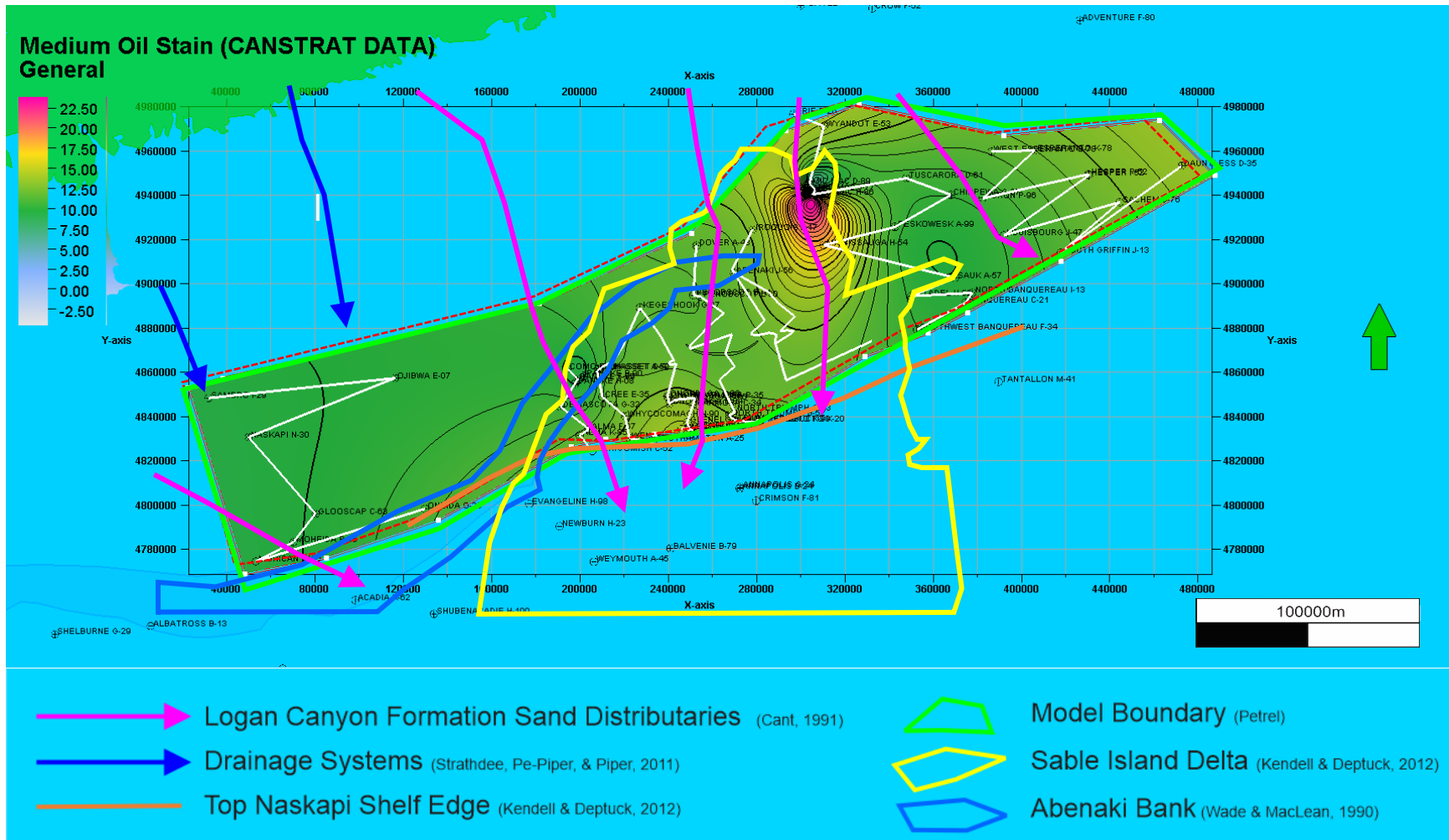


Figure 6.28: Meters of the Naskapi Member with medium oil stain as logged by Canstrat™. The peak of medium staining occurs near the Mic Mac and Missisauga H-54 wells. The white lines indicate the location of the cross sections. Significant amounts of oil stain predictably are seen in the Sable Delta region which would have had an influx of greater clast sizes, and more porosity and permeability to allow for the passage of hydrocarbons.

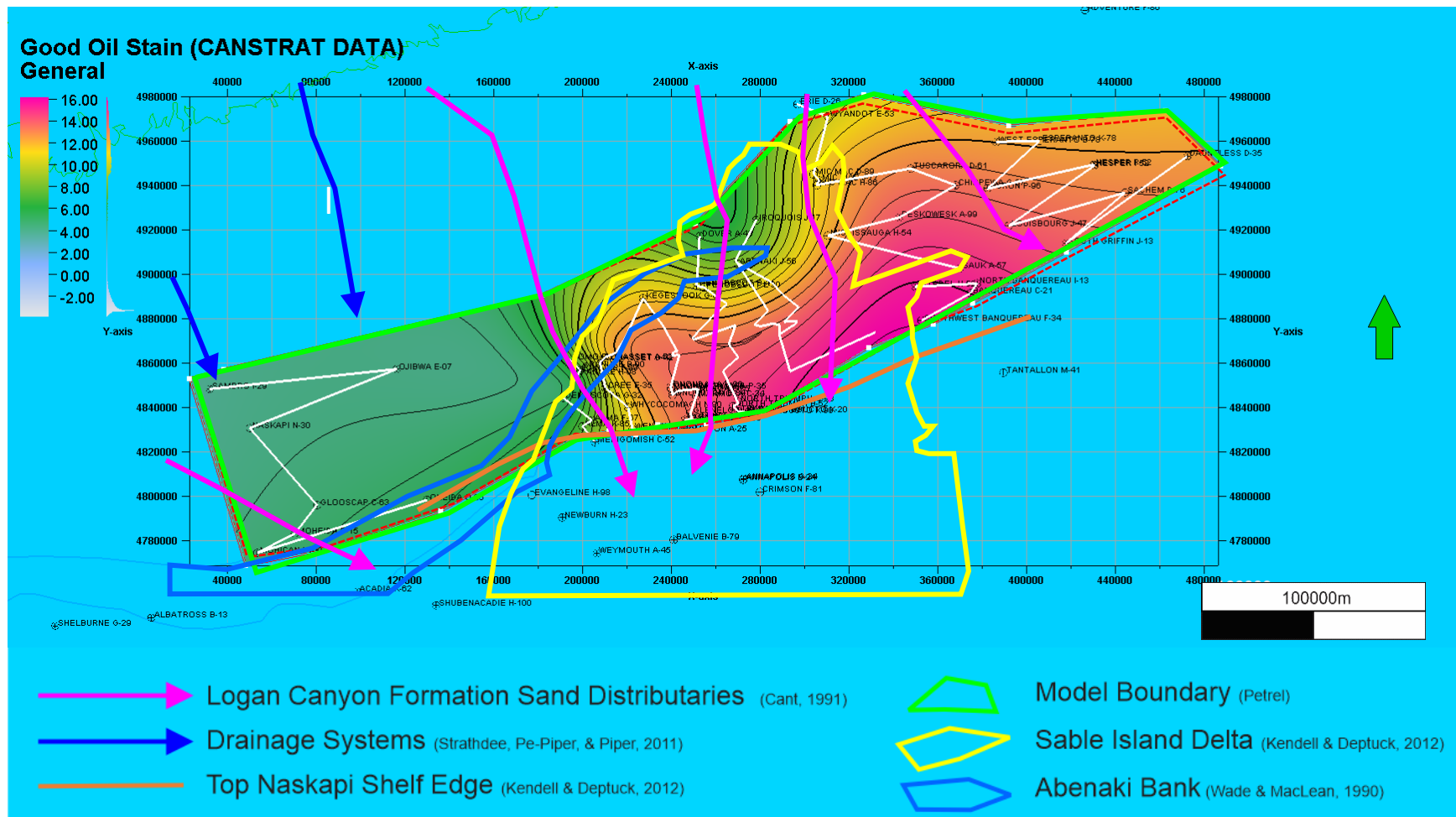


Figure 6.29: Meters of the Naskapi Member with good oil stain as logged by Canstrat™. The highest amount noted occurs in the southeast section of the study area. The white lines indicate the location of the cross sections. Good oil stain is seen in the Sable Delta region, and to the east, suggesting the limits of the delta region could be extended, as deltaic sediments with sufficient porosity and permeability that allowed for the passage of hydrocarbons were deposited there.

6.5.14 Visual Porosity

Visual porosity refers to the porosity as estimated from well cutting observation, rather than the calculated porosity as determined from wireline well logs. The porosity cut-offs used in the creation of these maps is based on the cut offs used in Canstrat™ sample logging method where porosity estimates are classified as greater than 3%, greater than 6%, greater than 9%, greater than 12%, 12-15%, 15-20%, greater than 20% and the maximum visible porosity of 33%.

Visually porosity maps are shown in Figures 6.30 – 6.38. These figures show the meters of Naskapi Member silt, sand and coarser clasts with visual porosity estimations as logged by Canstrat™. Their methodology recognises porosity values from 0-33% in lithologies with grain sizes greater than that of shale as seen in cuttings examinations. The Sable Delta area shows higher porosity as well as the area in the southwest near the Shelburne Delta drainage system and to the northeast of the Sable Delta in an area fed by the Logan Canyon distributaries.

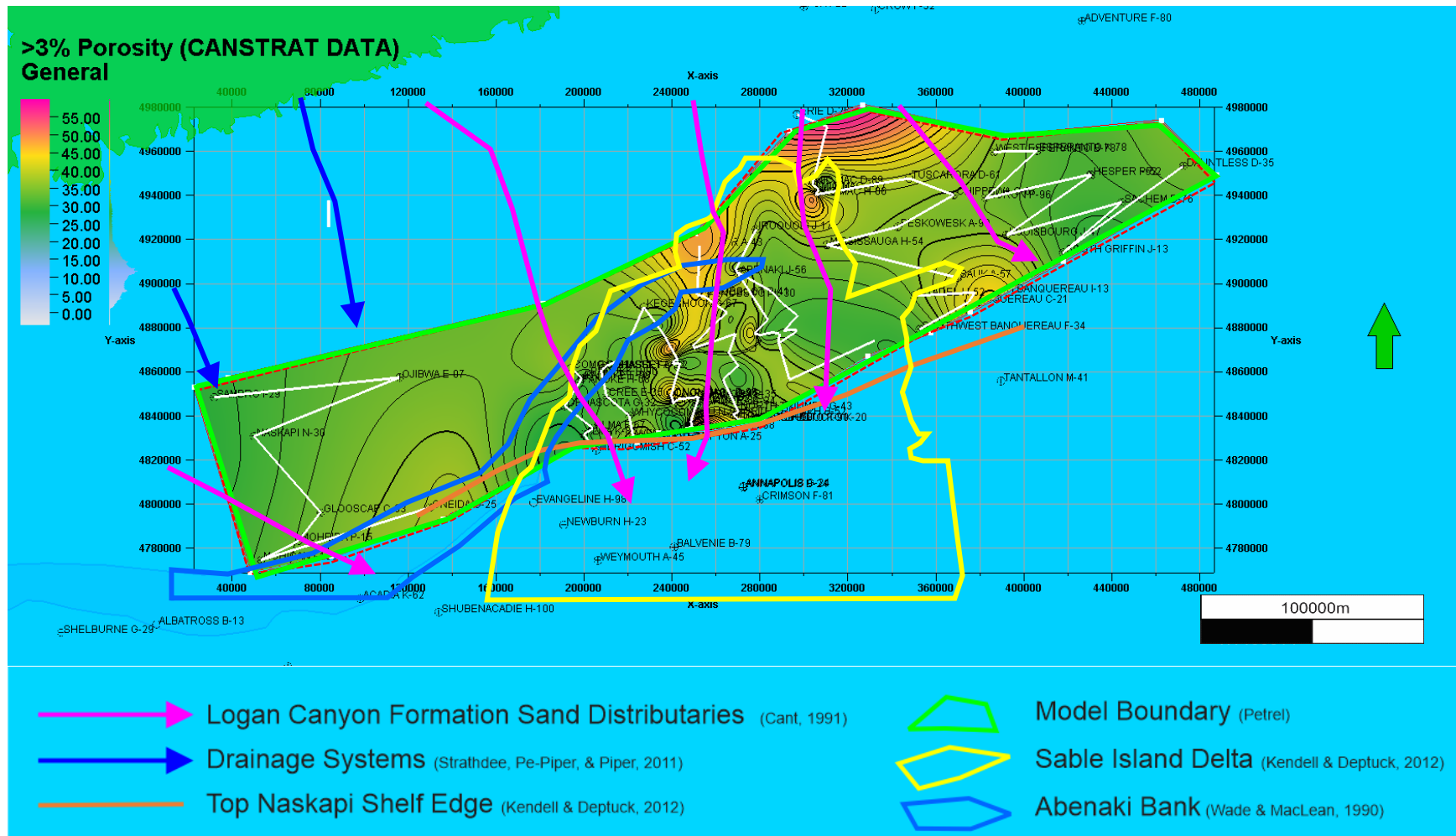


Figure 6.30: Meters of Naskapi Member silts and sands that show 3 – 6 % visual porosity as logged by Canstrat™. In this figure, the highest porosity is seen in the Sable Delta area of Erie D-26 and Wyandot E-53, and near Dover A-43. The white lines indicate the location of the cross sections.

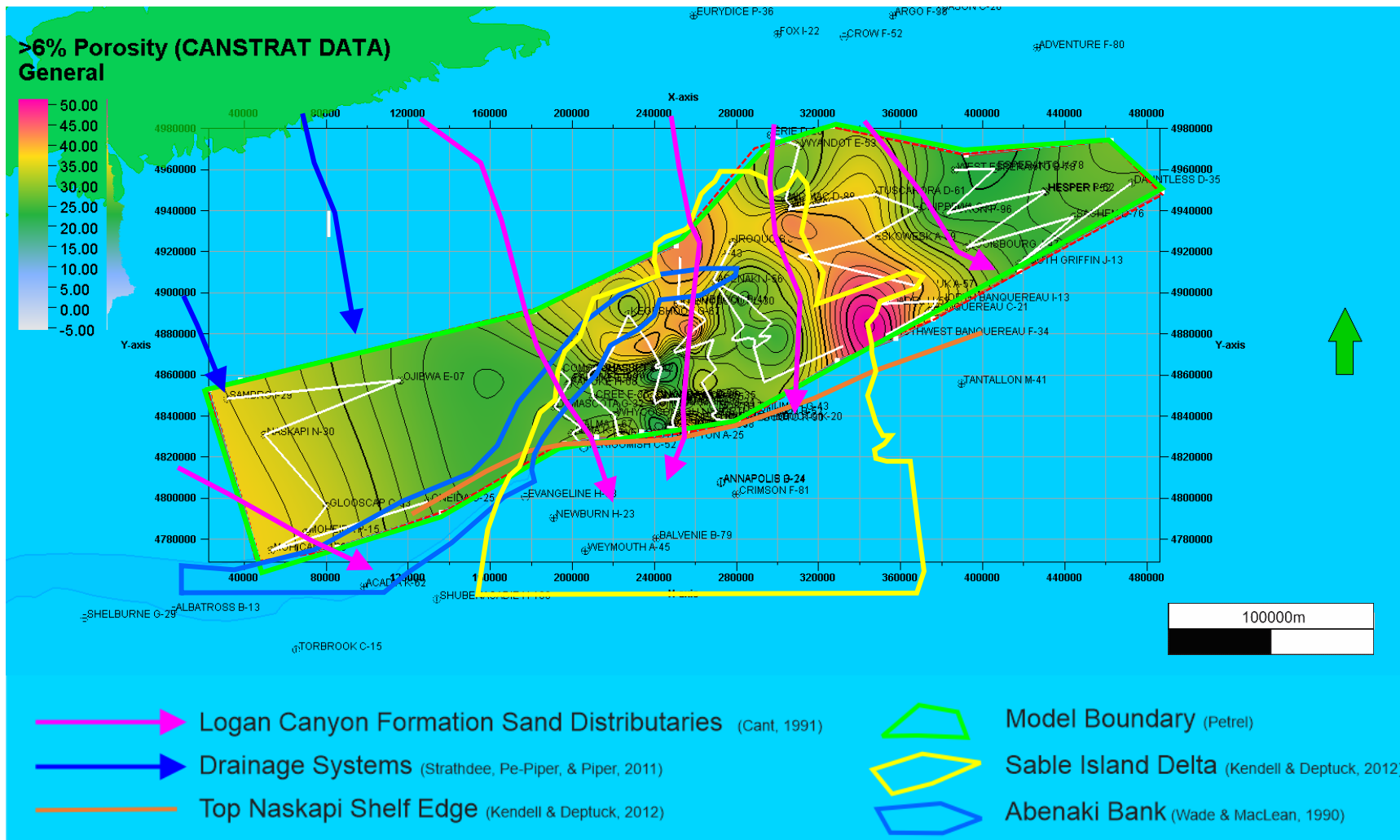


Figure 6.31: Meters of Naskapi Member that show 7-9 % visual porosity as logged by Canstrat™. The highest occurrences of porosity are in the area between Citadel H-52, Primrose A-41, and Southwest Banquereau F-34. The white lines indicate the location of the cross sections. The Sable Delta area shows higher porosities as well as the area in the southwest near the Shelburne Delta drainage system.

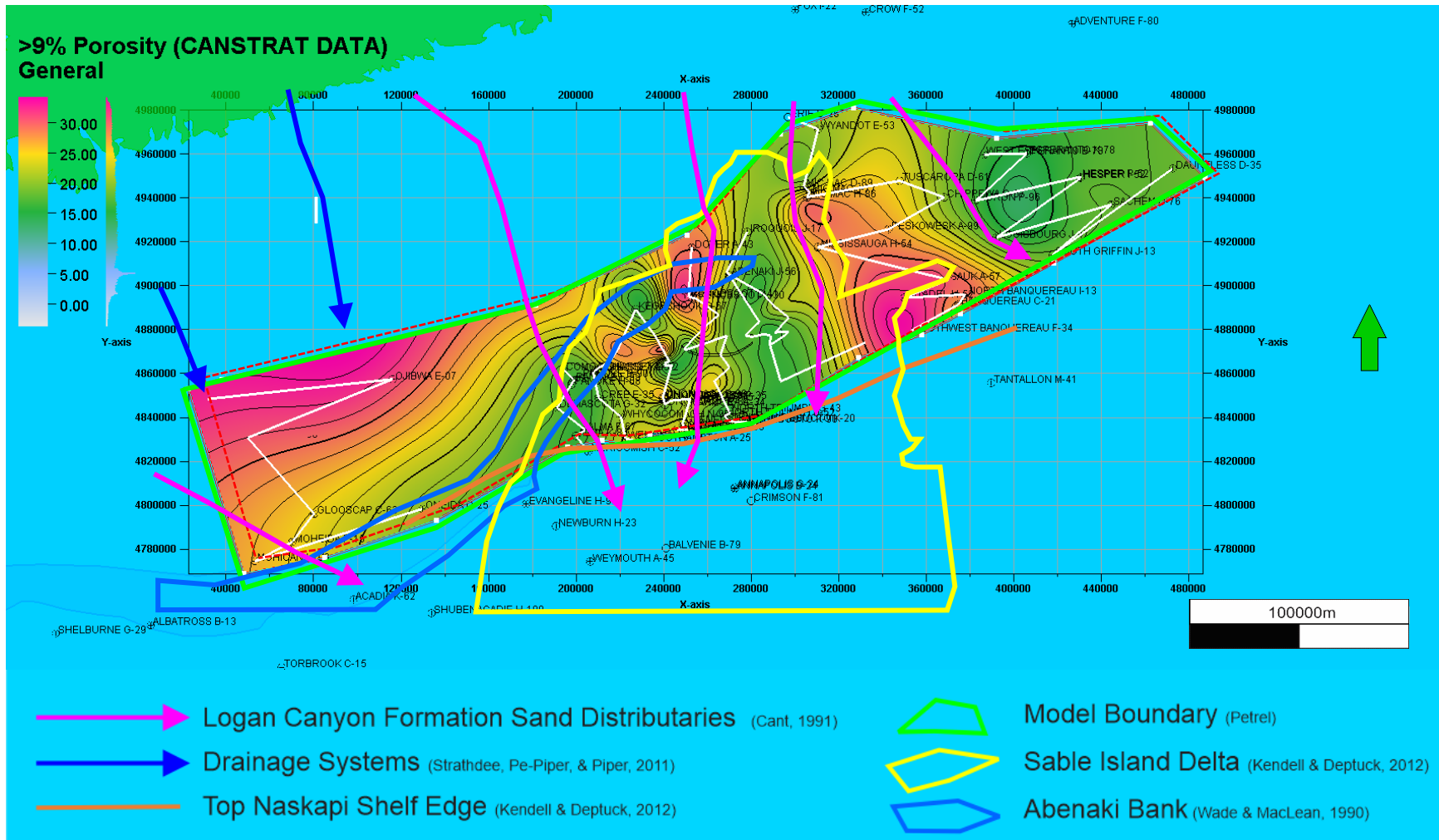


Figure 6.32: Meters of Naskapi Member that show 10 – 12 % visual porosity as logged by Canstrat™. The highest amount of 9 – 12% porosity grains lie in the region of the Shelburne Delta and Sambro I-29 and Ojibwa E-07 wells. The white lines indicate the location of the cross sections. The Sable Delta area has higher porosity in the area in the southwest near the Shelburne Delta drainage system.

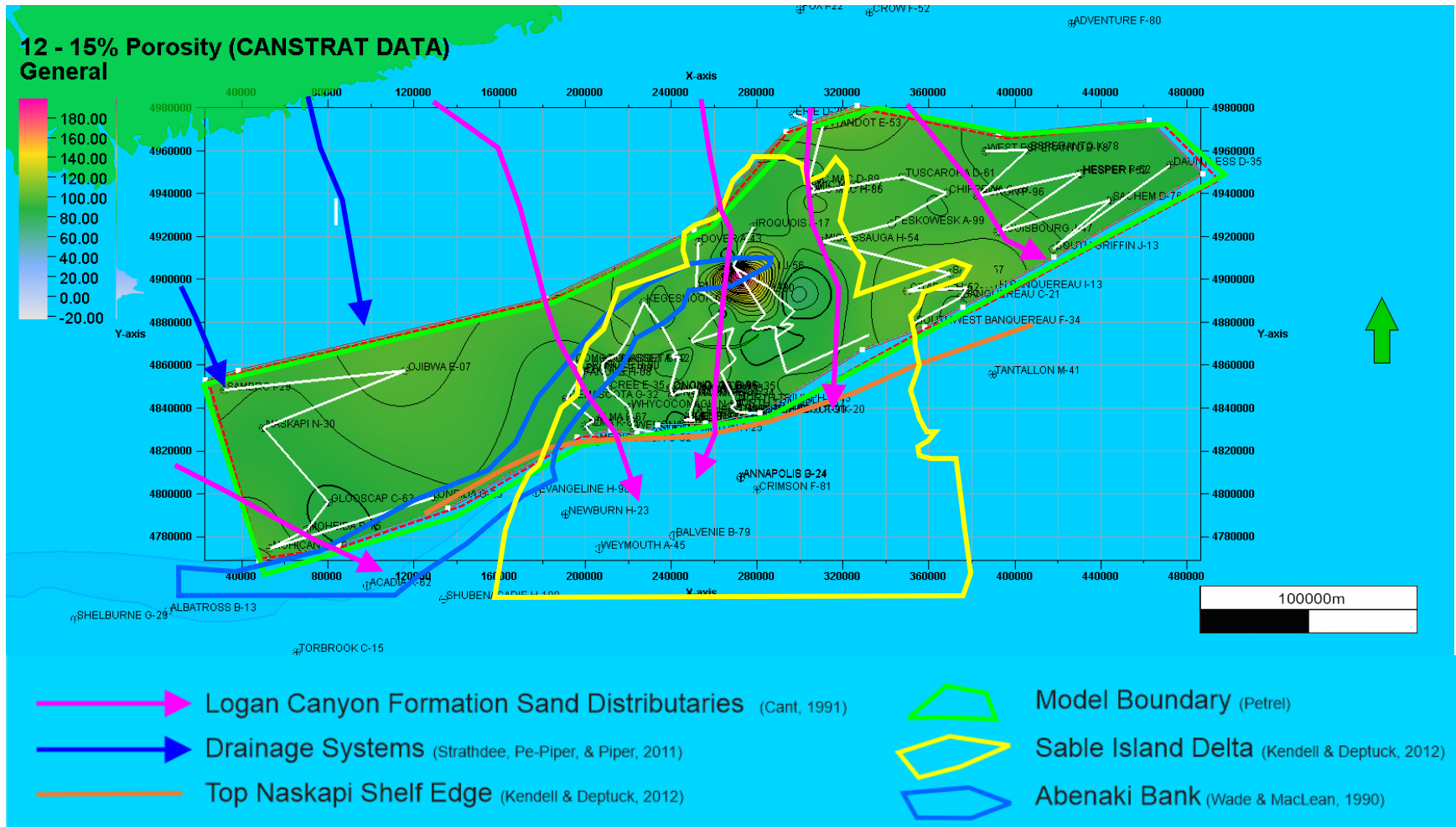


Figure 6.33: Meters of Naskapi Member that show 13-15% visual porosity as logged by Canstrat™. Peak amounts of 12-15% porosity lie near well Abenaki J-56. The white lines indicate the location of the cross sections. This map shows small areas with high porosity in the Sable Delta region.

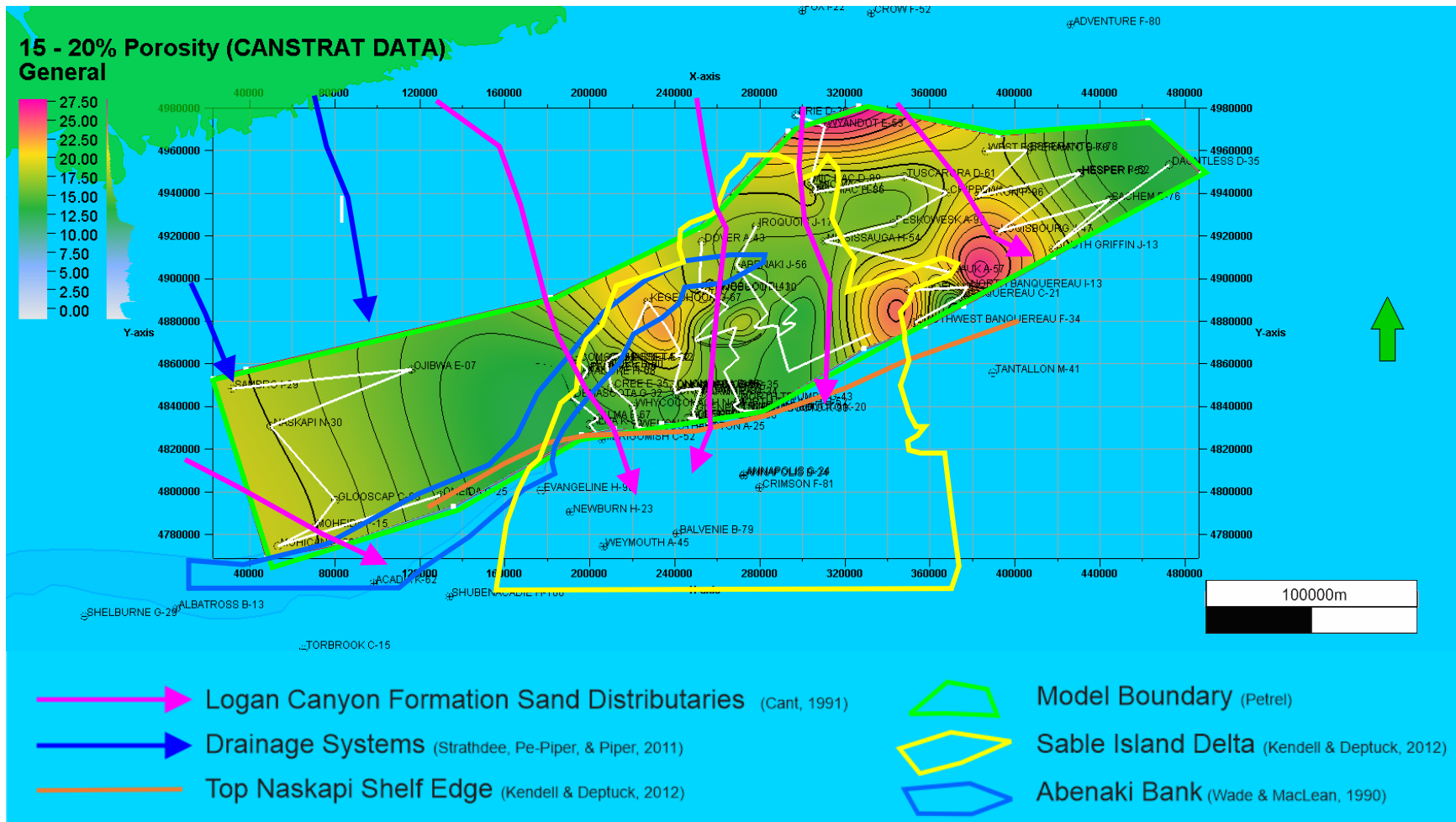


Figure 6.34: Meters of Naskapi Member that show 16 – 20 % visual porosity as logged by Canstrat™. The highest amount of porosity is seen in the north in the Sable Delta area, and two areas near the Erie D-26 and Wyandot E-53 wells. The white lines indicate the location of the cross sections. There are pockets of high porosity in the Sable Delta and also to the northeast of the Delta which is fed by Logan Canyon Formation distributaries.

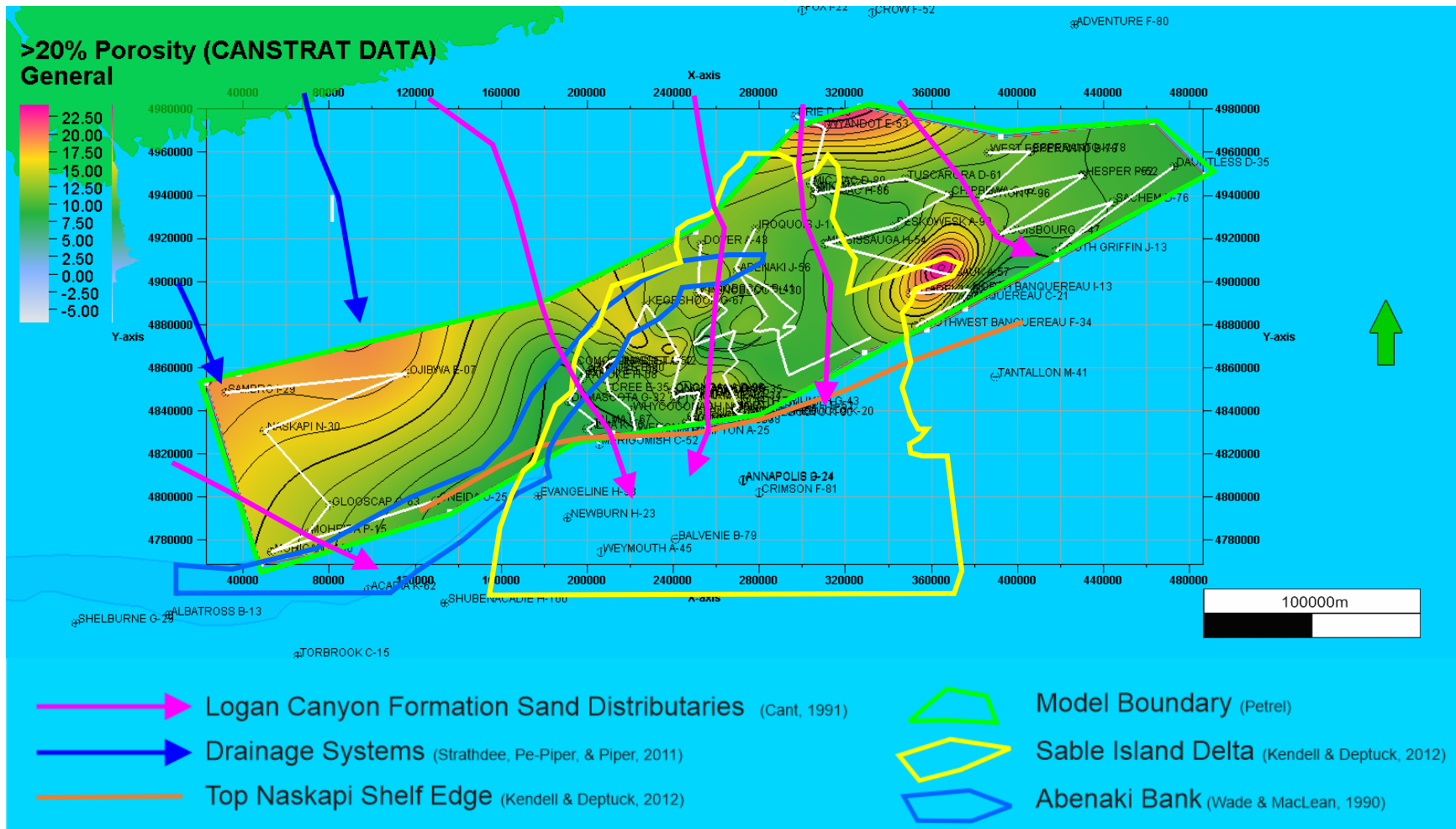


Figure 6.35: Meters of Naskapi Member silts and sands that show >20 % visual porosity as logged by Canstrat™. The highest porosity is seen on the area of the Sable Delta, the Shelburne Delta and regions with an influx of silt and sand. The white lines indicate the location of the cross sections.

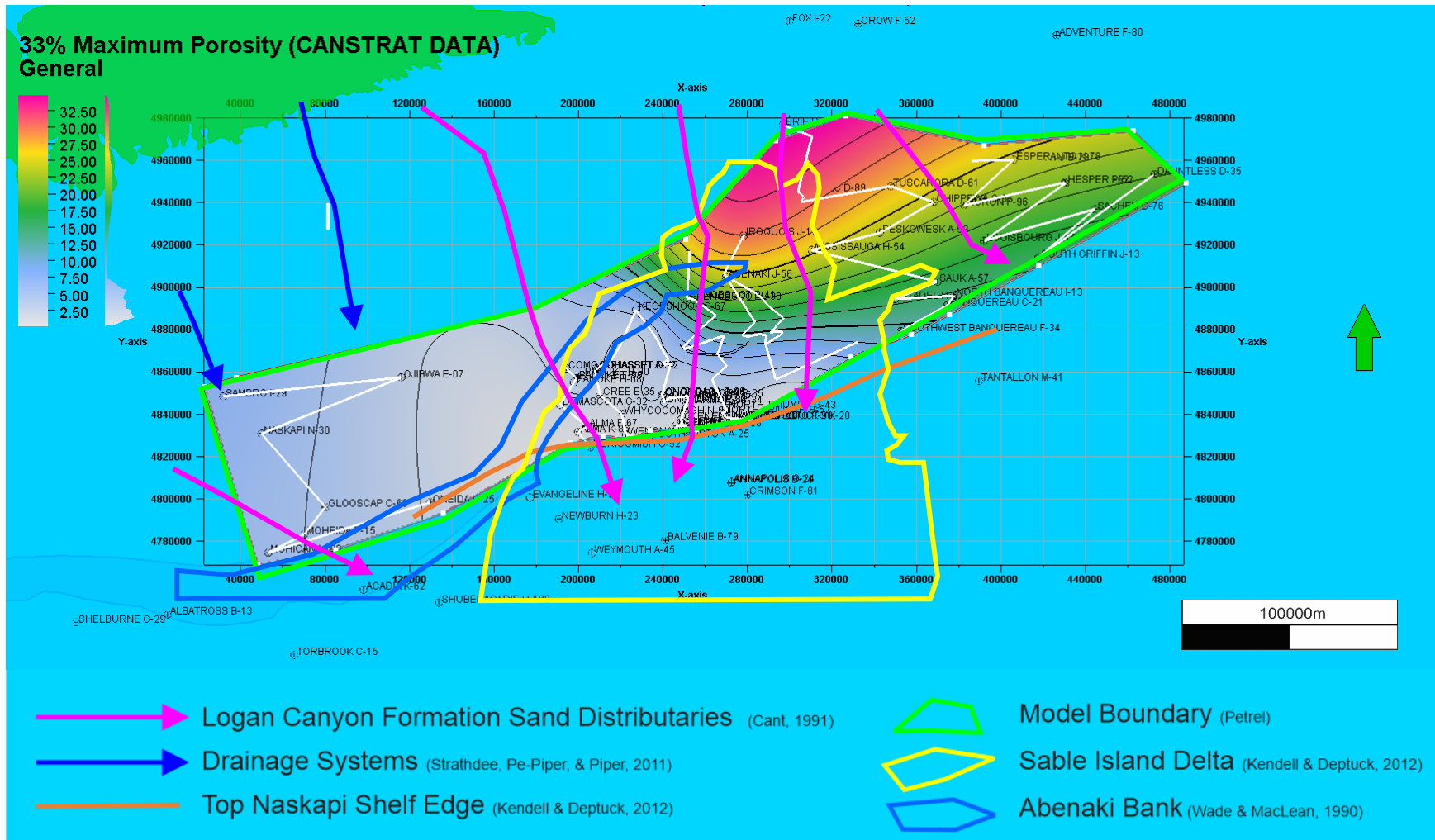


Figure 6.36: Meters of Naskapi Member that show 33% or maximum possible visual porosity as logged by Canstrat™. Overall, the highest amount of maximum porosity was seen in the area of the Sable Delta, and to the northeast, which was fed by the Logan Canyon Formation distributaries. Here, clean sands deposited on the delta have the highest porosity and have the potential to be reservoir rock. The white lines indicate the location of the cross sections.

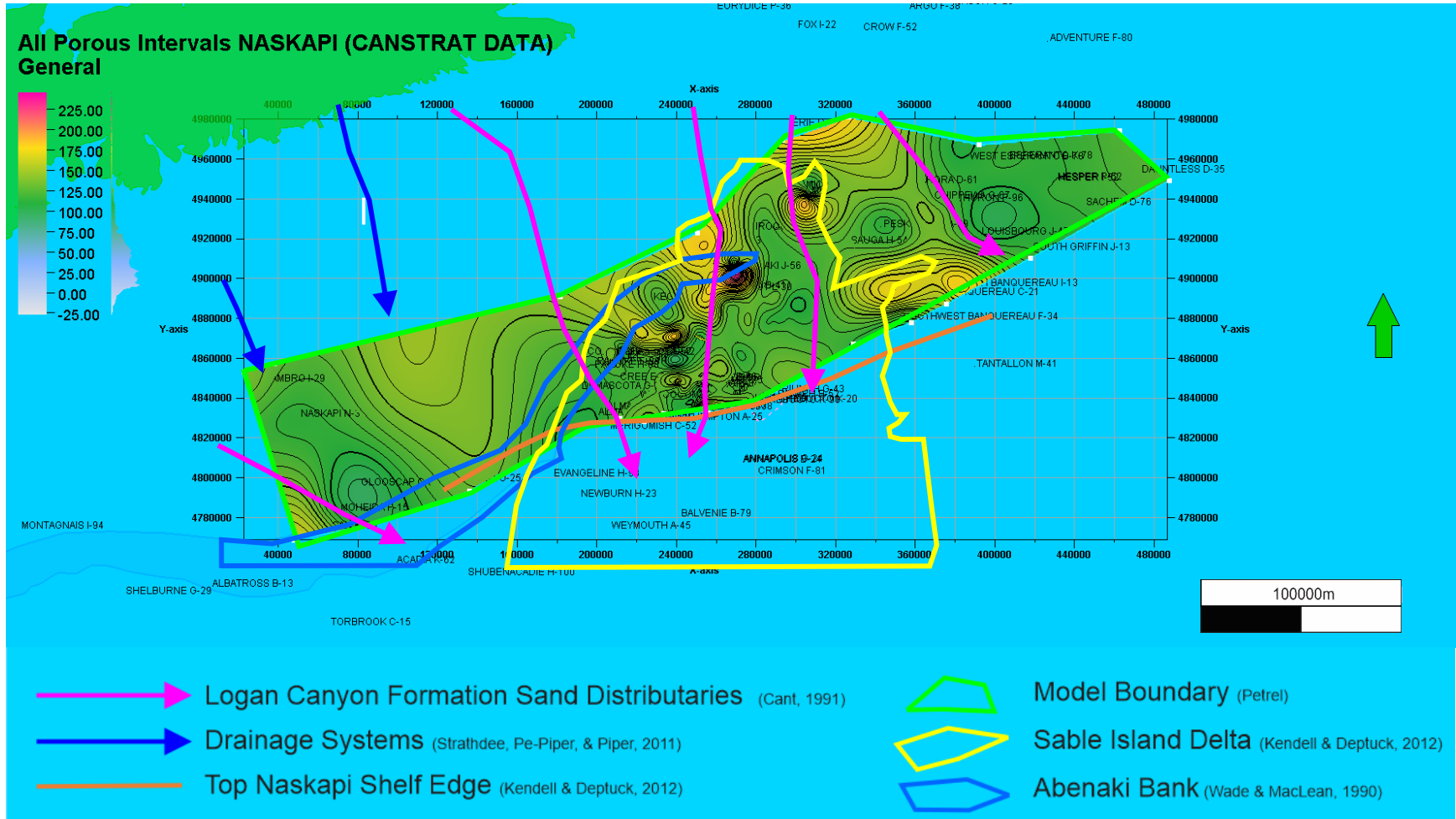


Figure 6.37: Meters of Naskapi Member that show a summary of all visual porosity estimations as logged by Canstrat™. The greatest amount of porous sands and silts are seen in the Sable Delta area in pockets near wells Erie D-26 and Wyandot E-53. The white lines indicate the location of the cross sections.

6.6 Continuous Wireline Log Data Maps in 2D and 3D

2D continuous wireline log data maps were created from gamma ray, density, resistivity, and sonic logs. 3D models were created from sonic logs.

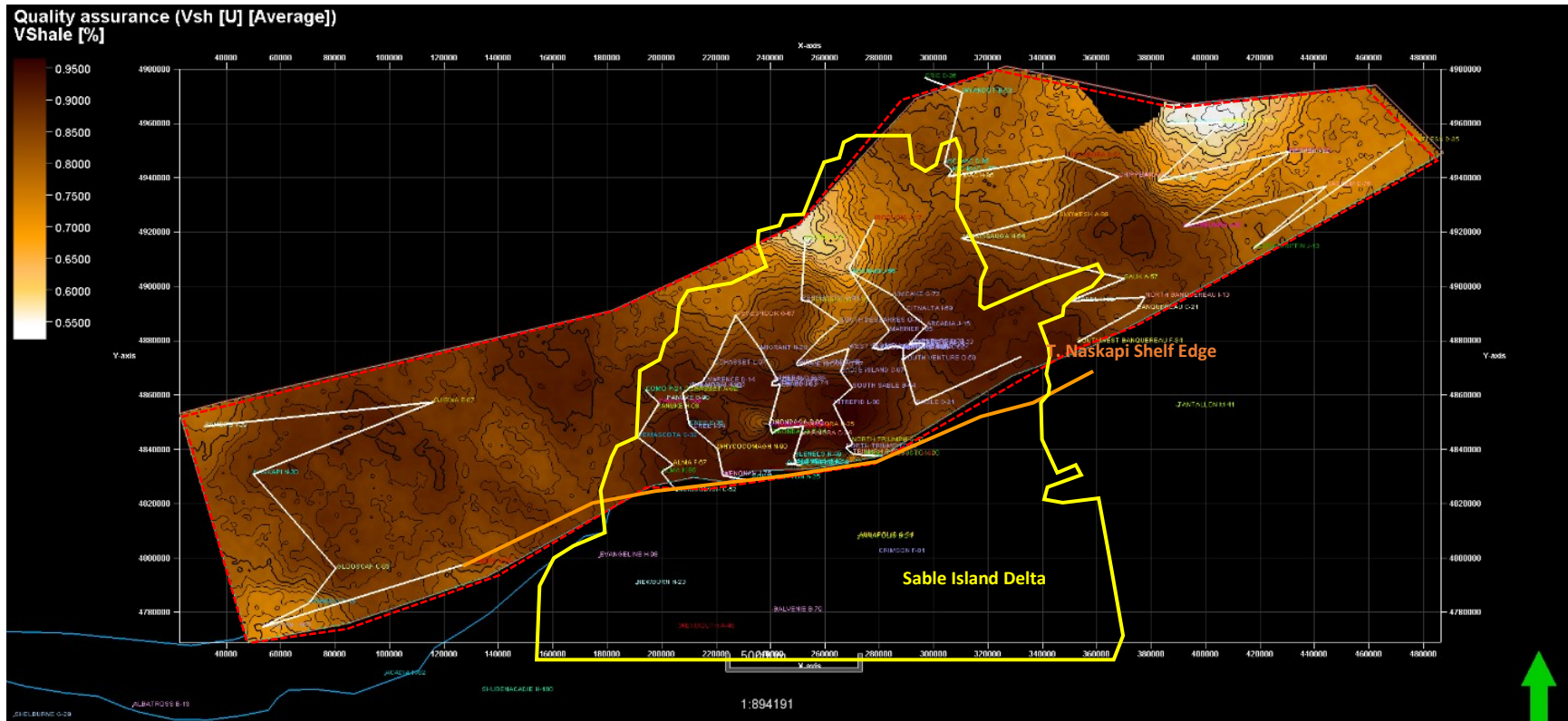
Gamma Ray logs show the amount of sand and shale in the rock interval. Low gamma ray values indicate sands and higher gamma ray values indicate shales. The gamma ray wireline log is also used to calculate the shale volume, which is the percentage of the total thickness of the Naskapi Member that is composed of shale. On Figures 6.38 and 6.39, one can see that relatively low shale volumes are in the area of the Sable delta to the northeast, in pockets to the south of the Abenaki bank in the Sable Island area, and to the north of the Abenaki Bank in the Glooscap C-63 area. Relatively large amounts of shale are to the southeast of the Sable Delta, in pockets to the southeast of the Abenaki Bank in the Sable Island area, and to the NW of the Abenaki Bank towards the Glooscap area. The shale volume in general thickens basinward.

Values from the density log are measured in g/cm³ and indicate rock type and the existence of pore space. Lower values indicate formation water type or the possibility that hydrocarbons are present. The lower density values could indicate hydrocarbons filling the pore space as they are less dense than salt water. The higher density areas could indicate rock types of quartz, calcite or dolomite without formation water content. Maps are seen in figures 6.40 and 6.41. In the region of the Alma F-67, Glenelg N-49, North Triumph G-43 and Southwest Banquereau F-34 wells, the density is the highest with values from 2.55 – 2.6 g/cm³ indicative of quartz clastic content. When compared with the cross sections and viewing the lithology data alongside, the following observations are noted: Southwest Banquereau F-34 has high density shales, along with Alma K-85, Glenelg H-38, Glenelg N-49, North Triumph G-43, North Triumph B-52 and Chebucto K-90. West Chebucto K-20 shows high density siltstone with some high-density shales while Glenelg E-58 shows high density limestones. Alma F-57 shows high density sands with limestone.

A quality assurance map showing average resistivity values using sequential Gaussian simulation is featured in Figure 6.42. Higher resistivity values point to lower conductivity of electricity. Purple areas indicate more fluid bearing sands and blue/yellow indicates more compacted shales (less fluid bearing). The areas of low resistivity could indicate zones of water saturation, the medium area could indicate gas and the highest measurements in the area of Citadel H-52 could indicate oil saturation. This map could also be interpreted to show all porous intervals and there is a similarity to figure 6.37 showing visual porosity from Canstrat™ data.

Figures 6.43 to 6.47 were all created using sonic log data. High sonic values indicate low velocity, and low sonic values indicate high velocity. An area of low velocity sediments was shed northwest of the Abenaki Bank. Low velocity can indicate higher amounts of organic matter being present, as seen near the Sambro I-29 and Ojibwa E-07 wells. Low sonic values near Southwest Banquereau F-34 points to high velocity and lower amounts of organic matter in the Naskapi Member. A velocity map was calculated from the sonic log values. Both sonic values and velocities were modelled in 3D.

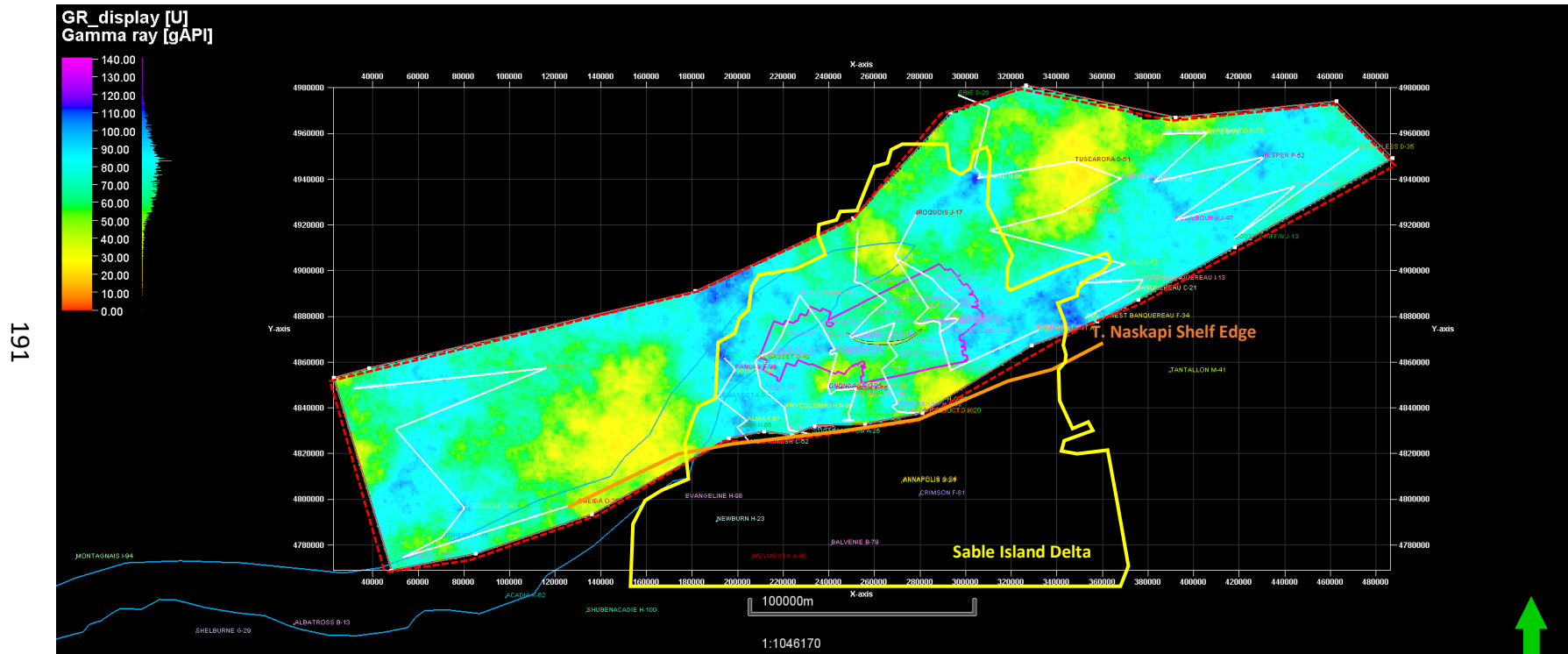
6.6.1 Shale Volume (V_{shale}) Calculated from Gamma Ray Logs Mapped in 2D



190

Figure 6.38: The Shale volume calculation is the percentage of the total meters of Naskapi Member that is composed of shale, using the gamma ray wireline log to calculate. On this map one can see that relatively low shale volumes are in the area of the Sable delta to the northeast, in pockets to the south of the Abenaki bank in the Sable Island area, and to the north of the Abenaki Bank in the Glooscap C-63 area. Relatively large amounts of shale are to the southeast of the Sable Delta, in pockets to the southeast of the Abenaki Bank in the Sable Island area, and to the NW of the Abenaki Bank towards the Glooscap area. The white lines indicate the location of the cross sections. Shale volume in general thickens basinward.

6.6.2 Gamma Ray Log Values Mapped in 2D



191

Figure 6.39: The map of gamma ray values made in Petrel™, showing the average of gamma ray values using sequential Gaussian simulation. Low gamma ray values indicate sands and higher gamma ray values indicate shales. The white lines indicate the location of the cross sections.

6.6.3 2D Density Log Values Mapped in 2D

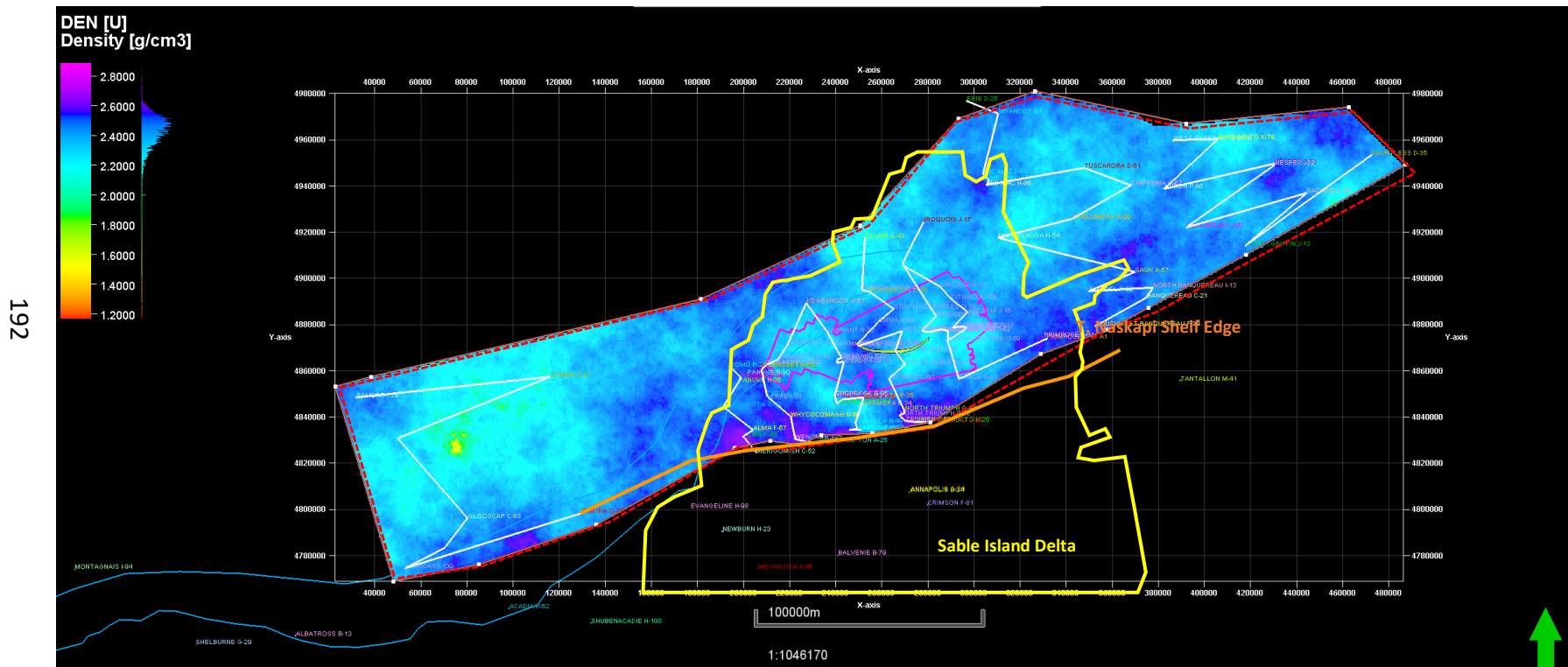


Figure 6.40: Map of the values from the density log in g/cm3. Compare this to the quality assurance map using average values is seen in Figure 6.41 below. The white lines indicate the location of the cross sections and the pink outline shows the location of the MegaMerge seismic cube. The lower density values mapped, shown in the small yellow area could indicate hydrocarbons filling the pore space as they are less dense than salt water. The higher density areas of dark and light blue could indicate rock types of quartz, calcite or dolomite without formation water content.

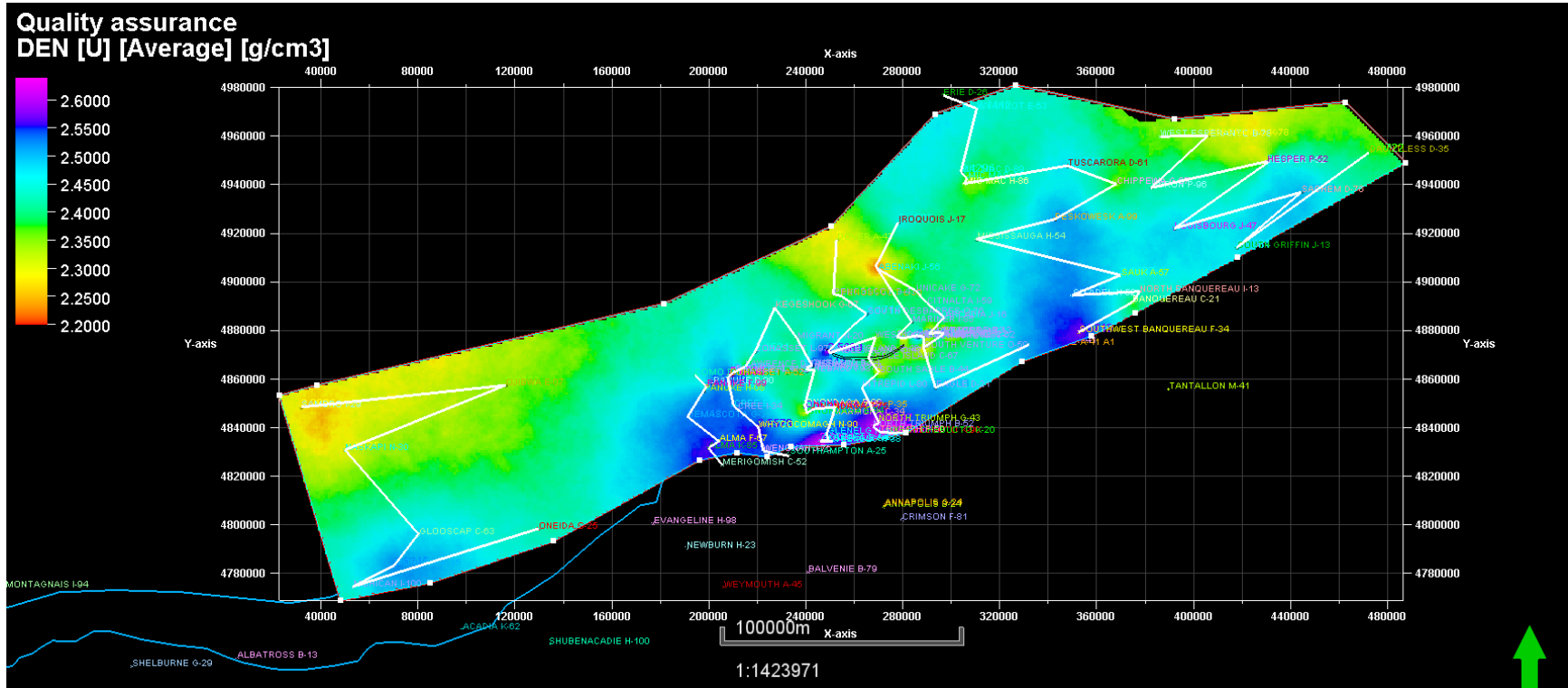


Figure 6.41: Quality assurance map of the average density values. In the region of the Alma F-67, Glenelg N-49, North Triumph G-43 and Southwest Banquereau F-34 wells, the density is the highest with values from 2.55 – 2.6 g/cm³ indicative of quartz clastic content. When compared with the cross sections and viewing the lithology data alongside, the following observations are noted: Southwest Banquereau F-34 has high density shales, along with Alma K-85, Glenelg H-38, Glenelg N-49, North Triumph G-43, North Triumph B-52 and Chebucto K-90. West Chebucto K-20 shows high density siltstone with some high-density shales while Glenelg E-58 shows high density limestones. Alma F-57 shows high density sands with limestone. The white lines indicate the location of the cross sections.

6.6.4 Resistivity Log Values Mapped in 2D

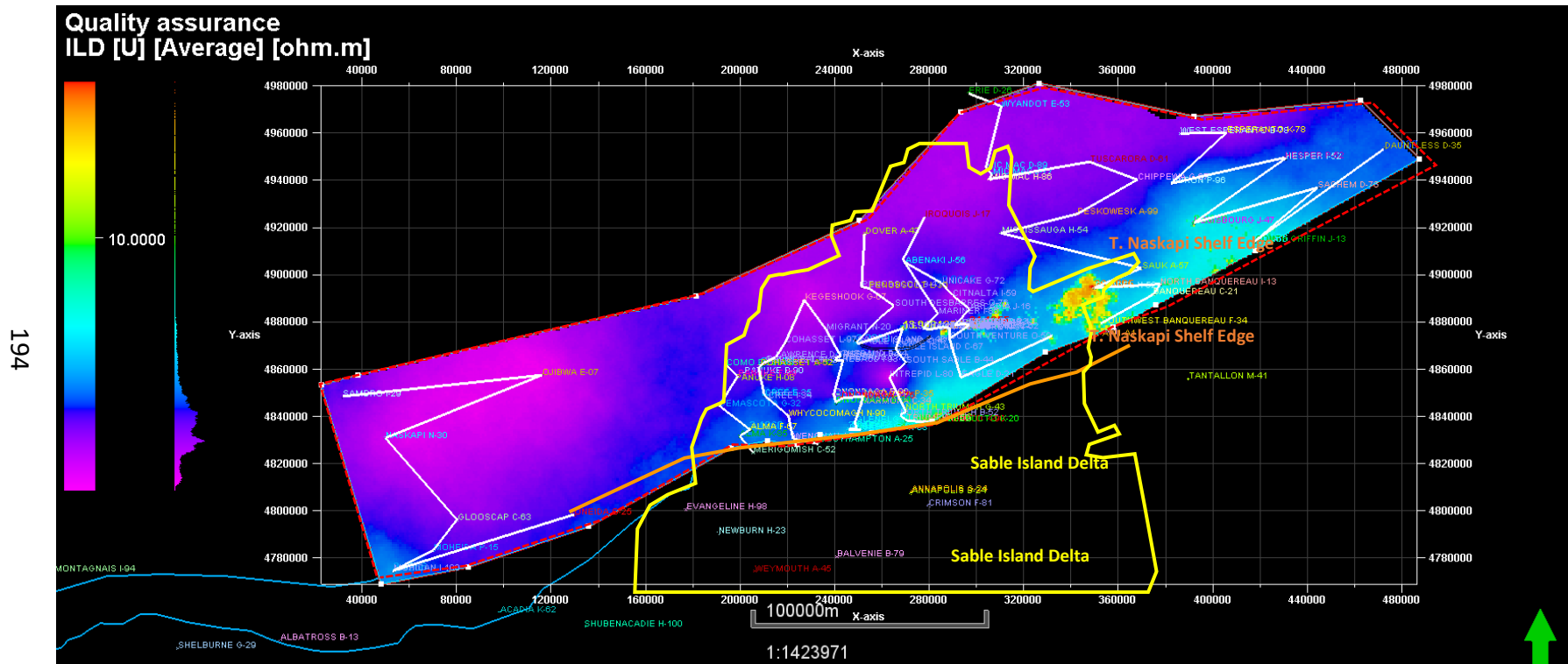


Figure 6.42: Quality assurance map showing average resistivity values using sequential Gaussian simulation. Higher resistivity values point to lower conductivity of electricity. Purple areas indicate more fluid bearing sands and blue/yellow indicates more compacted shales (less fluid bearing). The areas of low resistivity could indicate zones of water saturation, the medium area in turquoise could indicate gas and the highest measurements in the area of Citadel H-52 could indicate oil saturation. The white lines indicate the location of the cross sections. This map could also be interpreted to show all porous intervals and is similar to figure 6.37 using visual porosity from Canstrat™ data.

6.6.5 Sonic Log Values Mapped in 2D and Modelled in 3D

195

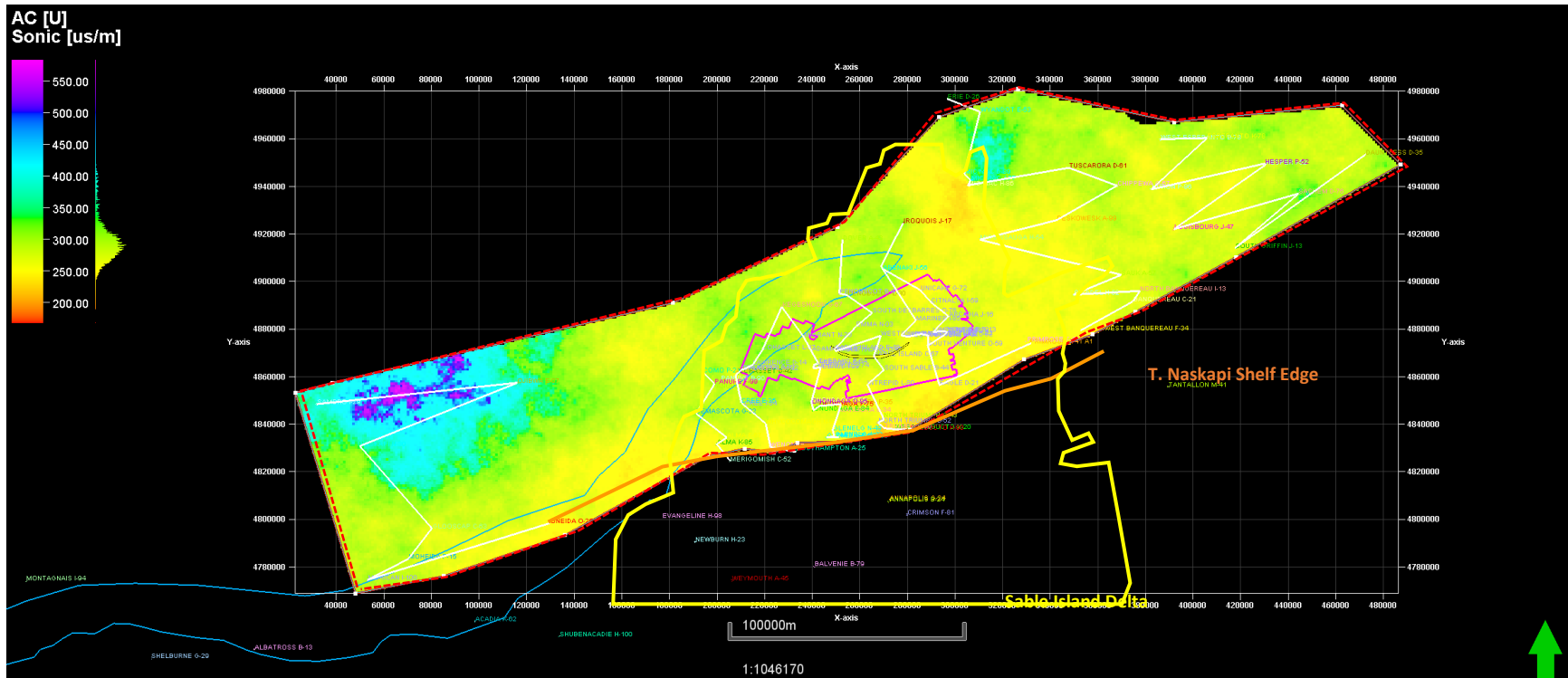


Figure 6.43: Map of the sonic log values in contrast with the quality assurance map seen in Figure 6.44 below. The white lines indicate the location of the cross sections. This map shows the actual values and the quality assurance map uses the average values.

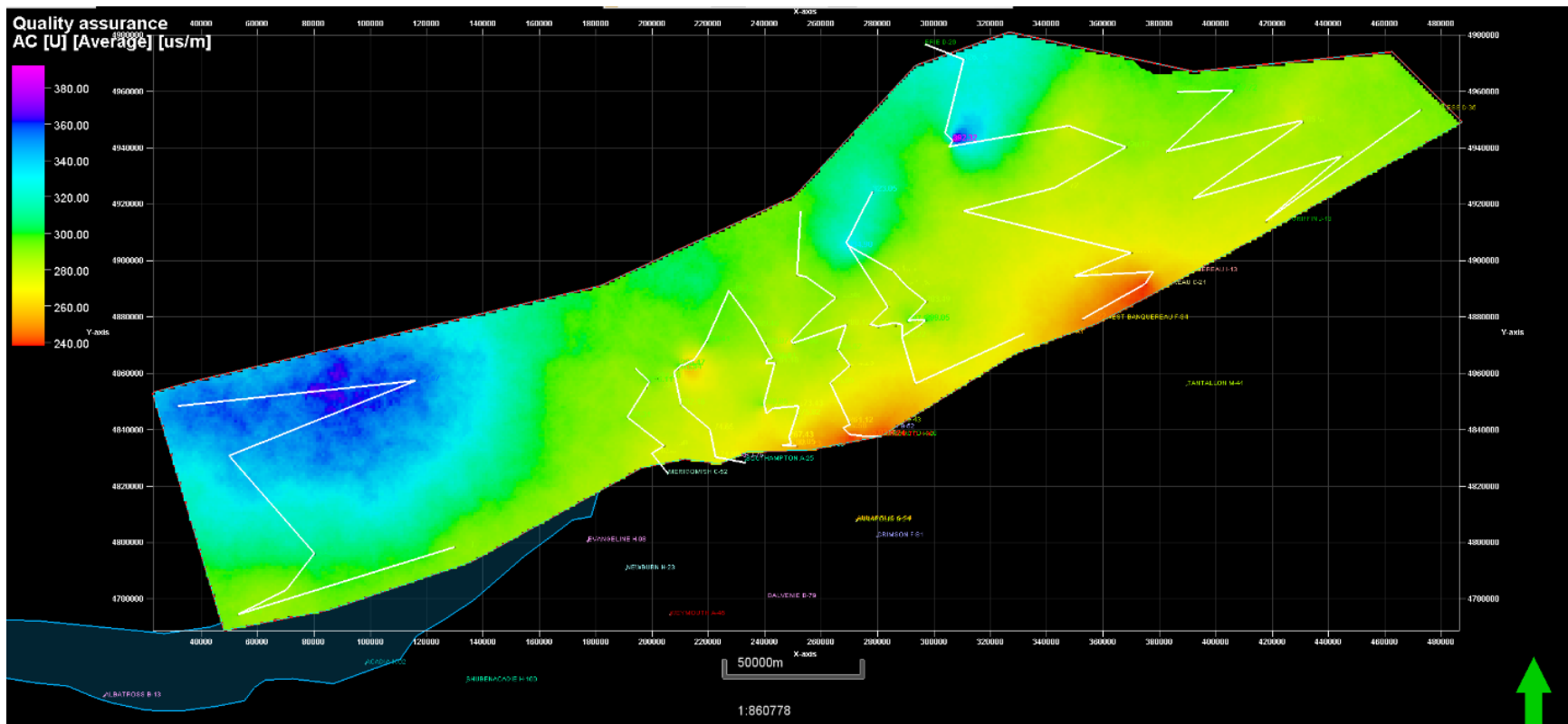


Figure 6.44: Quality assurance map of the AC (sonic) logs show the average values. The white lines indicate the location of the cross sections. Blue transparent zone indicates position of the Jurassic Abenaki Bank. A higher average sonic value indicates low velocity and perhaps higher amounts of organic matter, as seen near the Sambro I-29 and Ojibwa E-07 wells. Low sonic values near Southwest Banquereau F-34 points to high velocity and lower amounts of organic matter in the Naskapi Member.

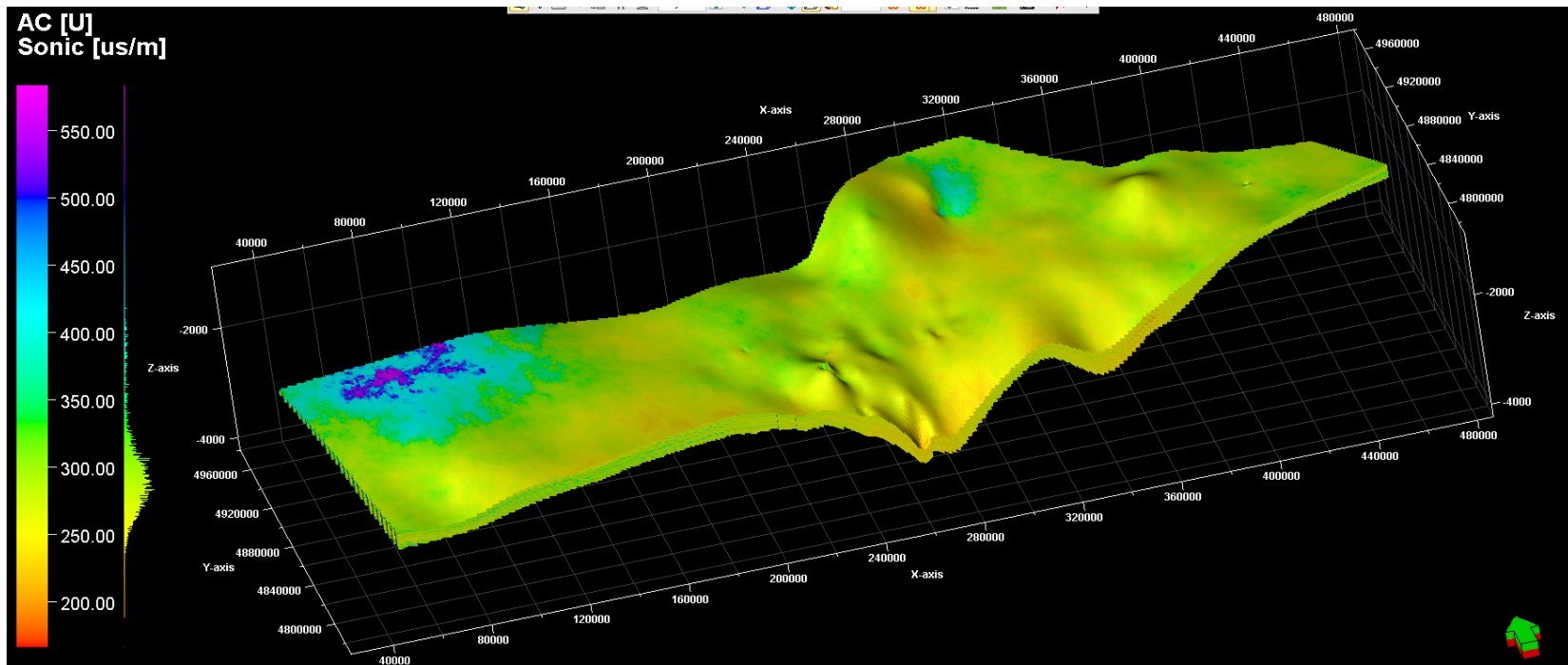


Figure 6.45: Sonic values modelled in 3D. High sonic values indicate low velocity, and low sonic values indicate high velocity. An area of low velocity sediments was shed northwest of the Abenaki Bank. Low velocity could indicate higher amounts of organic matter present in the Naskapi Member.

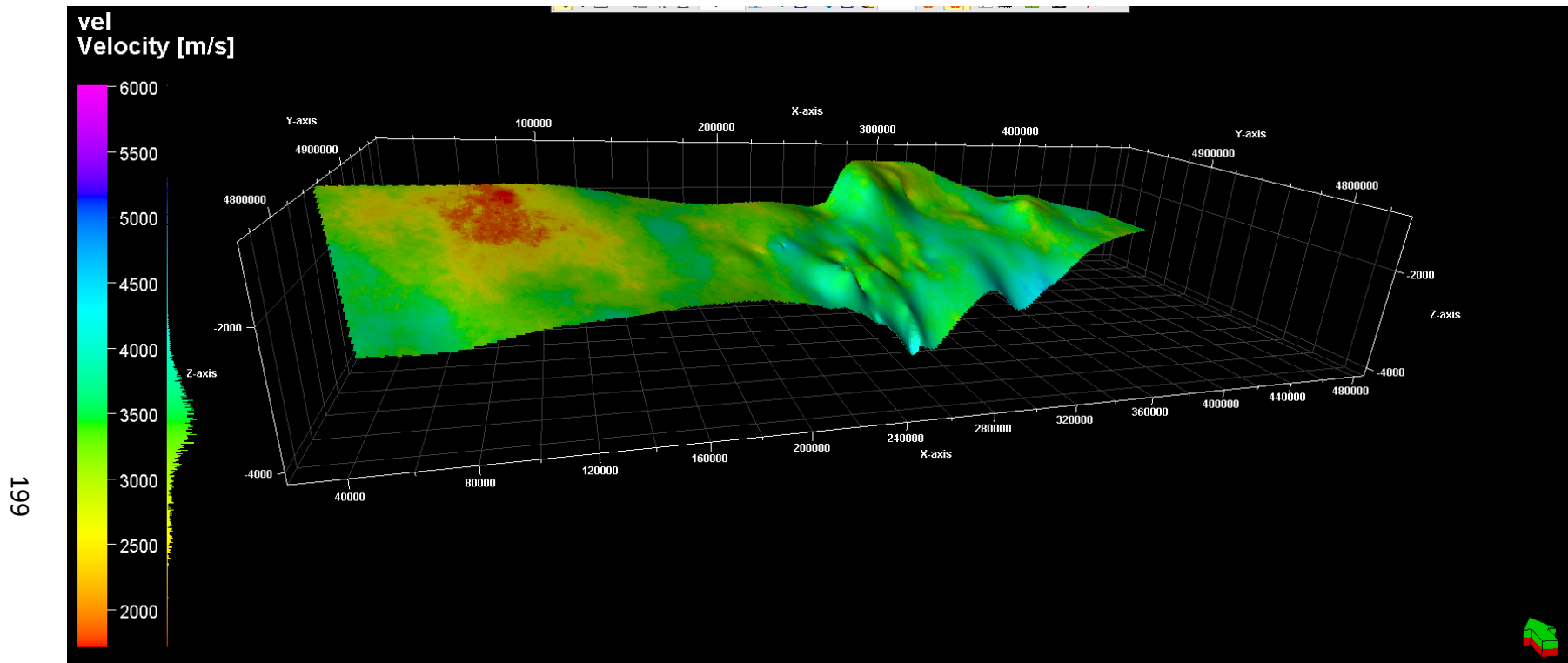


Figure 6.47: 3D model of velocity data. An area with low velocity is in the northwest near the Sambro I-29 and Ojibwa E-07 wells. This could indicate higher amounts of organic matter present in the Naskapi Member.

6.7 Seismic Horizon Maps

For the purposes of this study, seismic lines have been interpreted to show the extent of the Naskapi top and bottom, with the bottom pick being equivalent to the top of the Missisauga formation. An example is shown in Figure 6.48 where a cross section view of a seismic section shows Sable Island C-67, West Venture N-91 and Arcadia J-16 wells.

The top of the Missisauga formation is shown to be a zone of low impedance. High impedance zones are black peaks, followed by white troughs representing low impedance. Examples of high impedance zones are the distinctive and widespread Wyandot, Petrel™ and the O Marker tops.

6.7.1 2D and 3D Maps of the Naskapi Member and Missisauga Formation

Maps were made of the Naskapi and Missisauga horizon tops which are seen in Figures 6.49 and 6.50. 3D maps were made of the surfaces of the Naskapi Member and the Missisauga Formation which are seen in Figures 6.51 and 6.52.

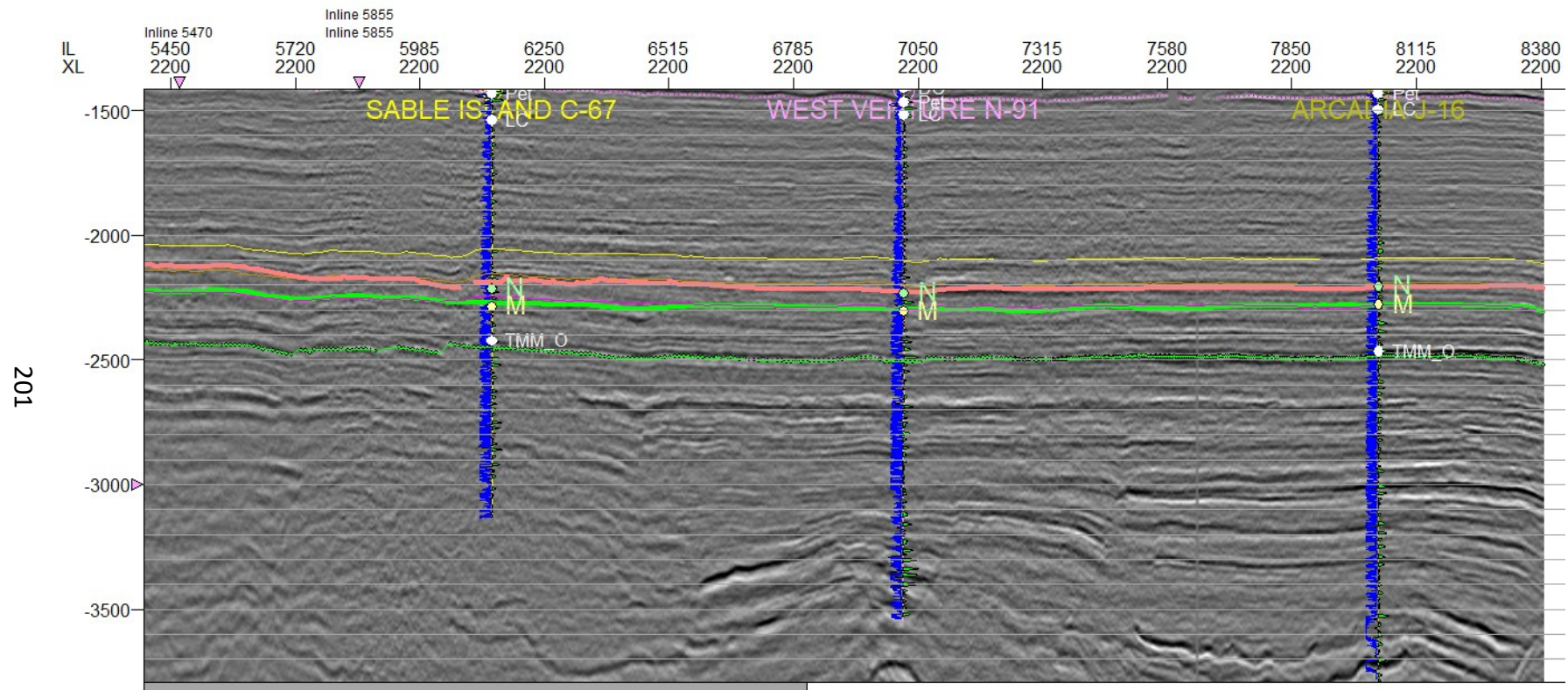


Figure 6.48: A cross section view of a seismic section showing Sable Island C-67, West Venture N-91 and Arcadia J-16 wells, which were used to pick the Naskapi Member and Missisauga Formation tops. The Naskapi Member horizon is indicated with a pink line and the Missisauga Formation horizon is indicated by the lime green line. The dotted green line indicates the location of the 'O' Marker.

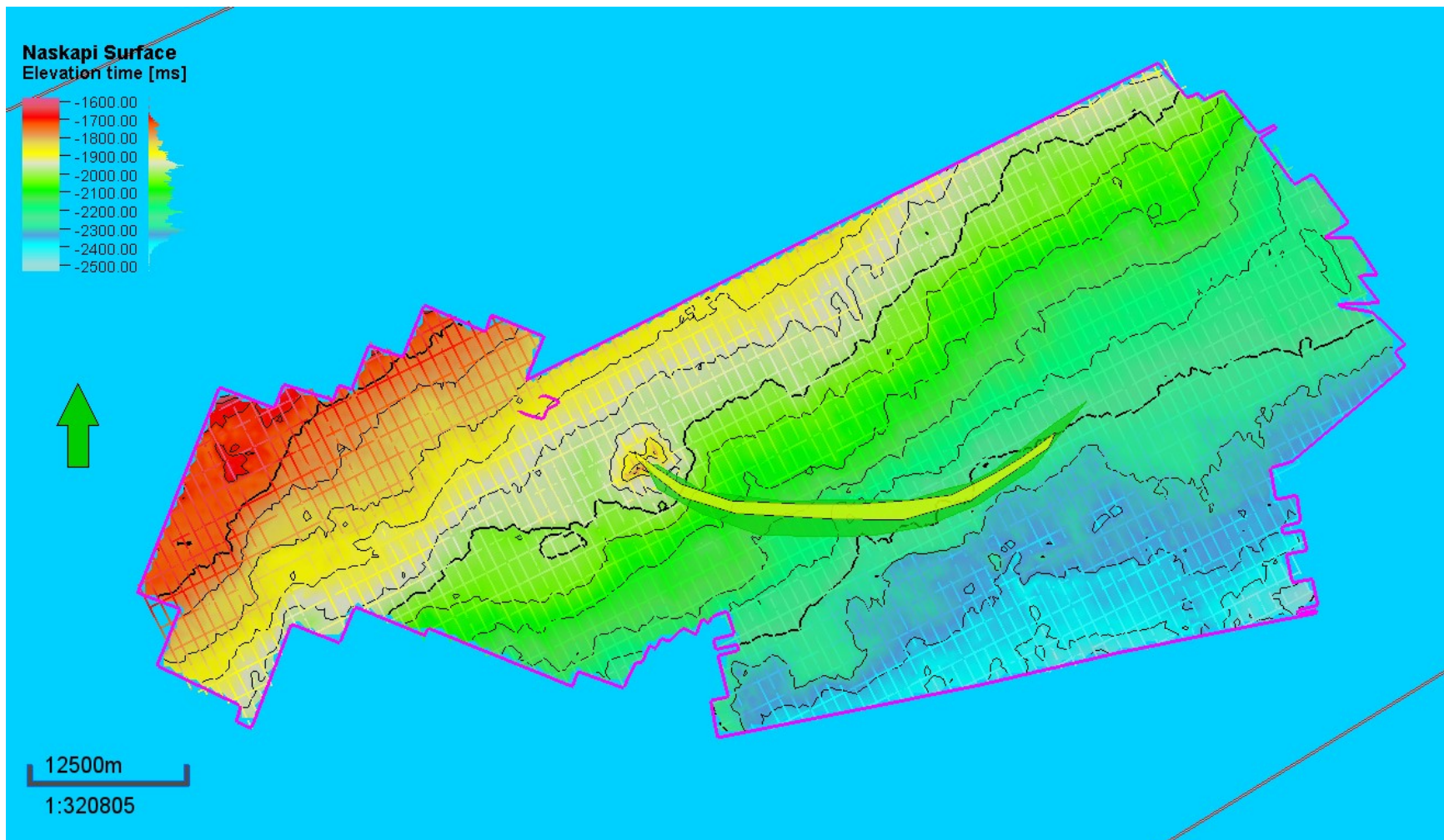


Figure 6.49: Contour map of the Naskapi Member horizon from seismic interpretation of the MegaMerge cube. The yellow crescent in the centre of the MegaMerge cube is Sable Island for reference. The cross-hatching indicates the density of the seismic lines that were used in the interpretation.

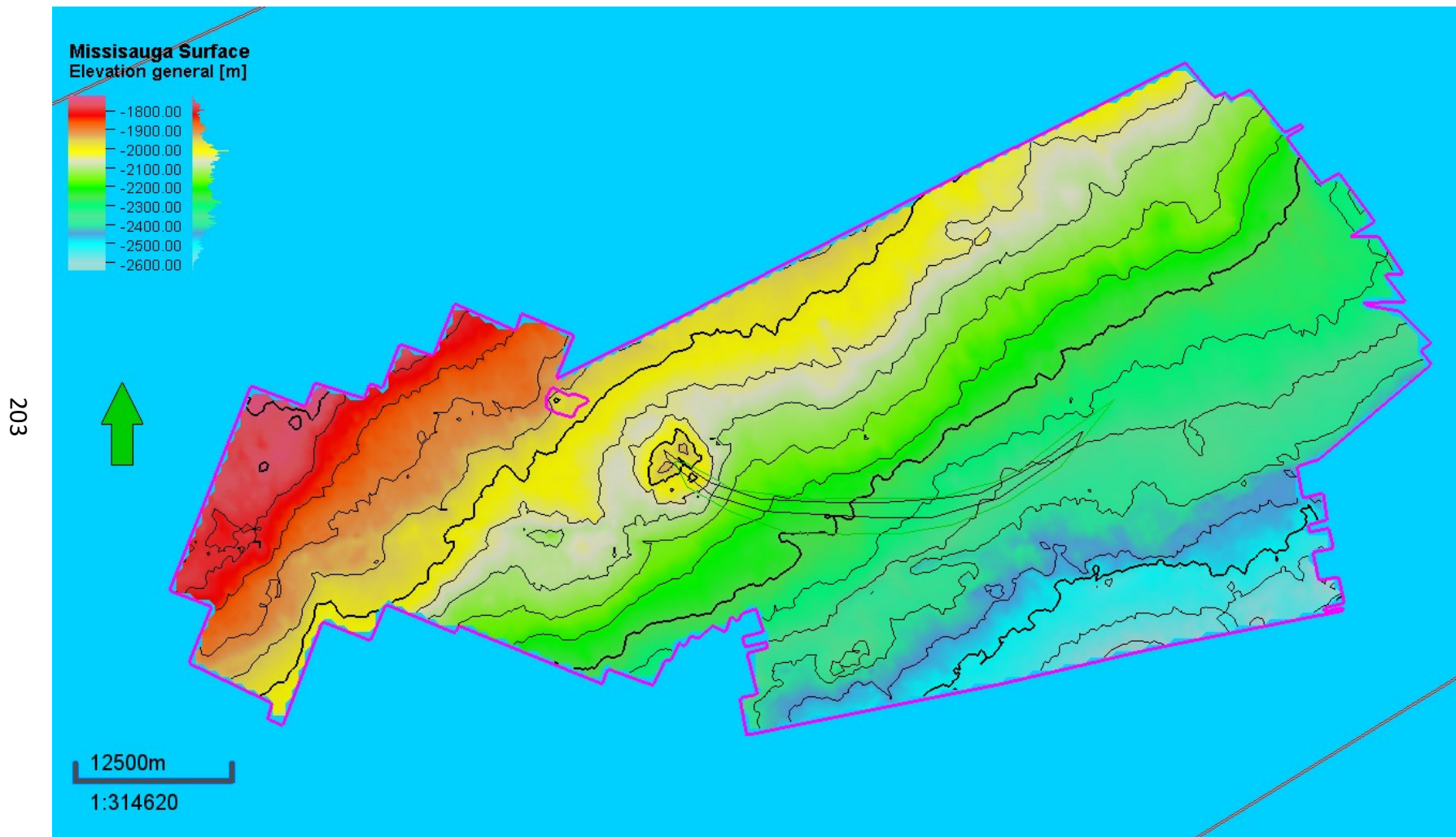


Figure 6.50: Contour map of the Missisauga Formation horizon depths from seismic interpretation of the MegaMerge cube. The black-line crescent shape in the centre of the cube is an outline of Sable Island.

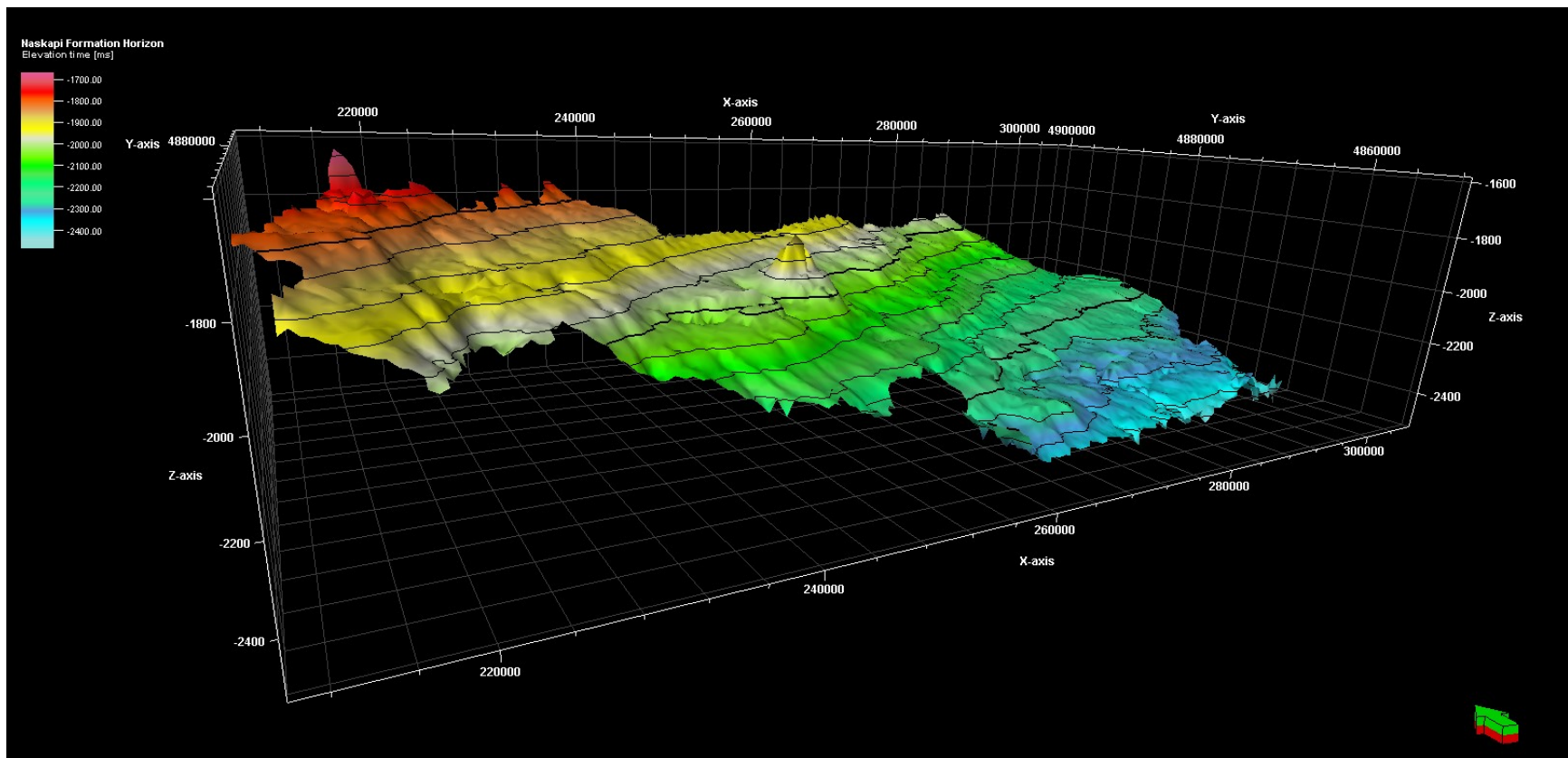


Figure 6.51: Naskapi Member horizon surface in 3D from seismic interpretation in the MegaMerge Cube.

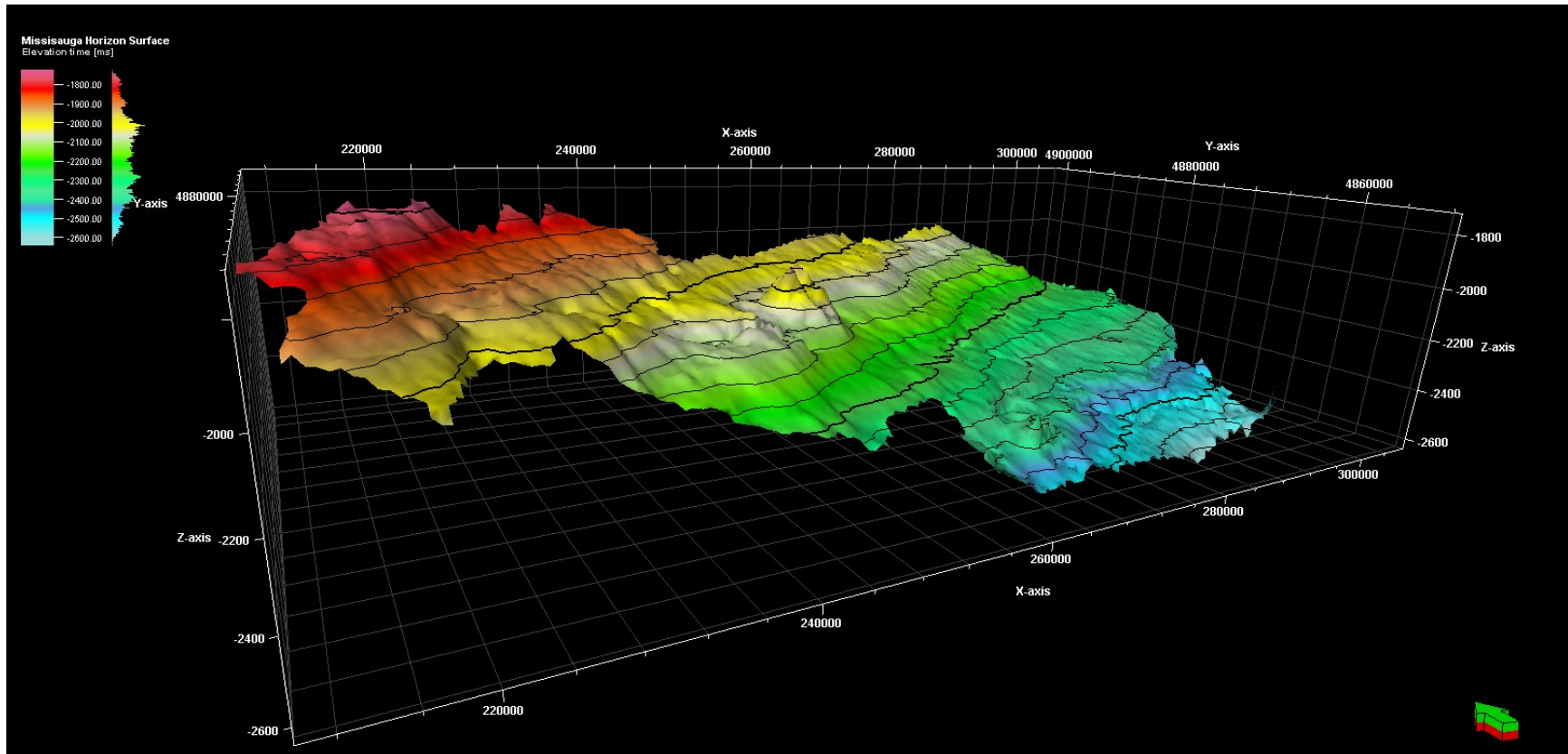


Figure 6.52: 3D image of the Missisauga Formation horizon surface as expressed from seismic interpretation in the MegaMerge Cube.

Chapter 7: Discussion

7.1 Discussion on Naskapi Member Deposition and Organic Content

The primary research objective for this study was to identify the stratigraphy and sedimentology of the Naskapi Member and determine the presence of organic-rich intervals and their potential to be effective source rocks. Relevant oceanic and depositional conditions in the Cretaceous proto-Atlantic that could affect the presence of organic-rich intervals in the Scotian Basin were examined, and a comparison with such deposits elsewhere in the circum-Atlantic was made.

The Naskapi Member does not contain the high levels of preserved organic matter as is seen elsewhere in the Cretaceous proto-Atlantic (Beicip-Franlab, 2016). It is not considered to have the potential to be a viable source rock, as there are insufficient amounts of intervals with high total organic carbon (TOC) making it volumetrically insignificant as an effective Cretaceous source rock. This was addressed with a hypothesis that a high delta-derived sediment load from the Sable Delta diluted the deposition of organic matter, and when combined with an ocean circulation pattern that did not foster preservation of said organic matter, resulted in ineffective source rock.

This hypothesis was tested by examining and mapping datasets through the Naskapi interval. The Naskapi interval was interpreted in the MegaMerge seismic cube and mapped. The mapped results were overlain with an outline of the Sable Delta as defined by Deptuck and Kendell (2012). Maps constructed with Canstrat™ data in Chapter 6 show sand, silt, limestone, marlstone, and variable shale content. These sets of maps, of seismic and lithology data, demonstrate dilution of the Naskapi shale due to input of siliciclastic sediments from the active Sable Delta, from deltaic sedimentary processes that likely continued during the Aptian.

The hypothesis also questioned whether adverse ocean circulation patterns affected the deposition and preservation of organic matter in the study area. Research into ocean currents, patterns, and supply of organic material via nutrients, and the location of zones of upwelling resulting in high productivity, indicated that ocean

processes had a significant effect on the productivity and preservation of organic material in the area of study (Trabucho-Alexandre et al., 2010). Current and circulation patterns control ocean productivity, nutrient supply, and zones of upwelling and downwelling. These determine the creation, location, deposition, and preservation of organic matter that can form effective source rocks (Trabucho-Alexandre et al., 2010). As discussed in 3.3.1, estuarine circulation of nutrient-rich waters can form nutrient traps, and the ensuing high production of biota results in deposits of organic-rich black shale, which if anoxic conditions prevail will create an oceanic anoxic event (Jenkyns, 1980). However, dilution can occur during a sea level highstand, as would have existed during the deposition of the Naskapi Member. Organic-rich sediments can be trapped and diluted with clastic sedimentary input (Bralower et al., 1994; Schlanger et al., 1987; Trabucho-Alexandre et al., 2010).

Another significant factor affecting ocean productivity in the study area, covered in section 4.5.2.8, was active mantle volcanism (Cloetingh and Haq, 2015). The breakup of Pangea and the opening of the proto-Atlantic resulted in upwelling magma at the mid ocean ridge and provided nutrients to the seawater. The newly opened Caribbean Seaway (see section 3.4.1) provided access and supplied nutrients derived from active volcanism in the Pacific Ocean (Hay et al., 1999; Trabucho-Alexandre et al., 2010). Elevated levels of volcanism also contributed to the increased sea level, discussed in 2.4.1.1, due to water expulsion from the mantle as it degassed, resulting in a net increase in water volume as less water was entrapped in subduction zones (Haq, 2014; Cloetingh and Haq, 2015).

The shifting ocean currents could alter the nutrient supply which feeds the biota, which in turn create organic-rich detritus, deposited in the shale (Arthur and Schlanger, 1979). Modelling of Cretaceous ocean currents indicates upwelling occurred to a large extent in the ITCZ zone near the equator, in the northern portion of present-day South America, and to a lesser degree in the basins of the northern proto-Atlantic in the Scotian Basin. According to modelling by Trabucho-Alexandre et al. (2010), the prevailing ocean currents moved in a west to east direction up the northern proto-

Atlantic coast to the Scotian Basin. However, clastic input from the Sable Delta and other sources diluted the mostly terrestrial organic matter supply, resulting in an ineffective source rock in these regions. Whereas elsewhere in the proto-Atlantic region, very rich undiluted beds of organic matter with significant TOC created outstanding effective source rock, for example the La Luna, within the Orinoco Belt in the eastern Venezuelan Basin and offshore Trinidad.

Today, the meridional overturning circulation transports heat and salinity by thermohaline circulation. In the Late Cretaceous, ocean circulation shifted from an east-west direction to a more north-south circulation as the southern Atlantic began to open along the southern Atlantic mid-ocean ridge. This contributed to a warmer polar gradient of approximately 30 degrees at that time, as compared to the present day 60 degrees, as discussed in section 3.1.4 (Hay and DeConto, 1999).

Organic-rich sediments can generate kerogens contributing to the TOC content. Thermal maturity (section 7.2) of these organic-rich sediments can generate a viable source rock for oil and gas exploration. In the Sable Delta area, the main kerogen is recognized as Type III, or terrestrial source material, which has generated mostly gas and minor liquids in the Scotian Basin. Type II kerogen and its associated black shale facies (and organic-rich deposits with good TOC) were deposited in anoxic or dysoxic conditions since the Late Paleozoic in the proto-Atlantic, especially on platforms and in circular or linear sags, sometimes in rifts and foredeeps but very rarely in half sags and deltas that exist in the Scotian Basin (see section 4.4.1). During the mid-Cretaceous in the eastern part of the North American marine shelf, the structural form for facies studies is classified as a half sag (a wedge of seaward-prograding clastics) or linear sag (elongated low areas with low angle sloping limbs) over a single rift (Klemme and Ulmishek, 1991).

Climate has also played a significant role in the accumulation of effective source rock in the Scotian Basin, as discussed in section 4.4.5. A warm climate with high humidity at middle latitudes is optimal for source rock deposition. However, the Scotian margin is thought to have had a dry climate. During the Aptian and Albian there was a

climate reversal which would have influenced sediment supply. During the Cretaceous it is thought the position of the ITCZ resulted in the Scotian Basin being in a dry zone with no monsoons, or other large storms, which would result in a lower sedimentation rate and a dryer climate in general (Trabucho-Alexandre et al., 2010). Oxygen isotope values were high during the Aptian, as they were during times when oceanic anoxic events were occurring. At those times, atmospheric CO² drawdown into seawater was significant.

7.2 Thermal Maturity

Significant deposits of TOC in organic-rich sediments are necessary for effective source rock. The quality of TOC is affected by maturity. If a potential source rock has been overheated or has generated hydrocarbons that have migrated away from the areas of interest, that source rock will not be effective. Maps of the vitrinite reflectance (VR) data, TOC values, temperature values, and shale thickness values from Canstrat™ data have been compared to determine the maturity of any potential source rock in the study area.

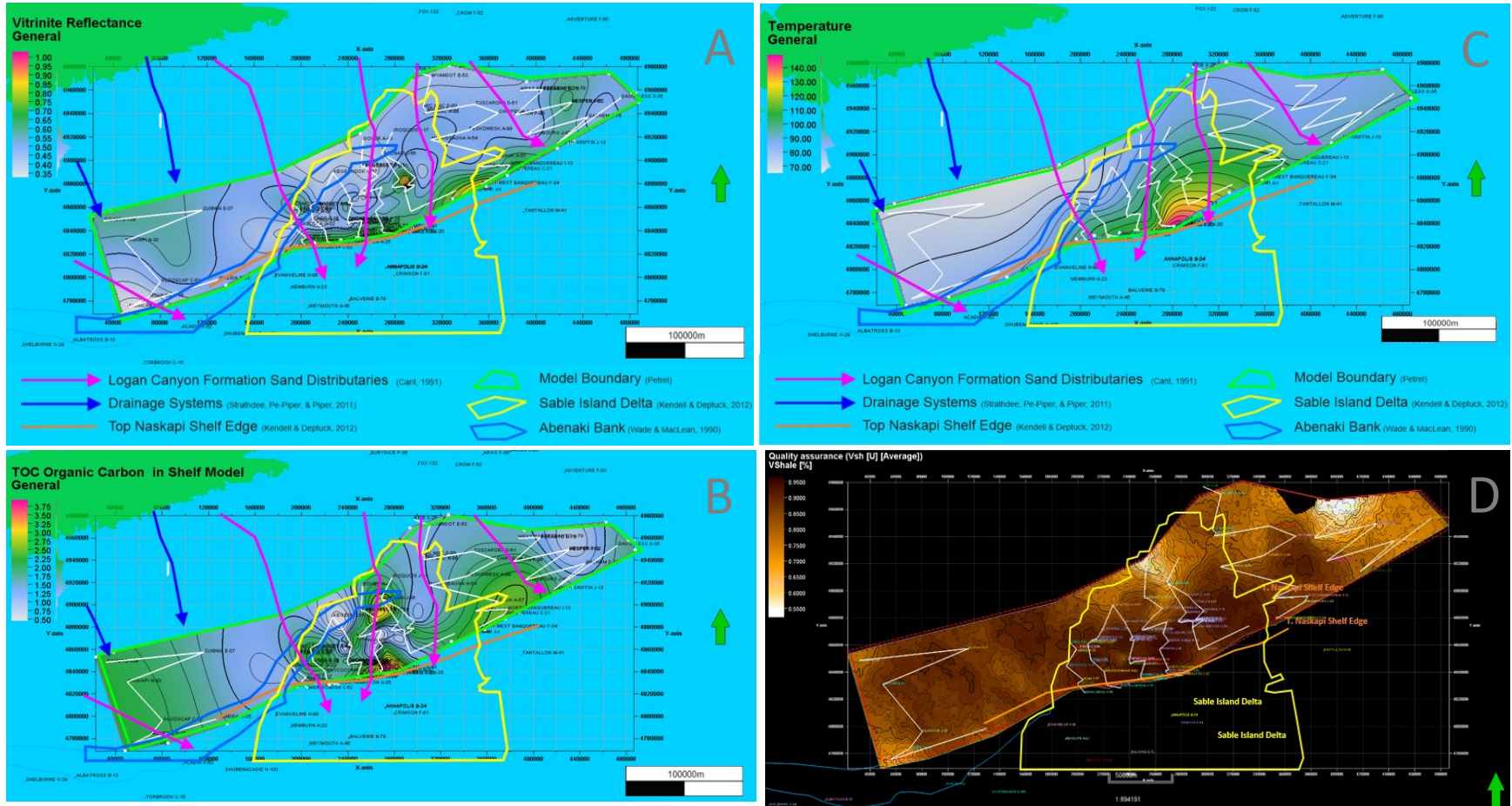


Figure 7.1: VR (A), TOC (B), temperature (C), and shale volume (D) maps as presented in Chapter 6, shown here to compare to comment on thermal alteration of organic matter in the Naskapi Member.

The four maps above in figure 7.1; TOC, VR, shale content, and temperature, can give some indication of thermal maturity of the study area. Vitrinite reflectance measures the thermal maturity of a rock, with higher values indicative of greater temperatures the rock was subject to, in turn indicating if the rock could have generated hydrocarbons. Based on the well data, the areas of peak VR values of approximately 0.9 exist near Southwest Banquereau F-34 well and south, as well as 0.8 near Venture B-43 well. This may indicate higher temperatures and possible over maturity in the Naskapi Member. VR values of 0.7 are mapped near the Alma wells and trend eastward and slightly north through Triumph towards the West Banquereau and South Griffin wells. To the west of the Alma well the VR is generally between 0.35 to 0.5 and these lower values trend east-northeast through the Kegeshook, Missisauga, Micmac, and Tuscarora wells and north from there, with the exception of a VR value of 0.65 near the Como well. Values from both the VR and shale content maps show that the northern part of the delta area had more sand with corresponding less organic matter accumulated and available to show vitrinite reflectance.

Thirty-eight of the subject wells had temperature data but only eight had DST data to plot. Log temperature data was not compiled and mapped, as these temperatures are usually cooler than the surrounding formation waters and would skew the results. Naskapi Member temperatures increase with depth, with the highest temperature near the Chebucto and Triumph wells with temperature decreasing towards the west within the member. Comparison of the temperature data with the vitrinite reflectance data shows variability that indicate that the temperature regime has changed with time.

Total organic carbon content increases in the south of the study area, the distal regions of the Sable Delta, which suggests less dilution from coarser deltaic siliciclastics. The temperature map also demonstrates higher values in the south region of the study area. The higher temperature regime may be a factor of increased burial depths. The shale content map shows the highest shale values in the south of the study area, with

lesser amounts in the north nearer to the mouth of the Sable Island Delta, which would contain more sand, silt, and clastics to dilute the shale and organic matter contents.

7.3 Cross Sections

Examination of the nine cross sections created (Appendix H) through the Naskapi Member, demonstrate a shale sequence of varying thickness with three to five pulses of coarse clastics comprised of sand, silt, and some thin limestones, most notably in the Sable Delta region. This indicates some distal deltaic influence during the transgressive sea level highstand environment when the Naskapi Member was deposited. The cross section located just north of the Abenaki Bank shows a lesser amount of sand and silt, but several noticeable layers of limestone-rich clay. Each cross section shows the progressive seaward thickening and increase in mud content of the Naskapi Member, while landward it becomes thinner and sandier.

7.4 Lithology Data Maps

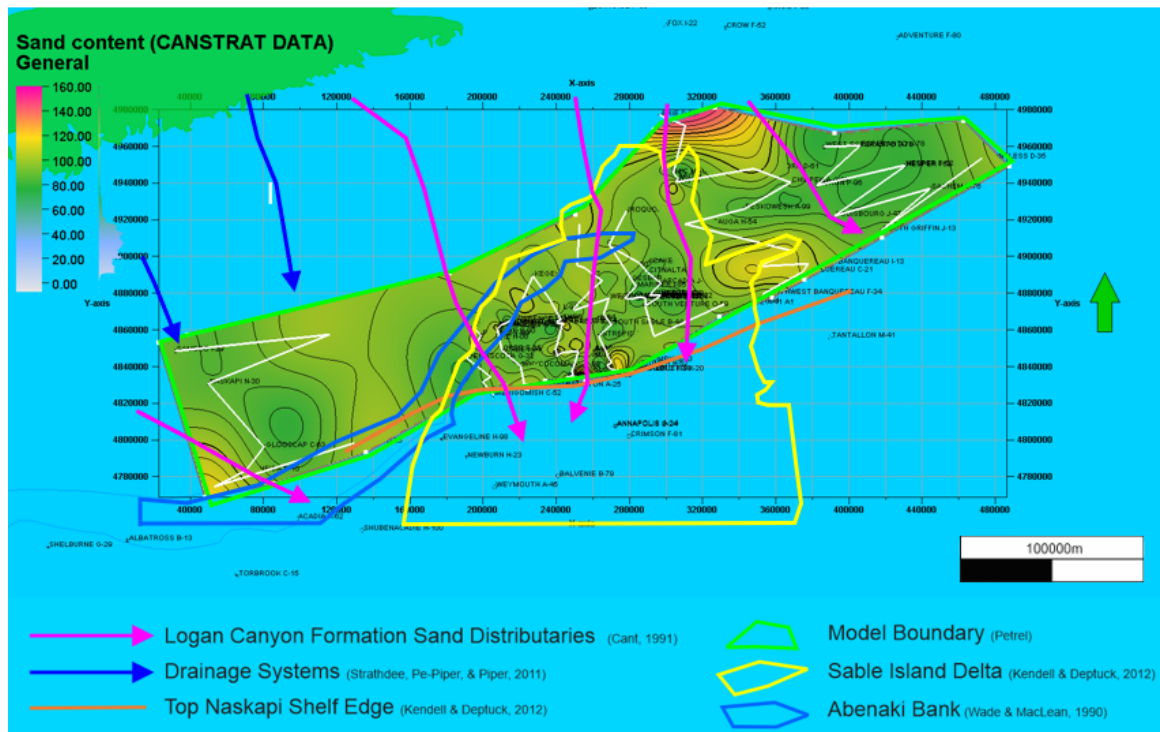


Figure 7.2: Sand content in the study area, with the outline of the Sable Island Delta.

Twenty-eight maps were made using the Canstrat™ lithology data derived from their detailed studies of drill cuttings. Interestingly, the consensus by the Aptian was that the Sable Delta was on the wane, yet maps created with the Canstrat™ lithology data indicate there was coarse clastic input into the Naskapi Member shale at that time. In figure 7.2 above, the outline of the Sable Delta is seen in yellow and is correlated with the map of sand content of the Naskapi Member. An area on the upper right-hand side of the delta shows a significant amount of sand content. This greater proportion of sand and silt reflects its position at the locus of the delta and contrasts with the Naskapi in other regions, implying the delta was still active though proximal to the basin margins. Southwest of the Sable Delta there is little evidence of input from the proposed Shelburne Delta during Naskapi Member deposition. Furthermore, to the north and east of the delta, outlined as proposed by Deptuck and Kendall (2012), significant sands and silts were deposited indicating that perhaps the eastern margin of the delta could be extended. Comparison with the maps constructed with Canstrat™ data, the position of the Sable Delta shows that the delta deposition continued to a limited extent during the Aptian with three or four sand, silt, and thin limestone layers seen in the lithology logs of the Naskapi Member, indicating pulses of deltaic clastics penetrating the deeper water Naskapi Member shales.

The higher amounts of sand content seen to the right of the Sable Delta outline towards the east, further indicate that the delta edge could be extended into this area as well. It is probable the movement of the fault and effects on the Meguma basement terrain (Pe-Piper and Piper, 2004) resulted in significantly reduced sediment shedding off the Appalachians, and an increase in transgressive shale deposition due to deeper water. However, the Sable Delta continued to be active post-Logan Canyon Formation deposition, albeit with a significantly lower volume of silts and sands.

The depositional environment of a rock and its subsequent diagenesis can affect the colour of a sample, and the oxidation-reduction balance of the sediments is important. The maps derived from Canstrat™ data denoting rock colour indicate where the individual colours are dominant (>50%) for the Naskapi Member. A notable area of

green colour is in the Sable Delta region and could indicate sediments with glauconite, however it could also refer to green shale as that showed in the green shale data map as well as in an area north of the Abenaki Bank. Greenish hued clay minerals such as illite, chlorite, or biotite could contribute to the colour and be a result of an influx of weathered source materials conducive to clay mineral formation. Red-coloured deposits in the Naskapi are most abundant northeast of the Sable Delta that could indicate oxidized sediments sourced from an area east of the distributaries feeding the delta. The provenance of the grains could come from an area adjacent to the northeast region with abundant aeolian sediments, or eroded volcanics or metamorphic rocks with abundant red minerals.

Limestone and marlstone content maps show their presence is restricted to an area north of the Abenaki Bank with virtually no input into the Sable Delta area. Likewise for fossil debris, as noted on Canstrat™ logs, and this could be attributed to shedding sediments from the Abenaki.

Oil staining within coarse clastic sediments is greatest in the Sable Delta area and linked to those with good porosity, with the highest amount near the Micmac wells (Abenaki Subbasin), as well as near the Southampton and Glenelg wells. The highest porosity is observed in wells on the northeast part of the Sable Delta. The map of total porosity corresponds to the Sable Delta area, and slightly to the northeast, again pointing to a possible extension of the delta area in that direction as proposed by Deptuck and Kendall (2012). The most cemented areas correlate to areas with low porosity in the Naskapi Member (e.g. Figure 6.30 and 6.31), as expected, not areas of maximum porosity.

7.5 Wireline Data Maps

Eight maps were created using the wireline log data available through NRCan's BASIN online database. The density values map shows highest values almost exclusively in the Sable Delta region: the areas of the Southwest Banquereau, Glenelg, Alma, North Triumph and Chebucto wells. Also, there is a low velocity anomaly of unknown

significance in the area west of the delta in the Ojibwa, Naskapi and Sambro wells (Mohican Graben) which correlates with a high sonic value anomaly in the same region. This could indicate an area of higher amounts of organic matter. Citadel H-52 shows the lowest average resistivity from the sandstone section of the Naskapi. An area of low density occurs near the Ojibwa E-07 and the Naskapi N-30 wells. When looking at the cross section in detail, high density readings in sands are seen in the Ojibwa well, and high-density shales are seen in the Naskapi well. The density average would be skewed lower if the lithologies seen with higher-than-average densities were hydrocarbon or saltwater bearing rocks.

Otherwise, areas of low resistivity which are seen in the northern half of the study area, could indicate more fluid bearing sands, and the southern part of the study area, which shows a higher resistivity indicated more compacted shales or a region that is less fluid bearing. When you compare the resistivity map of average values (quality assurance) in Figure 6.42, which can indicate all porous intervals based in fluid bearing capacity, to the Canstrat™ map of all porous intervals in Figure 6.37, there is a good correlation. Good correlation between Canstrat™ data derived maps and continuous wireline log maps validates the validity and reliability of the Canstrat™ data.

Chapter 8: Conclusion and Recommendations

8.1 Conclusions

The primary objectives in this study of the Naskapi Member were to elucidate:

- a) The stratigraphy, sedimentology, and diagenesis as interpreted from wireline, litholog, and seismic survey data in the study area,
- b) The extent of organic-rich intervals and/or potential source rocks,
- c) The oceanic and atmospheric conditions in the Cretaceous paleo Atlantic, which may have affected the deposition and accumulation of organic-rich deposits in the Scotian Basin, and
- d) Compare with Cretaceous organic-rich intervals and anoxic events found in other circum-Atlantic Ocean basins.

The Cretaceous Period reflects a time of a global greenhouse climate, with low sea levels in the Early Cretaceous, rising and peaking in the late mid-Cretaceous. These warmer temperatures increased the potential for oceanic anoxic events. However, the Scotian Basin did not accumulate or preserve significant amounts of organic-rich shale necessary to create an effective regional source rock during the Cretaceous (Aptian) global oceanic anoxic events. This was due in part to a high delta-derived sediment load focused in the Sable Subbasin during the Cretaceous that resulted in dilution of organic matter by siliciclastic material. A drier climate in the Aptian contributed to a largely terrestrial Type III kerogen being deposited via distributaries, and this did not result in creating effective source rock in the Scotian Basin as was seen further south. The very effective source rock, the La Luna in the eastern Venezuelan Basin, was deposited when prevailing ocean currents and upwelling of nutrient-rich water created a nutrient trap, resulting in rich undiluted beds of organic matter with significantly greater TOC than was found in the Cretaceous Aptian in the Scotian Basin.

8.2 Future Work Recommendations

There are three recommendations for future work:

- a) Lithologic maps data of the Naskapi Member using Canstrat™ data help define the Sable Delta. It would be very interesting to use the Canstrat™ data to map other units such as the Logan Canyon, Micmac, Wyandot, etc., to determine their respective sedimentation rates and further define when the Sable Delta ceased to be a significant contributor to the Scotian Basin. The lithology data has proved to be reliable when comparing Canstrat maps to maps created from wireline logs.
- b) Isopach data from this study show the Late Jurassic Micmac and Early Cretaceous Lower Missisauga formations of the Sable Delta are thinner on its western side, by the Abenaki Carbonate Bank. The delta's eastern extent (and indeed its definition) has long been uncertain though Deptuck and Kendall (2012) have recently generated an estimation of its extent. Further analysis using Canstrat™ data and examining sediment thickness and range of other formations could assist in further defining the delta's eastern limit.
- c) Climate affects oceanic anoxic events, as well as the deposition and preservation of organic-rich facies. Future work could involve climate simulations to delineate the correlation between climate patterns, ocean anoxic events/organic-rich deposits, and effective source rock occurrence, perhaps creating a timeline of historic climate patterns in the region.

References

Al-Hajeri, M.M., Al Saeed, M., Derks, J., et al., 2009. Basin and Petroleum System Modelling, *Oilfield Review*. **21**: 14 – 29.

American Association of Petroleum Geologists (AAPG) Wiki
[www.wiki.aapg.orghttps://wiki.aapg.org/Rock-Eval_pyrolysis](https://wiki.aapg.org/Rock-Eval_pyrolysis) retrieved April 8, 2021.

Arthur, M.A., Dean, W.E. and Stow, D.A.V., 1984. Models for the deposition of Mesozoic-Cenozoic fine-grained organic-carbon-rich sediment in the deep sea. Geological Society, London, Special Publications, **15**:527-560.

Arthur, M.A. and Dean, W.E., 1986. Cretaceous paleoceanography of the western North Atlantic Ocean. In: *The Western North Atlantic Region*. , ed. by Vogt, Peter R.. The Geology of North America, M . GSA, Boulder, Colo., 617-630. DOI [10.1130/DNAG-GNA-M.617](https://doi.org/10.1130/DNAG-GNA-M.617)

Arthur, M.A., and Sageman, B.B., 2005. Sea-level control on source-rock development: Perspectives from the Holocene Black Sea, the mid-Cretaceous Western Interior Basin of North America, and the Late Devonian Appalachian Basin, in the *Deposition of Organic Carbon-Rich Sediments: Models, Mechanisms, and Consequences*, edited by N.B. Harris. Special Publication SEPM Society of Sedimentary Geology, **82**: 35-59.

Arthur, M.A., and Schlanger, S.O., 1979. Cretaceous "Oceanic Anoxic Events" as causal factors in development of reef-reservoired giant oil fields. *AAPG Bulletin*, **63**: 870 - 885.

Arthur, M.A., Schlanger, S.O., and Jenkyns, H.C. 1987. The Cenomanian - Turonian oceanic anoxic event, II. Palaeoceanographic controls on organic - matter production and preservation. *In Marine Petroleum Source Rocks, Edited by J. Brooks, and A.J. Fleet, Geological Society Special Publ. No 26*: 401 - 420.

Arthur, M.A., Dean, W.E. and Pratt, L.M., 1988. Geochemical and climatic effects of increased marine organic carbon burial at the Cenomanian/Turonian boundary. *Nature*, **335**: 714-717.

Ascoli, P., 1976. Foraminiferal and Ostracod Biostratigraphy of the Mesozoic-Cenozoic, Scotian Shelf, Atlantic Canada. In: *Manit. Sediments. Int. Symp. Benthonic Foraminifera Cont. Margins.B; Halifax; 1975; Halifax, N.S.; DA. 1976; 653-771.*

Asquith, G. and Krygowski, D., 2004. *Basic Well Log Analysis*. Wecond edition, AAPG Methods in Exploration Series, **16**, 244 pp.

- Barron, E.J., 1983. A warm, equable Cretaceous: the nature of the problem. *Earth Science Reviews*, **19**: 305 – 338.
- Barron, E.J., Thompson, S.L., and Schneider, S.H. 1981. An ice-free Cretaceous? Results from climate model simulations. *Science*, **212**: 501 – 508.
- Barron, E.J., and Washington, W.M., 1985. Warm Cretaceous climates: High atmospheric CO₂ as a plausible mechanism, in Sundquist, E.T. and Broecker, W.S., eds, *The carbon cycle and atmospheric CO₂: Natural variations, Archaean to present: Washington C.C. American Geophysical Union Geophysical Monograph* **32**: 546 – 553.
- Barron, E.J., Fawcett, P.J., Peterson, W.H., Pollard, D. and Thompson, S.L., 1995. A “simulation” of mid-Cretaceous climate. *Paleoceanography*, **10**: 953-962.
- Beauchamp, W., Allmendinger, R.W., Barazangi, M., Demnati, A., El Alji, M. and Dahmani, M., 1999. Inversion tectonics and the evolution of the High Atlas Mountains, Morocco, based on a geological-geophysical transect. *Tectonics*, **18**: 163-184.
- Becker, R.W., Conrad, C.P., Buffett, B., and Mueller, R.D., 2009. Past and present seafloor age distributions and the temporal evolution of plate tectonic heat transport. *Earth Planet. Sci. Lett.* **278**: 233 – 242.
- Berner, R.A., 1983. Sedimentary pyrite formation: An update. *Geochimica et Cosmochimica Acta*, **48**: 605 - 615.
- Berner, R.A., 1994. Geocarb II: a revised model of atmospheric CO₂ over Phanerozoic time. *American Journal of Science*, **294**: 56 – 91.
- Beglinger, S.E., Doust, H. and Cloetingh, S., 2012. Relating petroleum system and play development to basin evolution: West African South Atlantic basins. *Marine and Petroleum Geology*, **30**: 1-25.
- Bertotti, G., and Gouiza, M., 2012. Post-rift vertical movements and horizontal deformations in the eastern margin of the Central Atlantic. Middle Jurassic to Early Cretaceous evolution of Morocco. *Int. J. Earth Sci*, **101**: 2151 – 2165.
- Benoit, W.R., Sethi, D.K., Fertl, W.H. and Mathews, M., 1980, January. Geothermal well log analysis at Desert Peak, Nevada. In *SPWLA 21st Annual Logging Symposium*. Society of Petrophysicists and Well-Log Analysts.

Bohacs, K.M., Grabowski Jr., G.J., Carroll, A.R., Mankiewicz, P.J., Miskell-Gerhardt, K.J., Schwalbach, J.R., Wegner, M.B., and Simo, J.A., 2005. Production, Destruction, and Dilution – the Many Paths to Source-Rock Development, in *The Deposition of Organic-Carbon Rich Sediments: Models, Mechanisms, and Consequences*, SEPM Special Publication **82**, 61 – 101.

Bowman, S. 2010. Cretaceous tectonism and volcanism in the eastern Scotian Basin, offshore Nova Scotia. M. Sc. Thesis, Applied Science, St Mary's University, Halifax, Nova Scotia.

Bralower, T.J., Arthur, M.A., Leckie, R.M., Sliter, W.V., Allard, D.J. and Schlanger, S.O., 1994. Timing and paleoceanography of oceanic dysoxia/anoxia in the Late Barremian to Early Aptian (Early Cretaceous). *Palaios*, **9**: 335-369.

Bralower, T.J., Fullagar, P.D., Paull, C.K., Dwyer, G.S. and Leckie, R.M., 1997. Mid-Cretaceous strontium-isotope stratigraphy of deep-sea sections. *Geological Society of America Bulletin*, **109**: 1421 – 1442.

Beicip-Franlab, 2011. Play Fairway Analysis, (PFA) offshore Nova Scotia Canada [online]. Halifax: Nova Scotia Department of Energy. Available from <http://energy.novascotia.ca/oil-and-gas/offshore/play-fairway-analysis>

Beicip-Franlab 2016. Play Fairway Analysis, (PFA) offshore Nova Scotia Canada [online]. Halifax: Nova Scotia Department of Energy. Available from <http://www.oera.ca/offshore-energy-research/geoscience/central-scotian-slope-atlas-2016>

Bertotti, G. and Gouiza, M., 2012. Post-rift vertical movements and horizontal deformations in the eastern margin of the Central Atlantic: Middle Jurassic to Early Cretaceous evolution of Morocco. *International Journal of Earth Sciences*, **101**: 2151-2165.

Brumsack, H.-J., 1980. Geochemistry of Cretaceous black shales from the Atlantic Ocean (DSDP Legs 11, 14, 36, and 41). *Chem. Geol.*, **31**: 1 – 25.

Brongersma-Sanders, M., 1971. Origin of major cyclicity of evaporites and bituminous rocks: An actualistic model. *Marine Geology*, **11**: 123-144.

Bujack, J.P., Barss, M.S. and Williams, G.L., 1980. Organic Type and Colour, and Hydrocarbon Potential: Offshore Eastern Canada. CSPG Special Publications, Memoir **6**: 984-984.

Burke, K., 1988. Tectonic Evolution of the Caribbean. *Annual Review of Earth and Planetary Science*, **16**: 201 – 230.

Burov, E., 2010. The equivalent elastic thickness (T_e) seismicity and the long-term tectonics of continental lithosphere: time to burn-out “crème brûlée”? Insights from large-scale geodynamic modeling. *Tectonophysics*, **484**: 4 – 26.

Burwood, R., 1999. Angola: source rock control for Lower Congo Coastal and Kwanza Basin petroleum systems. Geological Society, London, Special Pubs., **153**: 181 – 194.

Calvert, S.E. and Pedersen, T.F., 1996. Sedimentary geochemistry of manganese; implications for the environment of formation of manganiferous black shales. *Economic Geology*, **91**: 36-47.

Chavez, I., Piper, D.J.W., Pe-Piper, G., and Zhang, Yuanyuan, 2016. North Atlantic climatic events recorded in Aptian Naskapi Member cores, Scotian Basin. *Cretaceous Research*, **60**: 297 - 307.

Chavez, I., Piper, D.J. and Pe-Piper, G., 2018. Correlation of the Aptian Naskapi Member of the Scotian Basin and its regional implications. *Canadian Journal of Earth Sciences*, **55**: 514-535.

Cloetingh, S. and Haq, B.U., 2015. Inherited landscapes and sea level change. *Science*, **347**: 6220.

Cloetingh, S., Burov, E., and Francois, T., 2013. Thermo-mechanical controls on intra-plate deformation and the role of plume-folding interactions in continental topography. *Gondwana Res.*, **24**: 815 – 837.

Cloetingh, S., McQueen, H., and Lambeck, K., 1985. On a tectonic mechanism for regional sea level variations. *Earth Planet. Sci. Lett.*, **75**: 157 – 166.

Cloetingh, S., and Ziegler, P., 2007. In *Treatise on Geophysics*, 6: Crust and lithosphere dynamics. Watts, A.B., ed. Elsevier, Amsterdam, 486 – 611.

Coffin, M.F., and Eldholm, O., 1994. Large igneous provinces: crustal structure, dimensions, and external consequences. *Rev. Geophys.* **32**: 1 – 36.

Conrad, C.P., 2013. The solid Earth’s influence on sea level. *Geol. Soc Am Bulletin*, **125**: 1027 – 1052.

Courtillot, V., Besse, J., Vandamme, D., Montigny, R., Jaeger, J.J. and Cappetta, H., 1986. Deccan flood basalts at the Cretaceous/Tertiary boundary?. *Earth and Planetary Science Letters*, **80**: 361 – 374.

Coward, M.P., Purdy, E.G., Ries, A.C. and Smith, D.G., 1999. The distribution of petroleum reserves in basins of the South Atlantic margins. Geological Society, London, Special Publications, **153**: 101-131.

Cronin, T.M., 2010. Paleoclimates. Global Environmental Change. Handbook of Global Environmental Pollution, **1**: 49-54.

Crowley, T.J., 1991. Past CO₂ changes and tropical sea surface temperatures. *Paleoceanography*, **6**: 387 – 394.

de la Cruz, A.A. and Gabriel, B.C., 1974. Caloric, elemental, and nutritive changes in decomposing *Juncus roemerianus* leaves. *Ecology*, **55**: 882-886.

Dal Corso, J., Marzoli, A., Tateo, F., Jenkyns, H.C., Bertrand, H., Youbi, N., Mahmoudi, A., Font, E., Buratti, N. and Cirilli, S., 2014. The dawn of CAMP volcanism and its bearing on the end-Triassic carbon cycle disruption. *Journal of the Geological Society*, **171**: 153-164.

Davis, C, Pratt, L, Sliter, W, Mompert, L., and Murat, R., 1999. Factors influencing organic carbon and trace metal accumulation in the Upper Cretaceous La Luna Formation of the western Maracaibo Basin, Venezuela, in *Evolution of the Cretaceous Ocean/Climate System*, edited by E. Barrera and C. Johnson, Geological Society of America, Special Pubs., **332**: 203 – 230.

Davison, I., 1999. Tectonics and hydrocarbon distribution along the Brazilian South Atlantic margin. Geological Society of London, Special Pubs., **153**:133 – 151.

Dean, W.E. and Arthur, M.A., 1989. Iron-sulfur-carbon relationships in organic-carbon-rich sequences I: Cretaceous Western Interior Seaway. *American Journal of Science*, **289**: 708-743.

Dean, W.E., Claypool, G.E. and Thide, J., 1984. Accumulation of organic matter in Cretaceous oxygen-deficient depositional environments in the central Pacific Ocean. *Organic geochemistry*, **7**: 39-51.

Demaison, G.J., and Moore, G.T., 1980. Anoxic environments and oil source bed genesis, *AAPG Bulletin*, **64**: 1179 – 1209.

Denham, L.R., 1984. Seismic interpretation. *Proceedings of the IEEE*, **72**: 1255-1265.

Deptuck, M. E., 2003. Post-rift geology of the Jeanne d'Arc basin, with a focus on the architecture and evolution of early Paleogene submarine fans, and insights from modern deep -water systems. Ph.D. Thesis, Department of Earth Sciences, Dalhousie University, Halifax, Nova Scotia.

Deptuck, M., and Kendell, K., 2012. Contrasting salt tectonic styles on the western versus central parts of the Scotian Margin offshore Nova Scotia – Part 1 and Part 2. CNSOPB Geoscience Open File Poster 2012 – 001PF. 2 panels.

Desborough, G.A. and Poole, F.G., 1983. consists of marine oil shale that contains anomalous amounts. US Geological Survey Bulletin, **1694**: 91.

Dewey, J.F., and Pitman, W.C., 1997. Sea -level changes: Mechanisms, magnitudes and rates. SEPM Spec. Pub, **58**: 95 – 127.

Deynoux, M., Miller, J.M.G., and Domack, E.W., 1994. Eds., Earths Glacial Record, Cambridge Univ. Press, Cambridge.

Dickens, G.R., 2011. Down the rabbit hole: Toward appropriate discussion of methane release from gas hydrate systems during the Paleocene-Eocene thermal maximum and other past hyperthermal events. *Climate of the Past*, **7**: 831-846.

Douglas, R.G., and Savin, S.M., 1975. Oxygen and carbon isotope analyses of Tertiary and Cretaceous microfossils from the Shatsky Rise and other sites in the North Pacific Ocean, in Larson, R.L. Moberly, R., and others Initial reports of the Deep Sea Drilling Project, **32**: Washington, D.C., US Government Printing Office, 509 – 520.

Dupre, S., Bertotti, G., and Cloetingh, S., 2007. Tectonic history along the South Gabon Basin: anomalous early post-rift subsidence. *Marine Petroleum Geology*, **24**: 151 – 172.

Dymond, J., Suess, E. and Lyle, M., 1992. Barium in deep-sea sediment: A geochemical proxy for paleoproductivity. *Paleoceanography*, **7**:163-181.

Erba, E., 1994., Nannofossils and superplumes: the Early Aptian “nannoconid crisis”. *Paleoceanography*, **9**: 483 – 501.

Erlich, R.N., Astorga, A., Sofer, Z., Pratt, L.M., and Palmers, S.E., 1996. Palaeoceanography of organic-rich rocks of the Loma Chumico Formation of Costa Rica, Late Cretaceous, eastern Pacific. *Sedimentology*, **43**: 691 – 718.

Escobar, M., Marquez, G., Azuaje, V., da Silva, A., and Tocco, R., 2012. Use of biomarkers, porphyrins, and trace elements to assess the origin, maturity, biodegradation, and migration of the Alturitas oils in Venezuela. *Fuel*, **97**: 186 – 196.

Escobar, M., Márquez, G., Inciarte, S., Rojas, J., Esteves, I. and Malandrino, G., 2011. The organic geochemistry of oil seeps from the Sierra de Perijá eastern foothills, Lake Maracaibo Basin, Venezuela. *Organic Geochemistry*, **42**: 727-738.

Fassell, M.L., and Bralower, T.J., 1999. Warm, equable mid-Cretaceous: Stable isotope evidence, in *Evolution of the Cretaceous Ocean/Climate System*, edited by E. Barrera and C. Johnson, Geological Society of America, Special Pubs., **332**: 121 – 142.

Ferguson, K.M and Gregory, R.T., 1999. Lower Cretaceous (Aptian – Albian) secular changes in the oxygen and carbon isotope record from high paleolatitude, fluvial sediments, southeast Australia: Comparisons to the marine record. in *Evolution of the Cretaceous Ocean/Climate System*, edited by E. Barrera and C. Johnson, Geological Society of America, Special Pubs., **332**: 59 – 72.

Fisher, C.G., and Hay, W.W., 1999. Calcareous nannofossils as indicators of mid-Cretaceous paleofertility along an ocean front, U.S. Western Interior, in *Evolution of the Cretaceous Ocean/Climate System*, edited by E. Barrera and C. Johnson, Geological Society of America, Special Pubs., **332**: 161 – 180.

Fischer, A.G. and Arthur, M.A., 1977. Secular variations in the pelagic realm. Society of Economic Paleontologists and Mineralogists (SEPM) Special Publication **25**: 19 – 50.

Forster, A., Schouten, S., Moriya, K., Wilson, P.A. and Sinninghe Damsté, J.S., 2007. Tropical warming and intermittent cooling during the Cenomanian/Turonian oceanic anoxic event 2: Sea surface temperature records from the equatorial Atlantic. *Paleoceanography* **22**, PA 1219.

Föllmi, K.B., 1989. Evolution of the mid Cretaceous Tiad – Platform carbonates, phosphatic sediments, and pelagic carbonates along the northern Tethys margin. Springer Verlag, Lecture Notes in Earth Sciences, **23**, 153 pp.

Föllmi, K.B., Weissert, H., Bisping, M, and Funk, H., 1994. Phosphogenesis, carbon-isotope stratigraphy and carbonate-platform evolution along the Lower Cretaceous northern Tethyan margin. *Geological Society of American Bulletin*, **106**: 729 – 746.

Fowler, M., Webb, J., Obermajer, M., Monnier, F., Mort, A., Kuheshi, M., and MacDonald, A., 2016. Petroleum Systems of the Scotian Basin., In Proceedings of the AAPG 2016 Annual Convention and Exhibition, Calgary, AB. AAPG Search and Discovery, Article #10871.

Frakes, L.A., 1999. Estimating the global thermal state from Cretaceous sea surface and continental temperature data. , in Evolution of the Cretaceous Ocean/Climate System, edited by E. Barrera and C. Johnson, Geological Society of America, Special Pubs., **332**: 49 – 57.

Francois, T., Burov, E., Meyer, P., and Agard, P., 2013. Surface topography as key constraint on thermos-rheological structure of stable cratons. Tectonophysics, **602**: 106 – 123.

Gale, A.S., Jenkyns, H.C., Kennedy, W.J. and Corfield, R.M., 1993. Chemostratigraphy versus biostratigraphy: data from around the Cenomanian–Turonian boundary. Journal of the Geological Society, **150**: 29-32.

Geological Survey of Canada, Open-File Report 2006-1195.

Gibson, R.G., Dzou, L.I. and Greeley, D.F., 2004. Shelf petroleum system of the Columbus basin, offshore Trinidad, West Indies. I. Source rock, thermal history, and controls on product distribution. Marine and Petroleum Geology, **21**: 97-108.

Given, M.M., 1977. Mesozoic and early Cenozoic geology of offshore Nova Scotia. Bulletin of Canadian Petroleum Geology, **25**: .63-91.

Gradstein, F.M., Ogg, J., and Smith, S.G. 2005. A geological time scale 2004. Cambridge University Press, Cambridge. 589 pp.

Gradstein, F.M., Agterberg, F.P., Ogg, J.G., Hardenbol, J., Van Veen, P., Thierry, J. and Huang, Z., 1995. A Triassic, Jurassic and Cretaceous time scale.

Graham, D.K., Harland, R., Gregory, D.M., Long, D. and Morton, A.C., 1990. The biostratigraphy and chronostratigraphy of BGS Borehole 78/4, North Minch. Scottish Journal of Geology, **26**: 65-75.

Greene, A.R., Soates, J.S., and Weis, D., 2008. Wrangellia flood basalts in Alaska: a record of plume-lithosphere interaction in a late Triassic oceanic plateau. Geochem. Geophys. Geosyst. **9**: 1 - 12.

Grunau, H.R., 1983. Abundance of source rocks for oil and gas worldwide. *Journal of Petroleum Geology*, **6**: 39 - 54.

Gurnis, M., Turner, M., Zahirovic, S., DiCaprio, L., Spasojevic, S., Müller, R.D., Boyden, J., Seton, M., Manea, V.C. and Bower, D.J., 2012. Plate tectonic reconstructions with continuously closing plates. *Computers & Geosciences*, **38**: 35-42.

Haq, B.U., Hardenbol, J., and Vail, P.R. 1987. Chronology of fluctuating sea levels since the Triassic. *Science*, **235**: 1156–1167. doi:10.1126/science.235.4793.1156. PMID:17818978.

Haq, B.U. and Schutter, S.R., 2008. A chronology of Paleozoic sea-level changes. *Science*, **322**: .64-68.

Haq., B. U., 2014. Cretaceous eustasy revisited. *Global Planet Change*, **113**: 44 – 58.

Hay, W.W., 1995. Cretaceous palaeoceanography. *Geol. Car-path*. **46**: 257 – 266.

Hay, W.W. 1996. Tectonics and Climate, *Geol. Rundsch.*, **85**: 409 – 437.

Hay, W.W., 2008. Evolving ideas about the Cretaceous climate and ocean circulation. *Cretaceous Research*, **29**: 725-753.

Hay, W.W. and DeConto, R.M., 1999. Comparison of modern and Late Cretaceous meridional energy transport and oceanology, in *Evolution of the Cretaceous Ocean/Climate System*, edited by E. Barrera and C. Johnson, Geological Society of America, Special Pubs., **332**: 283 – 300.

Hay, W.W., DeConto, R., Wold, C.N., Wilson K.M., Voigt, S., Schulz, M. Wold-Rossby, A., Dullo, W.-C., Ronov, A.B., Balukhovskiy, A.M., and Soding E., 1999. An alternative global Cretaceous paleogeography, in *Evolution of the Cretaceous Ocean/Climate System*, edited by E. Barrera and C. Johnson, Geological Society of America, Special Pubs., **332**: 1 – 47.

Hay, W.W. and Wold, C.N., 1996. A simpler plate-tectonic history for the Caribbean. *Zentralblatt für Geologie und Palaeontologie*, **199**: 917 – 934.

Hays, J.D., Imbrie, J., and Shackleton, N.J. 1976. Variations in the Earth's Orbit: Pacemaker of the Ice Ages. *Science*, **194**: 1121 – 32.

Hartwig, A., di Primio, R., Anka, Z., and Horsfield, B., 2012. Source rock characteristics and compositional kinetic models of Cretaceous organic-rich black shales offshore southwestern Africa. *Organic Geochemistry* **51**: 17 – 34.

Heezen, B.C., MacGregor, I.D., Foreman, H.P., Forristal, G., Hekel, H., Hesse, R., Hoskins, R.H., Jones, E.J.W., Kaneps, A., Krasheninnikov, V. and Okada, H., 1973. Diachronous deposits: a kinematic interpretation of the post Jurassic sedimentary sequence on the Pacific plate. *Nature*, **241**: 25-32.

Herbert, T.D., Gee, J. and DiDonna, S., 1999. Precessional cycles in the Upper Cretaceous pelagic sediments of the South Atlantic: Long-term patterns from high-frequency climate variations. *SPECIAL PAPERS-GEOLOGICAL SOCIETY OF AMERICA*, pp.105-120.

Hickey, B.M., 1997. The response of a steep-sided, narrow canyon to time-variable wind forcing. *Journal of Physical Oceanography*, **27**: 697-726.

Hofman, P., Ricken, W., Schwark, L, and Leythaeuser, D., 1999. Coupled oceanic effects of climatic cycles from late Albian deep-sea sections of the North Atlantic, in *Evolution of the Cretaceous Ocean/Climate System*, edited by E. Barrera and C. Johnson, Geological Society of America, Special Pubs., **332**: 143 – 159.

Hofman, P., and Wagner, T., 2011. ITCZ Controls on Late Cretaceous black shale sedimentation in the tropical Atlantic Ocean, *Palaeoceanography*, **26**: 1 – 11, PA4223, doi:10.1029/2011PA002154.

Hollister, C.D., Nowell, A.R. and Jumars, P.A., 1984. The dynamic abyss. *Scientific American*, **250**: 42-53.

Hollister, C.D. and McCave, I.N., 1984. Sedimentation under deep-sea storms. *Nature*, **309**: 220-225.

Huang, Z. and Williamson, M.A., 1996. Artificial neural network modelling as an aid to source rock characterization. *Marine and Petroleum Geology*, **13**: 277-290.

Huber, B.T., Norris, R.D. and MacLeod, K.G., 2002. Deep-sea paleotemperature record of extreme warmth during the Cretaceous. *Geology*, **30**: 123 – 126.

Huber, B.T., Hodell, D.A., and Hamilton, C.P., 1995. Mid- to Late Cretaceous climate of the southern high latitudes: stable isotopic evidence for minimal equator-to-pole thermal gradients: *Geological Society of America Bulletin*, **107**: 1164 – 1191.

Ito, G., and Clift, P.D., 1998. Subsidence and growth of Pacific Cretaceous plateaus. *Earth Planet. Sci. Lett.* **161**: 85 – 100.

- James, K.H., 2005. A simple synthesis of Caribbean geology. *Caribbean Journal of Earth Science*, **39**: 69 – 82.
- Jansa, L.F. and Wade, J.A., 1975. Geology of the continental margin off Nova Scotia and Newfoundland; pp. 51-105: in W.J.M. Van der Linden and J.A. Wade (eds), *Offshore Geology of Eastern Canada*, Geological Survey of Canada, Paper **74-30**, 51-105.
- Jansa, L.F., et al., 1979. Mesozoic – Cenozoic sedimentary formations of the North American basin: Western North Atlantic, in M. Talwani, W.W., Hay and W.B.F. Ryan, eds., *Deep drilling results in the Atlantic Ocean: continental margins and paleoenvironments*: Washington, D.C., Am. Geophys. Union, Maurice Ewing Series **3**: 1 – 57.
- Jansa, L.F., and Wiedemann, J., 1982. Comparison of northwest Africa and Canary and Cape Verde Islands. *In*: Von Rad, U., Hinz, K., Sarnthein, M, Seibold, E. (Eds.), *Geology of the Northwest African Continental Margin*. Springer Verlag, Berlin, pp. 215-269.
- Jenkyns, H.C. 2010. Geochemistry of oceanic anoxic events. *AGU Geochemistry, Geophysics, Geosystems*, **11**: doi:10.1029/2009GC002788; 1 - 30.
- Jenkyns, H.C., Forster, A., Schouten, S. and Damsté, J.S.S., 2004. High temperatures in the late Cretaceous Arctic Ocean. *Nature*, **432**: 888 – 892.
- Jenkyns, H.C., 1980. Cretaceous anoxic events: from continents to oceans. *Journal of the Geological Society*, **137**: 171-188.
- Jones, M.T., Jerram, D.A., Svensen, H.H., and Grove, C., 2016. The effects of large igneous provinces on the global carbon and sulfur cycles. *Palaeogeography, Palaeoclimatology, Palaeoecology*, **441**: 4 – 21.
- Jungslager, E.H.A., 1999. Petroleum habitats of the Atlantic margin of South Africa, Geological Society, London, *Special Publications* **153**: 153 – 168.
- Kent, D.V. and Gradstein, F.M., 1985. A Cretaceous and Jurassic geochronology. *Geological Society of America Bulletin*, **96**: 1419-1427.
- Kerr, A.C., 1998. Oceanic plateau formation: a cause of mass extinction and black shale deposition around the Cenomanian – Turonian boundary? *J. Geol. Soc.* **155**: 619 – 626.
- Kaneps, A., 1976. Deep Sea Drilling Project. *Geotimes*, **21**: 16-17.

- Kim, S, Kramer, R.W., and Hatcher, P.G., 2003. Graphical Method for Analysis of Ultrahigh – Resolution Broadband Mass Spectra of Natural Organic Matter, the Van Krevelen Diagram. *Analytical Chemistry*, **75**: 5336 – 5344.
- Klemme, H.D. and Ulmishek, G.F. 1991. Effective petroleum source rocks of the world: stratigraphic distribution and controlling depositional factors. *AAPG Bulletin* **75**:1809 - 1851.
- Kominz, M.A., 1984. Oceanic ridge volumes and sea-level change – an error analysis. *AAPG Special Publication A* **166**: 109 – 127.
- Komar, P.D., 1972. Relative significance of head and body spill from a channelized turbidity current. *Geological Society of America Bulletin*, **83**: 1151-1156.
- Krygowski, D.A., 2003. *Guide to Petrophysical Interpretation*, Austin TX, USA, 147 pp.
- Kugler, H. 1959. *Geological Map of Trinidad*. Published by the Petroleum Association of Trinidad.
- Kulp, J.L., 1961. Geologic time scale. *Science*, **133**: 1105-1114.
- Kuypers, M.M., Lourens, L.J., Rijpstra, W.I.C., Pancost, R.D., Nijenhuis, I.A. and Damsté, J.S.S., 2004. Orbital forcing of organic carbon burial in the proto-North Atlantic during oceanic anoxic event 2. *Earth and Planetary Science Letters*, **228**: 465 – 482.
- Lambeck, K., Smither, C. and Ekman, M., 1998a. Tests of glacial rebound models for Fennoscandia based on instrumented sea-and lake-level records. *Geophysical Journal International*, **135**: 375-387.
- Lambeck, K., Smither, C. and Johnston, P., 1998b. Sea-level change, glacial rebound and mantle viscosity for northern Europe. *Geophysical Journal International*, **134**: 102-144.
- Langford, F.F., and Blanc-Valleron, M.-M. 1990. Interpreting rock-eval pyrolysis data using graphs of pyrolyzable hydrocarbons vs. total organic carbon. *AAPG Bulletin*, **74**: 799-804.
- Larson, R.L., 1991a. Latest pulse of Earth: Evidence for a mid-Cretaceous superplume, *Geology*, **19**: 547 – 550.
- Larson, R.L., 1991b. Geological consequences of superplumes. *Geology*, **19**: 963-966.

Law, C.A., 1999. Treatise of Petroleum Geology, Handbook of Petroleum Geology, Exploration for Oil and Gas Traps. Chapter 6, AAPG. Edited by E.A. Beaumont and N.H. Foster, 6-1 - 6-41.

Leckie, R.M., Bralower, T.J., and Cashman, R. 2002. Oceanic anoxic events and plankton evolution: biotic response to tectonic forcing during the mid-Cretaceous. *Paleoceanography*, **17**: 13-1 - 13-29.

Ledwell, J.R., Montgomery, E.T., Polzin, K.L., Laurent, L.S., Schmitt, R.W. and Toole, J.M., 2000. Evidence for enhanced mixing over rough topography in the abyssal ocean. *Nature*, **403**: 179-182.

Leventhal, J.S., 1983. An interpretation of carbon and sulfur relationships in Black Sea sediments as indicators of environments of deposition. *Geochimica et Cosmochimica Acta*, **47**: 133-137.

Liu, L., Spasojevic, S., and Gurnis, M, 2008. Reconstructing Farallon plate subduction beneath North American back to the Late Cretaceous. *Science*, **322**: 934 – 938.

Liu, X., and Millero, F., 2002. The solubility of iron in seawater. *Marine Chemistry*, **77**: 43-54.

Lonsdale, P. and Southard, J.B., 1974. Experimental erosion of North Pacific red clay. *Marine Geology*, **17**: M51-M60.

Matthews, R.K., and Poore, R.Z., 1980. Tertiary $\delta^{18}\text{O}$ record and glacio-eustatic sea-level fluctuations. *Geology*, **8**: 501 – 504.

Mattinson, J.M., 2013. Revolution and evolution: 100 years of U–Pb geochronology. *Elements*, **9**: 53-57.

McIver, N., 1972. Mesozoic and Cenozoic Stratigraphy of the Nova Scotia Shelf. *Canadian Journal of Earth Sciences*, **9**: 54 – 70.

MacLeod, K.G., Martin, E.E. and Blair, S.W., 2008. Nd isotopic excursion across Cretaceous ocean anoxic event 2 (Cenomanian-Turonian) in the tropical North Atlantic. *Geology*, **36**: 811-814.

McArthur, J.M., Algeo, T.J., Van de Schootbrugge, B., Li, Q. and Howarth, R.J., 2008. Basinal restriction, black shales, Re-Os dating, and the Early Toarcian (Jurassic) oceanic anoxic event. *Paleoceanography*, **23**: doi.org/10.1029/2008PA001607.

- Manspeizer, W., Puffer, J.H. and Cousminer, H.L., 1978. Separation of Morocco and eastern North America: a Triassic-Liassic stratigraphic record. *Geological Society of America Bulletin*, **89**: 901-920.
- Mello, M.R., Telnaes, N., Gaglianone, P.C., Chicarelli, M.I., Brassell, S.C., and Maxwell, J.R., 1988. Organic geochemical characterization of depositional palaeoenvironments of source rocks and oils in Brazilian marginal basins. *Organic Geochemistry*, **13**: 31 – 45.
- Meyers, S.R. and Sageman, B.B., 2007. Quantification of deep-time orbital forcing by average spectral misfit. *American Journal of Science*, **307**: 773-792.
- Meyer, K.M., and Kump, L.R., 2008. Oceanic euxinia in Earth history: causes and consequences. *Annual Review of Earth and Planetary Science*, **36**: 251 – 288.
- Miall, A.D., 2016. Stratigraphy: the modern synthesis. In *Stratigraphy: A modern synthesis*: 311-370. Springer, Cham.
- Miller, K.G., Sugarman, P.J., Browning, J.V., Kominz, M.A., Hernández, J.C., Olsson, R.K., Wright, J.D., Feigenson, M.D. and Van Sickel, W., 2003. Late Cretaceous chronology of large, rapid sea-level changes: Glacioeustasy during the greenhouse world. *Geology*, **31**: 585-588.
- Miller, K.G., Kominz, M.A., Browning, J.V., Wright, J.D., Mountain, G.S., Katz, M.E., Sugarman, P.J., Cramer, B.S., Christie-Blick, N. and Pekar, S.F., 2005. The Phanerozoic record of global sea-level change. *Science*, **310**: 1293 – 1298.
- Minette, D., 1996. Developments in understanding the physical foundation of formation density and lithology logging. SPWLA 37th Annual Symposium Transcript Paper **JJ**; 1 – 14.
- Mitrovica, J.X., and Peltier, W.R., 1991. On postglacial geoid subsidence over the equatorial oceans. *J. Geophys. Res.*, **96**: 20053 – 20071.
- Mosher, D.C., Xu, Z. and Shimeld, J., 2010. The Pliocene Shelburne mass-movement and consequent tsunami, western Scotian Slope. In *Submarine Mass Movements and Their Consequences* (pp. 765-775). Springer, Dordrecht.
- Mukhopadhyay, P.K., 2012. Conjugate Margin Petroleum Systems – Evaluation of the Shallower and Deepwater Hydrocarbon Prospects of the Scotian Basin, Offshore Nova Scotia. CSPG Lunchtime Talk June 5, 2012 Slide 28.
- Mukhopadhyay, P.K., Wade, J.A., and Kruger, M.A. 1995. Organic facies and maturation of Jurassic/Cretaceous rocks, and possible oil-source rock correlation based on pyrolysis of asphaltenes, Scotian Basin, Canada. *Organic Geochemistry*, **22**: 85 - 104.

Mueller, R.D., Sdrolias, M., Gaina, C., Steinberger, B., and Heine, C., 2008. Long-term sea-level fluctuations driven by ocean basin dynamics. *Science*, **319**: 1357 – 1362.

Muller, P.J., and Seuss, E., 1979. Productivity, sedimentation rate and sedimentary organic matter in the oceans - 1. Organic carbon preservation. *Deep Sea Res*, **26A**: 1347-1362.

Mutterlose, J., 1992. Migration and evolution patterns of floras and faunas in marine Early Cretaceous sediments of NW Europe. *Palaeogeography, Palaeoclimatology, Palaeoecology*, **94**: 261-282.

NRCan, 2009. Lexicon of Canadian Geological Names on-line. Natural Resources Canada. https://weblex.nrcan.gc.ca/weblexnet4/weblex_e.aspx

Neal, C.R., Mahone, J.J., Kroenke, L.W., Duncan, R.A., and Patterson, M.G., 1997. The Ontong-Java Plateau. *Geophysical Monograph-American Geophysical Union* **100**: 183-216.

Nagihara, S. and Smith, M.A., 2008. Regional overview of deep sedimentary thermal gradients of the geopressed zone of Texas-Louisiana continental shelf. *Bulletin of the American Association of Petroleum Geologists*, **92**: 1 – 14.

NASA, 2017 <http://oceanmotion.org/html/background/ocean-in-motion.htm>, <https://earthobservatory.nasa.gov/>).

Odin, G.S., Hancock, J.M., Antonescu, E., Bonnemaïson, M., Caron, M., Cobban, W.A., Dhondt, A.V., Gaspard, D., Ion, J., Jagt, J.W.M. and Kennedy, W.J., 1996. Definition of a global boundary stratotype section and point for the Campanian/Maastrichtian boundary. *Bulletin de l'Institut Royal des Sciences Naturelles de Belgique, Sciences de la Terre*, **66**(SUPPL.).

OETR, 2011. Offshore Energy Technology Research Associates (OETR), 2011. Play Fairway Analysis – Offshore Nova Scotia, Nova Scotia Department of Energy Report. NSDOE Records Storage File No. 88-11-0004-01, 347 pp., <http://www.oera.ca/Offshore-eneery-research/geoscience/play-fairway-analysis>

Ogg, J.G., Hinnov, L.A. and Huang, C., 2012. Cretaceous. In *The geologic time scale*: 793-853. Elsevier.

Orth, C.J., Attrep Jr, M., Quintana, L.R., Elder, W.P., Kauffman, E.G., Diner, R. and Villamil, T., 1993. Elemental abundance anomalies in the late Cenomanian extinction interval: a search for the source (s). *Earth and Planetary Science Letters*, **117**: 189-204.

Otto-Bliesner, B.L., Brady, E.C. and Shields, C., 2002. Late Cretaceous ocean: Coupled simulations with the National Center for Atmospheric Research climate system model. *Journal of Geophysical Research: Atmospheres*, **107**: ACL-11.

Parrish, J.T., and Curtis, R.L., 1982. Atmospheric circulation, upwelling and organic-rich rocks in the Mesozoic and Cenozoic eras. *Palaeogeography, Palaeoclimatology, Palaeoecology*, **40**: 31-66.

Parrish, J.T. and Spicer, R.A., 1988. Late Cretaceous terrestrial vegetation: A near-polar temperature curve. *Geology*, **16**: 22-25.

Passey, Q.R., Creaney, S., Kulla, J.B., Moretti, F.J., and Stroud J.D. 1990. A practical model for organic-richness from porosity and resistivity logs. *American Association of Petroleum Geologists Bulletin* **12**: 1777 - 1794.

Pedersen, T.F., and Calvert, S.E., 1990. Anoxia vs. productivity – what controls the formation of organic-carbon-rich sediments and sedimentary rocks? *American Association of Petroleum Geology Bulletin*, **74**: 454-466.

Persad, K., 2008. *The Petroleum Geology and Prospects of Trinidad and Tobago*. Geological Society of Trinidad and Tobago, 178 – 186.

Persad, K.M., Talukdar, S.C. and Dow, W.G., 1993. Tectonic control in source rock maturation and oil migration in Trinidad. *AAPG Bulletin*, **77**(CONF-930306-).

Pe-Piper, G., and Piper, D.J.W., 2004. The effects of strike-slip motion along the Cobequid – Chedabucto – southwest Grand Banks fault system on the Cretaceous–Tertiary evolution of Atlantic Canada. *Canadian Journal of Earth Sciences* ; **41** (7): 799–808.

Pe-Piper, G. and MacKay, R.M., 2006. Provenance of Lower Cretaceous sandstones onshore and offshore Nova Scotia from electron microprobe geochronology and chemical variation of detrital monazite. *Bulletin of Canadian Petroleum Geology*, **54**:.366-379.

Peters, K.E., 1986. Guidelines for evaluating petroleum source rock using programmed pyrolysis. *AAPG bulletin*, **70**:.318-329.

Piper, D.J.W., Bowman, S.J., Pe-Piper G., and MacRae, R.A. 2011. The ups and downs fo Guysborough County - the mid Cretaceous Naskapi Member in the Scotian Basin: eustasy or tectonics? *AGS Abstracts, 37th Annual Colloquium & Annual General Meeting 2011. Atlantic Geology*, **47**: 1 – 37.

Piper, D.Z., and Calvert, S.E., 2009. A marine biogeochemical perspective on black shale deposition. *Earth Science Review*, **95**: 63 – 96.

Piqué, A., Le Roy, P. and Amrhar, M., 1998. Transtensive synsedimentary tectonics associated with ocean opening: the Essaouira–Agadir segment of the Moroccan Atlantic margin. *Journal of the Geological Society*, **155**: 913-928.

Pitman III, W.C. and Golovchenko, X., 1983. The effect of sea level change on the shelf edge and slope of passive margins. *SEPM Spec. Pub.*, **33**: 41 – 58.

Pletsch, R., Erbacher, J., Holbourn, A.E.J., Kuhnt, W., Moullade, M. Oboh-Ikuenobe, F.E, Soding, E., and Wagner, T., 2001. Cretaceous opening history of the Equatorial Atlantic Gateway: the view from the West African continental margin (ODP Leg 159). *Journal of South American Earth Science*, **14**: 147 – 174.

Poag, C.W., 1982. Foraminiferal and seismic stratigraphy, paleoenvironments and depositional cycles in the Georges Bank basin, in P.A. Scholle and C.R. Wenkam, eds. *Geological studies of the COST nos. G-1 and G-2 wells, US North Atlantic outer continental shelf*: USGS Circ. **861**: 43 – 91.

Poulsen, C.J., Barron, E.J., Johnson, C.C., and Fawcett, P., 1999. Links between major climatic factors and regional oceanic circulation in the mid-Cretaceous, in *Evolution of the Cretaceous Ocean/Climate System*, edited by E. Barrera and C. Johnson, Geological Society of America, Special Pubs., **332**: 73 – 89.

Powell, A.J., 1987. Thanetian dinoflagellate cyst biostratigraphy and quantitative palynostratigraphy of the Andrew Field, central North Sea. Oral presentation made at British Micropalaeontological Society Meeting, 'Micropalaeontology, Palynology, and Petroleum Exploration, On- and Offshore Europe' University of Aberdeen, April 2-3, 1987.

Powers, M. C., 1953, Clastic Grain Rounding Chart, *Journal of Sedimentary Petrology*, **23**:118

Powell, A.J., Dodge, J.D., and Lewis, J. 1990. Late Neogene to Pleistocene palynological facies of the Peruvian continental margin upwelling. In *Proceedings of the Ocean Drilling Project, Scientific Results* (eds E. Suess and R. Von Huene), College Station, Texas, **112**: 297-321.

Raiswell, R. and Berner, R.A., 1985. Pyrite formation in euxinic and semi-euxinic sediments. *American Journal of Science*, **285**: 710-724.

- Rider, M and Kennedy, M, 2011. The Geological Interpretation of Well Logs, Rider-French Consulting Ltd, Glasgow, Scotland
- Redfern, J., Bertotti, G., Bulot, L., Lubert, T. and Duval-Arnould, A., 2017. NARG 2017, North Africa Research Group, Morocco Fieldtrip 2017, Argana Valley and Essaouira-Agadir Basin, Morocco, University of Manchester, UK www.narg.org.uk, 152 pp.
- Redfield, A.C., Ketchum, B.H. and Richards, F.A., 1963. The influence of organisms on the composition of seawater. *The Sea*, **2**: 26-77.
- Rey, J., Canérot, J., Peybernès, B., Taj-Eddine, K. and Thieuloy, J.P., 1988. Lithostratigraphy, biostratigraphy and sedimentary dynamics of the Lower Cretaceous deposits on the northern side of the western High Atlas (Morocco). *Cretaceous Research*, **9**: 141-158.
- Ridgwell, A., Hargreaves, J.C., Edwards, N.R., Annan, J.D., Lenton, T.M., Marsh, R., Yool, A. and Watson, A., 2007. Marine geochemical data assimilation in an efficient Earth System Model of global biogeochemical cycling. *Biogeosciences*, **4**: 87-104.
- Robertson, A.H.F. and Bliefnick, D.M., 1983. Sedimentology and Origin of Lower Cretaceous Pelagic Carbonates and Redeposited Clastics, Blake-Bahama Formation, Deep Sea Drilling Project Site 534, Western Equatorial Atlantic. Initial reports of the Deep Sea Drilling Project, **76**(NOV):795-828.
- Rodrigues, K., 1993. The Naparima Hill-Cruise/Forest/Gros Morne petroleum system of Trinidad: a quantitative evaluation of petroleum generated. Extended abstract, AAPG Annual Convention, New Orleans.
- Ronov, A.B., 1994. Phanerozoic transgressions and regressions on the continents: a qualitative approach based on areas flooded by the sea and areas of marine and continental deposition., *Am J. Sci.*, **294**: 777 – 801.
- Rowley, D.B., 2002. Rate of plate creation and destruction: 180 Ma to present. *Geol. Soc. Am. Bull.* **114**: 927 – 933.
- Sageman, B.B., Meyers, S.R. and Arthur, M.A., 2006. Orbital time scale and new C-isotope record for Cenomanian-Turonian boundary stratotype. *Geology*, **34**: 125-128.
- Schlanger, S.O., and Jenkyns, H.C. 1976. Cretaceous oceanic anoxic events: causes and consequences. *Geologie en Mijnbouw*, **55**: 179 - 184.

Schlanger, S.O., Arthur, M.A., Jenkyns, H.C., and Scholle, P.A. 1987. The Cenomanian - Turonian Oceanic Anoxic Event, I. Stratigraphy and distribution of organic carbon - rich beds and the marine $\delta^{13}\text{C}$ excursion. In *Marine Petroleum Source Rocks*, Edited by J. Brooks and A.J. Fleet, Geological Society Special Publ. no. **26**, pp 371 - 399.

Schlanger, S.O., Jenkyns, H.C. and Premoli-Silva, I., 1981. Volcanism and vertical tectonics in the Pacific Basin related to global Cretaceous transgressions. *Earth and Planetary Science Letters*, **52**: 435-449.

Schlumberger, 1989. *Log Interpretation, principles and applications*. Schlumberger Educational Services. Oilfield Glossary. Retrieved April 8, 2021.

Schlumberger Limited 2015. Oil Field Glossary [online]. Available at <http://www.glossary.oilfield.slb.com>

Schmitz, B., 1987. Barium, equatorial high productivity, and the northward wandering of the Indian continent. *Paleoceanography*, **2**: 63-77.

Schneider, S.H., Thompson, S.L., and Barron, E.J., 1985. Mid Cretaceous continental surface temperatures: Are high CO_2 concentrations needed to simulate above-freezing winter conditions? in Sundquist, E.T. and Broecker, W.S., eds, *The carbon cycle and atmospheric CO_2 : Natural variations, Archaean to present*: Washington C.C. American Geophysical Union Geophysical Monograph **32**: 554 - 560.

Scholle, P.A., and Arthur, M.A., 1980. Carbon isotope fluctuations in Cretaceous pelagic limestones: Potential stratigraphic and petroleum exploration tool. *AAPG Bulletin*, **64**: 67 – 87.

Schwarzacher, W. and Fischer, A.G., 1982. Limestone-shale bedding and perturbations of the Earth's orbit. In *Cyclic and event stratification* (pp. 72-95). Springer, Berlin, Heidelberg

Scotese, C.R., et al., 1988. Plate tectonic reconstructions of the Cretaceous and Cenozoic ocean basins. *Tectonophysics*, **155**, 27 – 48.

Scotese, C.R., 2003. <http://www.scotese.com/climate.htm>

Showman, A.P., 2009. Hadley Cell Dynamics, Chapter 1. Harvard Education online – Climate. <https://courses.seas.harvard.edu/climate/eli/Courses/EP5281r/Sources/Hadley-cell/2-Showman-2009.pdf>

[Silva, R., Wach, G., and Wong, C., 2015. Source Rocks and Petroleum Systems of the Scotian Basin. CSEG Recorder, 40: 22 – 27.](#)

Sinton, C.W. and Duncan, R.A., 1997. Potential links between ocean plateau volcanism and global ocean anoxia at the Cenomanian-Turonian boundary. *Economic Geology*, **92**: 836-842.

Skogseid, J., Planke, S., Faleide, J.I., Pedersen, T., Eldholm, O. and Neverdal, F., 2000. NE Atlantic continental rifting and volcanic margin formation. Geological Society, London, Special Publications, **167**: 295-326.

Smith, A.G., Briden, J.C. and Drewry, G.E., 1973. Phanerozoic world maps.

Southard, J.B., Young, R.A. and Hollister, C.D., 1971. Experimental erosion of calcareous ooze. *Journal of Geophysical Research*, **76**: 5903-5909.

Sorkhabi, R., 2016. Back to Source Rocks: Part II. *GeoEXPro* **12**: 22 – 24.

Stoll, H.M. and Schrag, D.P., 2000. High-resolution stable isotope records from the Upper Cretaceous rocks of Italy and Spain: Glacial episodes in a greenhouse planet?. *Geological Society of America Bulletin*, **112**: 308-319.

Suan, G., Pittet, B., Bour, I., Mattioli, E., Duarte, L.V. and Mailliot, S., 2008. Duration of the Early Toarcian carbon isotope excursion deduced from spectral analysis: consequence for its possible causes. *Earth and Planetary Science Letters*, **267**: 666-679.

Summa, L.L., Goodman, E.D., Richardson, M., Norton, I.O. and Green, A.R., 2003. Hydrocarbon systems of Northeastern Venezuela: plate through molecular scale-analysis of the genesis and evolution of the Eastern Venezuela Basin. *Marine and Petroleum Geology*, **20**: 323-349.

Summerhayes, C.P., 1981. Organic facies of Middle Cretaceous black shales in deep North Atlantic. *AAPG Bulletin*, **65**: 2364-2380.

Summerhayes, C.P. 1987. Organic-rich Cretaceous sediments from the North Atlantic. *In* *Marine Petroleum Source Rocks*, Edited by J. Brooks and A.J. Fleet, Geological Society Special Publication No. **26** pp. 301 - 316.

Takashima, R., Gautam, P. and Nishi, H., 2006. Recent advances in research on terrestrial and marine sequences from the Mid-Cretaceous Oceanic Anoxic Events (OAEs). *Scientific Drilling*, **2**: 50-51.

- Tarduno, J.A., Sliter, W.V., Kroenke, L., Leckie, M., Mayer, H., Mahoney, J.J., Musgrave, R., Storey, M. and Winterer, E.L., 1991. Rapid formation of Ontong Java Plateau by Aptian mantle plume volcanism. *Science*, **254**: 399-403.
- Tari, G.C., and Jabour, H., 2013. Salt tectonics along the Atlantic Margin of Morocco. In: W.U. Mohriak, A. Danforth, P.J. Post, D.E. Brown, G.C. Tari, M. Nemcok, and S.T. Sinha (eds), *Conjugate Divergent Margins Geological Society of London Special Publications* 369, p.337-353, doi 10.1144/SP369.23.
- Tari, G.C., Brown, D.E., Jabour, H., Hafid, M., Loudon, K., and Zizi, M., 2012. The conjugate margins of Morocco and Nova Scotia. In: D.G. Roberts and A.W. Bally (eds) *Regional Geology and Tectonics: Phanerozoic Rift Systems and Sedimentary Basins—Volume 1C—Passive Margins*. Elsevier, Amsterdam, p.265-300.
- Thiede, J., and Van Andel, T.H., 1977. The paleoenvironment of anaerobic sediments in the Late Mesozoic South Atlantic Ocean, *Earth. Planet. Sci. Lett.*, **33**: 301 – 309.
- Thierstein, H.R., and Berger, W.H., 1978. Injection events in ocean history, *Nature*, **276**: 461 – 466.
- Thomas, A., 2014. The hypothetical petroleum system of Trinidad and Tobago. *AAPG Search and Discovery* article 30373.
- Thurrow, J., Brumsack, H.J., Rullkötter, J., Littke, R. and Meyers, P., 1992. The Cenomanian/Turonian boundary event in the Indian Ocean: A key to understand the global picture. *Washington DC American Geophysical Union Geophysical Monograph Series*, **70**: 253-273.
- Tissot, B., Demaison, G., Masson, P., Delteil, J.R., and Combaz, A. 1980. Paleoenvironment and petroleum potential of mid-Cretaceous black shales in Atlantic basins. *AAPG Bulletin*, **64**: 2051 - 2063.
- Tissot, B.P. and Welte, D.H., 1984. *Petroleum Formation and Occurrence*, 2nd Ed., Springer-Verlag, Berlin.
- Tissot, B., Durand, B., Espitalie, J. and Combaz, A., 1974. Influence of nature and diagenesis of organic matter in formation of petroleum. *AAPG Bulletin*, **58**: 499-506.
- Trabucho-Alexandre, J, Tuenter, E., Henstra G.A., van der Zwan, K.J., van de Wal, R.S.W., Dijkstra, H.A., and de Boer, P.L., 2010. The mid-Cretaceous North Atlantic nutrient trap: Black shales and OAE's. *Paleoceanography*, **25**: PA4201, 1 - 14. Doi:10.1029/2010PA001925.

Trabucho-Alexandre, J., 2015. Organic Matter-Rich Shale Depositional Environments. *Fundamentals of Gas Shale Reservoirs*, 21-45.

Turgeon, S.C., and Creaser, R.A. 2008. Cretaceous oceanic anoxic event 2 triggered by a massive magmatic episode. *Nature*, **454**: 323 - 326.

Tucholke, B.E. and Vogt, P.R., 1979. Western North Atlantic: Sedimentary evolution and aspects of tectonic history. *Initial Reports of the Deep Sea Drilling Project*, **43**: 791-825.

Tyson, R.V., 1995. *Sedimentary Organic Matter – Organic facies and palynofacies*. Fossil Fuels and Environmental Geochemistry, University of Newcastle upon Tyne, UK. Chapman and Hall. Springer Science + Business Media, B.V.

Tyson, R.V. and Funnell, B.M., 1990. European Cretaceous shorelines, stage by stage. In *Cretaceous Resources, Events and Rhythms* : 237-272. Springer, Dordrecht.

Tyson, R.V., 2001. Sedimentation rate, dilution, preservation and total organic carbon: some results of a modelling study. *Organic Geochemistry*, **32**: 333 – 339.

Unternehr, P, Peron-Pinvidic, G, Manatschal, G., and Sutra, E., 2010. Hyper-extended crust in the South Atlantic: in search of a model. *Petrol. Geosc.* **16**, 207 – 215.

Utsunomiya, A., Ota, T., Windley, B.F., Suzuki, N., Uchio, Y., Munekata, K. and Maruyama, S., 2007. History of the Pacific superplume: implications for Pacific paleogeography since the Late Proterozoic. In *Superplumes: beyond plate tectonics* (pp. 363-408). Springer, Dordrecht.

United States Department of Energy (USDOE), 2017. Carbon Cycle 2.0. USDOE Environmental System Science Data (ESS-DIVE) – Lawrence Berkley National Lab and Office of Science (BER) Biological and Environmental Research Program. <http://ess-dive.lbl.gov>

Van Andel, T.H., Thiede, J., Sclater, J.G., and Hay, W.W., 1977. Depositional history of the South Atlantic during the last 125 million years. *J. Geol.*, **85**: 651 – 698.

van der Spuy, D., 2003. Aptian source rocks in some South African Cretaceous basins. *Geological Society, London, Special Pubs.*, **207**: 185 – 202.

Van Krevelen, D.W. and Schuyer, J., 1957. *Coal Science*. Elsevier Publishing Company, Amsterdam. 352 pp.

- Villamil, T., Arango, C.I., and Hay, W.W., 1999. Plate tectonic palaeoceanographic hypothesis for Cretaceous source rocks and cherts of northern South America., in *Evolution of the Cretaceous Ocean/Climate System*, edited by E. Barrera and C. Johnson, Geological Society of America, Special Pubs., **332**: 191 – 202.
- Villeneuve, M., 2004. Radiogenic isotope geochronology, in Gradstein, F.M., Ogg, J.G., and Smith, A.G., eds. *A geologic time scale*: Cambridge University Press, Cambridge, 87 – 95.
- Voigt, S., Hay, W.W., Hofling, R., and DeConto, R.M., 1999. Biogeographic distribution of late Early to Late Cretaceous rudist-reefs in the Mediterranean as climate indicators, in *Evolution of the Cretaceous Ocean/Climate System*, edited by E. Barrera and C. Johnson, Geological Society of America, Special Pubs., **332**: 91 – 103.
- Wach, G.D., 1991. *Sedimentology and stratigraphy of the Lower Cretaceous Channel Basin*. D. Phil. Dissertation, University of Oxford, 3 volumes.
- Wade, J.A., and MacLean, B. 1990. The geology of the southeastern margin of Canada. *In* *Geology of the continental margin of eastern Canada*. Edited by M.J. Keen and G.L. Williams. Geological Survey of Canada, Geology of Canada. pp. 167–238.
- Wagner, T., 2002. Late Cretaceous to early Quaternary organic sedimentation in the eastern Equatorial Atlantic. *Palaeogeography, Palaeoclimatology, Palaeoecology*, **179**: 113 – 147.
- Wagner, T. and Pletsch, T., 2001. No major thermal event on the mid-Cretaceous Côte d'Ivoire–Ghana Transform Margin. *Terra Nova*, **13**: 165-171.
- Wagner, T. and Pletsch, T., 1999. Tectono-sedimentary controls on Cretaceous black shale deposition along the opening Equatorial Atlantic Gateway (ODP Leg 159). Geological Society, London, Special Publications, **153**(1): 241-265.
- Welsink, H., Dwyer, J., Knight, R., 1989. Tectono-Stratigraphy of the Passive Margin Off Nova Scotia: Chapter 14: North American Margins. In *Extensional Tectonics and Stratigraphy of the North Atlantic Margins*, AAPG Special Volumes Memoir **46**: 215 – 231.
- Weston, J.F., MacRae, R.A., Ascoli, P., Cooper, M.K.E., Fensome, R.A., Shaw, D., and Williams, G.L. 2012. A revised biostratigraphic and well-log sequence stratigraphic framework for the Scotian Margin, offshore eastern Canada. *Canadian Journal of Earth Sciences*, **49**: 1478-1503.

Zeebe, R.E., Dickens, G.R., Ridgwell, A., Sluijs, A. and Thomas, E., 2014. Onset of carbon isotope excursion at the Paleocene-Eocene thermal maximum took millennia, not 13 years. *Proceedings of the National Academy of Sciences*, **111**: E1062-E1063.

Zeigler, P.A., and Cloeringh, S., 2004. Dynamic processes controlling evolution of rifted basins. *Earth Sci. Rev.* **64**: 1 – 50

List of Appendices

Appendix A: List of Canstrat™ Lithology Logs

The following list of Canstrat logs were used in this study. The thickness of the Naskapi formation is indicated in meters (column H - ISO NSK (m)).

Note: Tops indicated are Canstrat tops. Tops picked on the cross sections used in this study were changed in some instances.

UWI	Well name	Fm	Canstrat No.	TOP (m)	BOT (m)	ISO NSK (m)	Latitude	Longitude
300/J-56 44-20 059-45/50	ABENAKI J-56	NASKAPI	EC00022	1,978.8	2,074.5	95.7	44.2625	-59.884444
300/N-97 44-00 060-00/00	ADAMANT N-97	NASKAPI	EC00276	2,510.0	2,633.5	123.5	43.946667	-60.241111
300/F-67 43-40 060-30/00	ALMA F-67	NASKAPI	EC00198	2,543.3	2,843.8	300.5	43.605278	-60.665556
300/K-85 43-40 060-30/00	ALMA K-85	NASKAPI	EC00200	2,521.9	2,842.9	321.0	43.578889	-60.716944
300/J-16 44-10 059-30/00	ARCADIA J-16	NASKAPI	EC00176	2,769.7	2,895.9	126.2	44.095556	-59.533056
300/M-32 44-00 060-30/00	BALMORAL M-32	NASKAPI	EC00279	2,155.0	2,282.5	127.5	43.813611	-60.596389
300/C-21 44-20 058-30/00	BANQUEREAU C-21	NASKAPI	EC00163	3,118.4	3,574.7	456.3	44.168889	-58.566389
302/G-47 44-10 059-15/50	BLUENOSE 2G-47	NASKAPI	EC00180	2,779.5	2,945.3	165.8	44.106389	-59.356389
300/G-47 44-10 059-15/50	BLUENOSE G-47	NASKAPI	EC00062	2,785.9	2,935.8	149.9	44.105556	-59.3575
300/K-90 43-40 059-30/00	CHEBUCTO K-90	NASKAPI	EC00204	3,248.9	3,498.8	249.9	43.6625	-59.714444
300/G-67 44-40 058-30/00	CHIPPEWA G-67	NASKAPI	EC00038	2,305.2	2,450.0	144.8	44.605833	-58.6625
300/L-75 44-40 058-30/00	CHIPPEWA L-75	NASKAPI	EC00029	1,329.8	1,389.8	60.0	44.576667	-58.6975
300/H-52 44-20 058-45/50	CITADEL H-52	NASKAPI	EC00221	2,891.3	3,182.4	291.1	44.190278	-58.8775
300/I-59 44-10 059-30/00	CITNALTA I-59	NASKAPI	EC00088	2,584.7	2,670.7	86.0	44.145278	-59.625556
300/A-52 44-00 060-30/00	COHASSET A-52	NASKAPI	EC00196	2,447.8	2,596.0	148.2	43.852222	-60.628889
300/D-42 44-00 060-30/00	COHASSET D-42	NASKAPI	EC00067	2,122.9	2,247.9	125.0	43.851944	-60.620556

UWI	Well name	Fm	Canstrat No.	TOP (m)	BOT (m)	ISO NSK (m)	Latitude	Longitude
300/L-97 44-00 060-15/50	COHASSET L-97	NASKAPI	EC00127	2,109.0	2,220.0	111.0	43.943611	-60.499722
300/P-42 44-00 060-30/00	COHASSET P-42	NASKAPI	EC00124	2,132.5	2,259.5	127.0	43.863333	-60.604722
300/P-21 44-00 060-45/50	COMO P-21	NASKAPI	EC00262	2,049.0	2,174.5	125.5	43.846111	-60.805278
300/E-35 43-50 060-30/00	CREE E-35	NASKAPI	EC00015	2,407.9	2,574.3	166.4	43.739167	-60.598889
300/D-35 44-50 057-15/50	DAUNTLESS D-35	NASKAPI	EC00028	2,747.8	2,934.3	186.5	44.735556	-57.346389
300/G-32 43-50 060-45/50	DEMASCOTA G-32	NASKAPI	EC00089	2,214.1	2,397.9	183.8	43.690833	-60.831667
300/A-43 44-30 060-00/00	DOVER A-43	NASKAPI	EC00195	1,535.3	1,679.4	144.1	44.369444	-60.101944
300/D-21 44-00 059-30/00	EAGLE D-21	NASKAPI	EC00048	3,307.1	3,556.4	249.3	43.835278	-59.569167
300/N-03 44-10 060-00/00	EMMA N-03	NASKAPI	EC00275	2,472.0	2,625.5	153.5	44.046667	-60.014167
300/K-78 44-50 058-00/00	ESPERANTO K-78	NASKAPI	EC00024	2,212.8	2,334.8	122.0	44.791944	-58.188611
300/H-98 43-20 060-45/50	EVANGELINE H-98	NASKAPI	EC00209	3,392.7	3,889.9	497.2	43.290556	-60.980556
300/E-58 43-40 060-00/00	GLENELG E-58	NASKAPI	EC00186	3,102.5	3,364.0	261.5	43.621667	-60.147778
300/E-58 43-40 060-00/01	GLENELG E-58A	NASKAPI	EC00187	3,139.7	3,398.2	258.5	43.621667	-60.147778
300/H-38 43-40 060-00/00	GLENELG H-38	NASKAPI	EC00190	2,920.0	3,212.9	292.9	43.622222	-60.080278
300/J-48 43-40 060-00/00	GLENELG J-48	NASKAPI	EC00181	3,134.9	3,468.9	334.0	43.627222	-60.107222
300/N-49 43-40 060-00/00	GLENELG N-49	NASKAPI	EC00214	3,056.2	3,349.8	293.6	43.649722	-60.116667
300/C-63 43-20 062-00/00	GLOOSCAP C-63	NASKAPI	EC00185	1,861.7	2,216.8	355.1	43.202778	-62.165833
300/H-09 45-30 052-00/00	GRAND FALLS H-09	NASKAPI	EC00003	1,077.5	1,248.2	170.7	45.471944	-52.000833
300/I-52 44-50 057-45/50	HESPER I-52	NASKAPI	EC00115	2,669.1	2,752.3	83.2	44.694722	-57.875833
300/P-52 44-50 057-45/50	HESPER P-52	NASKAPI	EC00220	2,689.9	2,865.4	175.5	44.698889	-57.879444
300/P-96 44-40 058-15/50	HURON P-96	NASKAPI	EC00014	2,132.7	2,263.7	131.0	44.596389	-58.480833

UWI	Well name	Fm	Canstrat No.	TOP (m)	BOT (m)	ISO NSK (m)	Latitude	Longitude
300/L-80 43-50 059-45/50	INTREPID L-80	NASKAPI	EC00094	2,804.5	2,935.2	130.7	43.826667	-59.945556
300/J-17 44-30 059-45/50	IROQUOIS J-17	NASKAPI	EC00013	1,367.3	1,453.9	86.6	44.442222	-59.786667
300/C-20 45-30 058-30/00	JASON C-20	NASKAPI	EC00092	1,228.3	1,375.3	147.0	45.484722	-58.541111
300/G-67 44-10 060-15/50	KEGESHOOK G-67	NASKAPI	EC00223	1,948.0	2,072.9	124.9	44.108056	-60.408611
300/D-14 44-00 060-30/00	LAWRENCE D-14	NASKAPI	EC00277	2,146.5	2,245.0	98.5	43.884444	-60.547778
300/J-47 44-30 058-15/50	LOUISBOURG J-47	NASKAPI	EC00211	2,744.4	2,988.3	243.9	44.445556	-58.360833
300/C-34 43-50 060-00/00	MARMORA C-34	NASKAPI	EC00042	2,884.6	3,133.3	248.7	43.720556	-60.089444
300/P-35 43-50 060-00/00	MARMORA P-35	NASKAPI	EC00060	2,756.6	3,003.4	246.8	43.748056	-60.068333
300/C-52 43-40 060-30/00	MERIGOMISH C-52	NASKAPI	EC00230	2,498.4	3,029.7	531.3	43.5175	-60.6425
300/D-89 44-40 059-15/50	MICMAC D-89	NASKAPI	EC00114	1,678.5	1,742.5	64.0	44.635833	-59.471944
300/N-20 44-00 060-15/50	MIGRANT N-20	NASKAPI	EC00122	2,329.6	2,446.9	117.3	43.998889	-60.288333
300/H-54 44-30 059-15/50	MISSISAUGA H-54	NASKAPI	EC00012	2,313.7	2,414.3	100.6	44.388889	-59.38
300/I-00 43-00 062-15/50	MOHICAN I-100	NASKAPI	EC00041	2,215.3	2,450.3	235.0	42.994167	-62.480833
300/N-30 43-30 062-30/00	NASKAPI N-30	NASKAPI	EC00006	1,285.0	1,445.9	160.9	43.496389	-62.566667
300/I-13 44-20 058-30/00	BANQUEREAU I-13	NASKAPI	EC00169	3,020.6	3,459.5	438.9	44.209444	-58.530556
300/B-52 43-50 059-45/50	NORTH TRIUMPH B-52	NASKAPI	EC00242	3,406.5	3,756.5	350.0	43.683889	-59.8825
300/G-43 43-50 059-45/50	NORTH TRIUMPH G-43	NASKAPI	EC00238	3,490.0	3,778.0	288.0	43.705278	-59.856389
300/E-07 43-50 061-45/50	OJIBWA E-07	NASKAPI	EC00081	1,282.6	1,487.1	204.5	43.772222	-61.769722
300/A-12 44-10 059-45/50	OLYMPIA A-12	NASKAPI	EC00168	2,785.9	2,886.8	100.9	44.0175	-59.778889
300/O-25 43-20 061-30/00	ONEIDA O-25	NASKAPI	EC00005	2,232.0	2,468.8	236.8	43.248056	-61.560833
300/B-96 43-50 060-00/00	ONONDAGA B-96	NASKAPI	EC00113	2,468.5	2,646.8	178.3	43.751944	-60.234167

UWI	Well name	Fm	Canstrat No.	TOP (m)	BOT (m)	ISO NSK (m)	Latitude	Longitude
300/E-84 43-50 060-00/00	ONONDAGA E-84	NASKAPI	EC00001	2,503.0	2,701.7	198.7	43.721111	-60.221389
300/F-75 43-50 060-00/00	ONONDAGA F-75	NASKAPI	EC00030	2,693.8	2,973.9	280.1	43.738611	-60.1925
300/O-95 43-50 060-00/00	ONONDAGA O-95	NASKAPI	EC00034	2,651.7	2,859.0	207.3	43.746111	-60.231667
300/B-90 43-50 060-30/00	PANUKE B-90	NASKAPI	EC00263	2,150.5	2,281.6	131.1	43.82	-60.709722
300/F-99 43-50 060-30/00	PANUKE F-99	NASKAPI	EC00261	2,154.0	2,283.9	129.9	43.806944	-60.742778
300/M-79 43-50 060-30/00	PANUKE M-79	NASKAPI	EC00280	2,295.0	2,302.5	7.5	43.865	-60.697222
300/B-41 44-20 060-00/00	PENOBSCOT B-41	NASKAPI	EC00121	2,143.4	2,247.0	103.6	44.167222	-60.109722
300/L-30 44-10 060-00/00	PENOBSCOT L-30	NASKAPI	EC00116	2,139.1	2,251.3	112.2	44.162222	-60.069167
300/A-99 44-30 058-45/50	PESKOWESK A-99	NASKAPI	EC00219	2,376.2	2,460.3	84.1	44.470556	-58.978333
300/H-58 44-00 060-00/01	SABLE ISLAND IH-58	NASKAPI	EC00050	2,479.5	2,613.7	134.2	43.9575	-60.127222
302/H-58 44-00 060-00/00	SABLE ISLAND 2H-58	NASKAPI	EC00268	2,615.7	2,707.2	91.5	43.9575	-60.127222
303/H-58 44-00 060-00/00	SABLE ISLAND 3H-58	NASKAPI	EC10050	2,654.8	2,711.8	57.0	43.9575	-60.127222
304/H-58 44-00 060-00/00	SABLE ISLAND 4H-58	NASKAPI	EC00068	2,542.0	2,681.9	139.9	43.9575	-60.127222
305/H-58 44-00 060-00/00	SABLE ISLAND 5H-58	NASKAPI	EC00074	2,464.6	2,478.0	13.4	43.9575	-60.127222
300/C-67 44-00 059-45/50	SABLE ISLAND C-67	NASKAPI	EC00004	2,726.1	2,868.2	142.1	43.934722	-59.916944
300/E-48 44-00 060-00/00	SABLE ISLAND E-48	NASKAPI	EC00039	2,399.7	2,521.0	121.3	43.955833	-60.123333
300/O-47 44-00 060-00/00	SABLE ISLAND O-47	NASKAPI	EC00047	2,412.8	2,539.0	126.2	43.949167	-60.110556
300/D-76 44-40 057-30/00	SACHEM D-76	NASKAPI	EC00106	2,793.8	2,976.4	182.6	44.585833	-57.699444
300/I-29 43-40 062-45/50	SAMBRO I-29	NASKAPI	EC00090	1,011.0	1,104.0	93.0	43.643056	-62.804722
300/A-57 44-20 058-30/00	SAUK A-57	NASKAPI	EC00027	2,880.1	3,176.0	295.9	44.268333	-58.63
300/O-76 44-10 059-45/50	SOUTH DESBARRES O-76	NASKAPI	EC00205	2,384.8	2,507.3	122.5	44.098889	-59.933056

UWI	Well name	Fm	Canstrat No.	TOP (m)	BOT (m)	ISO NSK (m)	Latitude	Longitude
300/J-13 44-30 058-00/00	SOUTH GRIFFIN J-13	NASKAPI	EC00206	2,881.9	3,213.8	331.9	44.376944	-58.031944
300/B-44 44-00 059-45/50	SOUTH SABLE B-44	NASKAPI	EC00264	2,851.0	3,052.0	201.0	43.885	-59.861389
300/O-59 44-00 059-30/00	SOUTH VENTURE O-59	NASKAPI	EC00167	2,888.9	3,003.8	114.9	43.981389	-59.635833
300/F-34 44-10 058-45/50	SOUTHWEST BANQUEREAU F-34	NASKAPI	EC00178	3,532.9	3,917.9	385.0	44.054444	-58.839444
300/M-41 44-00 058-15/50	TANTALLON M-41	NASKAPI	EC00244	5,086.5	5,166.5	80.0	43.848889	-58.373611
300/C-74 44-00 060-00/00	THEBAUD C-74	NASKAPI	EC00217	2,525.3	2,646.3	121.0	43.884722	-60.193333
300/I-93 44-00 060-00/00	THEBAUD I-93	NASKAPI	EC00197	2,537.8	2,650.8	113.0	43.879167	-60.230833
300/I-94 44-00 060-00/00	THEBAUD I-94	NASKAPI	EC00123	2,516.1	2,632.6	116.5	43.895	-60.226944
300/P-84 44-00 060-00/00	THEBAUD P-84	NASKAPI	EC00052	2,517.0	2,610.3	93.3	43.9	-60.205278
300/P-50 43-40 059-45/50	TRIUMPH P-50	NASKAPI	EC00033	3,155.6	3,504.9	349.3	43.664444	-59.850556
300/D-61 44-50 058-45/50	TUSCARORA D-61	NASKAPI	EC00064	2,225.0	2,384.5	159.5	44.670278	-58.918611
300/G-72 44-20 059-30/00	UNIACKE G-72	NASKAPI	EC00191	2,452.7	2,563.4	110.7	44.191389	-59.736111
300/B-13 44-10 059-30/00	VENTURE B-13	NASKAPI	EC00144	2,841.0	2,966.5	125.5	44.036667	-59.534444
300/B-43 44-10 059-30/00	VENTURE B-43	NASKAPI	EC00147	2,836.0	2,967.0	131.0	44.033611	-59.610278
300/B-52 44-10 059-30/00	SOUTH VENTURE B-52	NASKAPI	EC00173	2,853.2	2,970.0	116.8	44.019444	-59.635556
300/D-23 44-10 059-30/00	VENTURE D-23	NASKAPI	EC00130	2,825.5	2,951.0	125.5	44.0375	-59.573611
300/H-22 44-10 059-30/00	VENTURE H-22	NASKAPI	EC00174	2,851.4	2,983.4	132.0	44.023333	-59.551944
300/N-01 44-10 059-45/50	VENTURE N-1	NASKAPI	EC00226	3,048.9	3,158.9	110.0	44.016389	-59.764167
300/J-75 43-40 060-15/50	WENONAH J-75	NASKAPI	EC00118	2,814.2	2,984.3	170.1	43.573889	-60.429167
300/K-20 43-40 059-45/50	WEST CHEBUCTO K-20	NASKAPI	EC00249	4,404.5	4,617.5	213.0	43.6625	-59.792222
300/B-78 44-50 058-15/50	WEST ESPERANTO B-78	NASKAPI	EC00175	2,152.8	2,324.4	171.6	44.784167	-58.436389

UWI	Well name	Fm	Canstrat No.	TOP (m)	BOT (m)	ISO NSK (m)	Latitude	Longitude
300/O-51 44-10 059-45/50	WEST OLYMPIA O-51	NASKAPI	EC00233	2,615.5	2,708.5	93.0	44.013056	-59.884444
300/N-91 44-10 059-30/00	WEST VENTURE N-91	NASKAPI	EC00224	2,824.9	2,934.9	110.0	44.012778	-59.741111
300/N-90 43-40 060-15/50	WHYCOCOMAGH N-90	NASKAPI	EC00259	2,632.0	2,878.0	246.0	43.664167	-60.467778

Appendix B: Naskapi Isopach for Wells in Study Area

Well name	NASKAPI TOP (m)	NASKAPI BOT (m)	NASKAPI ISOPACH (m)	UWI	Latitude	Longitude
ABENAKI J-56	1,970	2,075	105	300/J-56 44-20 059-45/50	44.2625	-59.884444
ADAMANT N-97	2,430	2,550	120	300/N-97 44-00 060-00/00	43.946667	-60.241111
ALMA F-67	2,543	2,844	301	300/F-67 43-40 060-30/00	43.605278	-60.665556
ALMA K-85	2,522	2,843	321	300/K-85 43-40 060-30/00	43.578889	-60.716944
ARCADIA J-16	2,770	2,896	126	300/J-16 44-10 059-30/00	44.095556	-59.533056
BALMORAL M-32	2,155	2,283	128	300/M-32 44-00 060-30/00	43.813611	-60.596389
BANQUEREAU C-21	3,250	3,575	325	300/C-21 44-20 058-30/00	44.168889	-58.566389
BLUENOSE 2G-47	2,780	2,945	166	302/G-47 44-10 059-15/50	44.106389	-59.356389
BLUENOSE G-47	2,786	2,936	150	300/G-47 44-10 059-15/50	44.105556	-59.3575
CHEBUCTO K-90	3,918	4,220	302	300/K-90 43-40 059-30/00	43.6625	-59.714444
CHIPPEWA G-67	2,305	2,450	145	300/G-67 44-40 058-30/00	44.605833	-58.6625
CHIPPEWA L-75	1,330	1,390	60	300/L-75 44-40 058-30/00	44.576667	-58.6975
CITADEL H-52	2,891	3,182	291	300/H-52 44-20 058-45/50	44.190278	-58.8775
CITNALTA I-59	2,585	2,671	86	300/I-59 44-10 059-30/00	44.145278	-59.625556
COHASSET A-52	2,448	2,610	162	300/A-52 44-00 060-30/00	43.852222	-60.628889
COHASSET D-42	2,123	2,248	125	300/D-42 44-00 060-30/00	43.851944	-60.620556
COHASSET L-97	2,085	2,220	135	300/L-97 44-00 060-15/50	43.943611	-60.499722
COHASSET P-42	2,133	2,260	127	300/P-42 44-00 060-30/00	43.863333	-60.604722
COMO P-21	2,049	2,175	126	300/P-21 44-00 060-45/50	43.846111	-60.805278
CREE E-35	2,408	2,574	166	300/E-35 43-50 060-30/00	43.739167	-60.598889
DAUNTLESS D-35	2,748	2,934	187	300/D-35 44-50 057-15/50	44.735556	-57.346389
DEMASCOTA G-32	2,214	2,398	184	300/G-32 43-50 060-45/50	43.690833	-60.831667
DOVER A-43	1,860	1,960	100	300/A-43 44-30 060-00/00	44.369444	-60.101944

Well name	NASKAPI TOP (m)	NASKAPI BOT (m)	NASKAPI ISOPACH (m)	UWI	Latitude	Longitude
EMMA N-03	2,420	2,550	130	300/N-03 44-10 060-00/00	44.046667	-60.014167
ERIE D-26	1,158	1,225	67	300/D-26 44-55 059-30/00	44.917644	-59.57495
ESPERANTO K-78	2,213	2,270	57	300/K-78 44-50 058-00/00	44.791944	-58.188611
EVANGELINE H-98	3,393	3,890	497	300/H-98 43-20 060-45/50	43.290556	-60.980556
GLENELG E-58	3,050	3,375	325	300/E-58 43-40 060-00/00	43.621667	-60.147778
GLENELG E-58A	3,140	3,398	259	300/E-58 43-40 060-00/01	43.621667	-60.147778
GLENELG H-38	3,125	3,448	323	300/H-38 43-40 060-00/00	43.622222	-60.080278
GLENELG J-48	3,135	3,469	334	300/J-48 43-40 060-00/00	43.627222	-60.107222
GLENELG N-49	3,056	3,350	294	300/N-49 43-40 060-00/00	43.649722	-60.116667
GLOOSCAP C-63	1,862	2,217	355	300/C-63 43-20 062-00/00	43.202778	-62.165833
GRAND FALLS H-09	1,078	1,248	171	300/H-09 45-30 052-00/00	45.471944	-52.000833
HESPER I-52	2,669	2,790	121	300/I-52 44-50 057-45/50	44.694722	-57.875833
HESPER P-52	2,690	2,865	176	300/P-52 44-50 057-45/50	44.698889	-57.879444
HURON P-96	2,095	2,264	169	300/P-96 44-40 058-15/50	44.596389	-58.480833
INTREPID L-80	2,805	2,935	131	300/L-80 43-50 059-45/50	43.826667	-59.945556
IROQUOIS J-17	1,367	1,454	87	300/J-17 44-30 059-45/50	44.442222	-59.786667
JASON C-20	1,228	1,375	147	300/C-20 45-30 058-30/00	45.484722	-58.541111
KEGESHOOK G-67	1,920	2,035	115	300/G-67 44-10 060-15/50	44.108056	-60.408611
LAWRENCE D-14	2,147	2,250	104	300/D-14 44-00 060-30/00	43.884444	-60.547778
LOUISBOURG J-47	2,744	2,988	244	300/J-47 44-30 058-15/50	44.445556	-58.360833
MARINER I-85	2,720	2,845	125	300/ I-85 44-10 059-30/00	44.075204	-59.702
MARMORA C-34	2,885	3,133	249	300/C-34 43-50 060-00/00	43.720556	-60.089444
MARMORA P-35	2,757	3,003	247	300/P-35 43-50 060-00/00	43.748056	-60.068333
MERIGOMISH C-52	2,498	3,030	531	300/C-52 43-40 060-30/00	43.5175	-60.6425
MIC MAC D-89	1,679	1,743	64	300/D-89 44-40 059-15/50	44.635833	-59.471944

Well name	NASKAPI TOP (m)	NASKAPI BOT (m)	NASKAPI ISOPACH (m)	UWI	Latitude	Longitude
MIC MAC H-86	1,912	2,000	88	300/H-86 44-40 059-15/00	44.59135	-59.45069
MIC MAC J-77	1,935	1,980	45	300/J-77 44-40 059-15/00	44.61189	-59.43636
MIGRANT N-20	2,290	2,447	157	300/N-20 44-00 060-15/50	43.998889	-60.288333
MISSISSAUGA H-54	2,314	2,414	101	300/H-54 44-30 059-15/50	44.388889	-59.38
MOHEIDA P-15	2,224	2,445	221	300/P15 43-10 062-15/00	43.08231	-62.27898
MOHICAN I-100	2,215	2,515	300	300/I-00 43-00 062-15/50	42.994167	-62.480833
NASKAPI N-30	1,285	1,446	161	300/N-30 43-30 062-30/00	43.496389	-62.566667
NORTH BANQUEREAU I-13	3,120	3,460	340	300/I-13 44-20 058-30/00	44.209444	-58.530556
NORTH TRIUMPH B-52	3,407	3,757	350	300/B-52 43-50 059-45/50	43.683889	-59.8825
NORTH TRIUMPH G-43	3,400	3,670	270	300/G-43 43-50 059-45/50	43.705278	-59.856389
OJIBWA E-07	1,283	1,487	205	300/E-07 43-50 061-45/50	43.772222	-61.769722
OLYMPIA A-12	2,755	2,887	132	300/A-12 44-10 059-45/50	44.0175	-59.778889
ONEIDA O-25	2,188	2,469	281	300/O-25 43-20 061-30/00	43.248056	-61.560833
ONONDAGA B-96	2,469	2,647	178	300/B-96 43-50 060-00/00	43.751944	-60.234167
ONONDAGA E-84	2,503	2,702	199	300/E-84 43-50 060-00/00	43.721111	-60.221389
ONONDAGA F-75	2,694	2,974	280	300/F-75 43-50 060-00/00	43.738611	-60.1925
ONONDAGA O-95	2,652	2,859	207	300/O-95 43-50 060-00/00	43.746111	-60.231667
PANUKE B-90	2,151	2,282	131	300/B-90 43-50 060-30/00	43.82	-60.709722
PANUKE F-99	2,154	2,284	130	300/F-99 43-50 060-30/00	43.806944	-60.742778
PANUKE H-08	2,180	2,330	150	300/H-08 43-50 060-45/00	43.789225	-60.755536
PANUKE M-79	2,295	2,303	8	300/M-79 43-50 060-30/00	43.865	-60.697222
PENOBSCOT B-41	2,135	2,247	112	300/B-41 44-20 060-00/00	44.167222	-60.109722
PENOBSCOT L-30	2,139	2,251	112	300/L-30 44-10 060-00/00	44.162222	-60.069167
PESKOWESK A-99	2,376	2,460	84	300/A-99 44-30 058-45/50	44.470556	-58.978333
SABLE ISLAND IH-58	2,480	2,614	134	300/H-58 44-00 060-00/01	43.9575	-60.127222

Well name	NASKAPI TOP (m)	NASKAPI BOT (m)	NASKAPI ISOPACH (m)	UWI	Latitude	Longitude
SABLE ISLAND 2H-58	2,616	2,707	92	302/H-58 44-00 060-00/00	43.9575	-60.127222
SABLE ISLAND 3H-58	2,655	2,712	57	303/H-58 44-00 060-00/00	43.9575	-60.127222
SABLE ISLAND 4H-58	2,542	2,682	140	304/H-58 44-00 060-00/00	43.9575	-60.127222
SABLE ISLAND 5H-58	2,465	2,478	13	305/H-58 44-00 060-00/00	43.9575	-60.127222
SABLE ISLAND C-67	2,726	2,868	142	300/C-67 44-00 059-45/50	43.934722	-59.916944
SABLE ISLAND E-48	2,400	2,521	121	300/E-48 44-00 060-00/00	43.955833	-60.123333
SABLE ISLAND O-47	2,413	2,539	126	300/O-47 44-00 060-00/00	43.949167	-60.110556
SACHEM D-76	2,794	2,976	182	300/D-76 44-40 057-30/00	44.585833	-57.699444
SAMBRO I-29	1,011	1,104	93	300/I-29 43-40 062-45/50	43.643056	-62.804722
SAUK A-57	2,880	3,135	255	300/A-57 44-20 058-30/00	44.268333	-58.63
SOUTHAMPTON A-25	3,490	3,880	390	300/A-25 43-40 060-15/00	43.569349	-60.304631
SOUTH DESBARRES O-76	2,385	2,507	123	300/O-76 44-10 059-45/50	44.098889	-59.933056
SOUTH GRIFFIN J-13	2,882	3,050	168	300/J-13 44-30 058-00/00	44.376944	-58.031944
SOUTH SABLE B-44	2,870	3,052	182	300/B-44 44-00 059-45/50	43.885	-59.861389
SOUTH VENTURE O-59	2,889	3,004	115	300/O-59 44-00 059-30/00	43.981389	-59.635833
SOUTHWEST BANQUEREAU F-34	3,533	3,918	385	300/F-34 44-10 058-45/50	44.054444	-58.839444
TANTALLON M-41	5,087	5,167	80	300/M-41 44-00 058-15/50	43.848889	-58.373611
THEBAUD C-74	2,525	2,646	121	300/C-74 44-00 060-00/00	43.884722	-60.193333
THEBAUD I-93	2,538	2,651	113	300/I-93 44-00 060-00/00	43.879167	-60.230833
THEBAUD I-94	2,516	2,633	117	300/I-94 44-00 060-00/00	43.895	-60.226944
THEBAUD P-84	2,517	2,610	93	300/P-84 44-00 060-00/00	43.9	-60.205278
TRIUMPH P-50	3,890	4,102	212	300/P-50 43-40 059-45/50	43.664444	-59.850556
TUSCARORA D-61	2,220	2,385	165	300/D-61 44-50 058-45/50	44.670278	-58.918611
UNIACKE G-72	2,453	2,563	111	300/G-72 44-20 059-30/00	44.191389	-59.736111
VENTURE B-13	2,841	2,967	126	300/B-13 44-10 059-30/00	44.036667	-59.534444

Well name	NASKAPI TOP (m)	NASKAPI BOT (m)	NASKAPI ISOPACH (m)	UWI	Latitude	Longitude
VENTURE B-43	2,836	2,967	131	300/B-43 44-10 059-30/00	44.033611	-59.610278
(SOUTH??) VENTURE B-52	2,853	2,970	117	300/B-52 44-10 059-30/00	44.019444	-59.635556
VENTURE D-23	2,826	2,951	126	300/D-23 44-10 059-30/00	44.0375	-59.573611
VENTURE H-22	2,851	2,983	132	300/H-22 44-10 059-30/00	44.023333	-59.551944
VENTURE N-1	3,049	3,159	110	300/N-01 44-10 059-45/50	44.016389	-59.764167
WENONAH J-75	2,814	3,056	242	300/J-75 43-40 060-15/50	43.573889	-60.429167
WEST CHEBUCTO K-20	3,755	4,015	260	300/K-20 43-40 059-45/50	43.6625	-59.792222
WEST ESPERANTO B-78	2,153	2,324	172	300/B-78 44-50 058-15/50	44.784167	-58.436389
WEST OLYMPIA O-51	2,616	2,735	120	300/O-51 44-10 059-45/50	44.013056	-59.884444
WEST VENTURE C-62	2,790	2,960	170	300/C-62 44-10 059-30/00	44.01744	-59.66692
WEST VENTURE N-91	2,810	2,935	125	300/N-91 44-10 059-30/00	44.012778	-59.741111
WYANDOT E-53	1,360	1,430	70	300/E-53 45-00 059-15/00	44.87216	-59.3988
WHYCOCOMAGH N-90	2,724	2,920	196	300/N-90 43-40 060-15/50	43.664167	-60.467778

Appendix C: Intervals of Naskapi Member Mapped – Lithology Counts

Meters of Naskapi interval showing Visual Porosity, Rock type, and Oil Stain. These intervals were determined from examination of drill cuttings and were derived from Canstrat™ data.

METERS OF NASKAPI INTERVAL:	INTERGRANULAR POROSITY (m)	>6%	>9%	>12%	>15%	>20%	3-30%	ALL POROSITY	ROCK TYPES (m)	SANDS TONE	SILTS TONE	SHALE	LIME STONE	GREEN SHALE	SIDERITE	MARLSTONE	CLAY	CONG L	OIL STAIN (m)	GOOD	MEDIUM	QUESTIONABLE	TOTAL OIL STAIN	
ABENAKI J-56	21.7			16.5		5.8	2.4	216.5		47.2	7.3			15.5										
ABENAKI L-57	13.4		12.5	8.3		5.5		39.7		30.6	4	30.4												
ADAMANT N-97	37.5	27.5	25	20	15	10		135		47.5	20	22.5	2.5				22.5							
ALMA F-67	5.2		1.8		0.9			7.9		31.3	61.1	194.1	2.5				10.6							
ALMA K-85	0.9							0.9		19.9	2.1		2.1		1.3	9.5	1.8					0.9	0.9	
ARCADIA J-16					0.9			0.9		22.2	28.6	74.1		2.1										
BALMORAL M-32	7.5							7.5		17.5	25	82.5	2.5											
BANQUEREAU C-21	27.6	27.7	21.8	10	4.8	0.9		87.8		58.7	29.4	143.3	1.5											
CHEBUCTO K-90	8.3	6.7	3.4	2.4				20.8		23.5	32.4	24.8	1.8			1.2								
CHIPPEWA G-67	14.6			13.4		3.7		31.7		25.4	3.7	48.9		6.6										
CHIPPEWA L-75	13.6	11.2	10.3	9.4		6.1		50.6		13.3			4.6				33							
CITADEL H-52		45.1	30.7	23.2	17.1			116.1		70	62.4	154.4	4.3											

METERS OF NASKAPI INTERVAL:	INTERGRANULAR POROSITY (m)							ROCK TYPES (m)									OIL STAIN (m)				
	>3%	>6%	>9%	>12%	>15%	>20%	30%	ALL POROSITY	SANDS TONE	SILTS TONE	SHAL	LIMESTONE	GREEN SHALE	SIDERITE	MARLSTONE	CLAY	CONG L	GOOD	MEDIUM	QUESTIONABLE	TOTAL OIL STAIN
COHASSET A-52	11.9	1.6	6.8	6.5		6.2	3.8	46.8	48.3	30.3	85.1							7.6	0.3		7.9
COHASSET D-42	11.9			9.8	7.9	6.4	1.9	37.9	22	4.9	98.7	2.8							3.4	3.3	6.7
COHASSET L-97		2.8	2.3	20.8	12.3	10		93.2	51.3	5.5	83.7									13.8	13.8
COHASSET P-42	12.5	9			5	3.5		30	19.5	23.5	84.5	3	17.5								
COMO P-21	12.4	5.9			2.4	1		21.7	27.9	34	65.6	1.5								1.4	1.4
CREE E-35	7.7	5.5		3				16.2	25.7	7.2	14.8.2		1.5								
DAUNTLESS D-35	10.7	8.3	5.5	1.5				26	37.4	33.8	11.5		3.1								
DEMASCOTA G-32		6.1	4.6	3.4				14.1	12.8	4.9	16.3.1	3									
DOVER A-43	37.2	3.4	2.4	19.4	8.7	5.8		130.7	52.6	20.4	25.2										
EAGLE D-21	17.7	1.6		8.7			3.3	42.3	38.3	17	15.8.6		5.2							2.7	2.7
EMMA N-03		3.9	1.5	14	4.5	2		79	48.5	14	32	3	2			3.6.5					
ERIE D-26	17.9			14.3		11	5.2	48.4	21.5	1.8	3.1					3.1.8					
ESPERANTO K-78	7.9			3.4				11.3	13.1	1.6	37.4		2.4								
GLENELG E-58	8.5	2						10.5	29.5	13.5	26.3	11.5			10						
GLENELG H-38	52.6	3.5	1.4	7.6	2.7			108.4	128.9	101.3	14.1.3								7	27	34

METERS OF NASKAPI INTERVAL:	INTERGRANULAR POROSITY (m)							ROCK TYPES (m)							OIL STAIN (m)					
	>6%	>9%	>12%	>15%	>20%	30-33%	ALL POROSITY	SANDS TONE	SILTS TONE	SHALE	LIME STONE	GREEN SHALE	SIDERITE	MARL STONE	CLAY	CONG L	GOOD	MEDIUM	QUESTIONABLE	TOTAL OIL STAIN
GLENELG J-48							0	17.9	68.7	24.1	2.1	7.9		5.2						
GLENELG N-49			2.4				2.4	17.2	4.3	26.4	7		2.8	2.5						
GLOOSCAP C-63							0	19.6	16.2	23.1	2.4		7.5		7.2					
HESPER I-52	5.8	4.8		3.3	2.1		16	7.6	5.7	37.9										
HESPER P-52		2.7					2.7	8.3	10.1	36.1										
INTREPID L-80		1.7	1.6	15.2		6.8	56.3	25.7	8.8	99								3.7	2.1	5.8
IROQUOIS J-17	17		8.5	6.4			31.9	32.5		55.3		5.8					2.1	5.4		7.5
KEGESHOOK G-67	15.6	1.4	2.4				32.1	32.5	7	56.5	4.6				1.5				14.1	14.1
LAWRENCE D-14	8				2.5		10.5	14	32.5	73.5					5		2.5	5		7.5
LOUISBOURG J-47			4				4	17.4	11.9	76.2										
MARMORA C-34	4.2	2.1					6.3	25.6	27.4	19.2									0.9	0.9
MARMORA P-35	17.2			15.6		5	1.9	39.7	48.1	12.5										
MICMAC D-89		1.3	1.0	7.9		4.2	36.3	22.1	1.2	42.6		15								
MICMAC H-86	33.6	2.8	2.1	19.7	10.1	4.3	117.6	44.6	2.4	37.8	1.8	15.2					8.2	18.2	10	36.4
MICMAC J-77	15.6			13.1	6.7	2.1	37.5	16.5	2.7	32.6		30.5						1.5	2.1	3.6
MIGRANT N-20	14		1.2	10.2		6.1	4.3	46.6	34.9	0.9										

METERS OF NASKAPI INTERVAL:	INTERGRANULAR POROSITY (m)							ROCK TYPES (m)										OIL STAIN (m)			
	>3% >6%	>9%	>12%	>15%	>20%	30%	ALL POROSITY	SANDS TONE	SILTS TONE	SHALE	LIMESTONE	GREEN SHALE	SIDERITE	MARLSTONE	CLAY	CONG L	GOOD	MEDIUM	QUESTIONABLE	TOTAL OIL STAIN	
MISSISSAUGA H-54	15.4		13		2.2		30.6	32.4		66.4		10.8									
MOHEIDA P-15			2.2				2.2	41.9	26.5	13.2.8	22.5										
MOHICAN I-100		25.3	18.9	11	9.2	5.5	89.7	74.7	41.9	16.7.7	16.2										
NASKAPI N-30	4		3.4				7.4	21.1		13.0.5	6.3	5.2									
NORTH BANQUEREAU I-13	28.6	26.8	25.3	17.7	0.9		123.6	54.2	46.4	26.5.1	1.5								0.9	0.9	
NORTH TRIUMPH B-52							0	16.5	72.3	26.1.2											
NORTH TRIUMPH G-43	15	5	2	1			23	57.9	68.3	14.4.3											
OJIBWA E-07		28.7	23.6		13.7	3	69	46.3	0.9	19.8	4		1.2			8.9.9					
OLYMPIA A-12	23.9	15.3	1.8				40.2	36.3	2.4	89.4											
ONEIDA O-25	18.5		9.3	8.1		2	37.9	41.4	1.2	24.0											
ONANDAGA B-96		19.2	18.9	11.6	6.4	2.5	62.3	41.3	8.9	13.3.6	5.1										
ONANDAGA E-84	12.1	8.1	4.6	4.8	1.5		32.5	23.5	3.5	15.3.2	3.3	1.5	11.3								
ONANDAGA F-75	21.6	20.1	9.7	6.4	5.5	1.8	65.1	48.8	8.4	22.4.7		6.1	1.2								
ONANDAGA O-95		25.9	17.9	11.5	7.6	6.7	98.8	80.6	7	12.9.4											
PANUKE F-99	5		4.3		1.5		10.8	38.8	46	47.7	3.5	3.1					1.5		3.5	5	

METERS OF NASKAPI INTERVAL:	INTERGRANULAR POROSITY (m)							ROCK TYPES (m)										OIL STAIN (m)				
		>3% %	>6 %	>9 %	>12 %	>15 %	>20 %	30 %	ALL POROSITY	SANDSTONE	SILTSTONE	SHALE	LIMESTONE	GREEN SHALE	SIDERITE	MARLSTONE	CLAY	CONGLOMERATE	GOOD	MEDIUM	QUESTIONABLE	TOTAL OIL STAIN
WHYCOCOMAGH N-90	7.8	6.8		5.8		1		21.4	22.6	50.4	127			2.5								
WYANDOT E-53	53			31	24	18		126	122		107		65									

Appendix D: Canstrat™ LAS Mnemonics

This appendix outlines the curve names and descriptions which were used to map in Petrel.

They were created to allow one to plot the lithological descriptions. The mnemonic integer display column will be shown on the various map legends seen in Chapter 6 results.

<i>LAS file name</i>	<i>LAS curve</i>	<i>Curve Mnemonic description</i>	<i>Mnemonic integer display</i>	<i>Integer description</i>
CS_main	RTC_ID	Rock type ID	0 - 40 1 2 3 4 8 9 12 13 16 17 18 19 20 22 24 26 27 30 35 37 39	Igneous basic Igneous acidic Metamorphic Volcanic Siderite Glacial till Conglomerate Breccia Chert Sandstone Siltstone Clay Shale Bentonite Coal Marlstone Limestone Dolomite Anhydrite Salt Gypsum

LAS file name	LAS curve	Curve Mnemonic description	Mnemonic integer display	Integer description
			40	Phosphate
	RTC_IDPERC	Rock type ID percentage - for all percentage values in LAS files...	0 - 100 10 20 30 40 50 60 70 80 90 100	10% 20% 30% 40% 50% 60% 70% 80% 90% 100%
	RTC_ RTC_CLAST_C G RTC_CLAST_F G RTC_EVAP RTC_CARB RTC_IGVOL	Rock type general composite Rock type clastic - coarse grained % Rock type clastic - fine grained % Rock type evaporite - % Rock type carbonates - % Rock type igneous, metamorphic, volcanic %	0 - 100 0 - 100 0 - 100 0 - 100 0 - 100	
	PORGRADE PORTYPE_PRI	Porosity grade % Porosity type ID primary	0 - 100 0 - 9 1 2 3	3% 6% 9%

<i>LAS file name</i>	<i>LAS curve</i>	<i>Curve Mnemonic description</i>	<i>Mnemonic integer display</i>	<i>Integer description</i>
			4 5 6 7 8 9	12% 15% 20% 26% 33% >33%
	GRAINS_MM	Grain size	mm 0.001 0.001 0.001 0.001 0.0176 0.0473 0.0781 0.1094 0.156 0.2185 0.313 0.438 0.625 0.875 1.5	cryptocrystalline lithographic shale, clay, marlstone volcanics 1/2 silt size silt size 1/2 very fine grained very fine grained 1/2 fine grained fine grained 1/2 medium grained medium grained 1/2 coarse grained coarse grained greater than 1 mm
	FRAMEW_PER	Framework %	-1 - 100 -1 0	uninterpretable 0% framework (100% matrix)

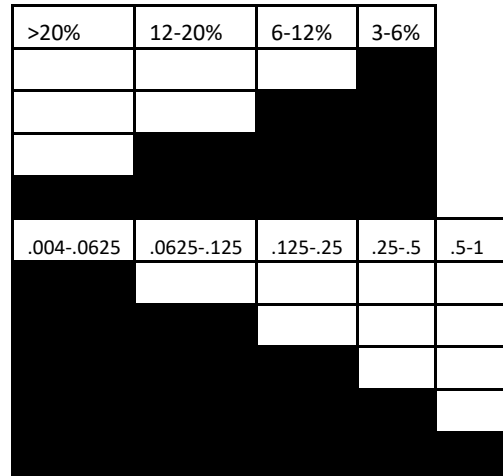
<i>LAS file name</i>	<i>LAS curve</i>	<i>Curve Mnemonic description</i>	<i>Mnemonic integer display</i>	<i>Integer description</i>
			10 20 30 40 50 60 70 80 90 100	10% framework (90% matrix) 20% framework (80% matrix) 30% framework (70% matrix) 40% framework (60% matrix) 50% framework (50% matrix) 60% framework (40% matrix) 70% framework (30% matrix) 80% framework (20% matrix) 90% framework (10% matrix) 100% framework (0% matrix)
	DIAC_ DIAC_CEM DIAC_FRAC DIAC_POR	Diagenesis composite Diagenesis cements composite % Diagenesis fracture composite % Diagenesis porosity composite %	0 - 100 0 - 100 0 - 100	
	ROUND	Rounding	0 - 4 1 2	Angular Sub angular

LAS file name	LAS curve	Curve Mnemonic description	Mnemonic integer display	Integer description
			3 4	Sub round Round
	SORT	Sorting	0 - 3 1 2 3	Poorly sorted Medium sorted Well sorted
	OILSTN	Oil staining	0 - 4 1 2 3 4	Questionable stain Dead stain Medium - spotted stain Good stain
	COLOUR	Colour ID	0 - 14 1 2 3 4 5 6 7 8 9 10 11 12 13 14	White Cream Buff-tan Yellow Salt and pepper Varicoloured Orange Red Purple Blue Green Brown Gray Black
	COLORINT	Colour intensity	0 - 9	

<i>LAS file name</i>	<i>LAS curve</i>	<i>Curve Mnemonic description</i>	<i>Mnemonic integer display</i>	<i>Integer description</i>
			1 3 5 7 9	Very light Light Medium Dark Very dark
	IFFOSSIL	Fossil occurrence	0 - 3 2	Fossil occurrence
	IFMINERAL	Mineral occurrence frequency	0 - 8 1 2 3 4	Rare Scattered Common Abundant

Appendix E: Canstrat™ Log Lithology Symbols

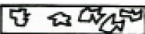


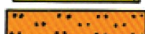



These symbols were used in Canstrat logs to represent a summary of geological characteristics seen in well cuttings. The information logged was then converted to a digital LAS 2.0 file format.



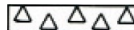






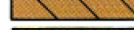










266









Porosity Types	x	Intercrystalline, intergranular, interfragmental
	Φ	interoolitic, interpelletoid
	v	vuggy
	P	pinpoint
	~	moldic
	o	organic, intrafossil
	F	fracture
	e	earthy, low permeability, crystals < 1/16 mm
	◻	fenstral, gas bubble voids, shrinkage cracks, birdseye texture
Oil Show	Good	Even staining, fluoresces in solvent
	Medium	Spotted staining, fluoresces in solvent
	Dead	Dead, asphaltic, bitumen, etc

	Questionable	No fluorescence, in solvent	
Porosity Grades	1	3 - 6%	Poor porosity with low permeability
	2	6 - 12%	Fair porosity
	3	12-20%	Good porosity
	4	>20%	Excellent porosity
Grain Size (Wentworth Scale)	1	.004 - .0625 mm	Silt Size
	2	.0625 - .125 mm	Very Fine Sand
	3	.125 - .250 mm	Fine Sand
	4	.250 - .500 mm	Medium Sand
	5	.500 - 1.000 mm	Coarse
Rounding	A	angular	
	a	subangular	
	R	rounded	
	r	subrounded	
Sorting	W	well	
	M	medium	
	P	poor	
Framework (Ratio of Framework to Filler)	0	0 - 5%	
	1	10%	
	2	20%	
	3	30%	
	4	40%	
	5	50%	
	6	60%	
	7	70%	
	8	80%	
	9	90%	
	C	100%	
?5	questionable interpretation		





















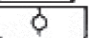
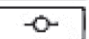
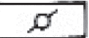






	?	uninterpretable
Diagenesis	M	Metasomatism
	D	Dolomitization
	R	Recrystallization
	F	Fracturing
	L	Leaching
	P	Pressure Deformation
	A	Anhydrite
	S	Silica
	K	Kaolin
	C	Calcite
	1	10%
	2	20%
	3	30%
	4	40%
	5	50%
	6	60%
	7	70%
8	80%	
9	90%	
C	100%	
	?	Uninterpretable
Lithology Types		Breccia
		Conglomerate
		Sandstone
		Siltstone
		Shale, gray
		Shale, black
		Shale, colored



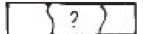





	Claystone, gray
	Bentonite
	Chert, bedded
	Marlstone, calcareous
	Limestone, mudsupported FW<7
	Limestone, grainsupported FW>7
	Marlstone, dolomitic
	Dolomite, primary
	Dolomite, secondary
	Siderite
	Anhydrite, primary
	Anhydrite, secondary
	Gypsum
	Salt
	Coal
	Glacial Till
	Igneous, basic
	Igneous, acidic
	Tuff
	Welded Tuff
	Metamorphic

Accessories

	Sandy
	Sandstone stringers
	Silty
	Siltstone stringers
	Pebbles >2mm
	Sand Grains 1 - 2 mm
	Argillite Grain
	Feldspar

	Breccia Fragment
	Siliceous
	Chert, light and dark
	Chert, tripolite
	Argillaceous
	Shale, laminae
	Carbonaceous flakes
	Coal
	Cementing bituminous substance
	Calcareous
	Marlstone stringers calcareous
	Limestone stringers
	Dolomitic
	Marlstone stringers dolomitic
	Dolomite stringers
	Anhydritic
	Anhydritic stringers
	Gypsum stringers
	Salt cast
	Phosphate pellets
	Ferruginous Grains
	Ferruginous
	Ferruginous stringers
	Nodules
	Tuffaceous
	Heavy dark min
	Glauconite
	Bentonite
	Pyrite

		Kaolin
		Plant spores
		Plant remains
		Fish remains
		Mineral Crystals
Rockbuilders		Foraminifera
		Crinoid
		Pelecypod
		Bioclastic debris
		Amphipora
		Coral
		Stromatoporoid
		Bryozoa
		Brachiopod
		Ostracod
		Cephalopod
		Gastropod
		Scaphopod
		Belemnite
		Echinoid
		Fossils
		Oolites
		Pisolite
		Pellets
		Intraclastics
		Skeletal
		Ootoid
		Non-descript algae
		Laminated algae

Miscellaneous	   	Karst Topography No Samples Uninterpretable Questionable
Textures	   	Earthy Chalky Lithographic Cryptocrystalline

Appendix F: Naskapi DST Temperature Values Plotted

The table below consists of all temperature data for wells with Naskapi intervals. The DST temperature values (in bold italics) are used to plot temperature map. Log temperature values are unreliable as they are impacted by drilling mud temperatures so were not included.

(Natural Resources Canada, Geological Survey of Canada, Geoscience Data Repository, BASIN Database, Date: May 30, 2016, 10:05 am ADT)

Well Name	Depth (m)	Temperature (C°)	Author	Source	Comments
ALMA F-67	2804	84	SHELL CANADA RESOURCES LTD	LOG	DUAL LATEROLOG-MICRO SHALLOW FOCUSED LOG ? [SFL]
ALMA K-85	2857	97	SHELL CANADA RESOURCES LTD	DST	
BALMORAL M-32	2296	72	LASMO NSRL	LOG	REPEAT FORMATION TESTER
BANQUEREAU C-21	3469	103	PETRO-CANADA EXPLORATION INC	DST	
BLUENOSE G-47	2981	78.9	ISSLER 1982	COR	
CHEBUCTO K-90	3397	87	HUSKY OIL OPERATIONS LTD	LOG	COMPLETION RECORD
NORTH TRIUMPH B-52	3357	97	HUSKY/BOW VALLEY EAST COAST PROJECT GROUP	DST	
COHASSET A-52	2484	74	PETRO-CANADA INC	LOG	TCP PERFORATIONS
COHASSET D-42	2255	79	MOBIL OIL CANADA LTD	DST	
GLENELG J-48	3330	100	SHELL CANADA RESOURCES LTD	LOG	CEMENT BOND-VARIABLE DENSITY LOG
GLENELG N-49	3078	90	SHELL CANADA LTD	LOG	REPEAT FORMATION TESTER
HESPER I-52	2796	73	ISSLER 1982	COR	
INTREPID L-80	2924	89	ISSLER 1982	COR	TEMPERATURES QUESTIONABLE
IROQUOIS J-17	1345	45	ISSLER 1982	COR	WELL HAS ENCOUNTERED SALT
LAWRENCE D-14	2273	73	LASMO NSRL	LOG	REPEAT FORMATION TESTER
LOUISBOURG J-47	2974	66	HOME OIL COMPANY LTD	LOG	DEPTH DERIVED BOREHOLE COMPENSATED SONIC LOG
MARMORA C-34	3138	83.7	SHELL CANADA LTD	LOG	FORMATION TESTER
MERIGOMISH C-52	2993	102	SHELL CANADA RESOURCES LTD	LOG	REPEAT FORMATION TESTER
NORTH TRIUMPH B-52	3777	117.5	SHELL CANADA LTD	DST	
OJIBWA E-07	1330	43.1	ISSLER 1982	COR	TEMPERATURES QUESTIONABLE
ONONDAGA E-84	2606	77	SHELL CANADA LTD	LOG	CONTINUOUS DIPMETER (3-ARM)
PANUKE F-99	2264	85	PETRO-CANADA INC	DST	

Well Name	Depth (m)	Temperature (C°)	Author	Source	Comments
PESKOWESK A-99	2395	71	SHELL CANADA RESOURCES LTD	LOG	REPEAT FORMATION TESTER
SABLE ISLAND 2H-58	2629	80	MOBIL OIL CANADA LTD	LOG	DUAL INDUCTION LATEROLOG
SABLE ISLAND 3H-58	2691	85.3	ISSLER 1982	COR	TRUE VERTICAL DEPTH?
SABLE ISLAND 4H-58	2706	76	MOBIL OIL CANADA LTD	LOG	CONTINUOUS DIPMETER (4-ARM)
SABLE ISLAND 5H-58	2478	73	MOBIL OIL CANADA LTD	LOG	DUAL INDUCTION LATEROLOG
SABLE ISLAND C-67	2894	90.6	MOBIL OIL CANADA LTD	LOG	FORMATION TESTER
SABLE ISLAND E-48	2543	78.9	ISSLER 1982	COR	WELL HAS ENCOUNTERED SALT
SAMBRO I-29	1059	27.1	ISSLER 1982	COR	TEMPERATURES QUESTIONABLE
SOUTH SABLE B-44	2835	64.5	MOBIL OIL CANADA LTD	LOG	BOREHOLE COMPENSATED SONIC LOG & DEPTH DERIVED BOREHOLE COMPENSATED [BHC] SONIC LOG
SOUTH VENTURE O-59	3072	86	MOBIL OIL CANADA LTD	LOG	LONG SPACING SONIC LOG
SOUTHWEST BANQUEREAU F-34	3940	107.5	PETRO-CANADA INC	DST	
VENTURE 1	3153	79	SABLE OFFSHORE ENERGY	LOG	CEMENT VOLUME LOG FROM 6 ARM CALIPER
VENTURE B-52	2959	82	MOBIL OIL CANADA LTD	LOG	CEMENT BOND-VARIABLE DENSITY LOG
VENTURE H-22	2956	89	MOBIL OIL CANADA LTD	LOG	DEPTH DERIVED BOREHOLE COMPENSATED SONIC LOG
WEST CHEBUCTO K-20	4660	142.1	HUSKY/BOW VALLEY EAST COAST PROJECT	DST	
WEST OLYMPIA O-51	2666	65	MOBIL OIL CANADA LTD	LOG	DEPTH DERIVED BOREHOLE COMPENSATED SONIC LOG

Appendix G: Naskapi TOC Values Plotted

All organic carbon values in the Naskapi from the BASIN Database and at the interval found.

http://basin.gdr.nrcan.gc.ca/index_e.php

Wells> Scotian Shelf>Well Name>Geochem> Rock Eval Pyrolysis>Organic Carbon

Some interval depths have multiple values obtained from different studies outlined in solid black.

These are averaged and are included in average of total Naskapi formation.

The average value of the TOC per well was plotted.

275

Well identifier	Surface	MD	TOC	TOC Ave Naskapi plotted
ALMA F-67	TOC	2500	1.94	1.58
ALMA F-67	TOC	2530	2.12	
ALMA F-67	TOC	2560	1.94	
ALMA F-67	TOC	2590	2.03	
ALMA F-67	TOC	2620	1.26	
ALMA F-67	TOC	2650	1.54	
ALMA F-67	TOC	2680	1.91	
ALMA F-67	TOC	2710	1.42	
ALMA F-67	TOC	2720	2.2	
ALMA F-67	TOC	2740	2.3	
ALMA F-67	TOC	2770	1.98	
ALMA F-67	TOC	2800	0.89	
ALMA F-67	TOC	2830	1.56	
ALMA F-67	TOC	2860	1.71	
ALMA F-67	TOC	2890	0.91	
ALMA F-67	TOC	2895	0.17	
ALMA F-67	TOC	2920	1.13	
ALMA F-67	TOC	2950	1.71	
ALMA F-67	TOC	2980	1.36	

276

Well identifier	Surface	MD	TOC	TOC Ave Naskapi plotted
ARCADIA J-16	TOC	2750	1.5	1.37
ARCADIA J-16	TOC	2780	1.15	
ARCADIA J-16	TOC	2810	1.83	
ARCADIA J-16	TOC	2840	1.05	
ARCADIA J-16	TOC	2930	1.33	
CHEBUCTO K-90	TOC	4075	5.13	3.78
CHEBUCTO K-90	TOC	4220	2.43	
COHASSET L-97	TOC	2080	0.98	1.66
COHASSET L-97	TOC	2110	2.07	
COHASSET L-97	TOC	2135	2.46	
COHASSET L-97	TOC	2140	2.44	
COHASSET L-97	TOC	2170	1.95	
COHASSET L-97	TOC	2210	0.59	
COHASSET L-97	TOC	2210	0.52	
COHASSET L-97	TOC	2240	1.16	
CREE E-35	TOC	2392.7	1.97	2.27
CREE E-35	TOC	2414	3.14	
CREE E-35	TOC	2542	1.71	
DAUNTLESS D-35	TOC	2700.5	1.06	1.63
DAUNTLESS D-35	TOC	2724.9	1.04	
DAUNTLESS D-35	TOC	2749.3	2.27	
DAUNTLESS D-35	TOC	2773.7	2.15	
DAUNTLESS D-35	TOC	2779.8	1.34	
DAUNTLESS D-35	TOC	2798.1	2.16	
DAUNTLESS D-35	TOC	2810.3	2.19	
DAUNTLESS D-35	TOC	2816.4	1.28	
DAUNTLESS D-35	TOC	2822.5	2.45	
DAUNTLESS D-35	TOC	2828.5	1.96	

Well identifier	Surface	MD	TOC	TOC Ave Naskapi plotted
DAUNTLESS D-35	TOC	2840.7	1.77	
DAUNTLESS D-35	TOC	2846.8	1.41	
DAUNTLESS D-35	TOC	2852.9	1.95	
DAUNTLESS D-35	TOC	2859	2.03	
DAUNTLESS D-35	TOC	2871.2	1.79	
DAUNTLESS D-35	TOC	2877.3	0.47	
DAUNTLESS D-35	TOC	2883.4	1.75	
DAUNTLESS D-35	TOC	2907.8	1.12	
DAUNTLESS D-35	TOC	2916.9	1.96	
DAUNTLESS D-35	TOC	2920	1.65	
DAUNTLESS D-35	TOC	2932.2	1.7	
DAUNTLESS D-35	TOC	2935.2	0.52	
DEMASCOTA G-32	TOC	2209.8	0.64	1.4
DEMASCOTA G-32	TOC	2240.3	2.25	
DEMASCOTA G-32	TOC	2267.7	1.48	
DEMASCOTA G-32	TOC	2331.7	1.25	
EAGLE D-21	TOC	3291.8	1.35	1.35
GLENELG J-48	TOC	3130	1.47	2.34
GLENELG J-48	TOC	3140	2.05	
GLENELG J-48	TOC	3150	2.38	
GLENELG J-48	TOC	3150	2.29	
GLENELG J-48	TOC	3160	2.37	
GLENELG J-48	TOC	3160	2.16	
GLENELG J-48	TOC	3170	2.21	
GLENELG J-48	TOC	3180	2.25	
GLENELG J-48	TOC	3190	2.11	
GLENELG J-48	TOC	3190	2.62	
GLENELG J-48	TOC	3200	2.09	

Well identifier	Surface	MD	TOC	TOC Ave Naskapi plotted
GLENELG J-48	TOC	3200	2.3	
GLENELG J-48	TOC	3210	2.54	
GLENELG J-48	TOC	3220	1.51	
GLENELG J-48	TOC	3230	2	
GLENELG J-48	TOC	3240	2.26	
GLENELG J-48	TOC	3250	2.36	
GLENELG J-48	TOC	3250	1.86	
GLENELG J-48	TOC	3260	2.21	
GLENELG J-48	TOC	3260	2.12	
GLENELG J-48	TOC	3270	1.67	
GLENELG J-48	TOC	3280	3.26	
GLENELG J-48	TOC	3290	1.95	
GLENELG J-48	TOC	3290	1.57	
GLENELG J-48	TOC	3300	3.85	
GLENELG J-48	TOC	3300	1.06	
GLENELG J-48	TOC	3310	2.35	
GLENELG J-48	TOC	3320	2.02	
GLENELG J-48	TOC	3330	2.55	
GLENELG J-48	TOC	3340	2.52	
GLENELG J-48	TOC	3350	2.37	
GLENELG J-48	TOC	3360	2.24	
GLENELG J-48	TOC	3370	2.26	
GLENELG J-48	TOC	3380	2.69	
GLENELG J-48	TOC	3390	2.9	
GLENELG J-48	TOC	3400	2.63	
GLENELG J-48	TOC	3410	2.54	
GLENELG J-48	TOC	3420	2.57	
GLENELG J-48	TOC	3430	2.72	

279

Well identifier	Surface	MD	TOC	TOC Ave Naskapi plotted
GLENELG J-48	TOC	3440	2.56	
GLENELG J-48	TOC	3450	2.72	
GLENELG J-48	TOC	3460	2.86	
GLENELG J-48	TOC	3470	2.76	
GLOOSCAP C-63	TOC	1850	0.16	2.03
GLOOSCAP C-63	TOC	1860	0.18	
GLOOSCAP C-63	TOC	1870	0.91	
GLOOSCAP C-63	TOC	1875	1.01	
GLOOSCAP C-63	TOC	1880	0.92	
GLOOSCAP C-63	TOC	1890	1.11	
GLOOSCAP C-63	TOC	1900	1.3	
GLOOSCAP C-63	TOC	1900	0.86	
GLOOSCAP C-63	TOC	1910	1.25	
GLOOSCAP C-63	TOC	1920	1.2	
GLOOSCAP C-63	TOC	1920	1.08	
GLOOSCAP C-63	TOC	1930	1.56	
GLOOSCAP C-63	TOC	1940	2.18	
GLOOSCAP C-63	TOC	1940	1.72	
GLOOSCAP C-63	TOC	1950	2.46	
GLOOSCAP C-63	TOC	1950	1.91	
GLOOSCAP C-63	TOC	1960	2.48	
GLOOSCAP C-63	TOC	1960	2.1	
GLOOSCAP C-63	TOC	1970	2.39	
GLOOSCAP C-63	TOC	1980	2.19	
GLOOSCAP C-63	TOC	1990	2.67	
GLOOSCAP C-63	TOC	1990	2.42	
GLOOSCAP C-63	TOC	2000	2.88	
GLOOSCAP C-63	TOC	2000	2.76	

Well identifier	Surface	MD	TOC	TOC Ave Naskapi plotted
GLOOSCAP C-63	TOC	2010	0.48	
GLOOSCAP C-63	TOC	2010	2.56	
GLOOSCAP C-63	TOC	2020	0.83	
GLOOSCAP C-63	TOC	2030	2.16	
GLOOSCAP C-63	TOC	2040	3	
GLOOSCAP C-63	TOC	2050	3.29	
GLOOSCAP C-63	TOC	2050	2.72	
GLOOSCAP C-63	TOC	2060	3.2	
GLOOSCAP C-63	TOC	2060	2.33	
GLOOSCAP C-63	TOC	2070	2.9	
GLOOSCAP C-63	TOC	2080	3.37	
GLOOSCAP C-63	TOC	2080	2.32	
GLOOSCAP C-63	TOC	2090	3.5	
GLOOSCAP C-63	TOC	2090	2.3	
GLOOSCAP C-63	TOC	2100	3.4	
GLOOSCAP C-63	TOC	2100	2.27	
GLOOSCAP C-63	TOC	2110	3.04	
GLOOSCAP C-63	TOC	2110	2.71	
GLOOSCAP C-63	TOC	2120	3.27	
GLOOSCAP C-63	TOC	2120	2.76	
GLOOSCAP C-63	TOC	2130	3.5	
GLOOSCAP C-63	TOC	2130	2.38	
GLOOSCAP C-63	TOC	2140	3.55	
GLOOSCAP C-63	TOC	2140	2.66	
GLOOSCAP C-63	TOC	2150	3.55	
GLOOSCAP C-63	TOC	2150	2.94	
GLOOSCAP C-63	TOC	2160	3.21	

281

Well identifier	Surface	MD	TOC	TOC Ave Naskapi plotted
GLOOSCAP C-63	TOC	2160	2.32	
GLOOSCAP C-63	TOC	2170	2.81	
GLOOSCAP C-63	TOC	2170	2.37	
GLOOSCAP C-63	TOC	2180	2.35	
GLOOSCAP C-63	TOC	2180	2.16	
GLOOSCAP C-63	TOC	2190	2.06	
GLOOSCAP C-63	TOC	2190	1.59	
GLOOSCAP C-63	TOC	2200	1.61	
GLOOSCAP C-63	TOC	2200	1.47	
GLOOSCAP C-63	TOC	2210	2.16	
GLOOSCAP C-63	TOC	2210	1.43	
GLOOSCAP C-63	TOC	2220	0.99	
HESPER P-52	TOC	2670	1.1	0.93
HESPER P-52	TOC	2700	1	
HESPER P-52	TOC	2730	0.71	
INTREPID L-80	TOC	2828.5	0.99	1
INTREPID L-80	TOC	2828.5	1	
LOUISBOURG J-47	TOC	2730	3.13	2.33
LOUISBOURG J-47	TOC	2740	1.64	
LOUISBOURG J-47	TOC	2750	3.11	
LOUISBOURG J-47	TOC	2760	3.17	
LOUISBOURG J-47	TOC	2770	2.6	
LOUISBOURG J-47	TOC	2780	2.41	
LOUISBOURG J-47	TOC	2790	2.86	
LOUISBOURG J-47	TOC	2800	2.22	
LOUISBOURG J-47	TOC	2810	2.09	
LOUISBOURG J-47	TOC	2820	2.17	

Well identifier	Surface	MD	TOC	TOC Ave Naskapi plotted
LOUISBOURG J-47	TOC	2830	2.26	
LOUISBOURG J-47	TOC	2840	1.74	
LOUISBOURG J-47	TOC	2850	1.01	
MERIGOMISH C-52	TOC	3730	3.8	3.8
MIGRANT N-20	TOC	2343.9	1.21	0.86
MIGRANT N-20	TOC	2371.3	0.83	
MIGRANT N-20	TOC	2401.8	0.54	
NORTH TRIUMPH B-52	TOC	3410	3.52	3.1
NORTH TRIUMPH B-52	TOC	3560	3.55	
NORTH TRIUMPH B-52	TOC	3660	3.4	
NORTH TRIUMPH B-52	TOC	3773.5	1.96	
NORTH TRIUMPH G-43	TOC	3360	3.01	3.81
NORTH TRIUMPH G-43	TOC	3600	3.75	
NORTH TRIUMPH G-43	TOC	3695	4.67	
OLYMPIA A-12	TOC	2750	1.58	1.31
OLYMPIA A-12	TOC	2760	1.67	
OLYMPIA A-12	TOC	2770	1.66	
OLYMPIA A-12	TOC	2780	1.79	
OLYMPIA A-12	TOC	2790	0.74	
OLYMPIA A-12	TOC	2800	1.15	
OLYMPIA A-12	TOC	2810	1.42	
OLYMPIA A-12	TOC	2820	2.15	
OLYMPIA A-12	TOC	2830	1.38	
OLYMPIA A-12	TOC	2840	1.15	
OLYMPIA A-12	TOC	2850	1.26	
OLYMPIA A-12	TOC	2860	1.08	
OLYMPIA A-12	TOC	2870	0.93	
OLYMPIA A-12	TOC	2880	0.94	

Well identifier	Surface	MD	TOC	TOC Ave Naskapi plotted
OLYMPIA A-12	TOC	2890	0.81	
ONONDAGA B-96	TOC	2468.9	1.88	1.89
ONONDAGA B-96	TOC	2468.9	1.89	
ONONDAGA E-84	TOC	2691.4	1.68	1.68
PENOBSCOT L-30	TOC	2118.4	2.17	1.92
PENOBSCOT L-30	TOC	2212.8	1.63	
PENOBSCOT L-30	TOC	2243.3	1.98	
SABLE ISLAND C-67	TOC	2770.6	0.74	0.75
SABLE ISLAND C-67	TOC	2770.6	0.75	
SABLE ISLAND E-48	TOC	2417.1	3.76	2.21
SABLE ISLAND E-48	TOC	2426.2	1.29	
SABLE ISLAND E-48	TOC	2456.7	1.92	
SABLE ISLAND E-48	TOC	2490	2.81	
SABLE ISLAND E-48	TOC	2490.2	2.81	
SABLE ISLAND E-48	TOC	2517.6	0.69	
SABLE ISLAND O-47	TOC	2475	1.65	1.78
SABLE ISLAND O-47	TOC	2581.7	1.92	
SOUTH DESBARRES O-76	TOC	2345	2.86	2.86
SOUTH GRIFFIN J-13	TOC	2880	4.25	1.89
SOUTH GRIFFIN J-13	TOC	2890	0.74	
SOUTH GRIFFIN J-13	TOC	2900	1.57	
SOUTH GRIFFIN J-13	TOC	2910	1.6	
SOUTH GRIFFIN J-13	TOC	2920	1.27	
SOUTH GRIFFIN J-13	TOC	2930	1.7	
SOUTH GRIFFIN J-13	TOC	2940	1.15	
SOUTH GRIFFIN J-13	TOC	2950	1.28	

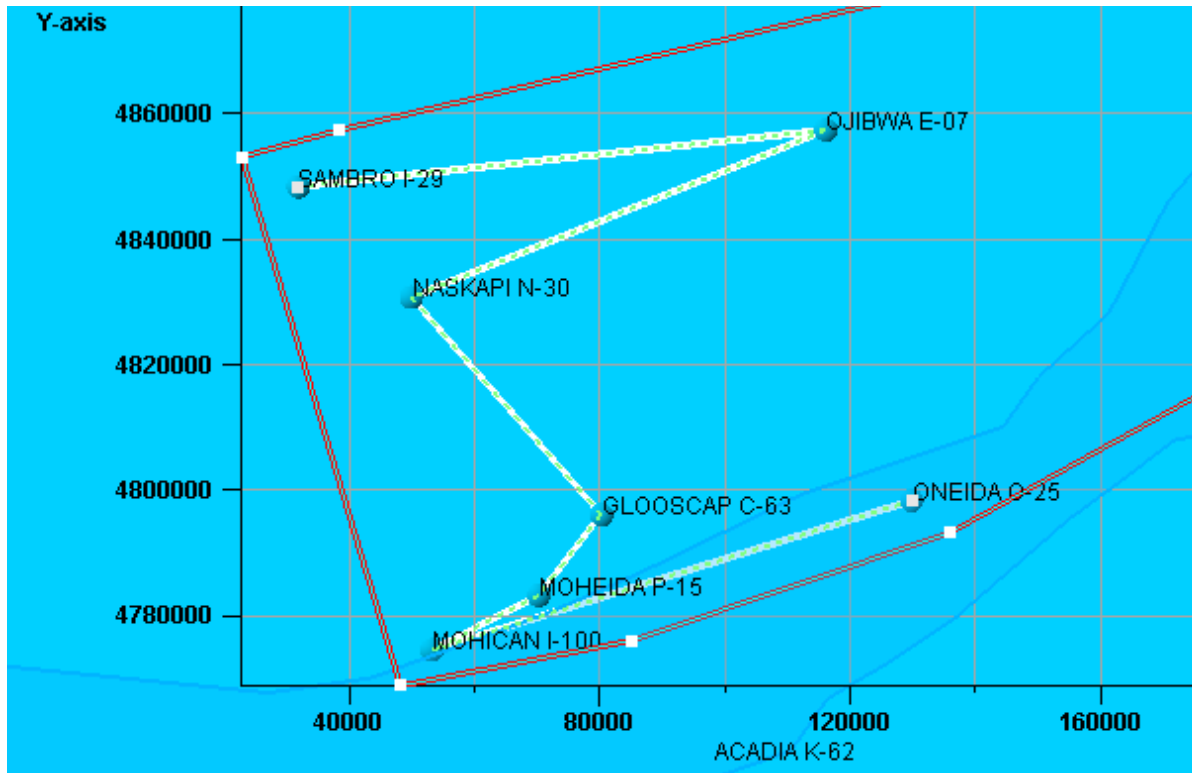
Well identifier	Surface	MD	TOC	TOC Ave Naskapi plotted
SOUTH GRIFFIN J-13	TOC	2960	1.86	
SOUTH GRIFFIN J-13	TOC	2970	1.92	
SOUTH GRIFFIN J-13	TOC	2980	1.69	
SOUTH GRIFFIN J-13	TOC	3000	1.95	
SOUTH GRIFFIN J-13	TOC	3010	2.02	
SOUTH GRIFFIN J-13	TOC	3020	2.5	
SOUTH GRIFFIN J-13	TOC	3030	2.89	
SOUTH GRIFFIN J-13	TOC	3040	2.19	
SOUTH GRIFFIN J-13	TOC	3050	1.69	
SOUTH SABLE B-44	TOC	2910	1.89	1.89
SOUTH VENTURE O-59	TOC	2880	1.45	1.13
SOUTH VENTURE O-59	TOC	2900	1.94	
SOUTH VENTURE O-59	TOC	2920	1.41	
SOUTH VENTURE O-59	TOC	2940	1.32	
SOUTH VENTURE O-59	TOC	2960	0.71	
SOUTH VENTURE O-59	TOC	2980	0.58	
SOUTH VENTURE O-59	TOC	3000	0.56	
THEBAUD C-74	TOC	2530	2.19	2.11
THEBAUD C-74	TOC	2540	2.34	
THEBAUD C-74	TOC	2560	2.09	
THEBAUD C-74	TOC	2580	2.09	
THEBAUD C-74	TOC	2600	2.18	
THEBAUD C-74	TOC	2630	2.32	
THEBAUD C-74	TOC	2640	1.62	
THEBAUD I-93	TOC	2530	0.98	1.2
THEBAUD I-93	TOC	2560	1.07	
THEBAUD I-93	TOC	2590	1.18	
THEBAUD I-93	TOC	2620	1.83	

285

Well identifier	Surface	MD	TOC	TOC Ave Naskapi plotted
THEBAUD I-93	TOC	2650	0.94	
VENTURE B-52	TOC	2860	1.91	1.63
VENTURE B-52	TOC	2875	1.64	
VENTURE B-52	TOC	2890	1.74	
VENTURE B-52	TOC	2920	1.24	
VENTURE H-22	TOC	2850	2	2.18
VENTURE H-22	TOC	2880	2.99	
VENTURE H-22	TOC	2910	2.2	
VENTURE H-22	TOC	2940	2.23	
VENTURE H-22	TOC	2970	1.48	
WENONAH J-75	TOC	2804.2	1.5	1.49
WENONAH J-75	TOC	2804.2	1.48	
WEST CHEBUCTO K-20	TOC	3760	3.6	3.26
WEST CHEBUCTO K-20	TOC	3775	3.99	
WEST CHEBUCTO K-20	TOC	3775	3.99	
WEST CHEBUCTO K-20	TOC	3780	3.37	
WEST CHEBUCTO K-20	TOC	3790	4.3	
WEST CHEBUCTO K-20	TOC	3800	3.93	
WEST CHEBUCTO K-20	TOC	3830	2.74	
WEST CHEBUCTO K-20	TOC	3850	3.06	
WEST CHEBUCTO K-20	TOC	3870	2.66	
WEST CHEBUCTO K-20	TOC	3890	3.15	
WEST CHEBUCTO K-20	TOC	3900	4.42	
WEST CHEBUCTO K-20	TOC	3910	3.44	
WEST CHEBUCTO K-20	TOC	3920	2.48	
WEST CHEBUCTO K-20	TOC	3930	2.72	
WEST CHEBUCTO K-20	TOC	3950	3.59	

Well identifier	Surface	MD	TOC	TOC Ave Naskapi plotted
WEST CHEBUCTO K-20	TOC	3950	3.66	
WEST CHEBUCTO K-20	TOC	3950	2.21	
WEST CHEBUCTO K-20	TOC	3960	2.96	
WEST CHEBUCTO K-20	TOC	3970	2.91	
WEST CHEBUCTO K-20	TOC	4000	2.96	
WEST CHEBUCTO K-20	TOC	4010	2.95	
WEST ESPERANTO B-78	TOC	2230	1.55	1.55
WEST OLYMPIA O-51	TOC	2610	0.61	0.82
WEST OLYMPIA O-51	TOC	2620	1.35	
WEST OLYMPIA O-51	TOC	2630	0.79	
WEST OLYMPIA O-51	TOC	2640	0.89	
WEST OLYMPIA O-51	TOC	2650	0.83	
WEST OLYMPIA O-51	TOC	2660	1.26	
WEST OLYMPIA O-51	TOC	2670	1.06	
WEST OLYMPIA O-51	TOC	2680	0.89	
WEST OLYMPIA O-51	TOC	2690	0.87	
WEST OLYMPIA O-51	TOC	2700	0.7	
WEST OLYMPIA O-51	TOC	2710	0.7	
WEST OLYMPIA O-51	TOC	2720	0.71	
WEST OLYMPIA O-51	TOC	2730	0.42	
WEST OLYMPIA O-51	TOC	2740	0.4	
WEST VENTURE N-91	TOC	2830	1.06	1.22
WEST VENTURE N-91	TOC	2860	1.38	

ii. Cross Section 1

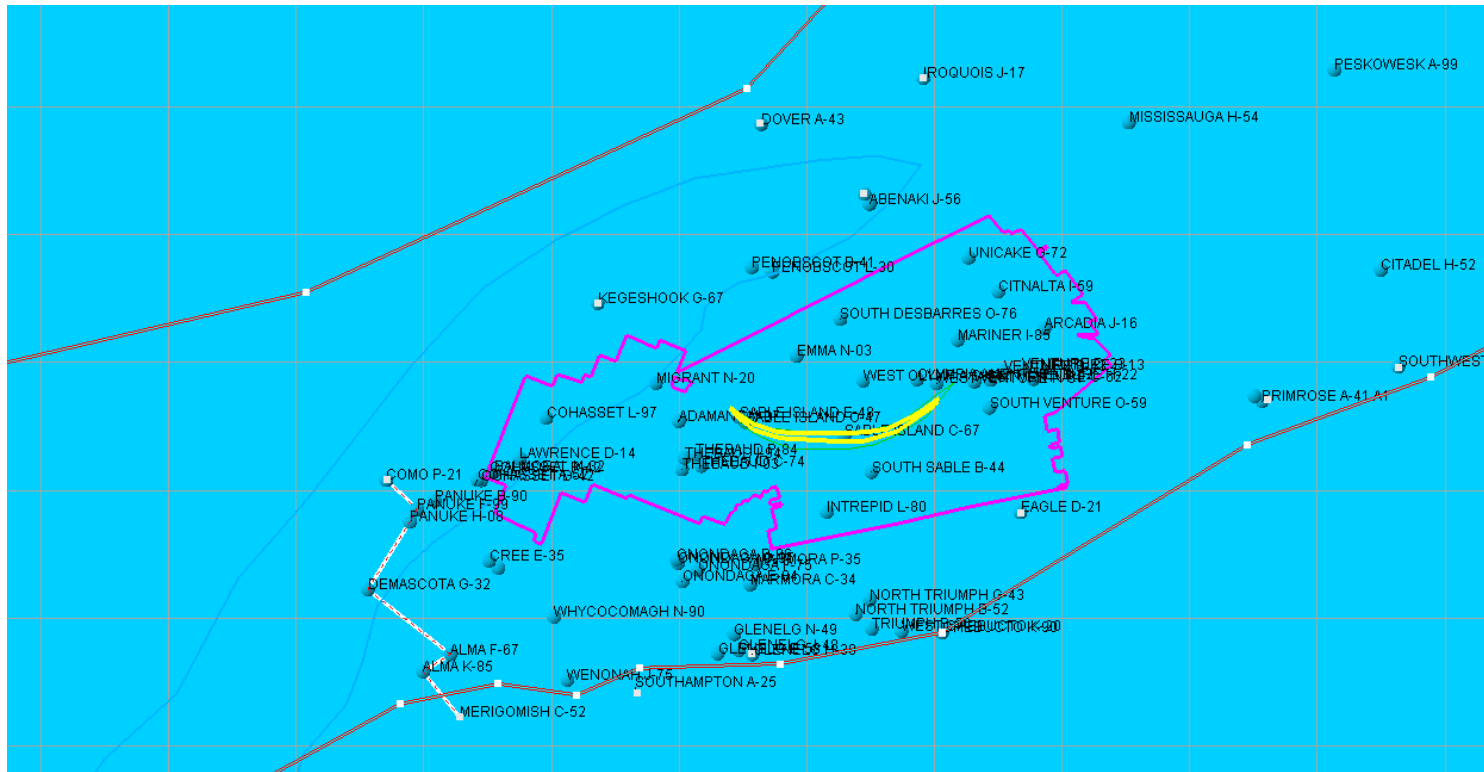


288

CROSS SECTION 1	SAMBRO I-29	300/I-29 43-40 062-45/50
	OJIBWA E-07	300/E-07 43-50 061-45/50
	NASKAPI N-30	300/N-30 43-30 062-30/00
	GLOOSCAP C-63	300/C-63 43-20 062-00/00
	MOHEIDA P-15	300/P15 43-10 062-15/00
	MOHICAN I-100	300/I-00 43-00 062-15/50
	ONEIDA O-25	300/O-25 43-20 061-30/00

iii. Cross Section 2

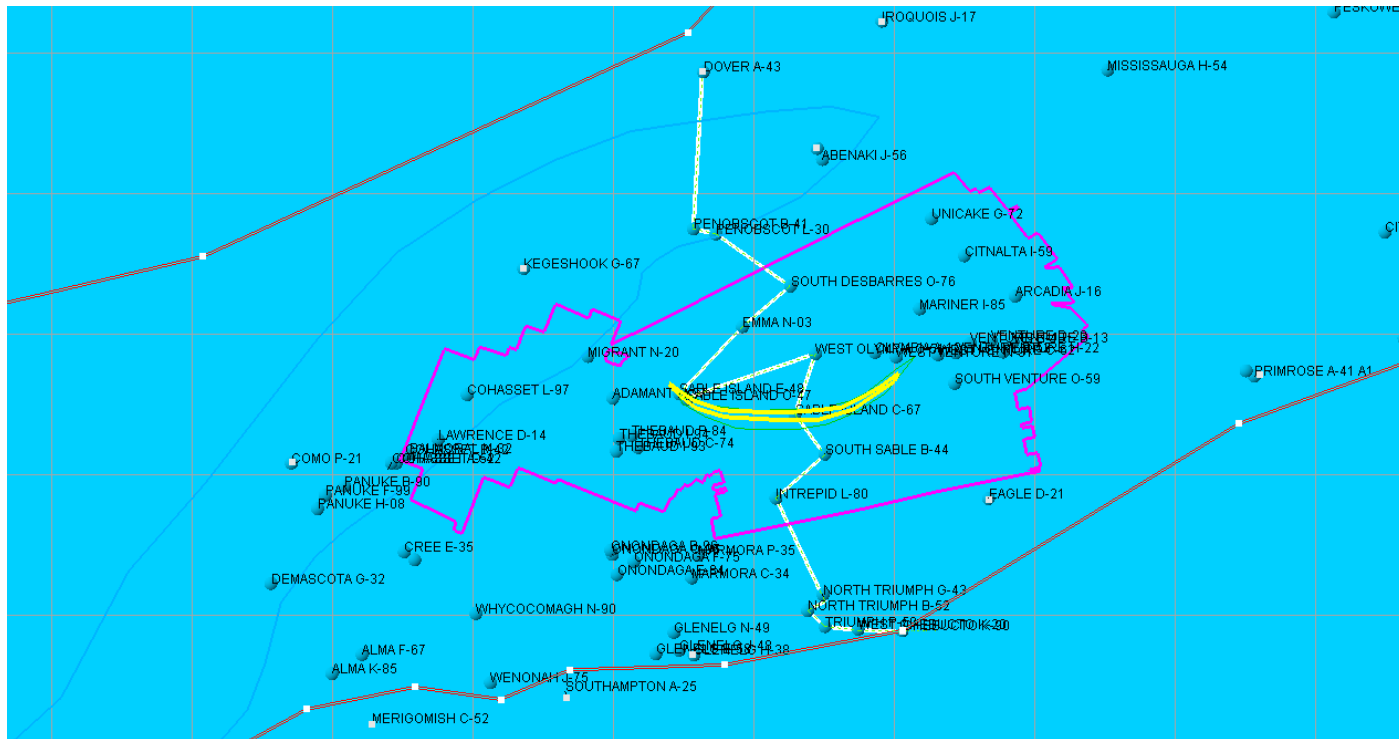
289



CROSS SECTION 2	COMO P-21	300/P-21 44-00 060-45/50
	PANUKE F-99	300/F-99 43-50 060-30/00
	PANUKE H-08	300/H-08 43-50 060-45/00
	DEMASCOTA G-32	300/G-32 43-50 060-45/50
	ALMA F-67	300/F-67 43-40 060-30/00
	ALMA K-85	300/K-85 43-40 060-30/00
	MERIGOMISH C-52	300/C-52 43-40 060-30/00

vi. Cross Section 5

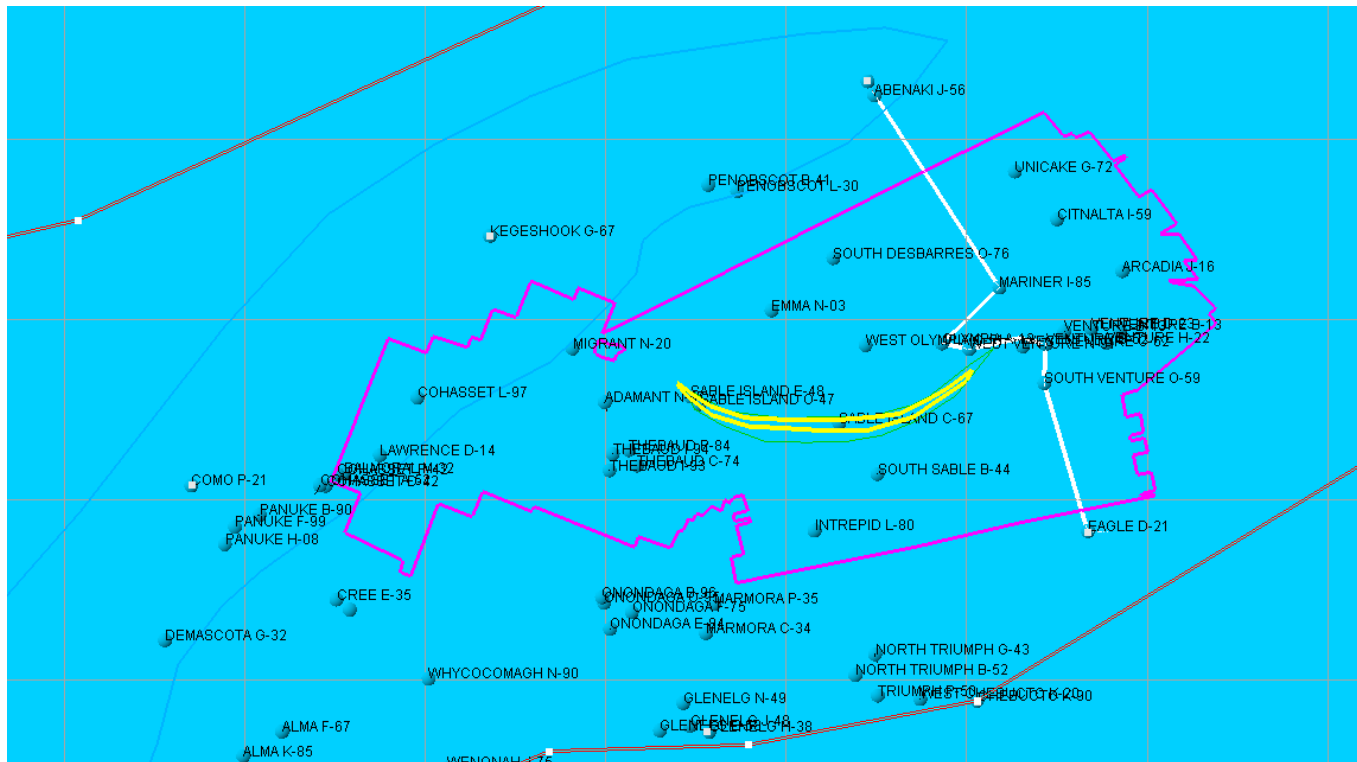
292



CROSS SECTION 5	DOVER A-43	300/A-43 44-30 060-00/00	SABLE ISLAND C-67	300/C-67 44-00 059-45/50
	PENOBSCOT B-41	300/B-41 44-20 060-00/00	SOUTH SABLE B-44	300/B-44 44-00 059-45/50
	PENOBSCOT L-30	300/L-30 44-10 060-00/00	INTREPID L-80	300/L-80 43-50 059-45/50
	SOUTH DESBARRES O-76	300/O-76 44-10 059-45/50	NORTH TRIUMPH G-43	300/G-43 43-50 059-45/50
	EMMA N-03	300/N-03 44-10 060-00/00	NORTH TRIUMPH B-52	300/B-52 43-50 059-45/50
	SABLE ISLAND E-48	300/E-48 44-00 060-00/00	TRIUMPH P-50	300/P-50 43-40 059-45/50
	SABLE ISLAND O-47	300/O-47 44-00 060-00/00	WEST CHEBUCTO K-20	300/K-20 43-40 059-45/50
	WEST OLYMPIA O-51	300/O-51 44-10 059-45/50	CHEBUCTO K-90	300/K-90 43-40 059-30/00

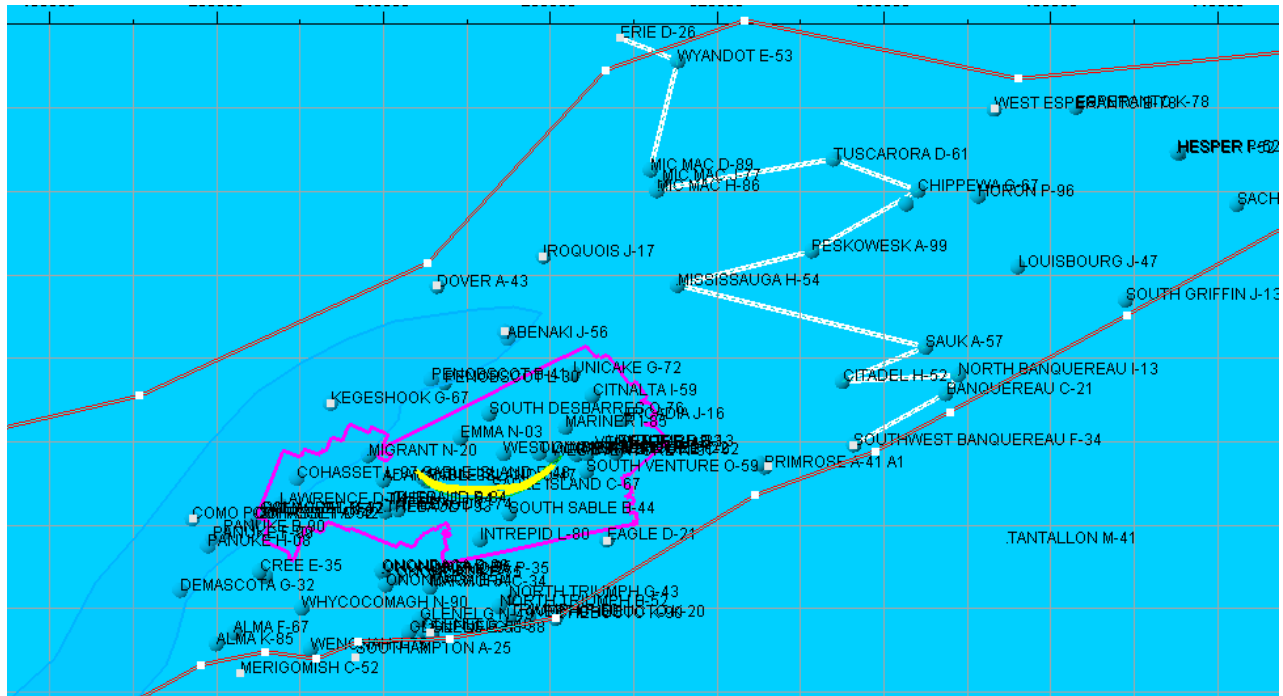
vii. Cross Section 6

293



CROSS SECTION 6	ABENAKI J-56	300/J-56 44-20 059-45/50
	MARINER I-85	300/ I-85 44-10 059-30/00
	OLYMPIA A-12	300/A-12 44-10 059-45/50
	WEST VENTURE N-91	300/N-91 44-10 059-30/00
	WEST VENTURE C-62	300/C-62 44-10 059-30/00
	SOUTH VENTURE O-59	300/O-59 44-00 059-30/00
	EAGLE D-21	300/D-21 44-00 059-30/00

ix. Cross Section 8

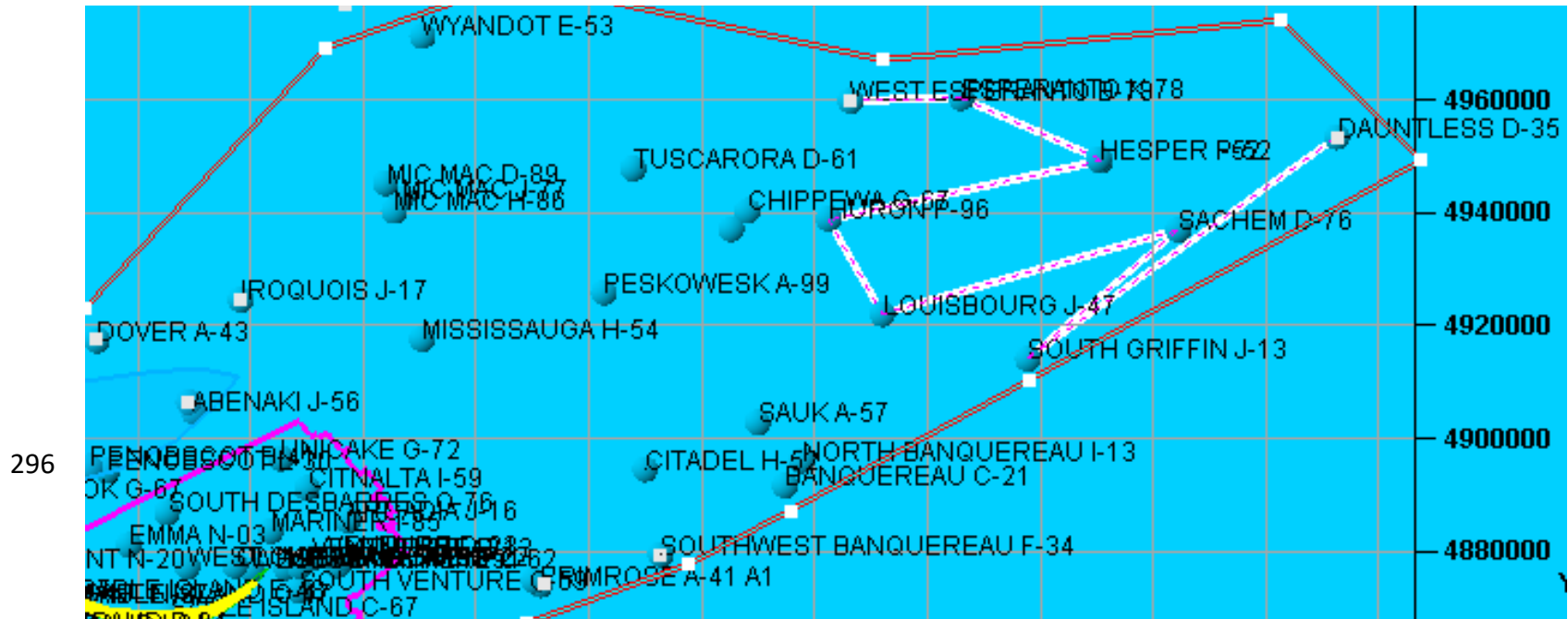


295

CROSS SECTION 8	ERIE D-26	300/D-26 44-55 059-30/00
	WYANDOT E-53	300/N-90 43-40 060-15/50
	MIC MAC D-89	300/D-89 44-40 059-15/50
	MIC MAC J-77	300/J-77 44-40 059-15/00
	MIC MAC H-86	300/H-86 44-40 059-15/00
	TUSCARORA D-61	300/D-61 44-50 058-45/50
	CHIPPEWA G-67	300/G-67 44-40 058-30/00
	PESKOWESK A-99	300/A-99 44-30 058-45/50

MISSISSAUGA H-54	300/H-54 44-30 059-15/50
SAUK A-57	300/A-57 44-20 058-30/00
CITADEL H-52	300/H-52 44-20 058-45/50
NORTH BANQUEREAU I-13	300/I-13 44-20 058-30/00
BANQUEREAU C-21	300/C-21 44-20 058-30/00
SOUTHWEST BANQUEREAU F-34	300/F-34 44-10 058-45/50

x. Cross Section 9



296

CROSS SECTION 9	WEST ESPERANTO B-78	300/B-78 44-50 058-15/50
	ESPERANTO K-78	300/K-78 44-50 058-00/00
	HESPER P-52	300/P-52 44-50 057-45/50
	HESPER I-52	300/I-52 44-50 057-45/50
	HURON P-96	300/P-96 44-40 058-15/50
	LOUISBOURG J-47	300/J-47 44-30 058-15/50
	SACHEM D-76	300/D-76 44-40 057-30/00
	SOUTH GRIFFIN J-13	300/J-13 44-30 058-00/00
	DAUNTLESS D-35	300/D-35 44-50 057-15/50

I. Average Vitrinite Reflectance Values

List of wells that have vitrinite reflectance values in the Naskapi formation in the area of interest.

<i>Well Name</i>	<i>Interval Top</i>	<i>Interval Bottom</i>	<i>Units</i>	<i>AVE VIT R</i>	<i>Ave Standard Dev</i>
ALMA F-67	2565	2840	M	0.62	0.05
ARCADIA J-16	2780	2870	M	0.515	0.055
BANQUEREAU C-21	3140	3530	M	0.616	
CHEBUCTO K-90	3430	3470	M	0.69	0.08
CITADEL H-52	2950	3190	M	0.53	0.04
COHASSET D-42	2247.9	2254.9	M	0.51	
COHASSET L-97	2135	2210	M	0.41	
CREE E-35	2414.05	2542.06	M	0.435	
DAUNTLESS D-35	2743.23	2926.12	M	0.51	
DEMASCOTA G-32	2209.83	2267.74	M	0.43	
DOVER A-43	1680	1680	M	0.43	
EAGLE D-21	3322.36	3557.06	M	0.595	0.065
EVANGELINE H-98	3380	3890	M	0.88	0.055
GLENELG J-48	3150	3390	M	0.705	0.095
GLOOSCAP C-63	1860	2080	M	0.475	0.06
HESPER I-52	2734.09	2734.09	M	0.6	0.08
INTREPID L-80	2828.58	2950.5	M	0.54	0.05
JASON C-20	1228.36	1228.36	M	0.36	
LOUISBOURG J-47	2710	2950	M	0.477	0.05
MERIGOMISH C-52	2515	3200	M	0.59	0.076
MIGRANT N-20	2343.94	2407.95	M	0.45	
MOHICAN I-100	2225.07	2346.99	M	0.336	
NASKAPI N-30	1325.9	1405.15	M	0.536	
NORTH BANQUEREAU I-13	3085	3395	M	0.64	0.06
NORTH TRIUMPH B-52	3415	3715	M	0.675	0.055

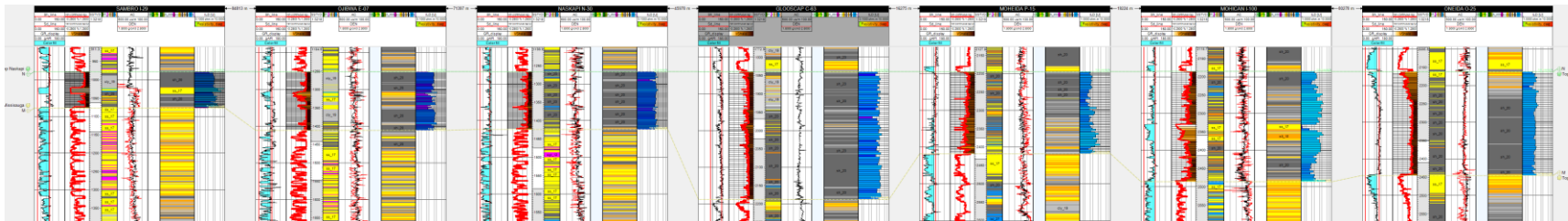
Well Name	Interval Top	Interval Bottom	Units	AVE VIT R	Ave Standard Dev
NORTH TRIUMPH G-43	3360	3710	M	0.6	0.05
OLYMPIA A-12	2795	2860	M	0.57	0.06
ONEIDA O-25	2255.55	2377.47	M	0.49	
ONONDAGA B-96	2468.91	2651.79	M	0.5	0.05
ONONDAGA E-84	2590.83	2691.42	M	0.45	
PANUKE B-90	2196.7	2217.7	M	0.58	
PENOBSCOT L-30	2212.87	2212.87	M	0.38	
SABLE ISLAND C-67	2770.67	2956.6	M	0.51	0.04
SABLE ISLAND E-48	2417.09	2517.68	M	0.47	0.06
SABLE ISLAND O-47	2475.01	2475.01	M	0.39	
SACHEM D-76	2840.77	2950.5	M	0.49	
SAUK A-57	2926.12	3139.48	M	0.57	
SOUTH DESBARRES O-76	2300	2465	M	0.41	
SOUTH GRIFFIN J-13	2840	3215	M	0.59	0.066
SOUTH SABLE B-44	2910	2910	M	0.52	0.04
SOUTH VENTURE O-59	2950	2950	M	0.6	0.08
SOUTHWEST BANQUEREAU F-34	3550	3915	M	0.84	0.084
TANTALLON M-41	5145	5155	M	0.68	0.05
THEBAUD C-74	2550	2620	M	0.43	
THEBAUD I-93	2560	2650	M	0.54	0.05
THEBAUD P-84	2560.35	2560.35	M	0.51	
TRIUMPH P-50	3200.44	3505.24	M	0.59	
UNIACKE G-72	2495	2505	M	0.53	0.06
VENTURE B-13	2865	2900	M	0.56	0.035
VENTURE B-43	2880	2940	M	0.99	0.06
VENTURE B-52	2860	3045	M	0.56	0.053
VENTURE H-22	2850	2940	M	0.58	
WENONAH J-75	2816.39	3048.04	M	0.72	0.08

Well Name	Interval Top	Interval Bottom	Units	AVE VIT R	Ave Standard Dev
WEST CHEBUCTO K-20	4445	4500	M	0.81	
WEST ESPERANTO B-78	2190	2335	M	0.46	0.04
WEST OLYMPIA O-51	2670	2670	M	0.58	0.06
WEST VENTURE N-91	2860	2860	M	0.64	0.05

J. Cross Sections 1-9

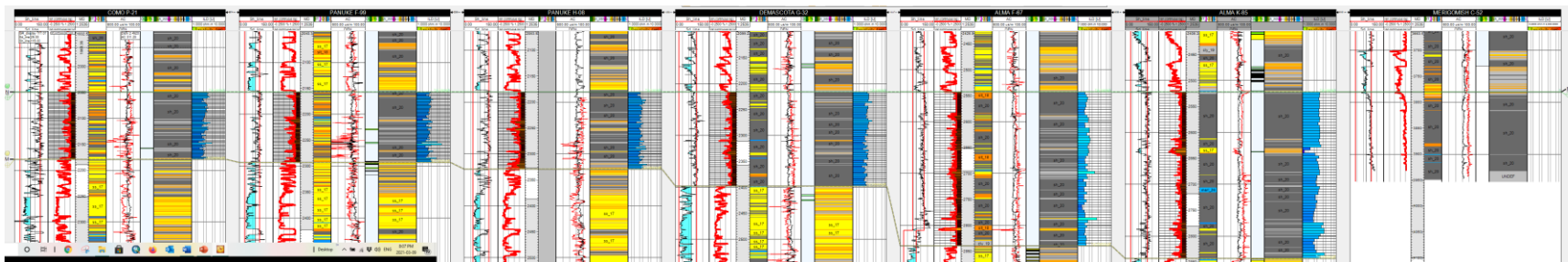


Cross Section 1



300

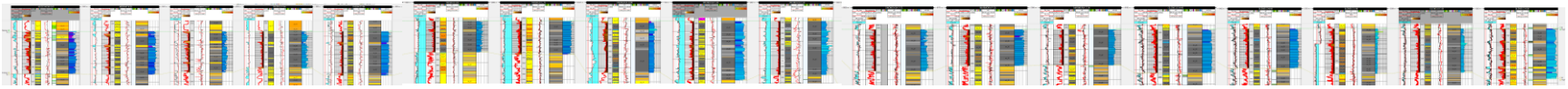
Cross Section 2



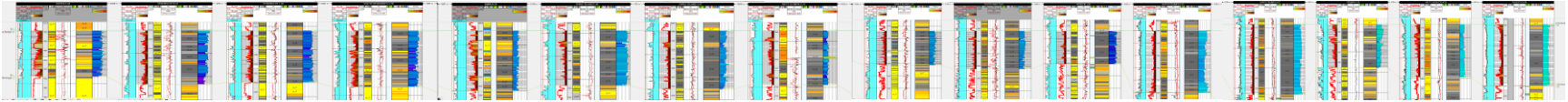
Cross Section 3



Cross Section 4

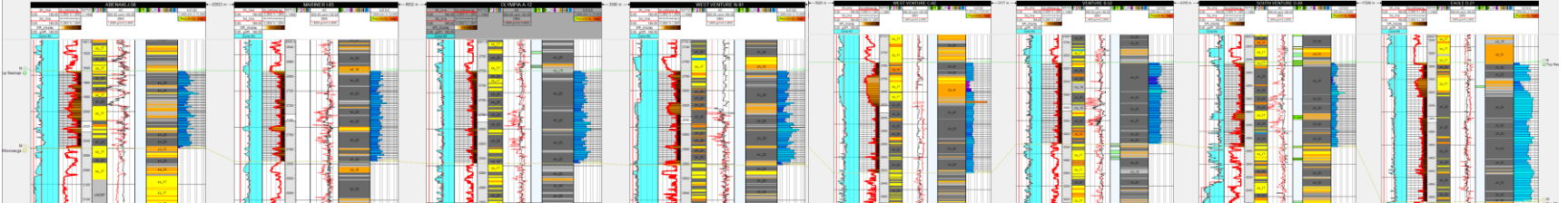


Cross Section 5

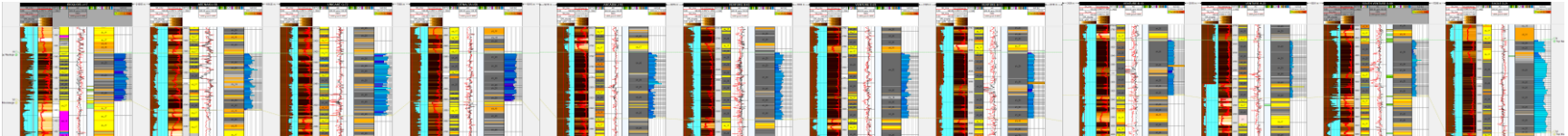


301

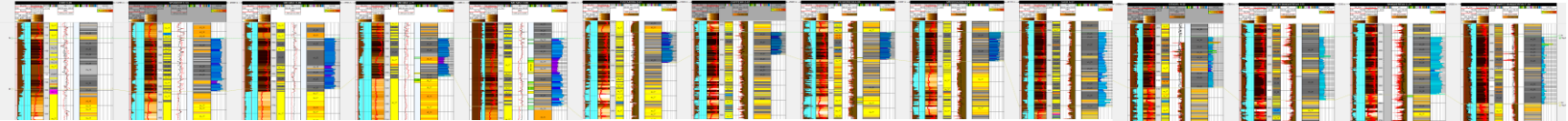
Cross Section 6



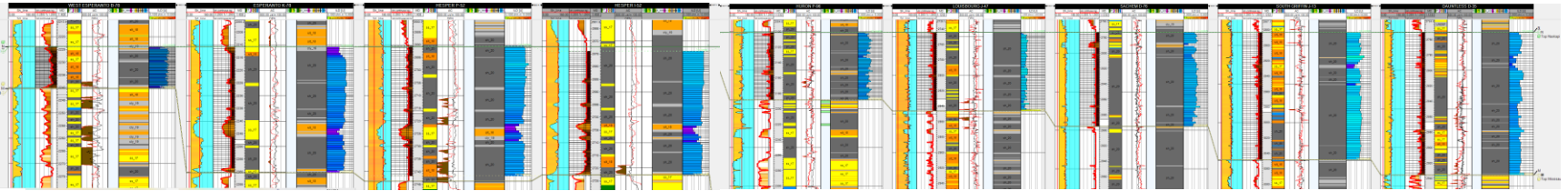
Cross Section 7



Cross Section 8



Cross Section 9



Appendix K: Anne Hargreaves Thesis Committee

Supervisor:

Dr. Grant Wach

Committee Members:

David Brown

Bill Richards

Appendix L: List of Equations

Equation 4.1: *Organic matter enrichment*

Equation 5.1: *Resistance*

Equation 5.2: *Resistivity*

Equation 5.3: *Resistivity R_o*

Equation 5.4: *Sonic derived porosity Φ_s*

304 Equation 5.5: *% Solid Space*

Equation 5.6: *Porosity Φ*

Equation 5.7: *Geothermal gradient G*

Equation 5.8: *Hydrogen Index*

Equation 5.9: *Oxygen Index*

Equation 5.10: *Production Index*

Appendix M: Extended Abstract

Identifying organic-rich intervals that contribute to viable source rocks helps in understanding petroleum systems and reducing risk in hydrocarbon exploration. The distal Cretaceous and Jurassic shale section offshore Nova Scotia has been viewed as a lean source rock. However, it is uncertain if there are sufficient concentrations of strata with elevated total organic carbon (TOC) values to form the continuous fluid phase necessary for effective primary hydrocarbon generation and migration. In many parts of the world, Cretaceous Oceanic Anoxic Events (OAE's) are associated with significant amounts of organic-rich matter which, with sufficient thermal maturity, have generated prolific volumes of petroleum.

The fluvial-deltaic successions of the Cretaceous Logan Canyon and Cretaceous-Upper Jurassic Missisauga formations in the Sable Subbasin, offshore Nova Scotia, have been the main sources of hydrocarbon production since the early 1990s. The distal and laterally equivalent stratas of the Jurassic-Cretaceous Verrill Canyon Formation (Bajocian – Barremian) and the Logan Canyon Formation (Aptian – Albian) are transgressive shale sequences within the two sand-rich successions. These appear to correspond to global oceanic anoxic events (OAEs). The Aptian Naskapi Member of the Logan Canyon formation is a significant one and is the focus of this study.

305 Datasets from 95 wells on the Scotian Shelf were examined, incorporating temperature, total organic carbon, x-ray fluorescence, gamma ray, sonic, density and neutron wireline logs, lithological descriptions from cuttings and cores, data on sedimentation rates, paleo-ocean currents and seismic interpretations of the Naskapi Member. This analysis resulted in the creation of an extensive suite of isochore maps and 3-D models. The ensuing maps portray the stratigraphy, sedimentology, and diagenesis of the Naskapi depositional interval.

When comparing existing levels of total organic carbon from the Scotian Basin with those from OAE's found elsewhere in the world, the Cretaceous Naskapi Member exhibits lower levels of organic matter. The results of this investigation demonstrate:

- a) A high delta-derived sediment load focused in the Sable Subbasin during the Cretaceous that resulted in high dilution rates of organic matter.
- b) The direction and strength of the ocean current regime during the Aptian was not conducive to sufficient preservation of organic matter.

Comparison of the Scotian Margin with time equivalent Cretaceous deposits from elsewhere on the circum-Atlantic margin, indicates that volumetrically insignificant amounts of organic-rich intervals with high TOC values are found, resulting in ineffective Cretaceous source rock. This is a result of paleo-ocean current patterns and the high volume of sediments shed from the adjacent Appalachian Mountains, which served to dilute the concentration of and impede the preservations of organic-rich intervals.